# The development of a fully suspended AMB system for a high-speed flywheel application

---

A dissertation presented to

The School of Electrical, Electronic and Computer Engineering

North-West University

---

In partial fulfilment of the requirements for the degree

Magister Ingeneriae

in Electrical and Electronic Engineering

by

Stefan Myburgh

Supervisors: Prof. G. van Schoor
Mr. E.O. Ranft

November 2007

Potchefstroom Campus

# *DECLARATION*

I hereby declare that all the material incorporated in this thesis is my own original unaided work except where specific reference is made by name or in the form of a numbered reference. The word herein has not been submitted for a degree at another university.

Signed: _____

Stefan Myburgh

# *SUMMARY*

The School of Electrical, Electronic and Computer Engineering at the North-West University is currently in the process of developing an active magnetic bearing (AMB) laboratory. The idea is to establish a knowledge base on AMBs within the school to support industries that make use of the technology. AMBs are seen as an enabling technology in a number of applications e.g. high-speed blowers and the Pebble Bed Modular Reactor (PBMR) where the oil in the bearings on the blowers poses a contamination risk. This project will be an application of the knowledge gained from past research on AMBs and control algorithms. Currently the most advanced AMB model within the McTronX research group is limited to four axes of freedom.

The main purpose of the project is the development of a fully suspended (five degrees of freedom) active magnetic bearing (AMB) system for a flywheel energy storage system (FESS) application. The FESS will be able to deliver 2 kW of electrical energy to a load for a period of 3 minutes. A high-speed permanent magnet synchronous machine (PMSM) is developed within the McTronX research group for the specific FESS application. The developed PMSM propels the rotor/flywheel at 30,000 rpm in order to mechanically store 527 kJ of energy. The rotor/flywheel is suspended by two radial AMBs and one axial AMB. The areas of focus that are addressed include the AMB system, the electrical control enclosure that will house the electrical system and the user interface. The system will be developed to and industrial standard.

An iterative design process was devised together with a simulation model for the AMB system in order to develop the 5-axis AMB system. The output parameters of the AMB design process were implemented in the simulation model in order to accurately simulate the responses of the AMBs. After the AMB designs were verified by means of simulation, the AMBs were implemented and the electrical components were sourced according to the specifications derived from the design process. The electrical control enclosure was also designed by means of simulation and the required components were sourced after verification by means of simulation. The interface board, the RTD drivers and the over-speed protection system were developed in-house along with the ControlDesk® graphical user interface (GUI) which enables the user to control the entire Fly-UPS system from a standalone personal computer.

The system was extensively tested to verify the stiffness and damping characteristics of the AMBs and the electrical system is determined to be fully functional. The sensitivity of the AMBs are characterised as being in zone A (which is the zone in which newly commissioned machines fall) in accordance to the ISO CD 14839-3 standard on magnetic bearings. The project will enable future research on the development and optimisation of flywheel energy storage systems as well as the optimisations of control algorithms and the implementation of redundancy within AMB systems.

# *ACKNOWLEDGEMENTS*

I would firstly like to thank M-Tech Industrial for funding this research and granting me the opportunity to further my studies.

I would also like to acknowledge the following people/entities, for their contributions during the course of this project:

- Professor George van Schoor, my supervisor, for his advice, patience and support;
- Mr. Eugén Ranft, my supervisor and the project leader, for his advice and guidance;
- Prof. Robert Holm, the designer of the PMSM;
- Instrument Manufacturers at North-West University for manufacturing;
- Hennie van Zyl, instrument maker, for his guidance and insight;
- My father Vic Myburgh and my mother Riëtte Myburgh for their advice and support;
- My friend and colleague (through tough times), Jan Janse van Rensburg.

*“To man belong the plans of the heart, but from the Lord comes the reply of the tongue.” Proverbs 16:1*

# *TABLE OF CONTENTS*

# NOMENCLATURE

## LIST OF FIGURES

# LIST OF TABLES

# LIST OF ABBREVIATIONS

| | |
|---|---|
| ac | Alternating current |
| ADC | Analogue to digital converter |
| AMB | Active Magnetic Bearing |
| CAD | Computer Aided Design |
| DAC | Digital to analogue converter |
| dc | Direct current |
| EM | Electromagnetic |
| EMI | Electromagnetic Interference |
| FEM | Finite Element Method |
| FESS | Flywheel Energy Storage System |
| IC | Integrated circuit |
| MMF | Magneto Motive Force |
| PA | Power Amplifier |
| PBMR | Pebble Bed Modular Reactor |
| PC | Personal Computer |
| PCB | Printed Circuit Board |
| PMSM | Permanent Magnet Synchronous Machine |
| PWM | Pulse Width Modulation |
| rms | Root mean square |
| rpm | Revolutions per minute |
| RTD | Resistive Temperature Detector |
| UPS | Uninterruptible Power Supply |

# LIST OF SYMBOLS

| | |
|---|---|
| $A_g$ | Air gap area |
| $B$ | Magnetic flux density |
| $b_{eq}$ | Equivalent damping |
| $C$ | Capacitance |
| $d$ | Duty cycle |
| $E$ | Electrical energy |
| $F$, $F_m$ | Electromagnetic force |
| $g$, $g_0$ | Air gap length |
| $G_s(s)$ | System open loop transfer function |
| $H$ | Magnetic field intensity |

| | |
|---|---|
| $I$ | rms / dc value of current |
| $i$ | Instantaneous current |
| $i$, $i_0$, $i_m$ | Control, bias and electromagnet currents respectively |
| $K_D$ | Differential gain of the PD controller |
| $k_{eq}$ | Equivalent position stiffness |
| $k_i$ | Force-current factor |
| $k_m$ | Electromagnet constants |
| $K_P$ | Proportional gain of the PD controller |
| $k_s$ | Force-displacement factor |
| $\ell$ | Magnetic path length |
| $L_c$ | Coil inductance |
| $m$ | Suspended body mass / current slope |
| $N$ | Number of coil turns |
| $P$ | Electrical power |
| $P.O.$ | Percentage overshoot |
| $Q$ | Electrical charge / thermal power |
| $R$ | Electrical resistance |
| $R_{coil}$ | Coil resistance |
| $R_\theta$ | Thermal resistance |
| $S$ | Apparent power |
| $s$ | Complex frequency |
| $T$ | Temperature |
| $t_{rr}$ | Reverse recovery time |
| $T_s$ | Settling time |
| $V$ | rms / dc value of voltage |
| $v$ | Instantaneous voltage |
| $x$, $x_0$, $x_s$ | Rotor position |
| $\omega$ | Rotational speed |
| $\omega_n$ | Natural frequency |
| $\zeta$ | Damping factor |
| $\Phi$ | Magnetic flux |
| $\theta$ | One half of the stator pole pitch |

# 1
# Chapter
# Introduction

*Chapter 1 firstly provides introductory information on high speed flywheels and active magnetic bearings in general. The problem statement is given, followed by the issues to be addressed and the methodology.*

## 1.1 Background

The School of Electrical, Electronic and Computer Engineering at the North-West University is in the process of developing an active magnetic bearing (AMB) research laboratory. The aim is to establish a knowledge base on AMBs in support of industries that make use of this environmentally friendly technology. AMB technology is seen as one of the technology drivers for the Pebble Bed Modular Reactor (PBMR) project currently in development in South Africa and is predicted to become largely conventional in this application.

The McTronX research group at the North-West University has done research on magnetically suspending objects and has successfully developed a 4 axis suspended rotor. The knowledge gained from previous experiments will be used to develop a fully suspended system. As an application of the AMB technology, a flywheel energy storage system (FESS) will be developed which will feature a fully magnetically suspended flywheel/rotor.

### *1.1.1 High speed flywheels*

Despite its current high-tech appearance, the flywheel is one of society's oldest inventions dating back to the time of the bible. These flywheels were purely mechanical consisting of a stone wheel attached to an axle. Today flywheels are complex machines which store energy mechanically and are able to transfer energy to- and from the flywheel by making use of a motor/generator set. The stone wheel has been replaced by a steel or carbon-fibre rotor which allows for higher rotational speeds as well as higher energy storage capacity. Many flywheels also run on magnetic bearings to reduce friction and allow for higher efficiency of energy storage [1].

### 1.1.2 Active magnetic bearings

The idea of suspending an object with magnetism was first conceived in the mid-1800s and since then many experiments and developments have taken place. In the field of engineering, magnetic bearings for practical application became a reality in the 1960s [2]. At that time magnetic bearings were characterized as being costly, specially designed systems for large scale applications such as gas compressors, power generation turbines etc.

A functional diagram of an active magnetic bearing (AMB) is shown in Figure 1-1. The system functions by using a sensor which measures the displacement of the rotor from its reference position. The controller derives a control signal from the measurement and the power amplifier transforms this control signal into a control current which generates the magnetic forces within the actuating magnet.

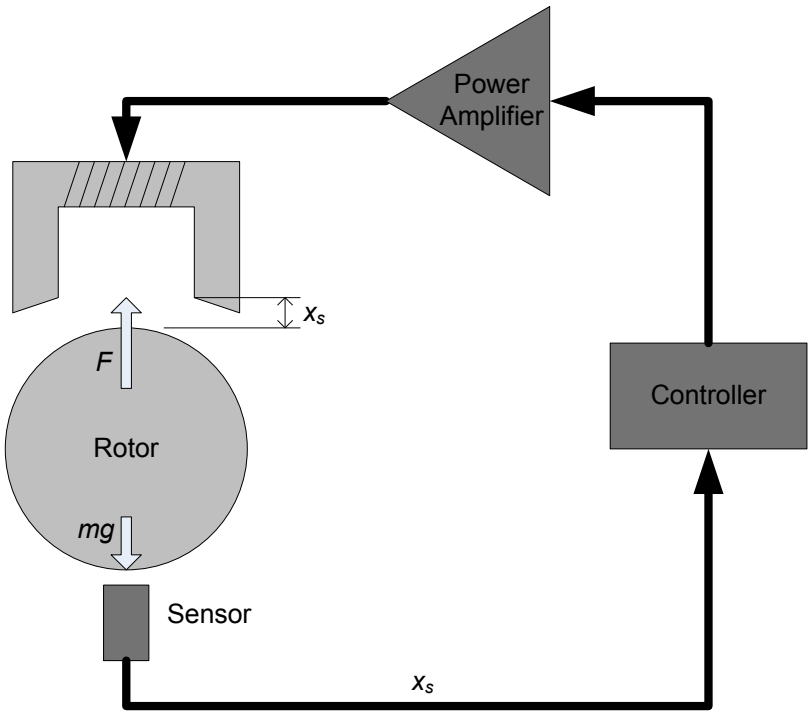


**Figure 1-1: AMB functional diagram**

## 1.2 Problem statement

The main purpose of the project is the development of a fully suspended active magnetic bearing (AMB) system for a flywheel energy storage system (FESS) application. The FESS will store energy mechanically in the flywheel and act as an uninterruptible power supply (UPS) when a power dip or power failure occurs. The FESS will be able to deliver 2 kW of power for a period of 3 minutes and will be named Fly-UPS. Figure 1-2 shows a breakdown of the Fly-UPS system. The areas which will be focused on include the two radial active magnetic bearings as well as the axial magnetic bearing

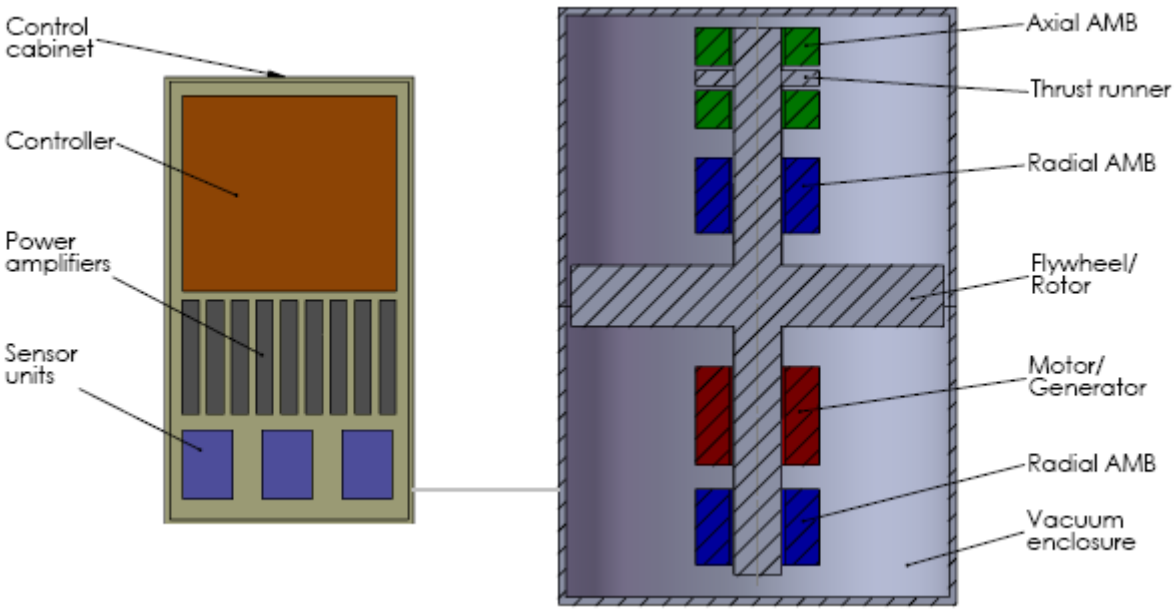


**Figure 1-2: Fly-UPS system diagram**

which will suspend the rotor/flywheel up to an operating speed of 30,000 rpm. The electrical cabinet will also form part of the project. The electrical cabinet will house the electrical system of the Fly-UPS system including the controller, the power amplifiers and the sensor units and the over-speed protection system. All the electrical systems will be integrated into one industrial standard electrical cabinet and interfaced with the dSPACE® controller. The dSPACE® controller is connected to a stand-alone personal computer running a ControlDesk® GUI which enables the operator to control the Fly-UPS system.

## 1.3 Issues to be addressed

### *1.3.1 System specification*

The main goal of this project is to design and implement a 5-axis Active Magnetic Bearing (AMB) system for a flywheel energy storage system (FESS). A detailed type-A specification has to be created in order to address the necessary requirements of the system. A type-A specification is a broad specification of the system in its entirety. After the type-A specification is drawn up type-B specifications will be derived which are detailed specifications of the various sub-systems of the Fly-UPS system.

### 1.3.2 Design process

A design process has to be devised in order to effectively design and implement the AMB system for the FESS as well as the electrical system for the Fly-UPS system. The design process has to be iterative in order to find the optimal design parameters.

### 1.3.3 System modelling

An accurate simulation model of the complete system must be developed from the physical model design parameters. The simulation forms an integral part of the design process and will be used to confirm the design and verify analytical predictions. Parameters for the controller, sensor and power amplifier will be verified with the detailed system simulation.

### 1.3.4 Hardware procurement

Low loss AMBs will be designed because it is a crucial part of the FESS. A major contributing factor in determining the overall efficiency of the system will be the efficiency of the AMBs. The AMBs will be designed to generate minimal amounts of heat as heat dissipation becomes a major issue in machines operating inside a vacuum. Hardware items which will be sourced include the following:

**Power amplifiers**

The Power Amplifiers (PAs) have to be off-the-shelf products. Factors like the efficiency, the maximum required current in the magnetic actuators and the bandwidth of the PAs will play a major role in deciding on which PAs will to use.

**Sensors**

The system requires displacement sensors to measure the position of the rotor. A radial AMB requires two displacement sensors and an axial AMB requires one displacement sensor. The sensors need to be accurate and be able to operate in conditions with high magnetic interference.

The temperatures of the coils of the AMBs will also have to be monitored as well as the temperature of the windings of the PMSM in order to ensure safe operation. The temperature of the rotor closest to the magnets of the PMSM will also have to be monitored in order to ensure that the maximum rated temperature of the magnets is not exceeded.

A speed sensor also has to be employed to monitor the rotational speed of the flywheel rotor. The speed sensor will act as an over-speed monitoring device to ensure that the maximum rated speed of the rotor/flywheel is not exceeded. Since the rotor/flywheel assembly of the Fly-UPS system will operate inside a vacuum, a vacuum sensor will be needed to monitor the pressure inside the mechanical enclosure.

**Controller**

A dSPACE® development system will be used to control the Fly-UPS system. The dSPACE controller features A/D- and D/A converters as well as a high I/O capacity. The dSPACE controller interfaces with a personal computer with a GUI which controls the system.

### *1.3.5 System integration*

After the development of the physical AMB hardware and the electrical enclosure, all the various electrical sub-systems have to be interfaced with the controller and the electrical enclosure has to be interfaced with the mechanical system into a fully functional system.

### *1.3.6 System evaluation*

After completion of the system integration, the model should be evaluated. The stiffness and damping parameters of the AMBs have to be experimentally verified as well as the sensitivity of the three AMBs in accordance to the ISO CD 14839-3 standard on magnetic bearings. The predicted values will be compared to the actual results and the degree of correlation will determine the effectiveness of the design process.

## 1.4 Research methodology

### *1.4.1 System specification*

A major part of the Fly-UPS project is the mechanical design of the flywheel which is done within the McTronX research group. Type-A specifications will be drawn up including the specifications for the AMB system, the electrical system, the flywheel and the mechanical enclosure. This information will be used as a starting point for the detailed system design.

System specifications will be compiled from information gathered from literature and the requirements of the end user. When the system specifications are drawn up, conceptual designs are done. With the conceptual designs in mind, detailed type-B specifications are drawn up for the various sub-systems of the Fly-UPS system.

### *1.4.2 Design process*

Figure 1-3 shows the design process that will be followed in the design of the AMB system. The mechanical specifications will be used to do a preliminary mechanical design of the flywheel. These design parameters will then be used to draw up the AMB specification. The preliminary AMB design

is then done and the system is evaluated. If the designs are not satisfactory the design procedure will be repeated until all the specifications are met. The AMB system will then be implemented.

The electrical system will be designed by making use of MultiSim® because it is able to simulate the operation of relays, contactors etc. which will be used in the protection circuit. It is also capable of PCB layout.

The system has to be constructed using off-the-shelf components as far as possible. The only major component that will be specifically designed for the system is the PMSM which will be designed within the McTronX research group as it is an application specific component.

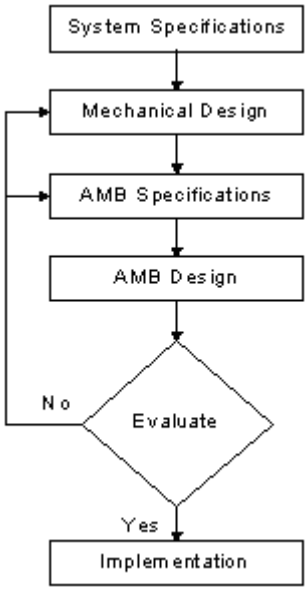


**Figure 1-3: Design Process**

### *1.4.3 System modelling*

A detailed and accurate model of the system will be developed using parameters obtained from the physical model design. This model will then be used to simulate the system response in MATLAB®'s Simulink® environment. The simulation enables the design and testing of the control system. Power amplifier and sensor specifications can also be extracted from the simulation. The design parameters will be updated using the simulation parameters and the process will be repeated until the correlation between these two sets of parameters is adequate.

### *1.4.4 Hardware procurement*

In order to design a low loss radial AMB, properties of laminated silicon steel will be investigated. The journals of the radial AMBs will be constructed of 0.35 mm silicon steel laminations which will

minimise eddy-current losses and increase overall efficiency of the AMBs. The stator of the radial AMBs will also be constructed of 0.35 mm silicon steel laminations. The axial AMB will be a non-symmetric configuration since the top actuator of the axial AMB will have to support the weight of the rotor/flywheel and exert the design dynamic force on the rotor. The bottom actuator of the axial AMB will only have to exert the design dynamic force. The axial AMB will be constructed from mild steel since the axial AMB is not in the presence of a rotating magnetic field which can induce eddy-currents.

**Power amplifiers**

The Fly-UPS system makes use of three AMBs; two radial- and one axial AMB. One radial AMB requires four power amplifiers (PAs) and an axial AMB require two PAs. This translates to ten PAs in the system. With the dimensions and weight of the flywheel/rotor in mind, the AMB hardware design yields the specifications of the PAs. The required amplifiers will be sourced together with an isolated power supply to power the PAs.

**Sensors**

From past experience Eddy-current sensors are chosen as displacement sensors because they can measure displacement on rotating surfaces and they offer high accuracy measurements. Eddy-current sensors are robust to operate at high temperatures. Theses sensors are also capable of operating in environments with high magnetic interference as is the case with magnetic bearings.

The temperature of the coils of the AMBs as well as the temperature of the windings of the PMSM will be monitored. Temperature sensors capable of operating at high temperatures will be investigated. The temperature sensors also have to compact in order to insert them into the coils of the AMBs and the PMSM windings.

An industrial standard pressure transducer will be investigated to monitor the pressure inside the mechanical enclosure. The pressure transducer will have be able to measure absolute pressure and has to be interfaced with the controller.

Non-contact speed sensors will also be investigated. This sensor will be used in the mechanical enclosure to monitor the rotational speed of the rotor/flywheel. The speed sensors' driver will have to be interfaced with the controller.

**Controller**

A dSPACE® development controller will be used to control the Fly-UPS system as it can be used for real-time development of the control software. The dSPACE® controller comprises of a high-speed A/D converter board, a multiplexed A/D board, a high-speed D/A board, a multi channel I/O board and a digital signal generation board. The dSPACE® controller is interfaced with a personal

computer running the Windows XP operating system via a fibre-optic cable. The software that is supplied with the dSPACE® development kit integrates with modelling software such as MATLAB® and Simulink® simplifies the control software development.

An interface board is used to interface the dSPACE® real time development system with the physical system. The main objectives of the interface board are to isolate the controller from high voltages and to scale the sensor signals to make them compatible with the dSPACE® controller. The interface board will also interface the power amplifiers and the various sensors within the system with the dSPACE® controller.

### *1.4.5 System integration*

After the development of the physical AMB hardware by an independent contractor, the electrical control enclosure will be developed which integrates all the various electrical sub-systems into one industrial electrical enclosure unit. The electrical enclosure houses the power amplifiers, the sensor drivers, the interface board, the over-speed protection circuit, the resistor bank and the dSPACE® controller. After completion of the electrical enclosure, the electrical system is interfaced with the mechanical system into a fully functional high-speed flywheel energy storage system.

### *1.4.6 System evaluation*

The Fly-UPS system will be evaluated against the type-A and B specifications. Various tests will be done on the AMBs in order to verify the stiffness and damping characteristics by making use of step disturbances on the rotor/flywheel. The sensitivity of the AMBs will also be verified by injecting a sinusoidal disturbance into the control loops of the AMBs. The output of the sensitivity analysis will then yield the sensitivity of the AMBs in accordance to the ISO CD 14839-3 standard on magnetic bearings. It will also display the natural frequencies of the rotor/flywheel which will be compared with the rotor-dynamic analysis done on the rotor/flywheel. The stability of the control system will also be tested because it must be able to operate under extreme conditions in industrial applications for prolonged periods of time.

## 1.5 Overview of the dissertation

Chapter 2 contains a detailed literature study on flywheel energy storage and active magnetic bearings (AMBs). It starts with an introduction to high speed flywheels and then discusses the basic operating principles of flywheels, a comparison to other power storage technologies and finally application areas of flywheels. AMBs are then discussed including the main components of an AMB system. Displacement sensors are also discussed followed by the PD controller design.

Chapter 3 contains detailed radial and axial AMB designs. First the design process that was followed is explained. This is followed by a detailed AMB specification that highlights the aspects of magnetic bearings that should be considered in the design process. This is followed by a detailed radial AMB design and a detailed axial AMB design. Finally the implementation of the three AMBs is discussed.

Chapter 4 contains a detailed electrical system design. First the design process that was followed is explained. This is followed by a detailed sub-system specification that highlights the aspects of the various sub-systems that should be considered in the design process. This is followed by a detailed sub-system design. Finally the implementation of the various sub-systems into the electrical enclosure is discussed.

Chapter 5 contains a detailed description of the Simulink® model of the controller of the Fly-UPS system as well as the layout of the Graphical User Interface (GUI) which was implemented in order to control the Fly-UPS system.

Chapter 6 starts off with a verification of the system's stiffness and damping characteristics by making use of a step response on each of the AMBs. This is followed by a verification of the sensitivity of the three magnetic bearings in accordance to the ISO CD 14839-3 standard on stability margins of AMBs.

Chapter 7 starts off with a discussion on the stiffness and damping discrepancies encountered within the experimental results. Conclusions are then drawn with regards to the active magnetic bearings as well as the electrical enclosure. Finally future work on the system is discussed followed by a closure statement.

*Chapter 1 gave some background on flywheels and AMBs after which the problem statement was given. The issues that need to be addressed are highlighted as well as the methodology that will be followed. A short overview of the dissertation is also presented. Chapter two contains a detailed literature study on some of the aspects needed to successfully complete the project*

# 2
# Chapter

# Literature study

*Chapter 2 contains a detailed literature study on Flywheel energy storage and Active Magnetic Bearings (AMBs). It starts with an introduction to high speed flywheels and then discusses the basic operating principles of flywheels, a comparison to other power storage technologies and finally application areas of flywheels. AMBs are then discussed including the main components of an AMB system. Displacement sensors are also discussed followed by the PD controller design.*

## 2.1 Introduction to high speed flywheels

Despite its current high-tech appearance, the flywheel is one of society's oldest inventions dating back to the time of the bible. These flywheels were purely mechanical consisting of a stone wheel attached to an axle. Today flywheels are complex machines that store energy mechanically and are able to transfer energy to- and from the flywheel by making use of a motor/generator set. The stone wheel has been replaced by a steel or carbon-fibre rotor that allows for higher rotational speeds as well as higher energy storage capacity. Many flywheels also run on magnetic bearings to reduce friction and allow for higher efficiency of energy storage [1].

Figure 2-1 shows a typical flywheel system with the main mechanical components sealed in a vacuum chamber. The flywheel and rotor are suspended by two radial active magnetic bearings (AMBs) and one axial AMB. The motor/generator powers the flywheel, spinning it up to its operating speed and acts as a generator when a power dip occurs. The flywheel is operated in a vacuum to reduce windage losses and thereby increasing the overall efficiency of the system. The flywheel system also has a controller unit that comprises a digital controller, power amplifiers to drive the AMBs and sensor drivers to drive the various sensors within the mechanical enclosure.

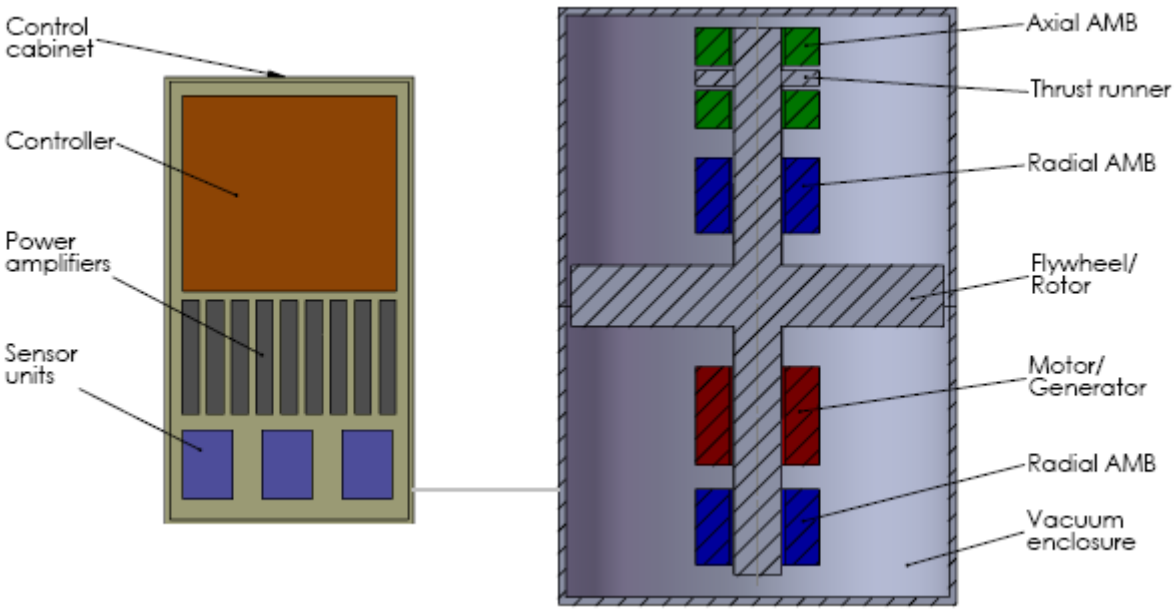


**Figure 2-1: Typical flywheel system**

### *2.1.1 Comparison of energy storage technologies*

Figure 2-2 shows the market area which flywheels occupy. Capacitors have a higher power density (W/kg) than flywheels and batteries but their energy density (Wh/kg) is considerably lower than batteries and flywheels which implies that capacitors are only able to supply energy for a short period of time [2].

Flywheels have a relatively high power density a well as a relatively high energy density which means that flywheels can deliver more power for a longer period of time compared to capacitors and batteries. The flywheel typically provides power during the period between the loss of supplied power and either the return of power or the start of a back-up power system (i.e. diesel generator).

Batteries typically have a lower power density than flywheels and capacitors [2]. High capacity batteries with higher power densities are very expensive and are made of chemicals that can be damaging to the environment.

Most popular UPS systems make use of lead-acid batteries to store electricity. However, these batteries are recognized as non-ecological batteries because they contain lead. Other chemical batteries such as lithium-ion (Li-Ion) and nickel-metal hydride (Ni-MH) are more suitable for the UPS purpose but these types of batteries are very expensive. Another drawback of UPS systems is the area they span. When constructing a high capacity UPS a large number of cells are needed. This translates to a large floor area. For these reasons, a flywheel is a very viable option for storing energy as it is ecologically friendly and does not take up a lot of space [2].

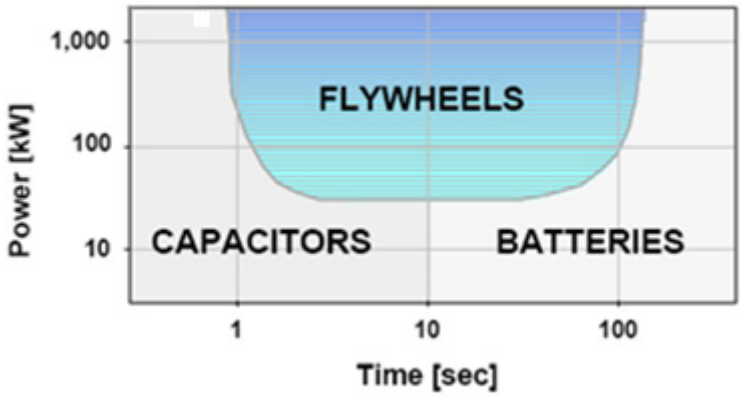


**Figure 2-2: Suitability of various energy storage technologies [2]**

### *2.1.2 Application areas of Flywheels*

High-speed flywheels are used in the hybrid vehicle market. The need for the conservation of fossil-fuels has become apparent in the last five years. Hybrid vehicles have become a focus area for researchers as hybrid vehicles are able to store energy which was previously lost. Flywheels are used in conjunction with batteries to deliver the peak current which is needed when accelerating the vehicle. This increases the life of the vehicle's batteries. When a vehicle decelerates by making use of its brake system, energy in the form of heat is dissipated in the brake discs and brake pads. Hybrid vehicles make use of regenerative braking to store the energy in batteries or flywheels which can be used at a later stage to drive the vehicle. This dramatically decreases fuel consumption which in turn helps to preserve fossil-fuels [3].

As previously mentioned, flywheels are also used to store energy. The stored energy can be converted to electricity by means of a motor/generator set and can be used when a power failure occurs. Back-up generators take 5-20 seconds to come online and a flywheel system typically provides a ride-through time of 1-30 seconds [2].

Electricity is the only major commodity created almost entirely on demand. Without local storage, the power grid must carry electricity from the power plant to the customer at the instant it is needed. The grid now operates at near capacity on peak demand days, degrading stability and causing more frequent outages [4]

Industries that require better power quality includes information networks, factories and hospitals. The systems in these industries consist of very sensitive electronic devices that can be damaged by power surges and momentary voltage drops [5]. This makes flywheels the ideal solution for providing continuous power.

## 2.2 Flywheel

A flywheel is a disc connected to an axel which when rotated stores kinetic energy. The stored energy is equal to the sum of the kinetic energy of the individual mass elements that comprise the flywheel. The kinetic energy of the flywheel is calculated using (2-1)

$$E_k = \frac{1}{2} I\omega^2 \quad [\text{J}] \tag{2-1}$$

where $I$ is the moment of inertia which is the ability of an object to resist changes in its rotational velocity and $\omega$ is the angular velocity. The moment of inertia is calculated using (2-2)

$$I = k \cdot M \cdot r^2 \quad [\text{kg.m}^2] \tag{2-2}$$

where $M$ is the mass- and $r$ is the radius of the flywheel. The inertial constant $k$ is dependent on the shape of the disc. Figure 2-3 illustrates the effect of different flywheel geometries on the value of $k$.

| Fly wheel geometry | Cross section | Shape factor K |
|---|---|---|
| Disc |  | 1.000 |
| Modified constant stress disc |  | 0.931 |
| Conical disc |  | 0.806 |
| Flat unpierced disc |  | 0.606 |
| Thin firm |  | 0.500 |
| Shaped bar |  | 0.500 |
| Rim with web | 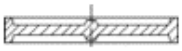 | 0.400 |
| Single bar |  | 0.333 |
| Flat pierced bar |  | 0.305 |

**Figure 2-3: Inertial constants of various flywheel shapes**

To optimize the energy-to-mass ratio the flywheel needs to spin at the maximum possible speed. This is because kinetic energy only increases linearly with mass but increases with the square of the rotational speed. Rapidly rotating objects are subject to centrifugal forces that can cause the object to shatter. The centrifugal force for a rotating object is calculated using (2-3).

$$F_C = Mr\omega^2 \quad [\text{N}] \tag{2-3}$$

While dense material can store more energy it is also subject to higher centrifugal force and thus fails at lower rotation speeds than low density material. Thus, the tensile strength of the material is more important than the density of the material [6].

## 2.3 Active Magnetic Bearings

The idea of suspending an object with magnetism was first conceived in the mid-1800s and since then many experiments and developments have taken place. In the field of engineering, magnetic bearings for practical application became a reality in the 1960s. At that time magnetic bearings were characterised as being costly, specially designed systems for large-scale applications such as gas compressors, power generation turbines etc. [7].

Over the past twenty years, technical breakthroughs have been made that reduce the size, complexity and cost of such systems making them economically feasible for many applications that were previously not considered [8]. Today, advanced software algorithms have been developed to increase performance beyond what was originally considered possible [9]. The use of modern computing power has reduced the size of the control systems to PC size units instead of the mainframe-sized units of the past [7].

A functional diagram of an Active Magnetic Bearing (AMB) is shown in Figure 2-4. The system works by using a sensor that measures the displacement of the rotor from its reference position. The controller derives a control signal from the measurement and the power amplifier transforms this control signal into a control current that generates the magnetic forces within the actuating magnet.

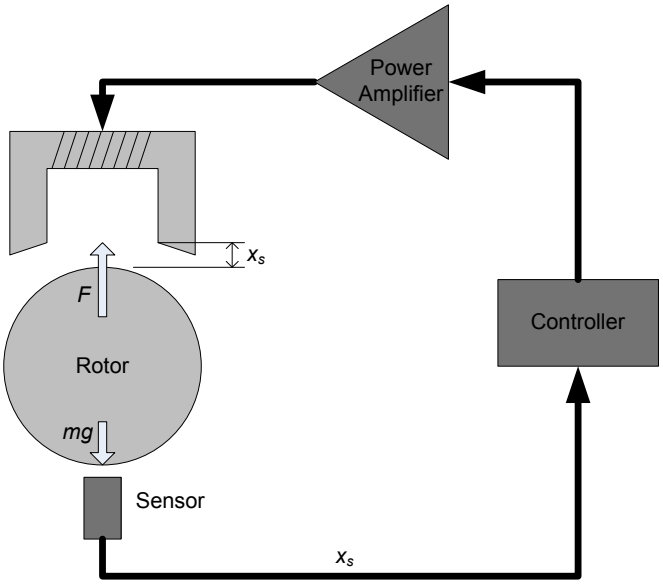


**Figure 2-4: AMB functional diagram**

Magnetic bearings do not require any lubricants. This makes magnetic bearings particularly suitable for machines operating in a vacuum, at high or low temperatures or in corrosive process fluids. Any machine with no tolerance for contamination by lubricants or in instances where the lubricant is incompatible with the process may be a candidate for a magnetic bearing solution [10].

Lubrication free operation also means that lubrication and associated auxiliary systems, such as pumps and filters, can be eliminated. Since magnetic bearings operate with almost zero friction and have no contacting moving parts, there is no wear within the system. This gives extremely long lifetimes with minimal maintenance, resulting in cost effective operation and ownership [8].

### *2.3.1 Radial Magnetic Bearing Geometry*

There are two main radial magnetic bearing geometries: homopolar and heteropolar. In homopolar magnetic bearings, the magnetic flux mainly flows parallel to the rotor axis as shown in Figure 2-5. Homopolar magnetic bearings have low hysteresis losses and laminating the rotor may not be necessary. These bearings are mostly used in applications where one of the design constraints is that the rotor cannot be laminated or where a massive rotor is employed [7].

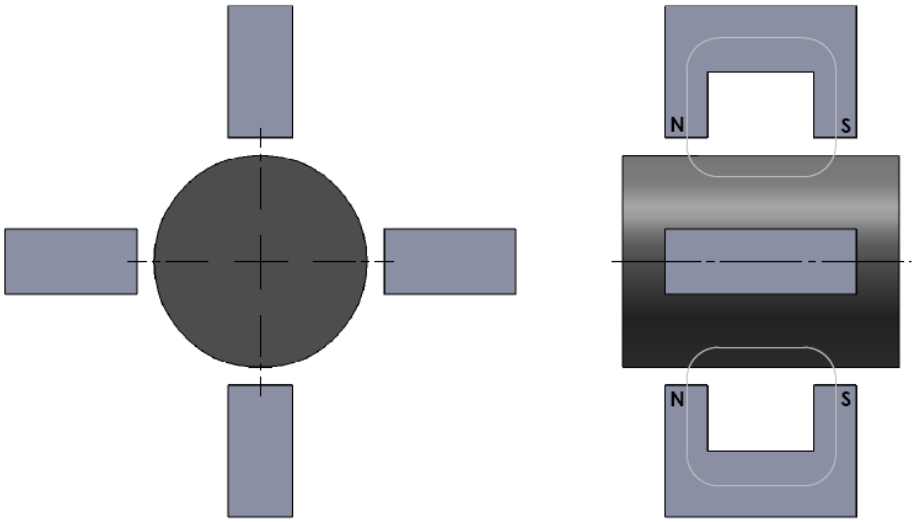


**Figure 2-5: Homopolar Radial AMB**

Heteropolar magnetic bearings are the most common. Magnetic flux flows mainly in the radial direction as shown in Figure 2-6. However, in order to keep the hysteresis and eddy-current losses as low as possible, the rotor has to be laminated, i.e. the magnetically active part of the rotor must be built from a compact bundle of circularly punched layers of metal sheets [7].

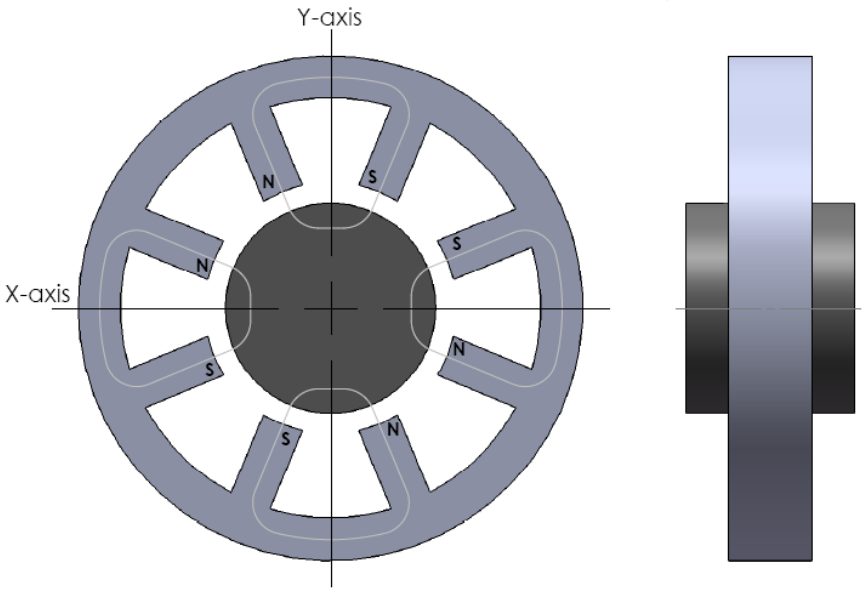


**Figure 2-6: Heteropolar radial AMB**

An advantage of eight-pole radial bearings is that two pole pairs each can be assigned to Cartesian coordinate x and y which are often used in mechanics. This simplifies bearing control because simulations and control design are usually based on these coordinates [7].

### *2.3.2 Axial magnetic bearing geometry*

The basic thrust bearing consists of an electromagnetic stator and a thrust runner placed on the rotor. The stator and the rotor are separated by an air gap to allow for rotation without physical contact. Figure 2-7a shows and exploded view of the stator, shaft, coil and the thrust collar. The stator comprises an inner and outer toroid connected to a common base. The inner and outer toroid and base may be constructed from one piece or separate pieces that are assembled together. The thrust collar is attached to the shaft. In many applications the thrust bearing is double acting with the thrust collar between two stators as shown in Figure 2-7b. This allows control of the shaft in both positive and negative axial directions.

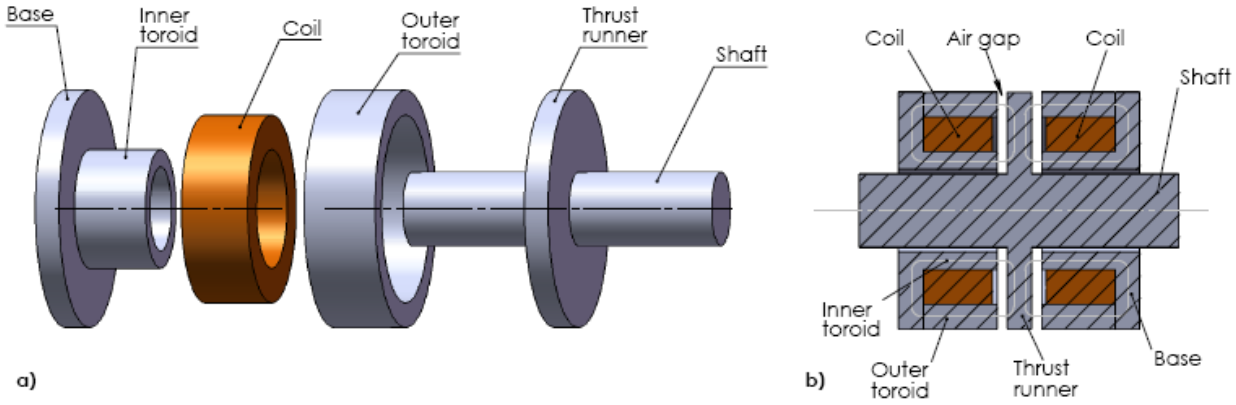


**Figure 2-7: a) Exploded view of the thrust bearing b) Double acting thrust bearing**

### 2.3.3 Magnetic Bearing forces

The magnetic part of the circuit, illustrated in Figure 2-8, is constructed of ordinary magnetic material such as silicon steel or other higher saturation level magnetic materials. The air gap has thickness *g* and area $A_g$. The magnetic flux in each horseshoe-shaped part of the actuator is produced by a coil of *N* turns of wire with a current *i* flowing through it. A power amplifier produces the desired current in the coil. The flux path of length *l* goes through the horseshoe, through the air gaps at the end of the pole face of the horseshoe magnet and through the rotor.

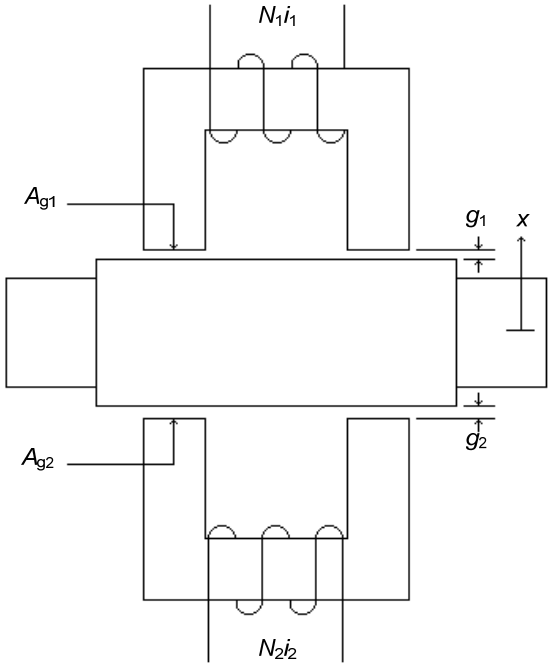


**Figure 2-8: Basic double-acting magnetic actuator geometry**

Ampere's circuital law indicates that the magnetic field intensity *H* induced by *N* wires carrying current *i* around a closed magnetic path of length *l* is given by (2-4)

$$H = \frac{Ni}{l} \quad [\mathrm{A \cdot turns/m}] \tag{2-4}$$

This assumes that the magnetic field intensity direction is parallel to the magnetic path and that the current in the wire is perpendicular to the magnetic path. The quantity *Ni* is called the magnetomotive force (*MMF*). The magnetic flux $\phi$ in the circuit is equal to the product of the flux density *B* and the pole face area $A_g$ which is also equal to the area of one air gap in the magnetic circuit as given by (2-5).

$$\phi = B \cdot A_g \quad [\mathrm{N \cdot m/A}] \tag{2-5}$$

Most of the reluctance in magnetic circuit resides in the air gaps. Air and other nonferrous materials have the same properties as free space. The flux density in such materials is related to the magnetic field intensity by the linear relation in (2-6).

$$B = \mu_0 \cdot H \quad [\mathrm{Wb/m^2}] \tag{2-6}$$

where the permeability of free space is given by (2-7).

$$\mu_0 = 4\pi \text{ x } 10^{-7} \quad [\mathrm{H \cdot m^{-1}}] \tag{2-7}$$

Magnetic bearings are normally constructed of ferrous materials and the air gaps are made as small as practical to minimize the required magnetomotive force. Considering the magnetic circuit shown in Figure 2-9, the reluctance of the material can be neglected in comparison to the reluctance of the air gaps due to the relatively high permeability of the magnetic materials.

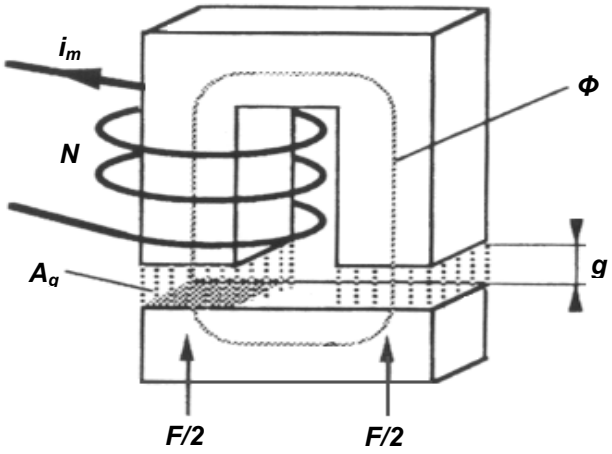


**Figure 2-9: Simple magnetic circuit**

The flux density *B* in each air gap as induced by *N* turns of wire and a current $i_m$ is obtained using (2-8) which is derived from (2-4) and (2-6) and making use of $l = 2 \cdot g$ [11].

$$B = \frac{\mu_0 N i_m}{2g} \quad [\mathrm{Wb/m^2}] \tag{2-8}$$

The attraction force is generated at the boundaries between differing permeability $\mu$. The calculation of these forces is based on the field energy. The energy *W* stored in the homogeneous field in the air gaps is obtained using (2-9).

$$\begin{aligned} W &= \frac{1}{2} BHV \\ &= \frac{1}{2} BHA_g 2g \end{aligned} \tag{2-9}$$

For small displacements *dg* the magnetic flux $B \cdot A_g$ remains constant. When the air gap increases by *dg* the volume $V = 2gA_g$ increases and the energy stored in the field increases by *dW*. This increase in energy is mechanically supplied where an attractive force must be overcome.

The attractive force is determined by obtaining the partial derivative of the field energy *W* with respect to the air gap *g*.

$$F_m = \frac{dW}{dg} = BHA_g = \frac{B^2 A_g}{\mu_0} \tag{2-10}$$

Equation (2-10) remains valid when the flux density remains constant. By substituting (2-8) into (2-10) the force is obtained as a function of coil current and the air gap:

$$F_m = \frac{\mu_0 N^2 {i_m}^2 A_g}{4g^2} \quad [\text{N}] \tag{2-11}$$

Actual magnetic circuits have effects such as fringing and leakage which is not modelled in the above mentioned equations. A factor $\varepsilon$ may be used to model the bearing force more accurately. The factor $\varepsilon$ is usually taken as 0.9 for thrust bearings and 0.8 for radial bearing geometries which yields the bearing force $F_m$

$$F_m = \varepsilon \frac{\mu_0 N^2 {i_m}^2 A_g}{4g^2} \quad [\text{N}] \tag{2-12}$$

In heteropolar geometries the poles are situated at an angle of 22.5° with respect to the vertical axis. This has to be taken into account when determining the force in the vertical direction. The resulting force produced by a single pole pair is then estimated using (2-13) [12].

$$F = \varepsilon \frac{\mu_0 N^2 {i_m}^2 A_g}{{x_s}^2} \cos(\theta) \quad [\text{N}] \tag{2-13}$$

The estimation of the force may be optimized because it does not allow for losses in magnetomotive force across the magnetic circuit. The factor $\varepsilon$ which was introduced in (2-12) can also be optimized by using a FEM analysis of the specific bearing geometry.

### 2.3.4 Force linearisation

The primary goal of the control is to stabilise the rotor in its equilibrium position. The equilibrium position is the position where the sum of all the forces acting on the rotor is zero. In the case of a horizontally orientated rotor there are only two forces acting on the rotor, the gravity $mg$ and the opposing magnetic force $F_m$. The sum of the two forces is given by

$$F = F_m - mg \quad [\text{N}] \tag{2-14}$$

The equilibrium is also called the operating point of the magnetic bearing. Operating point values are not only assigned to the position $x_s$=$x_0$, but also to the coil current $i_m$=$i_0$ at equilibrium. This is done to achieve a specific displacement for a specific coil current. Any deviation from the equilibrium position is then measured by a non-contact sensor and sent to the controller. The controller in turn generates a reference signal that drives the power amplifier to restore the equilibrium. Figure 2-10(a) displays the relationship between force and current and (b) the relationship between force and displacement.

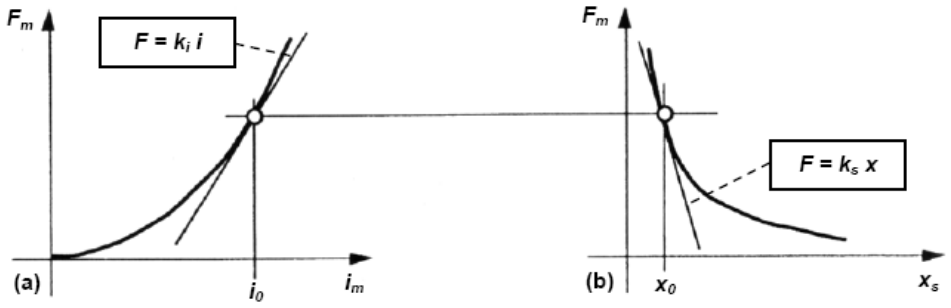


**Figure 2-10: Magnetic force as a function of (a) current and (b) air gap [13]**

For control design, only the slopes of the nonlinear force-current and force-displacement curves are considered at the operating point. The linearization of the force-current function is shown in Figure 2-10(a) with a new variable *i* introduced for the deviation of the winding current from the operating point value of $i_0$.

$$i = i_m - i_0 \quad [\text{A}] \tag{2-15}$$

The slope of the linearised function *f(i)* is called the force-current factor $k_i$, and is measured in Newton/ampere (N/A).

Similarly the force-displacement function is linearised in the operating point, with a new displacement variable, *x,* introduced as seen in Figure 2-10(b).

$$x = x_0 - x_s \quad [\text{m}] \tag{2-16}$$

The displacement x is positive when the air gap $x_s$ decreases from the operating point $x_0 = g_0$. The slope of *f(x)* is called the force-displacement factor $k_s$ and is measured in Newton/meter (N/m).

Now force, displacement and current (*mg,* $x_0$ and $i_0$) all have values in the operating point as well as variables (*F, x,* and *i*) in case of deviation from the operating point. Using these values and variables a total linearised function for instantaneous force in the operating point follows:

$$F(x,i) = k_s x + k_i i \quad [\text{N}] \tag{2-17}$$

The values of $k_i$ and $k_s$ can be obtained by determining the partial derivative of the nonlinear force equation (2-13) with respect to the displacement and current at the working point [11].
The current gain for a single actuator is defined as

$$k_i = \left.\frac{\partial F}{\partial i_m}\right|_{i_m = i_0,\ x_s = g_0} = 2\frac{\mu_0 N^2 i_0 A_g}{g_0^{\,2}}\cos(\theta) \tag{2-18}$$

where the derivative is evaluated with a control current equal to zero and a rotor position of $x = 0$. The current gain is positive because an increase in current produces an increase in force.

The position stiffness for a single actuator is defined as

$$k_s = \left.\frac{\partial F}{\partial x_s}\right|_{i_m=i_0,\ x_s=g_0} = -2\frac{\mu_0 N^2 {i_0}^2 A_g}{{g_0}^3}\cos(\theta) \qquad \textbf{(2-19)}$$

where the derivative is evaluated with a control current equal to zero and a rotor position of x = 0. The position stiffness is negative as the force increases with a decreasing air gap.

The operation of the magnetic bearing involves superposition of two fluxes: a bias flux and a control flux as shown in Figure 2-11. The bias flux density $B_{bias}$ is a steady state flux level induced in the air gap by a bias current $I_b$ in the coil of the actuator. The control flux density $B_{control}$ is a time varying control flux density developed by the control current $I_c$ in the coil. The total fluxes and currents in the coils are given by (2-20).

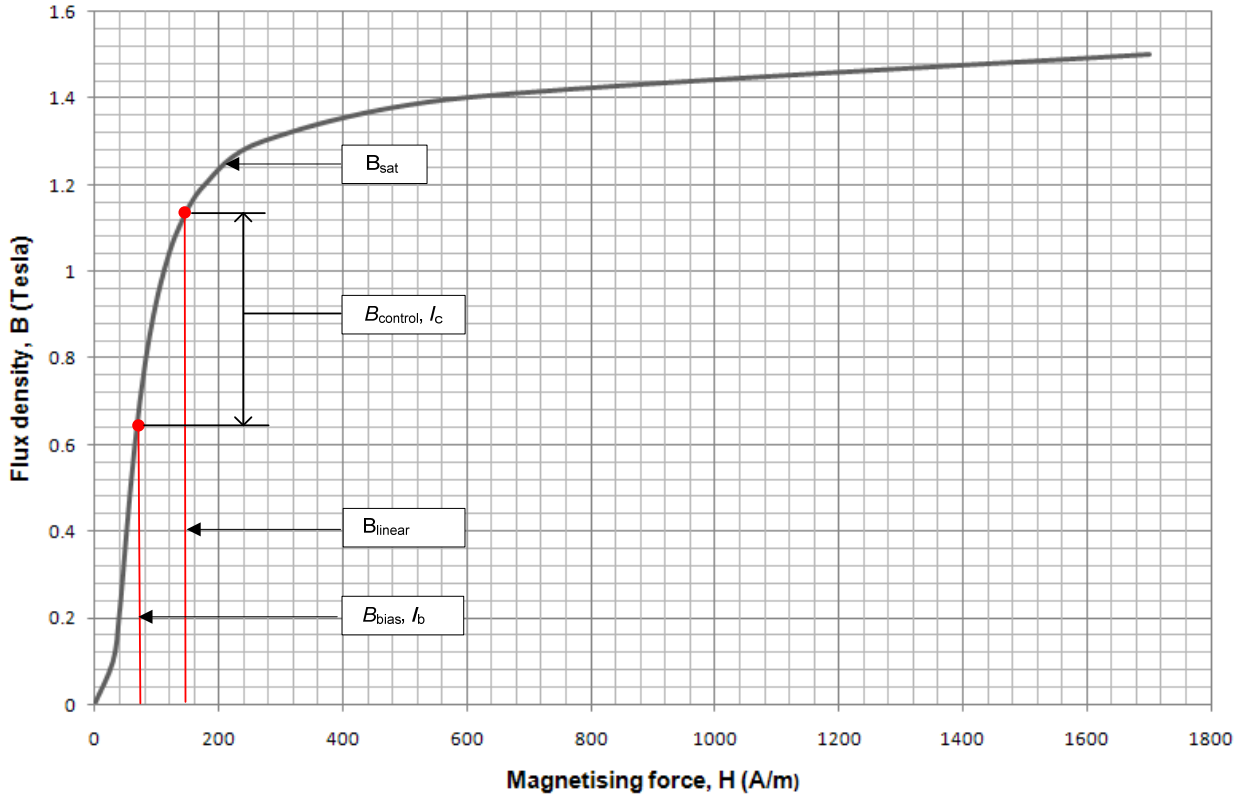


**Figure 2-11: B-H curve of M270-35A silicon steel**

$$\begin{aligned} B_{max} &= B_{bias} + B_{control} \\ I_{max} &= I_b + I_c \end{aligned} \qquad \textbf{(2-20)}$$

Usually the bias flux level $B_{bias}$ is set at half of the magnetic saturation level $B_{sat}$ shown in Figure 2-11 allowing for relatively large control flux levels up and down from the bias flux level. By setting the maximum flux density $B_{max}$ to occur at the maximum current $I_{max}$ it is ensured that the

bearing will operate within the linear range of the B-H curve of the specific material as shown in Figure 2-11.

### 2.3.5 Closed Loop Control

The purpose of control design is to stabilise the contact-free equilibrium. A restoring force, similar to that of a mass-spring-damper system, has to be provided by the control of the AMB in order to attenuate the oscillations caused by disturbance forces. This is achieved by exerting forces proportional to the displacement and the velocity of the suspended mass.

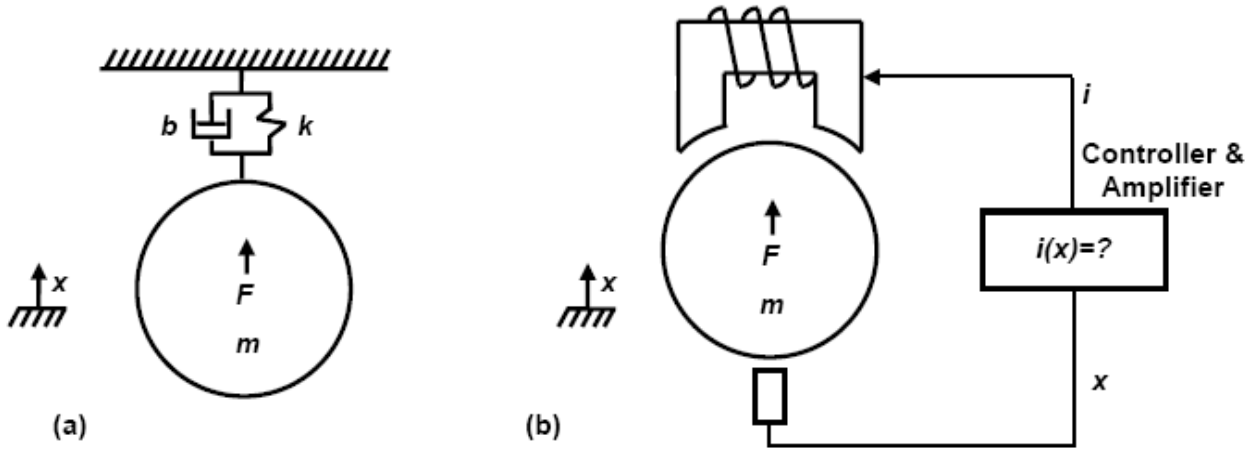


**Figure 2-12: Simple controller design to emulate mass-spring-damper behaviour [7]**

Assume a simple spring-mass-damper with a stiffness *k* and a damping *b* is required (Figure 2-12a). The force *F* of such a suspension in response to a displacement *x* is:

$$F = -kx - b\frac{dx}{dt} \tag{2-21}$$

The force *F* and the displacement *x* are deviations from equilibrium as defined in (2.12) and (2.14). Now solving for *i* in (2.15) and (2.16) the desired controller function is derived:

$$i(x) = \frac{-(k + k_s)x + b\dot{x}}{k_i} \tag{2-22}$$

Now assuming linear sensor and power amplifier behaviour without any noise and time delays, the dynamic behaviour of the masses in Figure 2-12(a) and Figure 2-12(b) are equivalent and suspension is realised. The characteristic equation for the two systems shown in Figure 2-12, is given by:

$$s^2 + \left(\frac{b}{m}\right)s + \frac{k}{m} = s^2 + \left(\frac{b_{eq}}{m}\right)s + \frac{k_{eq}}{m} \tag{2-23}$$

### 2.3.6 Symmetric magnetic actuators

The control configuration used in radial AMBs incorporates two opposing actuators with two current controlled power amplifiers and a single PD-controller to achieve magnetic suspension in a single axis. It is assumed that the two actuators are identical. Figure 2-13 displays the nonlinear system block diagram for this configuration with $k_{m1}$ and $k_{m2}$ the top and bottom electromagnet constants respectively.

An error signal is produced by subtracting the rotor position from a reference position. The error signal is scaled via the proportional constant ($K_P$) and the derivative of the error signal via the derivative constant ($K_D$) to produce a current reference signal ($i_{ref}$). The current reference signal is added and subtracted from a bias current reference signal ($i_{0ref}$) to produce reference current signals for the top and bottom power amplifiers (PAs) respectively.

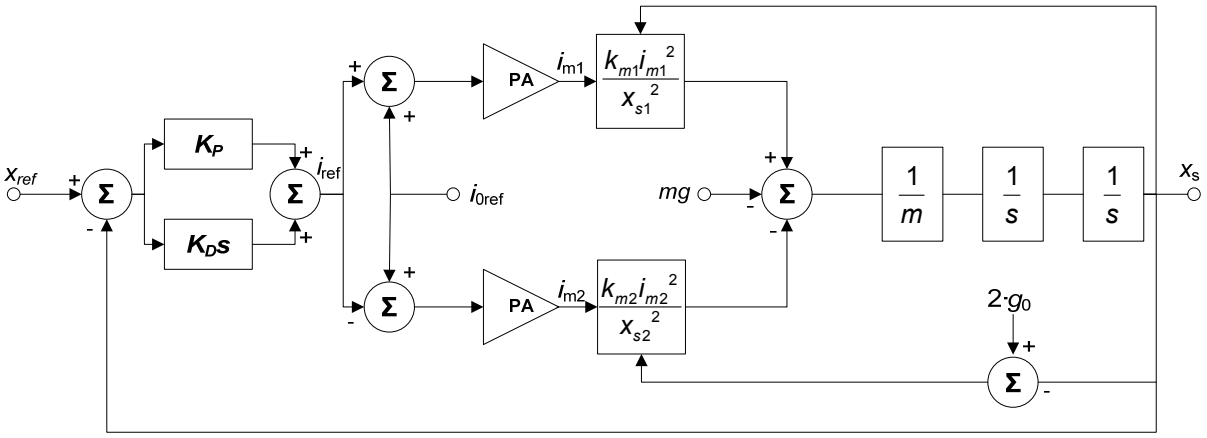


**Figure 2-13: Nonlinear system block diagram of symmetric magnetic actuator**

The nonlinear model of the symmetric AMB shown in Figure 2-13 is linearised around the working point to obtain the linear system block diagram shown in Figure 2-14. It is assumed that the force-current and force-displacement factors for the two magnets are identical. This is only valid if the working points of the two magnets are the same. For vertical suspension where no gravity applies this assumption is valid for small perturbations around the geometrical centre between the magnets. The PAs are assumed to be ideal with unity gain [13].

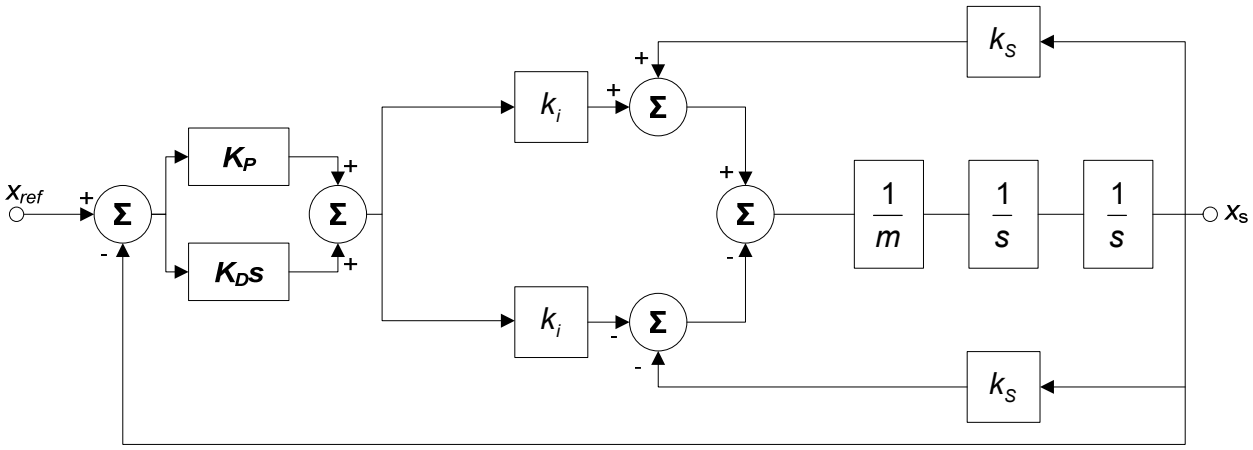


**Figure 2-14 Linear system block diagram**

Figure 2-15 displays a signal flow diagram derived from the system block diagram shown in Figure 2-14.

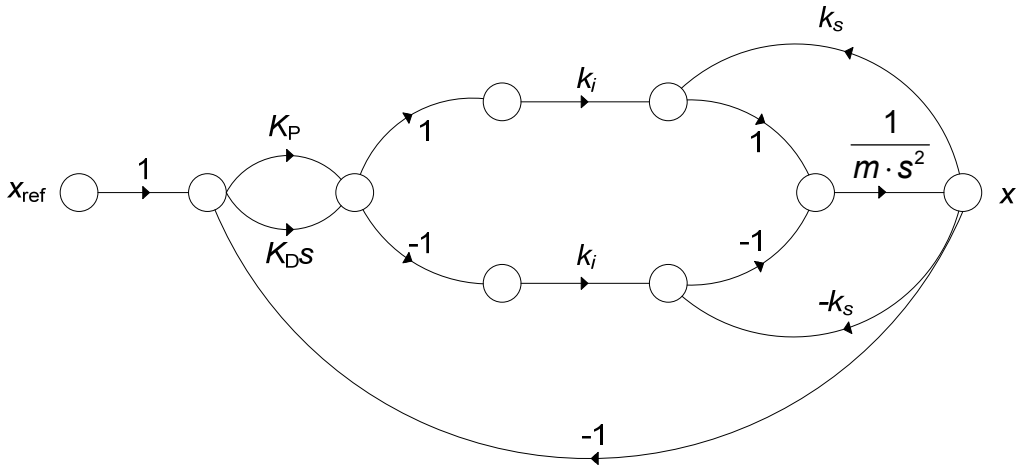


**Figure 2-15 Signal flow diagram of symmetric magnetic actuators**

From the signal flow diagram in Figure 2-15 the forward paths connecting the input to the output are:

$$P_1 = \frac{K_P k_i}{ms^2},\ P_2 = \frac{K_D k_i s}{ms^2} \qquad \textbf{(2-24)}$$
$$P_3 = \frac{K_P k_i}{ms^2},\ P_4 = \frac{K_D k_i s}{ms^2}$$

Six loops are identified:

$$L_1 = \frac{k_s}{ms^2},\ L_2 = \frac{k_s}{ms^2},\ L_3 = \frac{-K_P k_i}{ms^2} \qquad \textbf{(2-25)}$$
$$L_4 = \frac{-K_D k_i}{ms^2},\ L_5 = L_3,\ L_6 = L_4$$

Loops $L_1$ through to $L_6$ touches, therefore the determinant is:

$$\Delta = 1 - \left(L_1 + L_2 + L_3 + L_4 + L_5 + L_6\right) \tag{2-26}$$

The cofactor of each forward path is evaluated by removing the loops that touch that specific path from the determinant. Therefore the cofactors are:

$$\Delta_1 = \Delta_2 = \Delta_3 = \Delta_4 = 1 \tag{2-27}$$

The system transfer function is obtained using (2-28).

$$\begin{aligned} T &= \frac{P_1 \cdot \Delta_1 + P_2 \cdot \Delta_2 + P_3 \cdot \Delta_3 + P_4 \cdot \Delta_4}{\Delta} \\ &= \frac{\dfrac{2K_P k_i}{ms^2} + \dfrac{2K_D k_i}{ms}}{1 - \left(\dfrac{2k_s}{ms^2} - \dfrac{2K_P k_i}{ms^2} - \dfrac{2K_D k_i}{ms}\right)} \\ &= \frac{2K_P k_i + 2K_D k_i s}{ms^2 + 2K_D k_i s + \left(2K_P k_i - 2k_s\right)} \end{aligned} \tag{2-28}$$

The resulting characteristic equation for this system is as given by (2-29).

$$\begin{aligned} q(s) &= s^2 + \frac{2K_D k_i}{m} s + \frac{2K_P k_i - 2k_s}{m} \\ &= s^2 + \frac{b_{eq}}{m} s + \frac{k_{eq}}{m} \end{aligned} \tag{2-29}$$

The result in (2-29) is the same as that of (2-23) which implies that the AMB system with a single controller and two electromagnets will display dynamic behaviour equivalent to that of a spring-mass-damper system. The equivalent damping for this system is derived from (2-29)
as

$$b_{eq} = 2K_D k_i \tag{2-30}$$

and the equivalent stiffness as

$$k_{eq} = 2K_P k_i - 2k_s \tag{2-31}$$

The results obtained in (2-30) and (2-31) can now be used to design a simple PD controller for a symmetric magnetic actuator which will result in a stable system with the desired equivalent stiffness and damping values [13].

### 2.3.7 Asymmetric magnetic actuators

The purpose of asymmetric magnetic actuators is to overcome a certain static load in the equilibrium position e.g. the mass of the rotor. The control configuration used in the axial AMB incorporates two opposing actuators with two current controlled power amplifiers and a single PD-controller to achieve magnetic suspension in a single axis. The two actuators however differ in geometry, load capabilities as well as bias currents. Figure 2-16 displays the nonlinear system block diagram for this configuration with $k_{m1}$ and $k_{m2}$ the respective electromagnet constants.

An error signal is produced by subtracting the rotor position from a reference position. The error signal is scaled via the proportional constant ($K_P$) and the derivative of the error signal via the derivative constant ($K_D$) to produce a current reference signal ($i_{ref}$). The current reference signal ($i_{ref}$) is added to the top actuators bias current reference signal ($i_{0ref\_top}$) to produce a reference current signal for the top power amplifier. The current reference signal ($i_{ref}$) is also multiplied by a current gain ($K_i$) for the bottom actuator and subtracted from the bottom actuators bias current reference signal ($i_{0ref\_bottom}$) to produce a reference current signal for the bottom power amplifier.

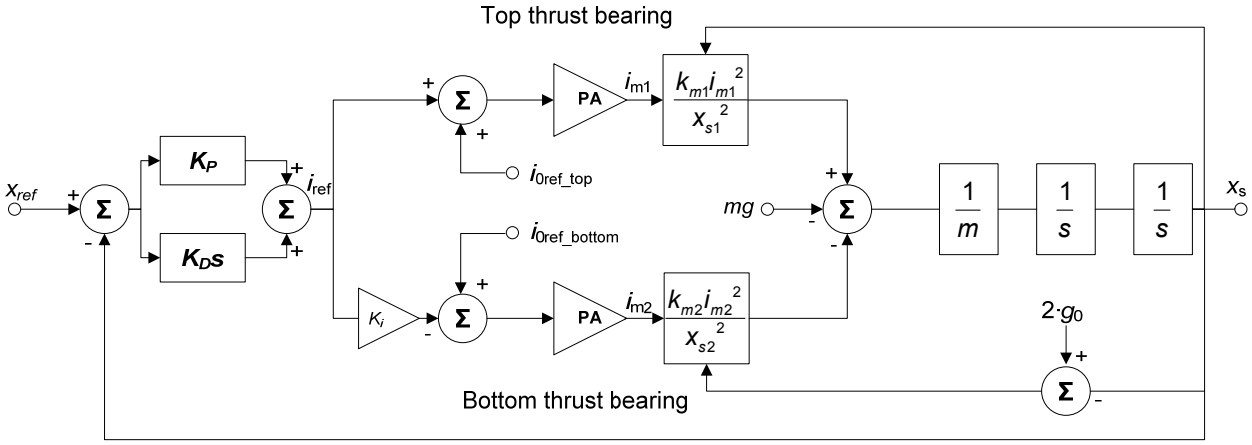


**Figure 2-16: Nonlinear system block diagram of asymmetric magnetic actuator**

The nonlinear model of the asymmetric AMB shown in Figure 2-16 is linearised around the working point to obtain the linear system block diagram shown in Figure 2-17. The force-current and force-displacement factors for the two magnets differ. The PAs are assumed to be ideal with unity gain.

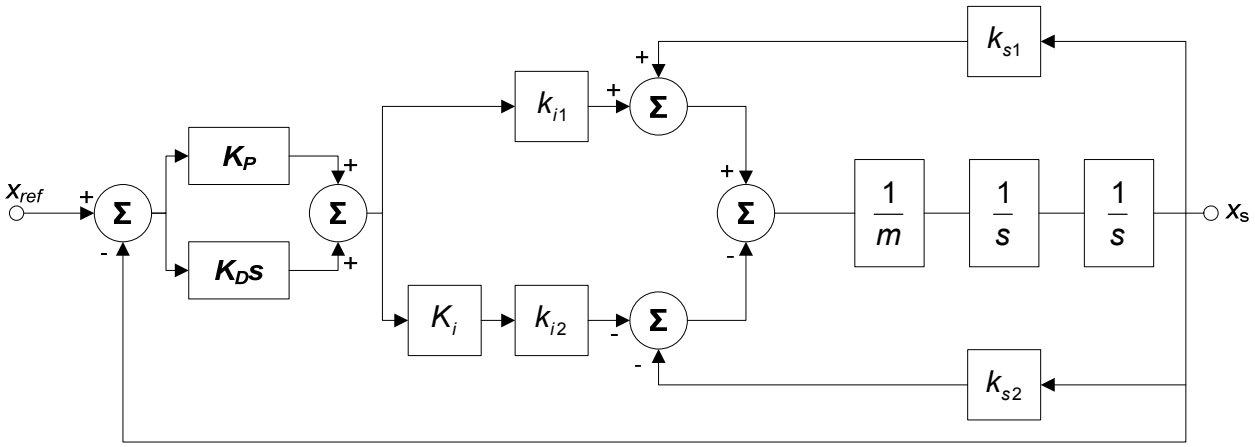


**Figure 2-17 Linear system block diagram**

Figure 2-18 displays a signal flow diagram derived from the system block diagram shown in Figure 2-17. It can be seen in Figure 2-18 that a current gain has been added in the bottom actuators path. This is done to scale the current gain of the bottom actuator to the top actuator.

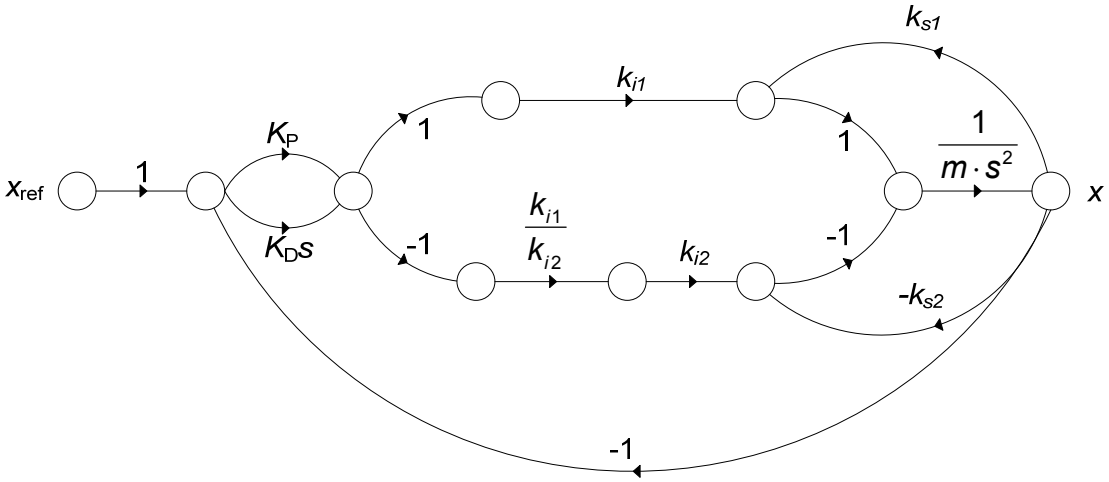


**Figure 2-18 Signal flow diagram of asymmetric magnetic actuators**

From the signal flow diagram in Figure 2-18 the forward paths connecting the input to the output are:

$$P_1 = \frac{K_P k_{i1}}{ms^2},\ P_2 = \frac{K_D k_{i1} s}{ms^2}$$
$$P_3 = \frac{K_P k_{i2}}{ms^2},\ P_4 = \frac{K_D k_{i2} s}{ms^2} \quad \textbf{(2-32)}$$

Six loops are identified:

$$L_1 = \frac{k_{s1}}{ms^2},\ L_2 = \frac{k_{s2}}{ms^2},\ L_3 = \frac{-K_P k_{i1}}{ms^2} \quad \textbf{(2-33)}$$
$$L_5 = \frac{-K_P k_{i2}\left(\frac{k_{i1}}{k_{i2}}\right)}{ms^2},\ L_4 = \frac{-K_D k_{i1}}{ms},\quad L_6 = \frac{-K_D k_{i2}\left(\frac{k_{i1}}{k_{i2}}\right)}{ms}$$

From (2-33) it can be seen that $L_5 = L_3$ and $L_6 = L_4$.

Loops $L_1$ through to $L_6$ touches, therefore the determinant is:

$$\Delta = 1 - \left(L_1 + L_2 + L_3 + L_4 + L_5 + L_6\right) \tag{2-34}$$

The cofactor of each forward path is evaluated by removing the loops that touch that specific path from the determinant. Therefore the cofactors are:

$$\Delta_1 = \Delta_2 = \Delta_3 = \Delta_4 = 1 \tag{2-35}$$

The system transfer function is obtained using (2-36).

$$T = \frac{P_1 \cdot \Delta_1 + P_2 \cdot \Delta_2 + P_3 \cdot \Delta_3 + P_4 \cdot \Delta_4}{\Delta} \tag{2-36}$$

$$= \frac{\frac{K_P k_{i1}}{ms^2} + \frac{K_P k_{i2}}{ms^2} + \frac{K_D k_{i1} s}{ms^2} + \frac{K_D k_{i2} s}{ms^2}}{1 - \left(\frac{k_{s1}}{ms^2} + \frac{k_{s2}}{ms^2} - \frac{2K_P k_{i1}}{ms^2} - \frac{2K_D k_{i1} s}{ms^2}\right)}$$

$$= \frac{K_P\left(k_{i1} + k_{i2}\right) + K_D s\left(k_{i1} + k_{i2}\right)}{ms^2 + 2K_D k_{i1} s + \left(2K_P k_{i1} - k_{s1} - k_{s2}\right)}$$

The resulting characteristic equation for this system is as given by (2-37).

$$q(s) = s^2 + \frac{2K_D k_{i1}}{m} s + \frac{2K_P k_{i1} - k_{s1} - k_{s2}}{m} \tag{2-37}$$

$$= s^2 + \frac{b_{eq}}{m} s + \frac{k_{eq}}{m}$$

The result in (2-37) is the same as that of (2-23) which implies that the AMB system with a single controller and two electromagnets will display dynamic behaviour equivalent to that of a spring-mass-damper system. The equivalent damping for this system is derived from (2-29)
as

$$b_{eq} = 2K_D k_{i1} \tag{2-38}$$

and the equivalent stiffness as

$$k_{eq} = 2K_P k_{i1} - k_{s1} - k_{s2} \tag{2-39}$$

The results obtained in (2-38) and (2-39) can now be used to design a simple PD controller for an asymmetric magnetic actuator which will result in a stable system with the desired equivalent stiffness and damping values. The proportional constant $K_P$ can be determined using (2-40)

$$K_P = \frac{k_{eq} + k_{s1} + k_{s2}}{2 \cdot k_{i1}} \tag{2-40}$$

whereas the differential constant $K_D$ can be determined using (2-41)

$$K_D = \frac{b_{eq}}{2 \cdot k_{i1}} \tag{2-41}$$

## 2.4 Sensors

The sensors are an important part of a magnetic bearing and are also one of the most expensive components in an AMB system. The effective operation of the magnetic bearing is dependent on the efficiency of the displacement sensors. Contact free sensors are used to determine the position of a moving rotor. The measurement results are dependent on the surface quality and the homogeneity of the rotor's material. A non-homogeneous surface will produce noise disturbances. Geometrical errors on the rotor material will cause disturbances at the rotational frequency [7].

Displacement sensors are characterised by the following:

- *Measuring range:* The range in which there is a linear correlation between the measured quantity and the output signal;
- *Linearity:* To what extent the measured quantity deviates from a linear relationship between measured quantity and output signal;
- *Sensitivity:* The ratio of the output signal over the quantity to be measured;
- *Resolution:* The value of the useful signal that can be distinguished from the noise disturbance.

There are several types of displacement sensors available including, Eddy-current sensors, inductive displacement sensors, capacitive displacement sensors and magnetic displacement sensors.

### *2.4.1 Eddy current sensors*

An eddy current probe is basically a coil enclosed in the tip of the probe. A high frequency magnetic field is radiated into the target material. When a conductive surface passes by the sensor tip, eddy currents are induced in the target material as shown in Figure 2-19. These eddy currents interfere with the magnetic field the probe generates. The probe linearises the amplitude of the oscillation to a voltage which is proportional to a clearance.

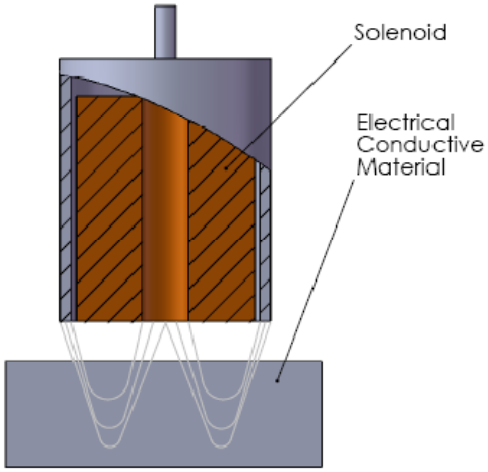


**Figure 2-19: Eddy-current displacement sensor**

The sensitivity of the Eddy-current sensors is dependent on the type of material on which it measures and is specified by the manufacturer. These sensors also have to be shielded in applications where the probes are close to high frequency magnetic fields. When several sensors are used in the system, the modulation frequencies should be synchronised. This may however not be possible with all sensor systems [7].

### *2.4.2 Inductive displacement sensors*

An inductive sensor comprises an inductor in a ferrite core as part of an oscillating circuit as shown in Figure 2-20. When a ferromagnetic surface enters the area of the sensor, the inductance of the circuit changes and the circuit becomes detuned. When the signal is demodulated and linearised, the signal is proportional to the clearance between the sensor and the measured surface.

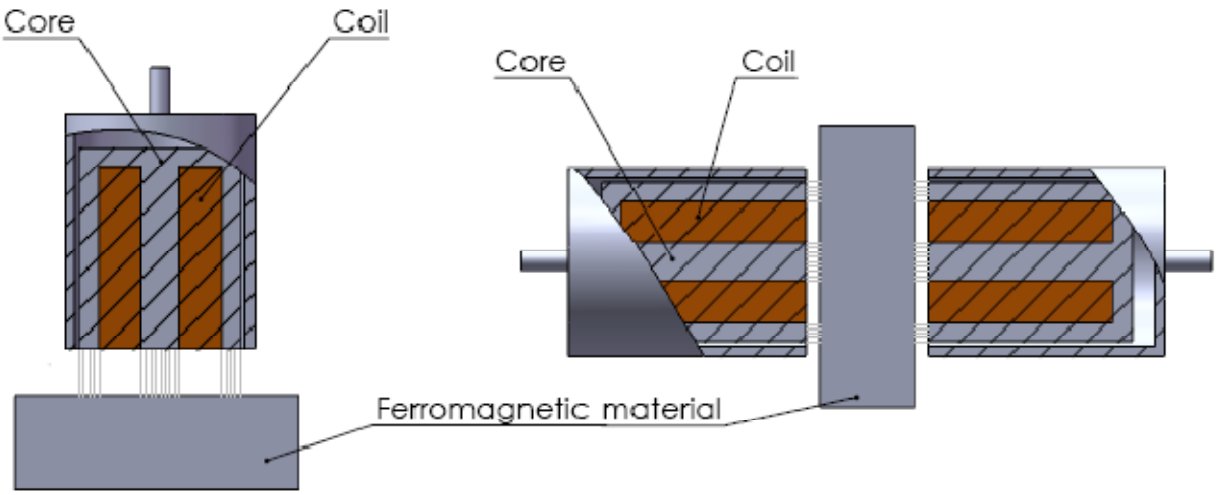


**Figure 2-20: Inductive displacement sensor**

A frequently used arrangement is two opposing sensors on the sensing material. They are operated differentially to produce a close to linear output signal.

Inductive sensors are not usually sensitive to external magnetic fields since the coil is shielded by the ferrite core. Disturbances may however occur when the magnetic bearings are powered by switching power amplifiers and their switching frequency is close to the modulation frequency of the sensors [7].

### 2.4.3 Capacitive displacement sensors

In plate capacitors, the capacitance changes with a change in clearance. The same principle is used in capacitive displacement sensors. The sensor and the opposing object to be measured, form one electrode of a plate capacitor each as shown in Figure 2-21. An alternating current with a constant frequency is passed through the sensor. The voltage amplitude at the sensor is proportional to the air gap between the sensor and the measured object. The voltage output is amplified to give a linearised output signal. These sensors are sensitive to electrostatic charges in the object to be measured as well as dirt because of the dielectric changes dirt causes.

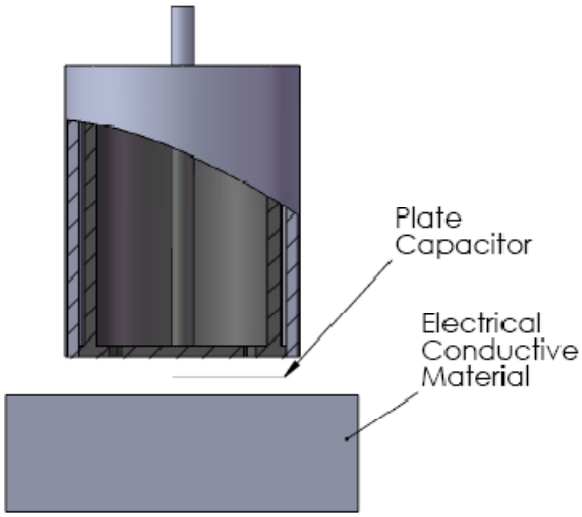


**Figure 2-21: Capacitive displacement sensor**

### 2.4.4 Magnetic displacement sensors

When using a magnetic loop with an air gap as shown in Figure 2-22, the flux density *B* can be measured by passing a constant current *i* through the circuit. Flux density can then in turn be used to measure the air gap between the magnetic core and the object to be measured. The difference between the measured flux densities yields a linearised displacement signal. Flux density can be measured with Hall sensors or with field plates.

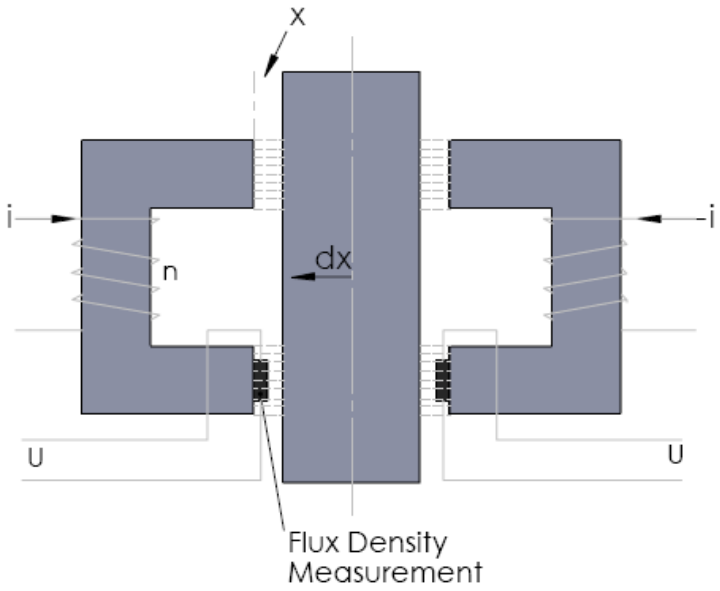


**Figure 2-22: Magnetic displacement sensor**

These sensors are sensitive to external magnetic interferences. When selecting a displacement sensor, measuring range, linearity, sensitivity and resolution have to be taken into account as well as the temperature range and the noise immunity against other sensors [7].

## 2.5 Power Amplifiers

Power amplifiers are responsible for generating control currents required to stably suspend the rotor in its reference position. The PA receives a current or a voltage command from the controller. The controller command is proportional to the position error of the rotor and normally in the form of a small signal voltage representing the desired coil current or voltage. The PA adjusts its output to closely match the control reference with an actual coil voltage or current.

AMB system loads are reactive loads that require high power (VA rating) to achieve high frequency actuation dynamics. The basic function of the PA is to regulate the energy flow in the magnetic circuit according to the controller's output i.e. to track the current or voltage command within the PA's bandwidth limit. The resulting current flows through the actuator producing the required forces.

Different types of PAs may be employed to regulate the energy in an AMB actuator. The main type of amplifier that is commonly used is linear PAs which track the desired signal at the expense of efficiency but with excellent noise immunity. Switch-mode PAs offer better efficiency than linear PAs but generate high levels of noise [12].

AMB systems have two control strategies that may be employed during the design process; current control and voltage control [10]. The PAs are specified according to the employed AMB control strategy. AMB control strategies include current control and voltage control. In the current controlled AMB systems, the current in to the coil is regulated and in voltage controlled AMB systems the voltage across the coil is regulated. For a current controlled AMB system, the linearised relation between the generated magnetic forces and current is given by (2-42).

$$F = k_i i + k_s x \tag{2-42}$$

with $F$ the magnetic force, $k_i$ the force-current factor, $k_s$ the force-displacement factor, $i$ the coil current and $x$ the position of the rotor.

In a voltage controlled AMB, the relation between the magnetic forces and the voltage is given by (2-43).

$$F = \frac{4B_0}{u_0 N} \int v_r dt \tag{2-43}$$

$B_0$ is the flux density in the air gap, $N$ the number of turns per pole and $v_r$ the coil voltage. The strategy employed in AMB systems therefore influences the design of the PA [12].

### 2.5.1 Linear power amplifier

Linear PAs operate switching devices in their linear regions. The output devices (transistors) are modelled as voltage controlled variable resistors. Figure 2-23 displays a linear PA used to deliver power to the load. The voltage controlled variable resistor is represented by the pass element which continuously varies the load voltage. The linear PA features a very high signal quality due to their continuous signal control. This is associated with a low efficiency as the power is dissipated in both the load and the pass element.

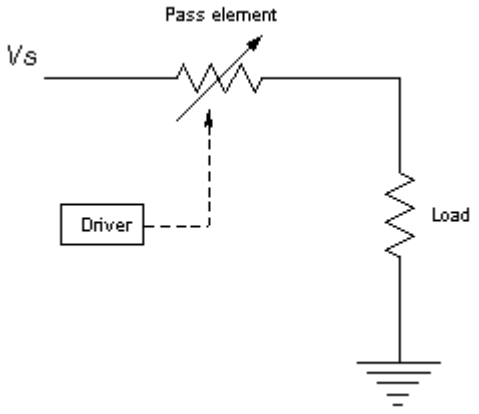


**Figure 2-23: Linear PA**

A maximum current reference causes the resistance of the pass element to reduce to a minimum value allowing maximum current to flow through the load, resulting in minimal losses. A minimum current reference causes the resistance of the pass element to approach infinity and the losses are still minimal. The problem with linear PAs arises when the resistance of the pass element is almost equal to the load resistance. At this point the power loss in the transistor will equal the power dissipated in the load.

Due to the high VA rating required by AMBs, linear PAs are not sufficient in driving magnetic coils with high inductance and low resistance. When used to drive such magnetic coils requiring high dynamic performances, the efficiency of the amplifier is reduced to less than 5 % due the high voltage rating of the systems. The linear PAs are useful in systems requiring a low voltage [12].

### *2.5.2 Switching power amplifier*

Switching PAs are mostly employed in magnetic bearing systems due to their high efficiency. The use of switching PAs in AMB systems has its own advantages and disadvantages. The major drawback of switching PAs includes electromagnetic interference on the position sensors and heating of the rotor due to induced eddy currents. The induced eddy currents are due to the ripple component of the coil current. For AMB systems, the required PA characteristics include a wide power bandwidth and reduced switching losses [7].

Figure 2-24 displays a basic switch-mode PA schematic. A PWM control block generates a variable duty cycle to control the amount of energy delivered to the load. When maximum currents are required, the PWM controller generates maximum duty cycles to turn the switch on for longer periods of time. The resulting losses are mainly due to the on-resistance of the switch. When minimum current is required, the PWM controller generates minimum duty cycles to turn the switch on for shorter periods of time [12].

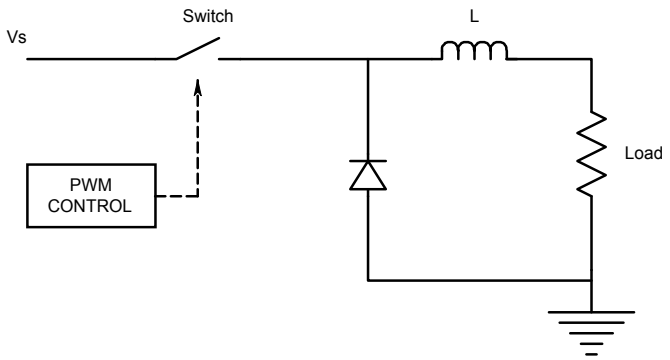


**Figure 2-24: Switch-mode PA [12]**

Due to low losses, switch-mode PAs are very efficient means of controlling power flow in AMB actuators.

### 2.5.3 Power amplifier bandwidth

The bandwidth of a PA is specified in terms of both a small-signal bandwidth and a power bandwidth. The small signal bandwidth describes the small signal behaviour of the magnetic actuator. The power bandwidth describes the large signal behaviour and specifically the frequency where a current of half the specified maximum current of the PA can still be supplied without being deformed. Deformation will occur above the power bandwidth due to the finite voltage at the bus.

**Small signal bandwidth**

The small signal bandwidth is defined as the frequency where the actual current is attenuated by -3dB for arbitrarily small reference currents. In AMB systems, the small signal bandwidth is limited by the load, the PA, the PA voltage ($V_{BUS}$) and it is controlled by the proportional gain ($K_p$) of the PI-controller. The integral gain ($K_i$) is responsible for compensating the influence of the back-emf of the system.

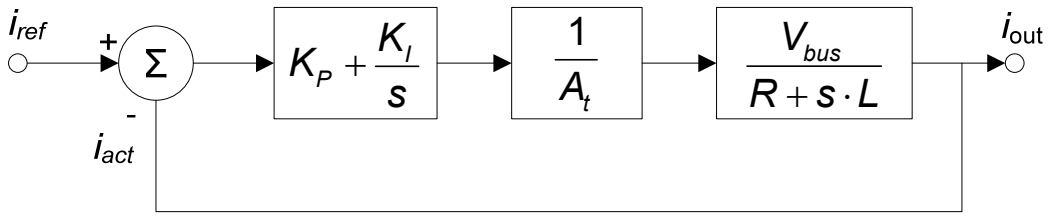


**Figure 2-25: PA small signal bandwidth prediction**

Figure 2-25 displays the closed loop block diagram used to determine the small signal bandwidth of the AMB PAs. The closed loop transfer function of the power amplifier is determined as (2-44),

$$\frac{I_{act}}{I_{ref}} = \frac{\frac{K_p}{A_t}\frac{V_{BUS}}{R+sL}}{1+\frac{K_p}{A_t}\frac{V_{BUS}}{R+sL}} = \frac{K_p V_{BUS}}{A_t(R+sL)+K_p V_{BUS}} \quad \textbf{(2-44)}$$

$I_{act}$ is the actual load current, $I_{ref}$ the reference signal, $R$ the resistance of the load and $L$ the inductance of the load. The small signal bandwidth of the amplifier occurs when (2-45) is satisfied.

$$\omega_{bw} L A_t = R A_t + K_p V_{BUS} \quad \textbf{(2-45)}$$

From (2-45), the small signal bandwidth is determined as (2-46).

$$\omega_{bw} = \frac{R A_t + K_p V_{BUS}}{L A_t} \quad \textbf{(2-46)}$$

From (2-46) the $K_p$ value of the controller is used to specify the small signal bandwidth of the PA. In order to achieve a wide small signal bandwidth for a specific AMB load with fixed supply voltage or VA rating, the $K_p$ value of the controller is increased. Care should be taken to avoid exceeding the linear limits of the controller's proportional gain.

**Power bandwidth**

The power bandwidth of the PA is the frequency at which the PA can produce half the maximum current without distortion. At the power bandwidth, the actual current can still follow the reference signal without attenuation or distortion. The power bandwidth is limited by the slew rate of the PA. The maximum slew rate of the switching PA is defined by (2-47).

$$\frac{di}{dt} \leq \frac{V_{BUS}}{L} \tag{2-47}$$

Assuming the sinusoidal input reference signal is limited to half the maximum signal as given by (2-48), the maximum rate of change of the input signal is expressed as (2-49).

$$i_{0.5ref} = 0.5 I_{\max} \sin(\omega t) \tag{2-48}$$

$$\left.\frac{di_{0.5ref}}{dt}\right|_{\max} = 0.5 I_{\max} \omega \tag{2-49}$$

The switching PA will respond to the desired half reference signal when the maximum rate of change of the input signal is below the maximum slew rate of the PA.

$$0.5 \cdot I_{\max} 2\pi f \leq \frac{V_{BUS}}{L} \tag{2-50}$$

From (2-50), the power bandwidth of the PA is limited to a maximum frequency of (2-51).

$$f_{pbw} = \frac{V_{BUS}}{\pi I_{\max} L} \tag{2-51}$$

For AMB loads, the power bandwidth is usually less than the signal bandwidth. The power bandwidth depends on the supply voltage, the maximum input current level and the inductance of the AMB load. Figure 2-26 displays the dynamic performance of the PA. From the figure, the frequency band in which the switching PA can achieve the desired performance when half the maximum current level is desired is defined as the operating range of the AMB system. At frequencies above the power bandwidth, the output signal will enter saturation and the dynamic performance of the PA becomes nonlinear.

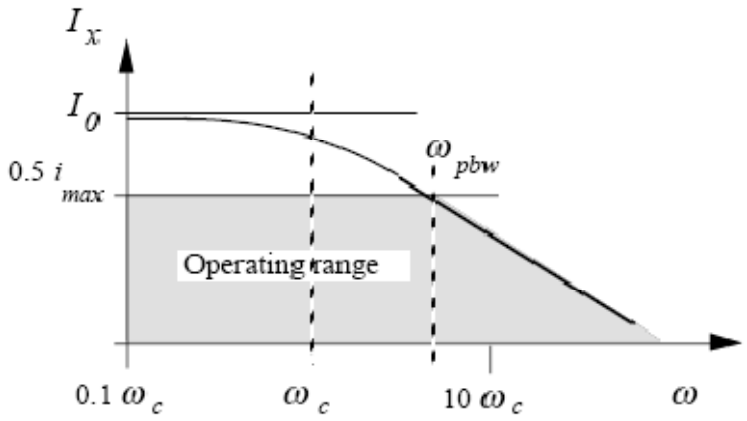


**Figure 2-26: Operating range of the magnetic actuator [7]**

## 2.6 Controller

### *2.6.1 Introduction*

A typical digital controller consists of the processor, analog-to-digital converters (A/D), digital-to-analog converters (D/A), filters, memory and interfacing components. Development systems such as dSPACE® include a host computer and peripherals [9].

Magnetic bearing control systems are commercially available and these systems combine a high number of A/D- and D/A-channels, analog filters and digital I/O with a DSP and memory on a single Euro-format card [7]. Magnetic bearings usually require twice as many D/A-channels than A/D channels as a single axis control channel has one input from the sensor and two outputs for the positive and negative coils.

For relatively simple controller structures, integer arithmetic are sufficient even when operated at high speed, but for more complex structures such as a state estimator or a high order controller combined with fast response time, floating point arithmetic is a major advantage. This plays an important role in deciding on the controller that will be used. In the case of A/D- and D/A-converters the right combination between accuracy, speed and cost has to be found. Eight bit accuracy may not be enough for most applications, but sixteen bit accuracy at high speeds is expensive. Twelve bit accuracy for A/D-D/A converters gives a good combination of high speed and cost efficiency [7].

The decision on the controller also depends on factors like software availability, past experience, compatibility to given environments and cost, but it can be said that DSPs will meet the demands of fast control as required for magnetic bearings [11].

A recent acquisition of the McTronX research group is a dSPACE® modular hardware system. This dSPACE® system comprises a dedicated processor board, digital I/O capability, PWM generation, high-speed A/D and D/A converters. The system is used to control the Fly-UPS system as discussed is section 4.7.

### *2.6.2 DS1005 processor board*

The DS1005 PPC board is one of dSPACE's processor boards that form the core of dSPACE's modular hardware. Processor boards provide the computing power for real-time systems and also function as interfaces to the I/O boards and the host PC. The DS1005 is the board of choice for applications with high sampling rates and high I/O capacity. Great processor power plus fast access to I/O hardware with minimum latencies make the DS1005 processor board considerably faster than solutions based on commonly available PCs.

**Table 2-1: DS1005 processor board specifications**

| Parameter | Specification |
|---|---|
| Processor | - IBM PowerPC 750GX 1 GHz chip<br>- Up to 4 instructions in parallel<br>- 32 kB L1 data cache<br>- 32 kB L1 instruction cache |
| Memory | - 1 MB L2 cache<br>- Cache running at processor clock<br>- 128 MB SDRAM global main memory for host data exchange and applications<br>- 16 MB flash memory for boot firmware and specific applications |
| Serial interface | - RS232 interface with standard UART allowing transfer rates of up to 115.2 Kbaud |
| Connection to I/O bus | - PHS++ bus Interface<br>- 32-bit I/O bus for modular I/O configuration<br>- Peak transfer rate 30 MB/s<br>- Up to 64 PHS bus interrupts |

Table 2-1 lists some of the specifications of the DS1005 processor board. The processor board boasts a 1 GHz IBM PowerPC chip with 32 kB date cache as well as 32 kB of instruction cache. The processor board also has 128 MB SDRAM global memory in which host data and applications can be stored. It also has a high-speed PHS++ bus that connects all the expansion boards to the processor board giving high transfer rates of up to 30 MB/s. These features make the DS1005 board ideal for real time system monitoring and control of a given system.

### 2.6.3 DS2004 high-speed A/D board

Each of the DS2004's 16 channels has an independent A/D converter with a resolution of 16 bits and differential inputs. It also has a conversion time of 800 ns per channel. The board has 4 external triggers and extensive trigger functions enabling the board to do single value conversions as well as whole sample bursts. It buffers up to 16,384 values per channel and then transfers them to the processor board via the PHS++ bus as a burst.

**Table 2-2: DS2004 high-speed A/D board specifications**

| Parameter | Specification |
|---|---|
| General | 16 A/D differential input channels |
| | 16 independent A/D converters |
| | 16-bit resolution |
| | ±5 V and ±10 V input voltage range on channel |
| | 4 external trigger inputs |
| ADCs | 800 ns conversion time |
| | 1 MΩ input impedance |
| | ± 50 V input overvoltage protection |
| Interfacing | 16 bit ISA slot for power supply |
| | Connects to PHS++ bus |

Table 2-2 lists the key specifications of the DS2004 high-speed A/D board.

### 2.6.4 DS2003 multi channel A/D board

The DS2003 boasts 32 A/D input channels and is used for hardware-in-the-loop (HIL) development. It also has a wide range of programmable resolutions and sampling times depending on the number of ADCs used. The board is ideal for the interfacing of temperature- and pressure sensors and is mainly used for rapid control prototyping.

**Table 2-3: DS2003 multi-channel A/D board specification**

| Parameter | Specification |
|---|---|
| General | 32 A/D input channel (single ended) |
| | 2 independent A/D converters |
| | Simultaneous sample-and-hold |
| | 4-,8-,10-,12-,13-,14-,15-,16-bit resolution (programmable) |
| | ±5 V and ±10 V input voltage range |
| | 1 external trigger |

| | |
|---|---|
| A/D channels | Conversion time of 1.2..4.2 µs (resolution dependent) |
| | S/H acquisition time of 1 µs |
| | ±15 V input overvoltage protection |
| Interfacing | 16 bit ISA slot for power supply |
| | Connects to PHS++ bus |

The main specifications of the DS2003 multi-channel A/D board is listed in Table 2-3

### *2.6.5 DS4002 timing and digital I/O board*

The DS4002 timing and digital I/O board combines a variety of digital I/O tasks on one board. It provides the functionality you expect from an ordinary digital I/O board plus additional features that help you perform specific control tasks easily. Eight channels can be programmed for either capturing digital signals or generating flexible pulse patterns. 32 additional I/O lines can be used for further digital I/O tasks, for example, to control single input lines (switches, sensors) or output lines (relays, displays).

**Table 2-4: DS4002 timing and digital I/O board specifications**

| **Parameter** | **Specification** |
|---|---|
| General | 8 channels (timing I/O) with 200 ns resolution |
| | Each channel individually programmable as input or output |
| | Common 30 bit/200 ns time base |
| | Fast dual-port RAM for data storage |
| | 32 additional digital I/O lines (TTL) |
| | 2 external trigger input lines |
| Digital I/O | 32 lines with ESD (electrostatic discharge) protection:<br>24 lines input/output<br>(programmable in 8-bit groups, as direct input, strobed input or output)<br>4 lines fixed input mode<br>4 lines fixed output mode |
| | 1 strobe input |
| | 2 handshake lines for acknowledge and output ready |
| | Direct and/or latched input mode, used to control |

| | |
|---|---|
| | single input or output lines |
| | Voltage range: TTL input/output level<br>Output current: Max. -64 mA/+16 mA |
| Interfacing | 16 bit ISA slot for power supply |
| | Connects to PHS++ bus |

Table 2-4 shows the functionality of the DS2004 timing and digital I/O board.

### *2.6.6 DS5101 digital waveform output board*

Digital pulse patterns are required in almost any control application. The demands made on PWM resolution and flexibility are very high, especially in drives control. The DS5101 autonomously generates any TTL pulse patterns on up to 16 channels with high accuracy. With a time resolution of 25 ns, the DS5101 meets even the toughest requirements. The ability to change pulse widths in real time combined with various trigger and interrupt mechanisms gives the DS5101 board great flexibility and programmability.

**Table 2-5: DS5101 digital waveform output board specifications**

| **Parameter** | **Specification** |
|---|---|
| General | 16 timing I/O channels<br>External reset input<br>Interrupt controller |
| Dual-port memory (DPMEM) | DPMEM for program (states) and data (delays)<br>Stores 512 delay parameters (30 bits) and 128 program states (90 bits) for each channel |
| Timing I/O channels | 25 ns time resolution<br>40 MHz internal or 20 ... 40 MHz external common time base<br>2 MHz maximum output frequency<br>250 ns ... 26 s pulse widths |
| | Voltage range: TTL input/output level<br>Output current: Max. -15 mA/+64 mA |
| Interfacing | 16 bit ISA slot for power supply |
| | Connects to PHS++ bus |

The specifications of the DS5101 digital waveform output boards specifications are listed in Table 2-5. The board is able to generate 1-phase PWM signals, 3-phase PWM signals, 3-phase/6-channel PWM signals, simulate Incremental sensors and generate monoflop signals.

### *2.6.7 DS2103 D/A board*

D/A conversion is required by many rapid control prototyping applications to provide the control signal for actuators. In hardware-in-the-loop applications, sensors that provide analog signals have to be simulated. The D/A boards provide various channel numbers, resolutions, and speeds to choose from. This board can be configured from Simulink® with Real-Time Interface. The voltage range can be set for each channel individually

**Table 2-6: DS2103 D/A board specifications**

| Parameter | Specification |
|---|---|
| General | 32 parallel D/A converters<br>14-bit resolution<br>±5 V or ±10 V ouput voltage range (programmable)<br>Reset to zero on I/O error (programmable) |
| D/A channels | 10 µs to ±0.012% of FSR (full-scale range)<br>Output current: ±5 mA max |
| Interfacing | 16 bit ISA slot for power supply |
| | Connects to PHS++ bus |

Table 2-6 lists the specifications of the DS2103 D/A board.

*All the components contained in the Flywheel Energy Storage System (FESS) were discussed in detail and the knowledge contained in each paragraph will be used in chapter 3 to design the AMB system. The choice of actuator configuration can now be based on knowledge obtained from previous work. The type of sensor to use with a specific power amplifier was also discussed and will influence the final decision. Some valuable information about the controller design was also discussed which enables the designer to obtain the controller parameters from the specified stiffness and damping values of the system. The next chapter contains a detailed electrical system design.*

# 3
# Chapter

# Magnetic bearing designs

*Chapter 3 contains detailed radial and axial AMB designs. First the design process that was followed is explained. This is followed by a detailed AMB specification that highlights the aspects of the magnetic bearings that should be considered in the design process. This is followed by a detailed radial AMB design and a detailed axial AMB design. Finally the implementation of the three AMBs is discussed.*

## 3.1 Design process

Applications where rotating machinery are supported by magnetic bearings are expected to prove that real loads can reliably be controlled by AMBs during normal operation and also when disturbance forces are present [14]. In order to optimally design an AMB system for a certain application, knowledge about the rotor dynamic behaviour during operation is needed as well as the specific forces acting on the rotor. Therefore static and dynamic forces as well as specific process demands, including accuracy of rotor position and maximum allowable rotor displacement, must be considered [7].

In magnetic bearing, as in conventional bearings, the load capacity and the stiffness can be defined. The static load capacity $F_{max}$ is the maximum load capacity for a static force over an unlimited time period and is defined by the maximum forces of the application, the geometry of the arrangement and the design of the machine. The stiffness $k_{eq}$ of the magnetic bearing is given by the negative position stiffness $k_s$ of the electromagnet and the controller gain. The stiffness of an AMB is however also dependent on the operating frequency $\omega$ of the disturbance force [7].

The procedure followed to design the magnetic bearings is shown in Figure 3-1. Firstly the necessary AMB force $F_d$ is determined from the rotor dynamic analysis. This is followed by an adjustment of the sensors and amplifiers and a first optimisation of the control loop. Based on the required AMB features, a necessary stiffness $S_n$ is defined which the bearing has to conform to:

$$S_n = \frac{F_{max}}{X_{al}} \quad \textbf{(3-1)}$$

where $F_{max}$ is the sum of the design force $F_d$ and the reserve force $F_{res}$. The allowable rotor displacement $X_{al}$ is determined by the mechanical layout of the machine. The accessible dynamic stiffness ($S_d$) of the AMB system is given by (3-2).

$$S_d(\omega) = \frac{F_d + F_{dist}(\omega)}{X(\omega)} \quad \textbf{(3-2)}$$

The intersection between the simulated dynamic stiffness ($S_d$) and the necessary stiffness ($S_n$) is the maximum frequency $\omega_{max}$ for acting disturbance forces. This frequency limits the allowable operating range and is thus the design limit. The criterion for reliable performance of the AMB is therefore given by (3-3) [15].

$$S_{op} > S_n \quad \textbf{(3-3)}$$

If the relationship in (3-3) is not satisfied in the first step, a controller fine tuning follows. If the tuning is not successful, the AMB's parameters have to be determined again and the AMB has to be redesigned.

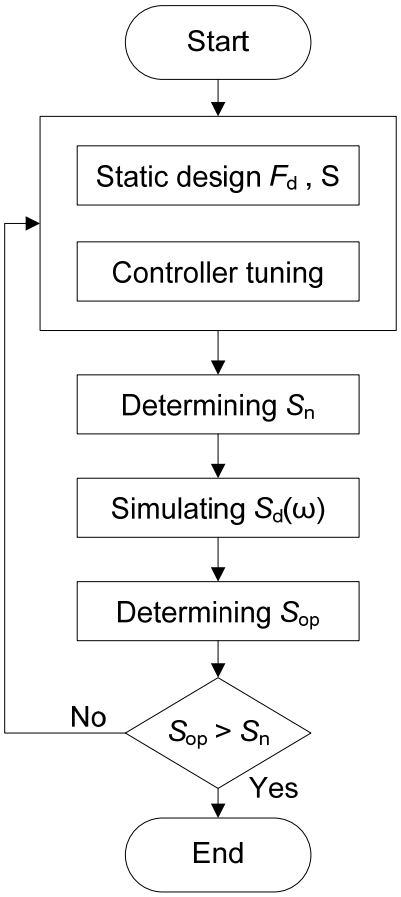


**Figure 3-1: Algorithm to prove reliable AMB operation [15]**

## 3.2 Radial AMB design

The AMB designs were performed using the MathCAD® software suite and the complete design can be found on the data CD in Appendix D. The program allows one to easily manipulate variables and equations can easily be simplified and solved. The design steps used in this design are based on the heteropolar radial bearing design process outlined in [11].

### *3.2.1 Design choices and performance requirements*

As discussed earlier, the Fly-UPS system will make use of two radial AMBs as well as one axial AMB. The AMBs will be powered by switching power amplifiers, and the rotor/flywheel will be propelled by a PMSM. The rotor/flywheel will be able to operate at 30,000 rpm. To ensure that the rotor is capable of high rotational speeds, the losses in the magnetic circuit should be minimized. In order to reduce the high speed losses, the magnetic circuit is laminated. Since it is difficult to manufacture laminated homopolar radial AMBs, it was decided to make use of laminated heteropolar configuration and since knowledge is already established on heteropolar AMBs at the North-West University [13].

The maximum disturbance force is determined from rotor dynamic analysis. An unbalance of G6 is used in the analysis to determine the maximum force after the rotor is balanced to a G1 standard which ensures a good safety margin. It was determined that $F_{dist}$ = 105 N for a G6 unbalance. It is also specified that the maximum displacement may be 20 % of the nominal air gap, thus the worst case scenario will be when the air gap is at 120 % of the nominal air gap and a disturbance of 105 N occurs. Under these conditions the bearing must still be able to generate 105 N of force.

With $F_{dist}$ = 105 N and $g_0$ = 500 µm, the electromagnetic constant $k_{em}$ is determined with the air gap at 120 % of the nominal air gap using (3-4)

$$k_{em} = F_{dist} \cdot (g_0 \cdot 1.2)^2 = 3.78 \times 10^{-5} \quad \frac{\text{kg} \cdot \text{m}^3}{s^2} \tag{3-4}$$

The maximum bearing force necessary for the AMB to generate 105 N of force at 120 % of the nominal air gap can then be determined by substituting (3-4) into (3-5)

$$F_{\max} = \frac{k_{em}}{{g_0}^2} = 151.2 \text{ N} \cong 150 \text{ N} \tag{3-5}$$

The linear force requirement of the AMB is then determined by making use of the maximum disturbance force as specified by the rotor dynamic analysis as well as the maximum rotor displacement. The linear force requirement is specified by making use of (3-6) with $F_{dist}$ = 105 N and $g_0$ = 500 µm and a maximum rotor displacement of 15 µm.

$$k_m = F_{dist} \cdot \left(g_0 + 15 \times 10^{-6}\right)^2 \qquad \textbf{(3-6)}$$
$$= 2.785 \times 10^{-5} \quad \frac{\text{kg} \cdot \text{m}^3}{s^2}$$

The maximum linear force $F_{linear}$ of the bearing is then determined by making use of (3-7)

$$F_{linear} = \frac{k_m}{g_0} \qquad \textbf{(3-7)}$$
$$= 111.4 \ \text{N}$$

Other choices that simplify the design are:

- Poles are paired which implies no flux splitting (NNSSNNSS). This configuration does not make effective use of the magnetic material but does simplify the control and reduces power losses.
- Quadrant control is implemented. Each pole pair (NS) is wound in series and powered by a single power amplifier.
- Removable coils are used.

Figure 3-2 displays a standard 8-pole configuration with removable coils that will be used in this design. As shown in Figure 3-2 the magnetic material is not optimally utilised since there are areas in the material which experience no flux. This configuration however simplifies the control requirements.

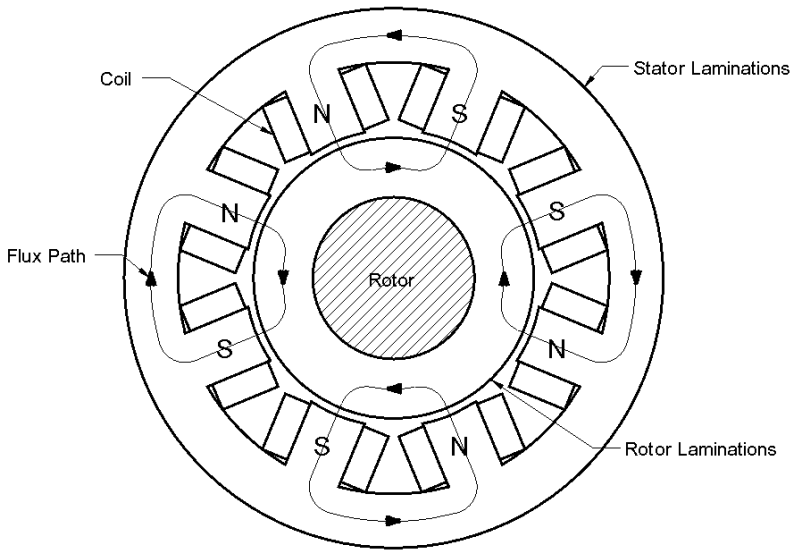


**Figure 3-2 Typical 8-pole heteropolar radial bearing [11]**

The material used for the laminations is Cogent[tm] silicon steel (M270-35A). This is machine grade silicon steel with a lamination thickness of 0.35 mm. Using thin lamination will reduce the core losses at high-speed operation. 0.35 mm laminations are not the ideal choice, but they were readily available.

Through the iterative process that was followed, the following performance requirements were compiled from the rotor dynamic analysis and mechanical configuration:

- Rotor laminations inside diameter ($2r_r$) are equal to 30 mm and is an output of the rotor design [16]
- Peak load capacity ($F_{max}$) of 150 N and was determined by the rotor dynamic analysis.
- Bearing stiffness $k_{eq}$ of 500 N/mm
- Bearing damping $b_{eq}$ of 2.5 N.s/mm
- The air gap ($g_0$) is equal to 0.5 mm which was chosen to represent a typical air gap that is used
- The saturation flux density $B_{sat}$ is chosen to be 1 T at maximum current to ensure that the bearing operates in the linear region of the magnetic material
- The maximum operating speed was set to be 30,000 rpm which is the speed at which the magnets on the rotor/flywheel can safely operate [16]

### *3.2.2 Amplifier specification*

The amplifier specifications are obtained from the maximum slew rate needed to implement the desired control. The maximum slew rate is calculated by determining the maximum change in force over a period of time. The maximum rotational speed of 30,000 rpm relates to a rotational frequency ($f_{rot}$) of 500 Hz. The resulting force caused by an unbalance on the shaft will represent a sinusoidal function with the same frequency as the rotational frequency. In order to utilise the full range of the magnetic arrangement the maximum amplitude of this unbalance force is chosen to be 150 N. The maximum slew rate is determined using (3-8).

$$\begin{aligned}\frac{dF}{dt} &= F_{\max} \cdot \Omega_{\max} \\ &= 150 \cdot 2 \cdot \pi \cdot 500 \text{ N/s} \\ &= 471.2 \times 10^3 \text{ N/s}\end{aligned} \quad \textbf{(3-8)}$$

The power amplifier maximum VA rating is now determined using (3-9) with the maximum slew rate.

$$\begin{aligned}VA_{\max} &= \frac{dF}{dt} \cdot g_0 \\ &= 471.2 \times 10^3 \cdot 0.5 \times 10^{-3} \text{ VA} \\ &= 235.6 \text{ VA}\end{aligned} \quad \textbf{(3-9)}$$

With the maximum VA rating specified the maximum current is chosen to be 5 A. Next the maximum voltage is obtained using (3-10).

$$V_{\max} = \frac{VA_{\max}}{I_{\max}} \quad \textbf{(3-10)}$$
$$= \frac{235.6}{5} \text{ V}$$
$$= 47.12 \text{ V}$$

The biasing ratio ($\beta$) is then determined in (3-11) by making use of the maximum force capability ($F_{max}$) and the linear force capability ($F_{linear}$) of the AMB as determined in (3-5) (3-7). Since quadrant coil control is employed, a factor $\sigma$ is added in (3-11).

$$\beta = \sqrt{\frac{F_{linear} \cdot \sigma}{F_{\max}}} \quad \textbf{(3-11)}$$
$$= \sqrt{\frac{111.4 \times 0.231}{150}}$$
$$= 0.414$$

By making use of the bias ratio, the bias current is now determined in (3-12)

$$I_b = \beta \cdot I_{max} \quad \textbf{(3-12)}$$
$$= 0.414 \times 5 \text{ A}$$
$$= 2.07 \text{ A}$$

The number of turns per coil is now determined using (3-13).

$$N = \frac{B_{sat} \cdot g_0}{I_{\max} \cdot \mu_0} \quad \textbf{(3-13)}$$
$$= \frac{1 \cdot 0.5 \times 10^{-3}}{5 \cdot 4 \cdot \pi \times 10^{-7}} \text{ turns}$$
$$\approx 80 \text{ turns}$$

### 3.2.3 Journal sizing and stator design

Figure 3-3 displays the mechanical layout of the electromagnetic design with the relevant dimensions.

| | |
|---|---|
| $r_s$ | stator radius |
| $r_c$ | coil space radius |
| $r_j$ | journal radius |
| $r_r$ | rotor shaft radius |
| $r_p$ | pole radius |
| $g_0$ | air gap |
| $w$ | pole width |
| $n$ | number of poles |
| $l$ | axial length |
| $a_r$ | journal stator aspect ratio $(r_j-r_r)/w$ |
| $A_g$ | air gap area |
| $N$ | number of coil turns |

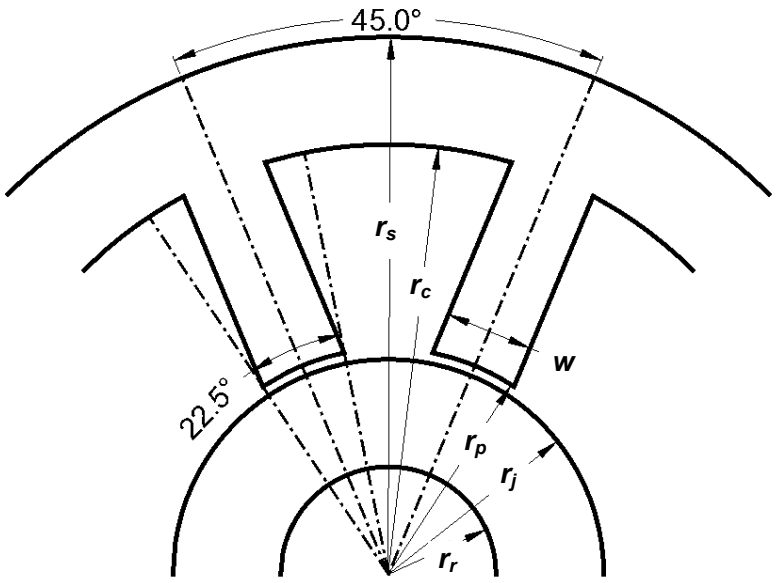


**Figure 3-3 Stator iron geometry [11]**

A maximum load capacity per unit area constraint is placed on an AMB due to material properties such as flux saturation and maximum current density. This implies that the peak load capacity dictates the air gap area. Using the configuration as shown in Figure 3-3, the air gap area is obtained using (3-14).

$$A_g = \frac{2 \cdot \mu_0 \cdot F_{\max}}{2 \cdot B_{sat}{}^2 \cdot \cos(\theta)} = 204.03 \times 10^{-6} \text{ m}^2 \quad \textbf{(3-14)}$$

Using an aspect ratio ($AR$) of 1 between the rotor lamination material width ($r_j$ - $r_r$) and the pole width ($w$), the pole width is determined using (3-15).

$$w = \frac{\theta \cdot (r_r + g_0)}{1 - \theta \cdot AR} = 10.04 \times 10^{-3} \text{ m} \quad \textbf{(3-15)}$$

The journal outside radius is now determined using (3-16).

$$r_j = w \cdot AR + r_r = 25 \times 10^{-3} \text{ m} \quad \textbf{(3-16)}$$

The pole radius is determined next making use of

$$r_p = r_j + g_0 = 25.5 \times 10^{-3} \text{ m} \quad \textbf{(3-17)}$$

The axial length of the journal can now be determined using (3-18)

$$l = \frac{A_g}{w} \qquad \textbf{(3-18)}$$
$$= 20.374 \times 10^{-3} \text{ m}$$
$$\cong 21 \times 10^{-3} \text{ m}$$

The number of laminations per radial AMB stator is determined next using (3-19)

$$N_{lam} = \frac{l}{350 \times 10^{-6}} \qquad \textbf{(3-19)}$$
$$= 60$$

### *3.2.4 Coil design*

Since this is a test model, removable coils are implemented in order to allow the interchanging of coils. Figure 3-4 displays the removable coil configuration with the applicable coil design parameters.

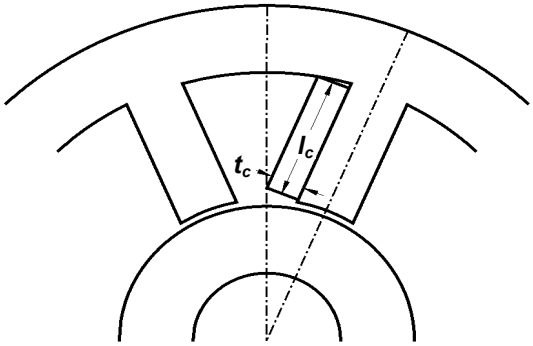


**Figure 3-4 Removable coil configuration [11]**

These parameters are obtained using:

$$t_c = r_p \cdot \tan\left(\frac{\pi}{n}\right) - \frac{w}{2} \qquad \textbf{(3-20)}$$
$$= 5.556 \times 10^{-3} \text{ m}$$

with $n$ the number of pole pairs. Using the thermal limit of $3 \times 10^6$ A/m$^2$ ($J_{max}$), and a copper fill factor of 0.5 ($FF_c$), the coil window area is determined using (3-21).

$$A_v = \frac{N \cdot I_{\max}}{FF_c \cdot J_{\max}} \qquad \textbf{(3-21)}$$
$$= 268.6 \times 10^{-6} \text{ m}^2$$

From (3-20) and (3-21) $l_c$ is obtained using (3-22).

$$l_c = \frac{A_v}{t_c} \qquad \textbf{(3-22)}$$
$$= 48.374 \times 10^{-3} \text{ m}$$

The coil space radius $r_c$ can now be determined using (3-23).

$$r_c = \sqrt{\left(l_c + r_p\right)^2 + \left(\frac{w}{2} + t_c\right)^2} \quad \textbf{(3-23)}$$
$$= 74.6 \times 10^{-3} \text{ m}$$
$$\cong 75 \times 10^{-3} \text{ m}$$

The pole length is obtained from the coil space radius $r_c$ and the pole radius $r_p$ using (3-24).

$$l_p = r_c - r_p \quad \textbf{(3-24)}$$
$$= 49.1 \times 10^{-3} \text{ m}$$

The stator radius is obtained using (3-25).

$$r_s = r_c + w \quad \textbf{(3-25)}$$
$$= 84.612 \times 10^{-3} \text{ m}$$
$$\cong 85 \times 10^{-3} \text{ m}$$

### 3.2.5 Coil resistance and inductance

The wire size needed for this configuration is determined using (3-26).

$$r_{wire} = \sqrt{\frac{FF_c \cdot A_v}{\pi \cdot N}} \quad \textbf{(3-26)}$$
$$= 0.733 \text{ mm}$$

Standard 1.5 mm diameter wire is sourced. The wire copper area is now obtained using (3-27).

$$A_{wire} = \pi \cdot \left(r_{wire}\right)^2 \quad \textbf{(3-27)}$$
$$= 1.688 \times 10^{-6} \text{ m}^2$$

The coil length ($l_{coil}$) is obtained by determining the pole perimeter using (3-28).

$$l_{coil} = 4 \cdot N \cdot \left[\left(t_c + w\right) + \left(t_c + l\right)\right] \quad \textbf{(3-28)}$$
$$= 13.409 \text{ m}$$

A copper specific resistance ($\rho_c$) of 1.912x10$^{-8}$ Ω.m is used to determine the coil resistance as shown in (3-29).

$$R_{coil} = \rho_c \cdot \frac{l_{coil}}{A_{wire}} \quad \textbf{(3-29)}$$
$$= 0.1519 \ \Omega$$

The nominal coil inductance ($L_c$) is now obtained using (3-30).

$$L_c = \frac{2 \cdot \mu_0 \cdot A_g \cdot N^2}{g_0} = 6.494 \text{ mH} \quad \textbf{(3-30)}$$

### 3.2.6 AMB stiffness and damping

The force within the magnetic actuator changes with both current and air gap. Equation (3-31) gives a linearization for the instantaneous force as a function of current and displacement.

$$F(x,i) = k_s x + k_i i \quad \textbf{(3-31)}$$

The ratio of a change in force due to a change in current is called the current gain ($k_i$) and the ratio of a change in force due to a change in position is called the position stiffness ($k_s$). The position stiffness and current gain can now be determined by calculating the partial derivative of the force equation with respect to displacement and current at the working point. The force generated by a single power amplifier and a set of coils can be described by (3-32).

$$F = \frac{B^2 A_g}{\mu_0}\cos(\theta) = \frac{\mu_0 N^2 {i_m}^2 A_g}{{x_s}^2}\cos(\theta) \quad \textbf{(3-32)}$$

The current gain for a single actuator is defined as

$$k_i = \left.\frac{\partial F}{\partial i_m}\right|_{i_m = i_0,\ x_s = g_0} = 2\frac{\mu_0 N^2 i_0 A_g}{{g_0}^2}\cos(\theta) \quad \textbf{(3-33)}$$

where the derivative is evaluated with a control current equal to zero and a rotor position of $x$ = 0. The current gain is positive because an increase in current produces an increase in force.

The position stiffness for a single actuator is defined as

$$k_s = \left.\frac{\partial F}{\partial x_s}\right|_{i_m = i_0,\ x_s = g_0} = -2\frac{\mu_0 N^2 {i_0}^2 A_g}{{g_0}^3}\cos(\theta) \quad \textbf{(3-34)}$$

where the derivative is evaluated with a control current equal to zero and a rotor position of $x$ = 0. The position stiffness is negative as the force increases with a decreasing air gap.

To obtain the desired bearing stiffness and damping the PD controller parameters are determined using (3-35) and (3-36).

$$b_{eq} = 2K_D k_i \quad \textbf{(3-35)}$$

$$k_{eq} = 2K_P k_i - 2k_s \quad \textbf{(3-36)}$$

The proportional constant is obtained using (3-37).

$$K_P = \frac{\frac{k_{eq}}{2} + k_s}{k_i} = 14213 \tag{3-37}$$

Take note, $k_s$ assumes positive values due to chosen position reference. The derivative constant is determined using (3-38). An additional pole is also introduced in the differential path in order to ensure stable operation. The differentiator pole is chosen to

$$K_D = \frac{b_{eq}}{2k_i} = 50.4 \tag{3-38}$$

From a differentiator's frequency response it can be seen that as the frequency increases, the differentiator gain also increases. To ensure that the high frequency noise does not become dominant, an additional pole is introduced that limits high frequency gain. The transfer function is given by

$$G_D(s) = \frac{s \cdot \omega_n}{s + \omega_n} \tag{3-39}$$

The additional pole in the differentiator path is included in the MATLAB® simulations in order to ensure that the simulations and the actual results will correlate closely.

### 3.2.7 MATLAB® simulations

In order to simulate the behaviour of an active magnetic bearing, an accurate model of the AMB system is a necessity. Figure 3-5 shows a nonlinear model of an AMB which was implemented in MATLAB® to simulate the system.

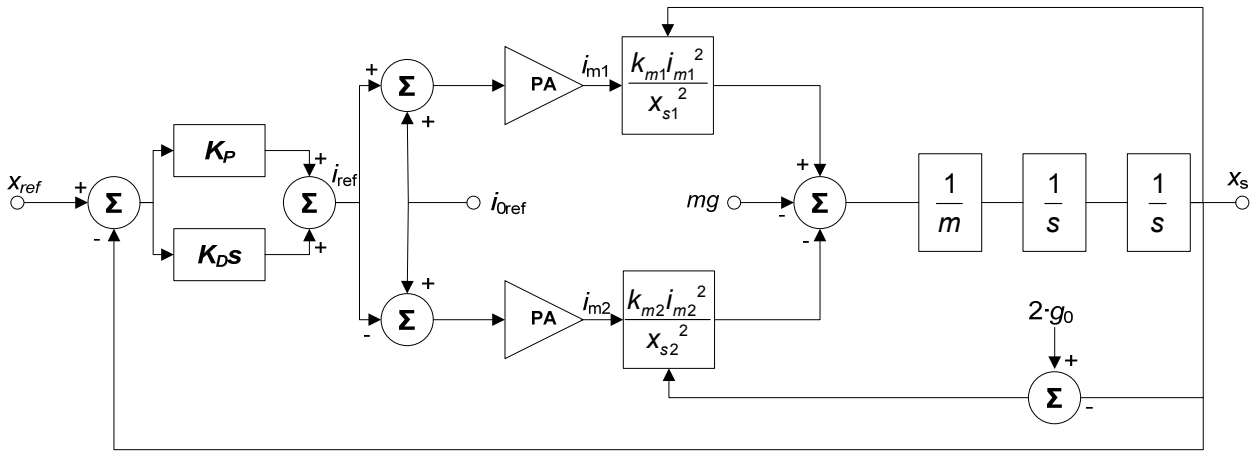


**Figure 3-5: Nonlinear model of the radial AMB system**

The actual rotor position is subtracted from the reference position to generate an error signal. A single PD controller then generates an appropriate current reference signal ($i_{ref}$). The current reference signal is then added and subtracted from a bias current signal ($i_{0ref}$) to produce reference signals $i_{m1}$ and $i_{m2}$ for the top and bottom power amplifiers (PAs) respectively. The actuator

characteristic equation then converts the currents produced by the PAs to forces. The two forces are opposing and therefore subtracted from each other. The rotor acceleration is obtained by dividing the resulting force with the rotor mass. The rotor position is then determined from the rotor acceleration [11].

The nonlinear force to displacement relationship as well as the nonlinear force to current relationship was implemented in the simulation program. The simulation program also simulates the power amplifiers by making use of the bandwidth of the specified power amplifiers and controlling the current output with a simple PI-controller as discussed in section 2.5.3. Figure 3-6 shows the PI-controller of the simulated power amplifier.

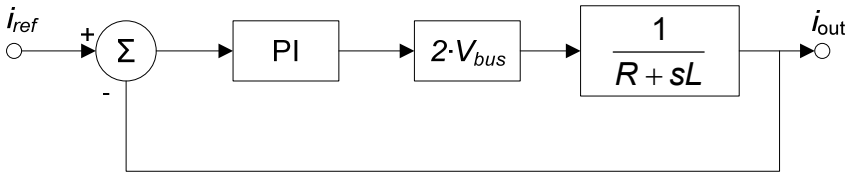


**Figure 3-6: PI-controller of power amplifier**

The proportional constant $K_p$ was determined by using (3-40) making use of a bandwidth of 2.5 kHz, coil inductance $L$ = 6.494 mH, a coil resistance $R$ = 0.152 Ω and the bus voltage $V_{bus}$ = 51 V.

$$K_p = \frac{2 \cdot \pi \cdot f_{bw} \cdot L - R}{2 \cdot V_{bus}} \qquad \textbf{(3-40)}$$

$$= \frac{2 \times \pi \times 2500 \times 6.494 \times 10^{-3} - 0.152}{2 \times 51}$$

$$= 1$$

The integral constant $K_i$ was chosen to be 10 % of the proportional constant and is given by

$$K_i = 0.1 \cdot K_p \qquad \textbf{(3-41)}$$

$$= 0.1$$

The sample rate of the simulation was chosen to be 1 MHz. The dSPACE® controller can however only sample at rates in the order of 20 kHz. The MATLAB® source code for the simulation can be found on the data CD in Appendix D.

The equivalent masses of the rotor also have to be determined at the location of each of the two radial AMBs. This was accomplished by simplifying the rotor to a point mass system as shown in Figure 3-7. The total weight ($M_t$) of the rotor is determined to be 18.6 kg [16]. The equivalent mass of the rotor at the top radial AMB is determined using (3-42)

$$M_{top} = M_t \cdot \left( \frac{L_2}{L_t} \right) \quad \textbf{(3-42)}$$
$$= 18.6 \times \left( \frac{159.97}{222.2} \right) \text{ kg}$$
$$= 13.22 \text{ kg}$$

The equivalent mass of the rotor at the bottom radial AMB is determined by (3-43).

$$M_{bottom} = M_t \cdot \left( \frac{L_1}{L_t} \right) \quad \textbf{(3-43)}$$
$$= 18.6 \times \left( \frac{64.253}{222.2} \right) \text{ kg}$$
$$= 5.38 \text{ kg}$$

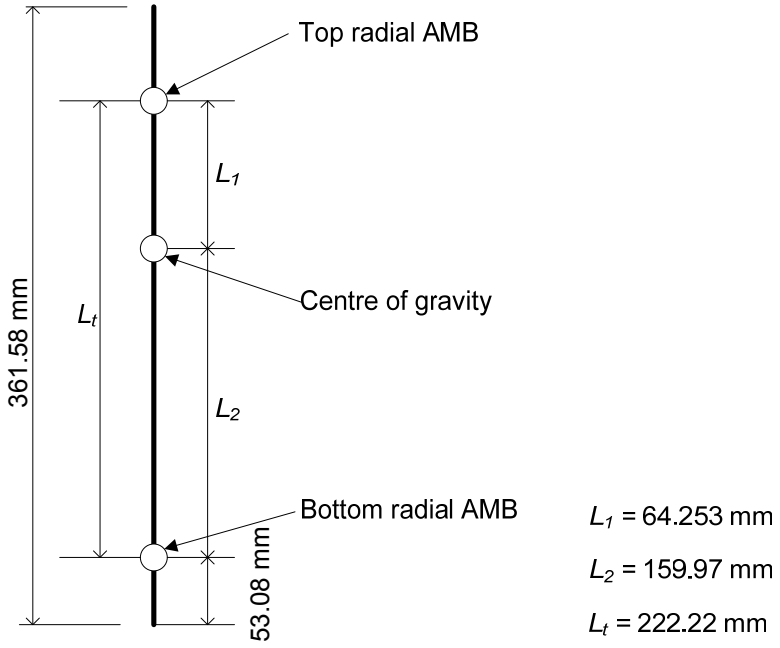


**Figure 3-7: Equivalent mass of rotor at each AMB**

The analytical bearing stiffness and damping are now verified using the simulation. Firstly a 10 µm step response was introduced on the bottom AMB at 0.075 s as shown in Figure 3-8. The point mass which the AMB will act on at the bottom AMB is 5.38 kg as determined.

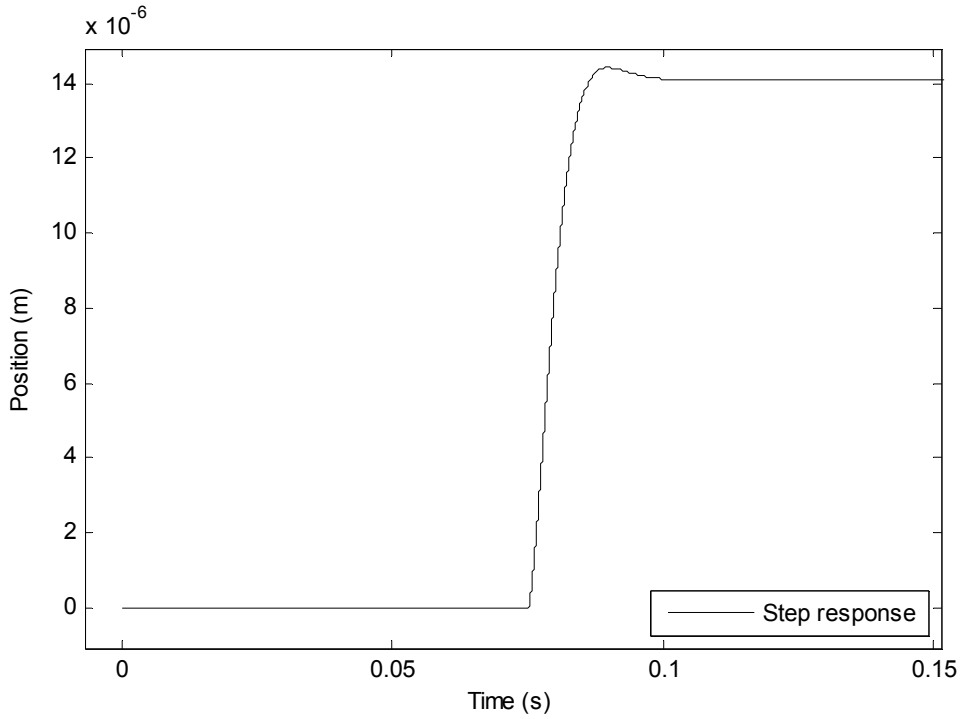


**Figure 3-8: Step response of 10 µm on the bottom radial AMB**

From Figure 3-8 the percentage overshoot (P.O.) is determined using (3-44)

$$P.O. = \frac{14.422\times10^{-6} - 14.103\times10^{-6}}{14.103\times10^{-6}} \times 100\ \% \\ = 2.26\% \tag{3-44}$$

and settling time ($T_s$) (to within 2 % of the final value) is determined as 0.0117 s. This system can be seen as a second-order system close to its working point. It is for this reason that a step response can be used to obtain the equivalent stiffness and damping value of the system. The equivalent bearing stiffness and damping are now obtained using the process outlined in section 3.2.6. The system damping ratio is obtained using (3-45)

$$P.O. = 100e^{\frac{-\pi\zeta}{\sqrt{1-\zeta^2}}} \\ \therefore\ \zeta = 0.7698 \tag{3-45}$$

The natural frequency of the system is now determined using (3-46)

$$\omega_n = \frac{4}{T_s\zeta} = 396.8\ \text{rad/s} \tag{3-46}$$

The equivalent stiffness for the system is now obtained using (3-47)

$$k_{eq} = \omega_n{}^2 m \\ = 520\times10^3\ \text{N/m} \tag{3-47}$$

The system's equivalent damping value is determined using (3-48)

$$b_{eq} = \zeta\left(2\sqrt{k_{eq} \cdot m}\right) = 2.574 \times 10^3 \text{ N.s/m} \quad \textbf{(3-48)}$$

This translates to a 4 % deviation on the predicted value of the equivalent stiffness and a 2.96 % deviation from the predicted value of the damping. These deviations may be attributed to the way in which the percentage overshoot and settling time was determined. In order to verify the simulation model with the physical model a series of step responses are performed. Since the Fly-UPS rotor will be mounted vertically, only one axis of each of the radial AMB has to be simulated. The step size is enlarged to ensure that the nonlinear nature of the system can be compared to that of the simulation model.

Figure 3-9 shows a step response of 50 µm introduced to the AMB at 0.075 s. The system shows little overshoot and yields the following parameters: P.O. = 2.09 %, $\zeta$ = 0.7758, $T_s$ = 0.0166 s, $k_{eq}$ = 519x10$^3$ N/m and $b_{eq}$ = 2.592 x10$^3$ N.s/m. These parameters correlate closely to the predicted stiffness and damping parameters.

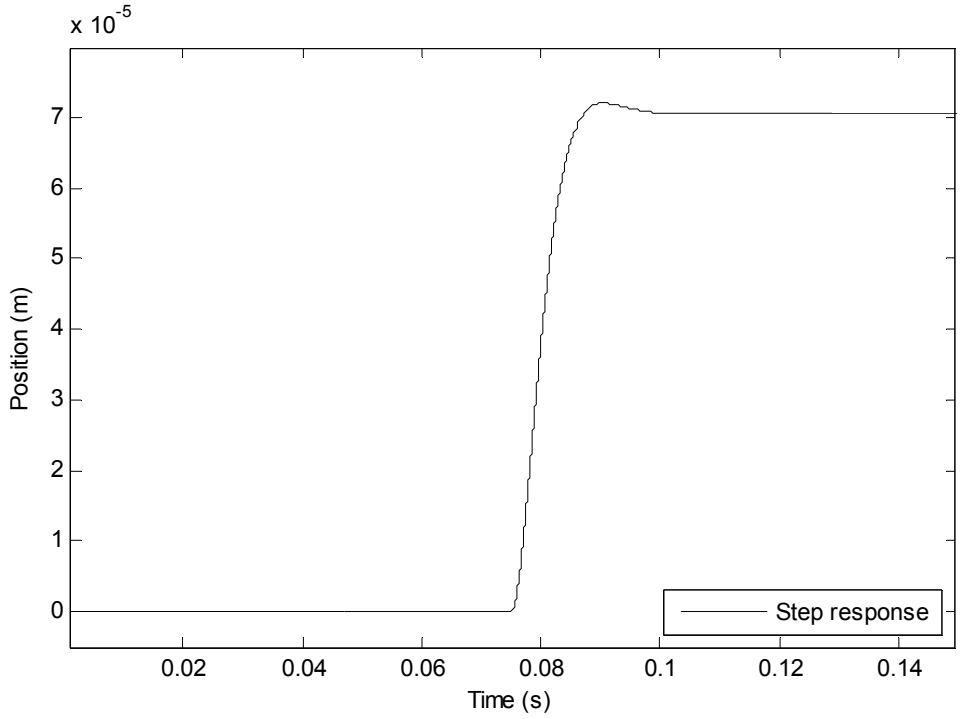


**Figure 3-9: Step response of 50 µm on the bottom radial AMB**

Next, a step response of 10 µm was introduced to the top AMB. The point mass on which this AMB will act on is 13.22 kg as determined. Figure 3-10 shows the response of the top AMB.

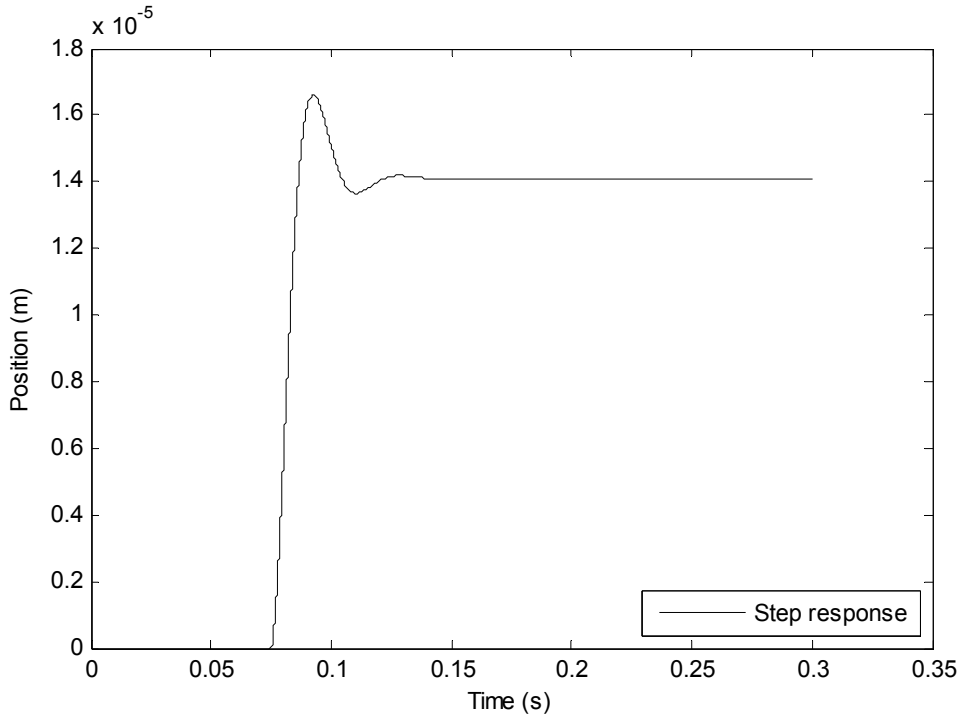


**Figure 3-10: Step response of 10 µm on the top radial AMB**

The system shows more overshoot than the bottom AMB because of the increase in mass at the top AMB. The simulation yields the following parameters: P.O. = 17.9 %, $\zeta$ = 0.48, $T_s$ = 0.041 s, $k_{eq}$ = 546x10$^3$ N/m and $b_{eq}$ = 2.578 x10$^3$ N.s/m. The equivalent stiffness yields a 9.2 % deviation whereas the equivalent damping yields a 3.12 % deviation from the predicted stiffness and damping parameters. This is largely due to the increased mass at the top AMB because it is situated closer to the heavy flywheel.

Finally a 50 µm step was introduced to the top AMB which yielded the following parameters: P.O. = 17.65 %, $\zeta$ = 0.4832, $T_s$ = 0.041 s, $k_{eq}$ = 538x10$^3$ N/m and $b_{eq}$ = 2.575 x10$^3$ N.s/m. The response of the top AMB is shown in Figure 3-11.

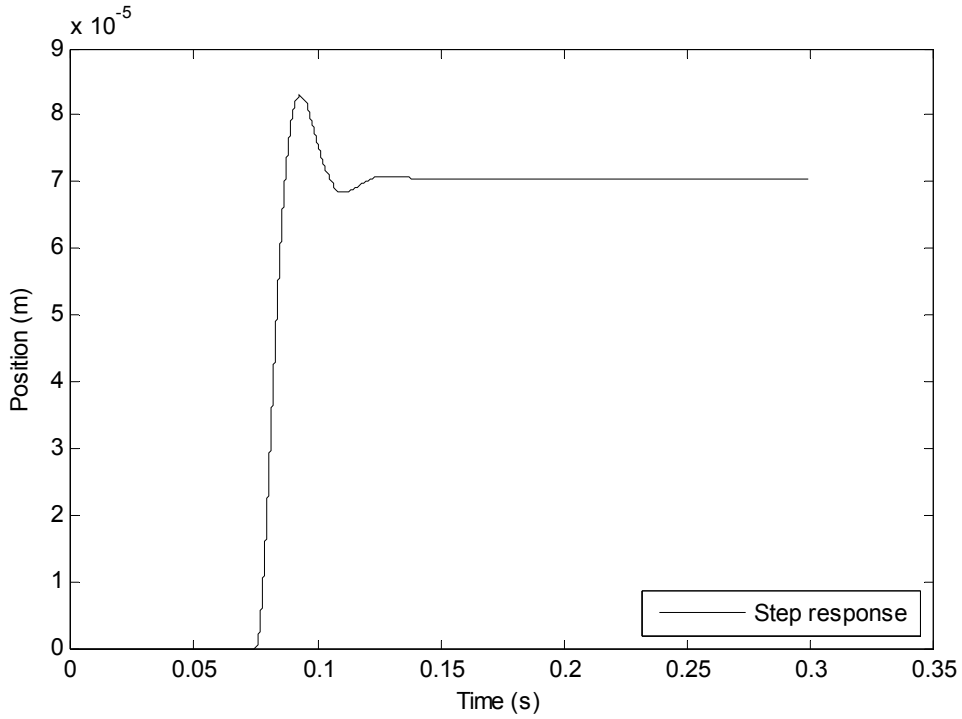


**Figure 3-11: 50 µm step response on top radial AMB**

These simulated step responses will be tested against the physical system in order to compare the results and to determine how closely the simulated and the actual results correlate.

### *3.2.8 Dynamic stiffness verification*

The next step in the design phase is to verify the dynamic stiffness of each AMB by making use of the position simulation used to determine the step responses. Firstly the necessary stiffness is determined using (3-49) with the design force ($F_D$) and the reserve force ($F_{res}$) of the AMB and the maximum allowable rotor displacement ($X_{al}$). The maximum allowable rotor displacement is determined by the mechanical constraints of the system, like seals and delevitating devices.

$$S_n = \frac{F_D + F_{res}}{X_{al}} \quad \textbf{(3-49)}$$

$$= \frac{105 + 45}{250 \times 10^{-6}} \text{ N/m}$$

$$= 600 \times 10^3 \text{ N/m}$$

The accessible dynamic stiffness of the given AMB is then determined using (3-50). A sinusoidal disturbance force is then applied to the system throughout the operating frequency range of the system.

$$S_d(\omega) = \frac{F_D + F_{dist}(\omega)}{X(\omega)} \quad \textbf{(3-50)}$$

Firstly the bottom AMB's dynamic stiffness was determined making use of the point mass the AMB will act on. The mass of the rotor at the bottom AMB is 5.378 kg, and a 5 N sinusoidal disturbance force is applied to the rotor. Figure 3-12 shows a qualitative representation of $S_d(\omega)$.

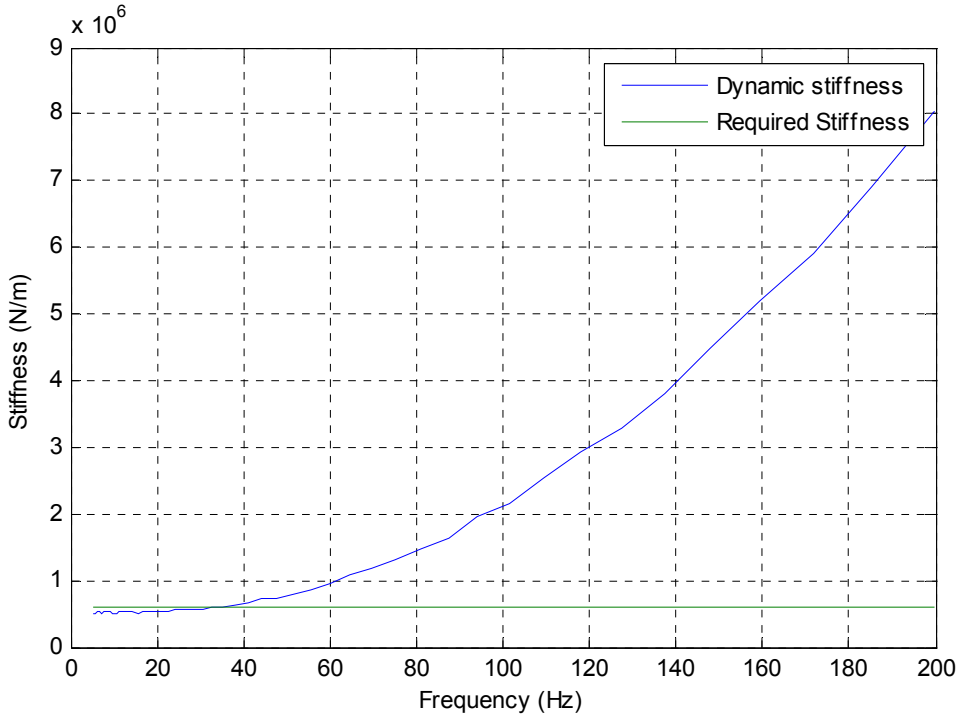


**Figure 3-12: Dynamic stiffness of the bottom radial AMB**

The result at the point of intersection between the simulated dynamic stiffness and the necessary stiffness $S_n$ is the maximum frequency $\omega_{max}$ for acting disturbance forces. This frequency limits the allowable operating range and is therefore the design limit. The criterion of the reliable performance of the AMB is $S_{op} > S_n$. From Figure 3-12 it can be seen that the operating stiffness of the AMB is below the necessary stiffness from 0 Hz up to 37 Hz. The operating stiffness increases above the necessary stiffness from 37 Hz.

It is therefore necessary to adjust the PD-controllers' parameters in order to obtain an operating stiffness above the necessary stiffness throughout the operating range of the system [15]. The proportional constant of the PD-controller was increased by 20 % from $K_p$ = 14214 to $K_p$ = 17056 and the dynamic stiffness analysis simulation was done again. Figure 3-13 shows the dynamic stiffness with the increased proportional constant.

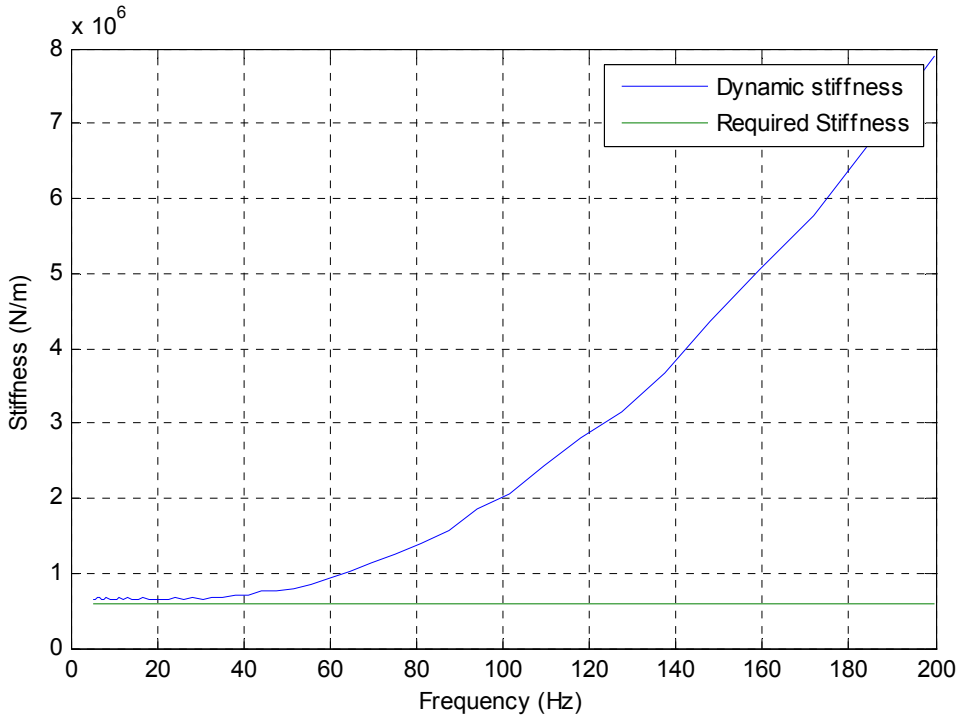


**Figure 3-13: Adjusted dynamic stiffness of the bottom radial AMB**

From the updated simulation it can be seen that the dynamic stiffness of the bottom AMB is above the necessary stiffness throughout the operating range and the criterion for reliable operation, $S_{op} > S_n$, has been satisfied. The design procedure of the bottom AMB has thus successfully been completed.

The same procedure is then followed to ensure reliable performance of the top AMB. The dynamic stiffness analysis has been done with the design parameters of the PD-controller. Figure 3-14 shows the dynamic stiffness as well as the necessary stiffness of the top AMB. The stiffness of top AMB differs from the stiffness of the bottom AMB because of the increased mass of 13.2 kg on which the top AMB acts.

It can be seen that the dynamic stiffness of the top AMB is below the necessary stiffness from 0 Hz up to 38 Hz. From 38 Hz upwards the stiffness increases above the necessary stiffness. An adjustment also has to be made to the proportional constant of the top AMBs' PD-controller. The proportional constant was increased by 100 % in order for the dynamic stiffness to be above the necessary stiffness throughout the operating range [15].

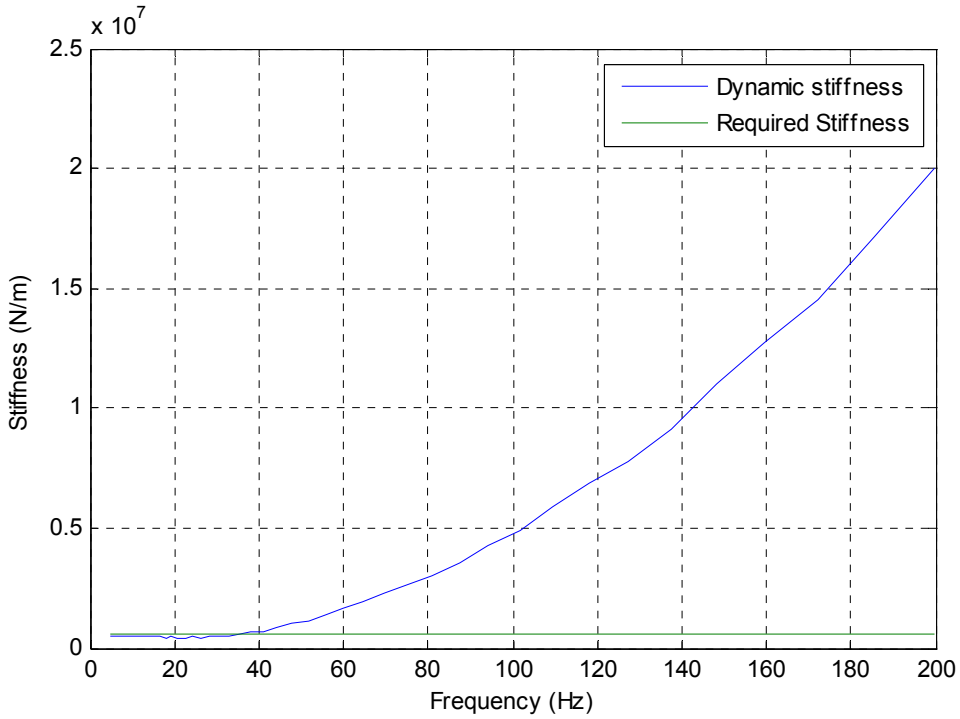


**Figure 3-14: Dynamic stiffness of the top radial AMB**

The dynamic stiffness analysis was done using the adjusted proportional constant of $K_p$ = 28428. Figure 3-15 shows the dynamic stiffness with the adjusted proportional constant.

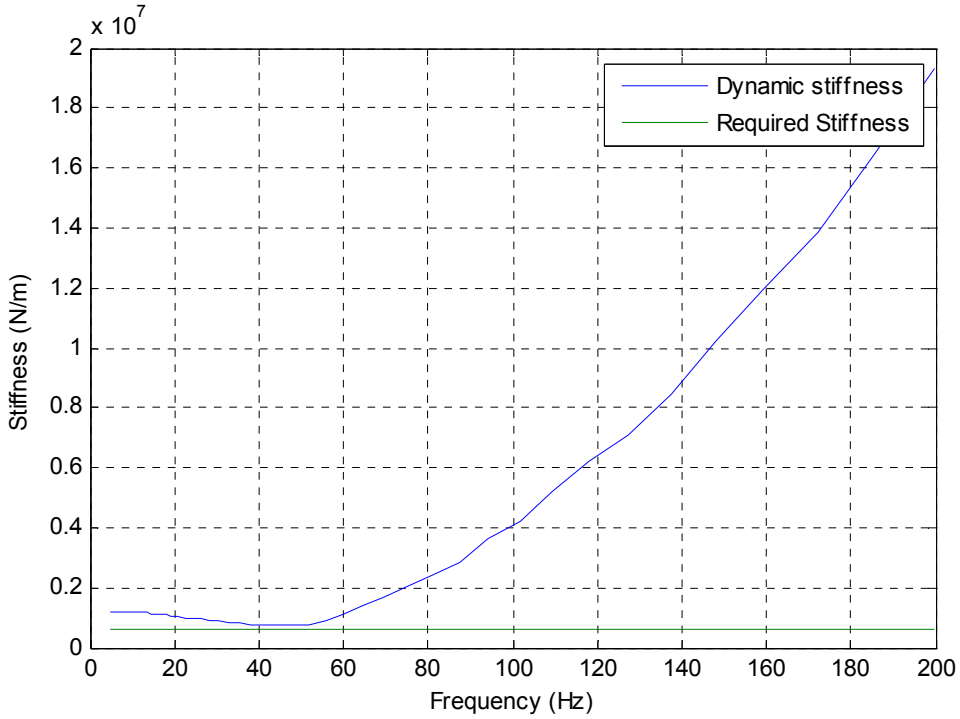


**Figure 3-15: Adjusted dynamic stiffness of the top radial AMB**

It can be seen that the dynamic stiffness is above the necessary stiffness throughout the operating range and the criterion for reliable performance $S_{op} > S_n$ has been satisfied. The design procedure of the top AMB has thus successfully been completed.

### 3.2.9 FEMM analysis

The final stage of the verification process was to do a Finite Element Method (FEM) analysis of the magnetic bearing design. The FEM analysis was done using the FEMM software package that was created by David Meeker and is a freeware program.

Similar to the bias current ($I_b$), the bias flux density ($B_b$) is determined by making use of the biasing ratio as determined in (3-11). The bias flux density is determined in (3-51) using the maximum flux density $B_{sat}$ = 1 T.

$$\begin{aligned} B_b &= \beta \cdot B_{sat} \\ &= (0.414 \times 1) \ \text{T} \\ &= 0.414 \ \text{T} \end{aligned} \tag{3-51}$$

The AMB stator and the laminated rotor were constructed within the FEMM program and all the materials including the Silicon steel, coils and the air gap were defined. Firstly the analysis was done at the bias current of 2.07 A as determined in (3-12). Figure 3-16 shows the flux density within the stator of the AMB at bias current.

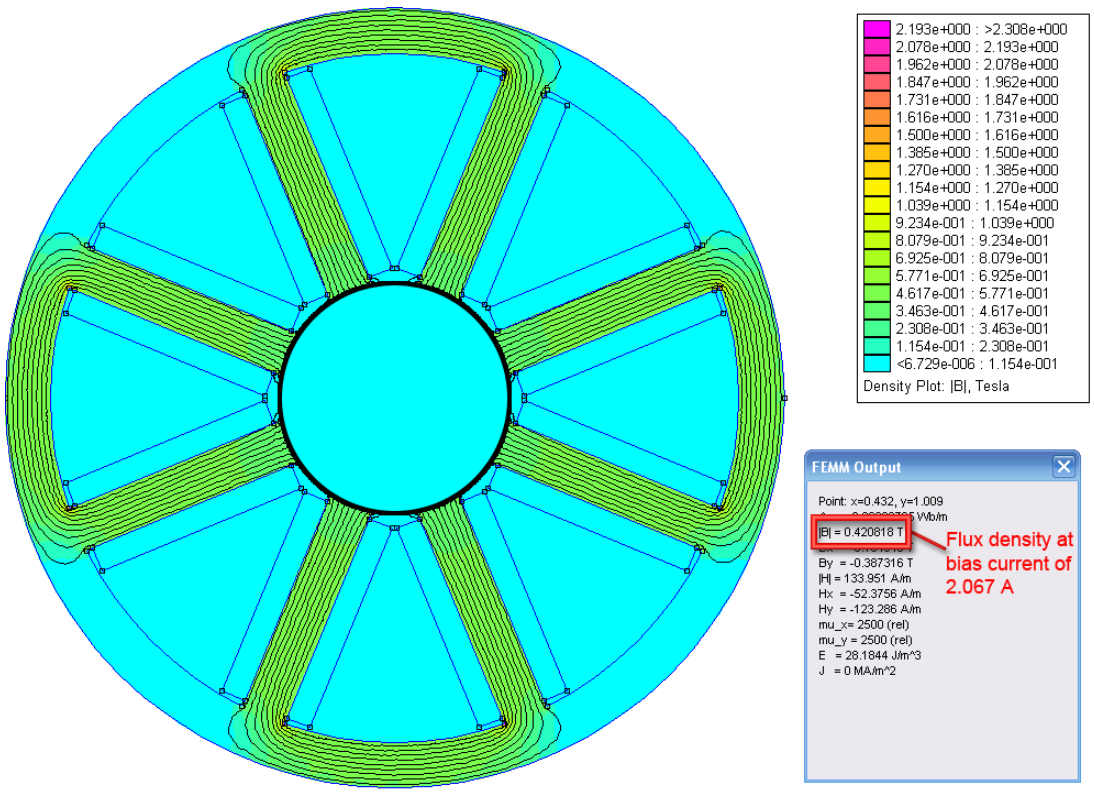


**Figure 3-16: FEM analysis of radial AMB at bias current**

It can be seen that the flux density inside the pole leg of the AMB is 0.42 T which correlates closely with the design bias flux density of 0.414 T.

The FEM analysis was also done on the AMB at the maximum current of 5 A. Figure 3-17 shows the flux density within the stator of the AMB.

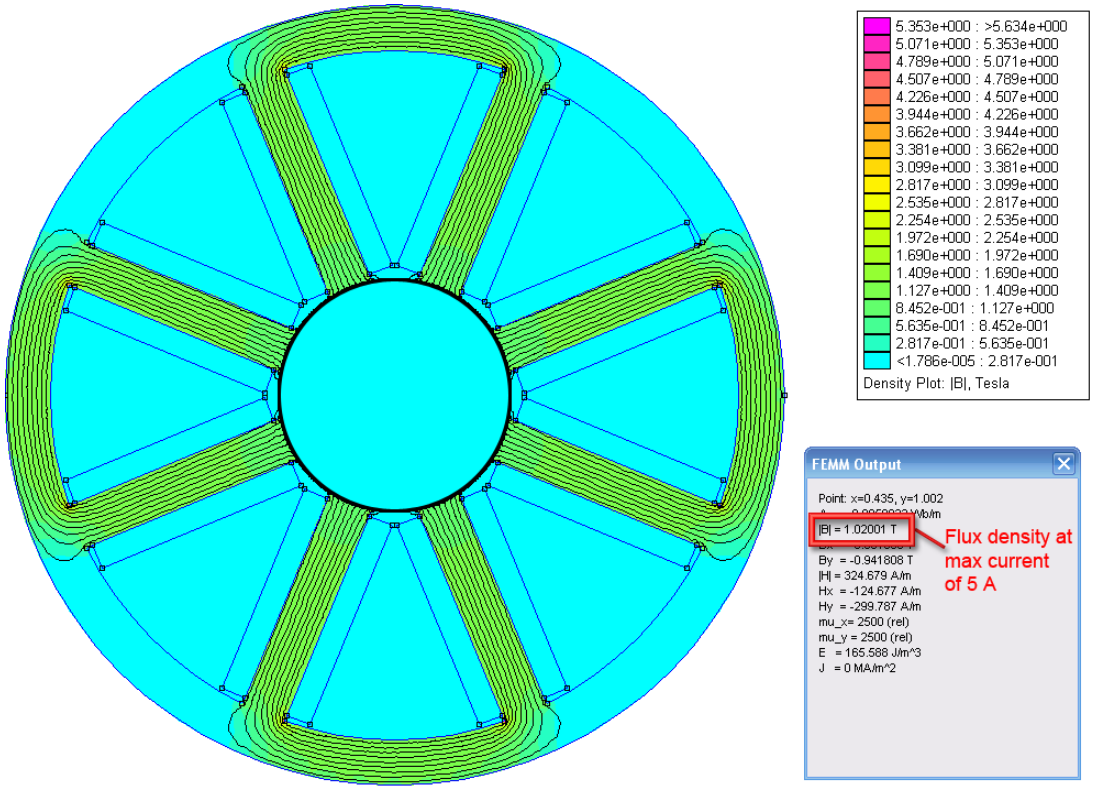


**Figure 3-17: FEM analysis of radial AMB at maximum current**

Form this analysis it can be seen that the flux density within the pole leg is 1.02 T. The design flux density at the maximum current of 5 A was 1 T. The results of the FEM analysis correlate closely to the design results, and it was decided that the radial AMBs can be implemented.

### *3.2.10 Radial AMB implementation*

After the designs of the radial AMBs have been completed, and the designs were verified by means of a step response analysis, a dynamic stiffness analysis and a FEM analysis it was decided to implement the AMBs. A SolidWorks® machine drawing was done in order to manufacture the laminations. Detailed machine drawings and SolidWorks® assemblies can be found on the data CD in Appendix D. As discussed in section 3.2.3, the AMB stator packs were made up of 60 laminations of 0.35 mm thickness.

The coils were wound using 1.5 mm P.I. Grade II copper wire with a temperature rating of 180 °C. Each coil has 80 turns and was wound around a jig and then removed and inserted onto the legs of the AMB stator. After all eight coils were wound and inserted onto the legs of the AMB stator, the stator/coil assembly was vacuum impregnated (VPI) with resin and baked at 80 °C for 5 hours. After the VPI process has been completed, the AMB was cleaned and mounted in the modular

vacuum enclosure [16]. The Conax® vacuum feedthroughs were connected to the coils of the AMB and the RTD was inserted into one of the coil and also connected to its own feedthrough.

Figure 3-18(a) shows the completed bottom AMB with the AMB stator mounted in the modular vacuum enclosure and connected to the feedthroughs. Figure 3-18(b) shows the top AMB mounted in the modular vacuum enclosure and also connected to its feedthroughs.

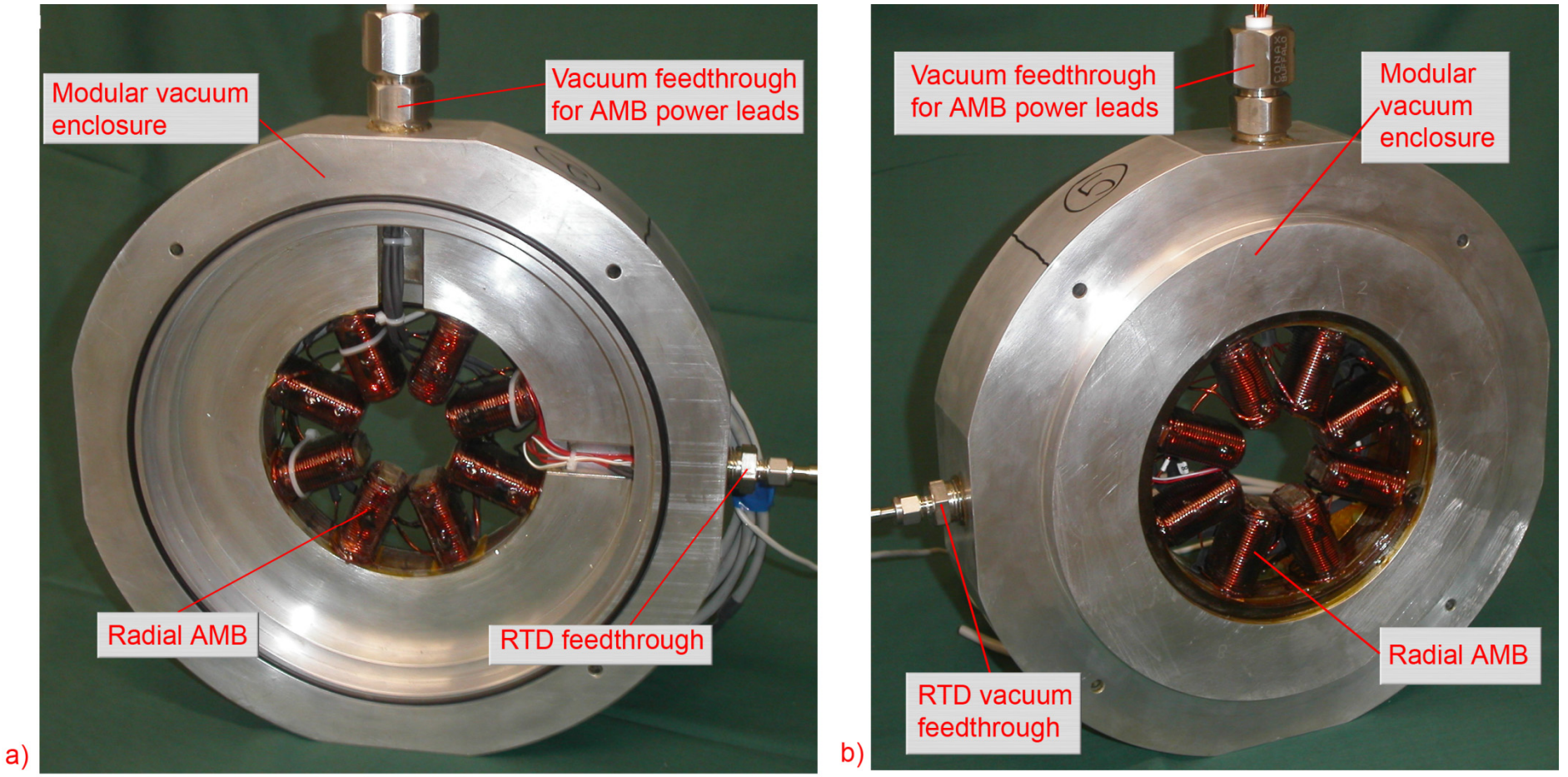


**Figure 3-18: (a) Bottom AMB final assembly (b) Top AMB final assembly**

## 3.3 Axial AMB design

The axial AMB designs were performed using MATLAB®. The program allows one to easily manipulate variables and solve equations numerically. The design process used in this design is based on the double acting thrust bearing design process outlined in [11] [17]. The axial AMB design can be found on the data CD in Appendix D together with the MATLAB® simulations.

### *3.3.1 Thrust bearing geometry*

A double acting thrust bearing consists of two actuators which acts on a thrust collar as discussed in section 2.3.2. Figure 3-19 shows the mechanical layout of the electromagnetic design of a double acting thrust bearing with the relevant dimensions.

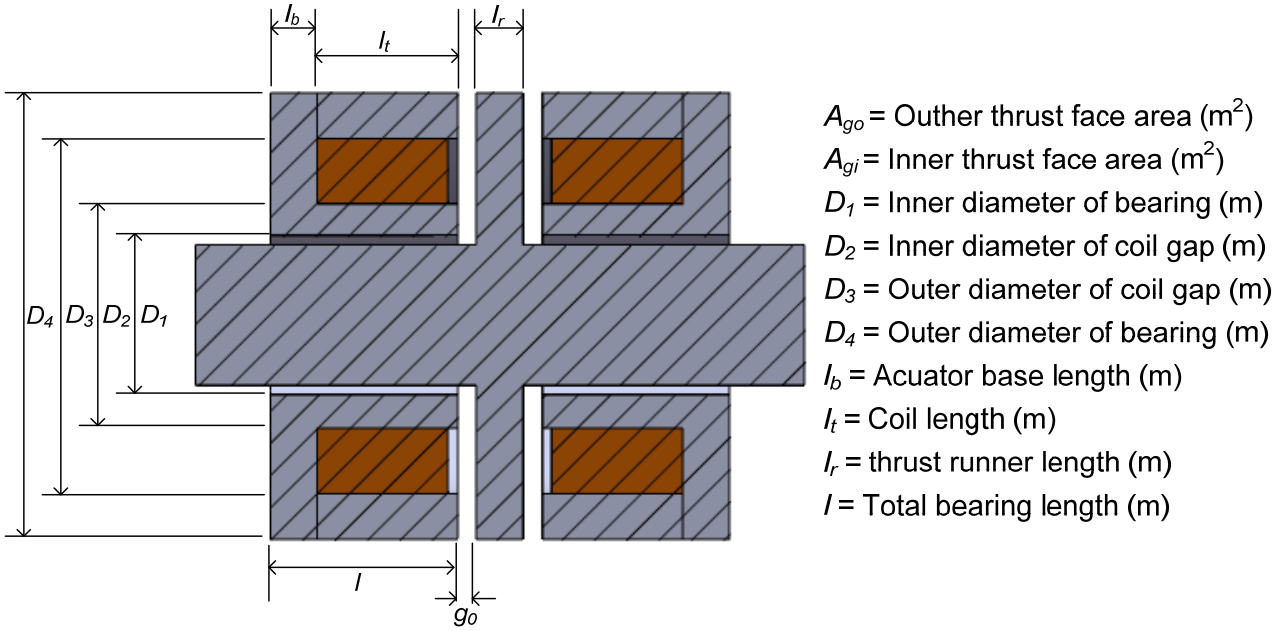


**Figure 3-19: Thrust bearing geometry**

### *3.3.2 Design choices and performance requirements*

Since the rotor/flywheel of the Fly-UPS system is mounted vertically, an axial magnetic thrust bearing had to be designed and implemented to fully suspend the rotor/flywheel. From the rotor/flywheel design the axial AMB will be situated at the top part of the rotor where the thrust disc is mounted on the shaft.

The magnetic thrust bearing must be able to lift the rotor from the delevitating devices and control the position of the rotor in the axial direction. The axial AMB will have an air gap of 0.5 mm, and the delevitating device will be positioned at 0.25 mm of the air gap. This means that the

top axial magnetic thrust bearing must be able to lift the weight of the rotor over an air gap of 0.75 mm from the bottom delevitating device.

From rotor dynamic analysis it was determined that there will be little disturbance forces acting on the axial AMB because of the orientation of the rotor and the weight of the rotor [16]. It was however decided to design the axial AMB with a dynamic force capability of 100 N. The dynamic force capability of 100 N was chosen to give the axial AMB more flexibility. Since the top magnetic thrust bearing will carry the weight of the rotor and be able to exert a dynamic force of 100 N on the rotor, it will be more powerful than the bottom magnetic thrust bearing which will only have to be able to exert a dynamic force of 100 N.

In order to determine the maximum design force $F_{\text{design}}$ of the top magnetic thrust bearing the force which translates to the weight of the rotor was determined to be 184 N. A safety factor of 25 % was added bringing the required force to 230 N. The top magnetic thrust bearing thus has to be able to exert a force of 230 N over an operating air gap of 0.5 mm. However, when the rotor is not magnetically suspended and is resting on the delevitating devices, the air gap is 0.75 mm. The electromagnetic constant $k_m$ then determined using (3-52) with $F_{design}$ = 230 N, $g_0$ = 500 µm and the air gap at 150 % of the nominal air gap.

$$k_m = F_{design} \cdot \left(g_0 \cdot 1.5\right)^2 = 1.294 \times 10^{-4} \quad \frac{\text{kg} \cdot \text{m}^3}{s^2} \tag{3-52}$$

The maximum nominal position bearing force necessary for the AMB to generate 230 N of force over 150 % of the nominal air gap can then be determined by substituting (3-52) into (3-53)

$$F_{\max} = \frac{k_m}{{g_0}^2} = 517.5 \ \text{N} \tag{3-53}$$

Other choices that are needed for the design of the two axial actuators are:

- Nominal operating air gap $g_0$ = 500 x $10^{-6}$ m
- Maximum operating air gap of the top actuator $g_0$ = 750 x $10^{-6}$ m
- Fringing and leakage factor of the toroids ε = 0.9
- Maximum allowable coil current in both actuators $I_{max}$ = 5 A
- Copper current density $J_{cu}$ = 3 x $10^6$ $\frac{\text{A}}{\text{m}^2}$
- Copper stacking factor $F_{cu}$ = 0.5
- Operational speed $\omega$ = 30000 rpm
- Permeability of silicon steel $\mu_r$ = 3500
- Copper resistance constant $\rho_c$ = 1.912 x $10^{-8}$ (Ω.m)

- Bearing stiffness $k_{eq}$ of 1000 N/mm
- Bearing damping $b_{eq}$ of 5 N·s/mm

Figure 3-20 shows the layout of the axial AMB with regards to the rotor. Another design choice include the inside diameter $D_4$ of the top and bottom actuator. The inside diameter has to be chosen in order for the reluctance $\Re_{gap}$ (which is the reluctance between the rotor and the inside of the inner toroid) to be much larger than the reluctance of the air gap $\Re_{g0}$ in order to avoid flux leakage to the rotor. From the rotor design, the diameter of the rotor was determined to be $D_{rotor}$ = 30 x $10^{-3}$ m [16]. The inside diameter of the bottom actuator was chosen to be $D_{1\_bottom}$ = 48 x $10^{-3}$ m and the inside diameter of the top actuator was chosen to be $D_{1\_top}$ = 24 x $10^{-3}$ m. This yields large reluctances in comparison to the reluctance of the air gap and ensures that there will be no leakage from the inside toroid to the rotor. Another design specification, which is an output of the rotor dynamic analysis, is the diameter of the thrust runner which in turn defines the outside diameter of the two toroids. The outside diameter was determined to be $D_{4\_top} = D_{4\_bottom}$ = 80 x $10^{-3}$ m.

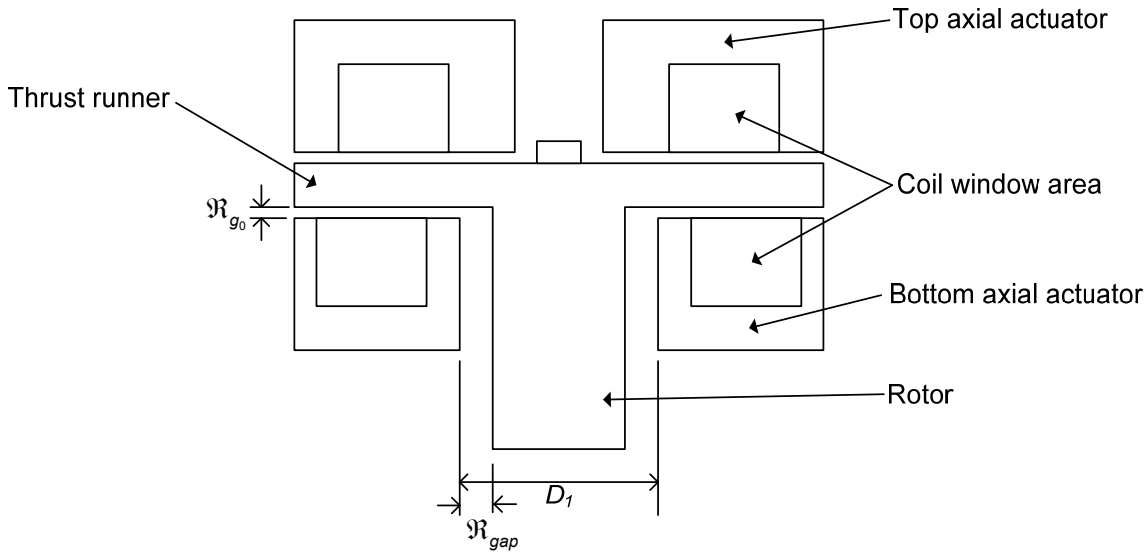


**Figure 3-20: Axial AMB layout**

### *3.3.3 Thrust bearing geometry*

The design procedure is the same for both the top and bottom thrust bearings. Firstly the design forces ($F_{d\_top}$ and $F_{d\_bottom}$) has to be calculated. The design force is higher than the required force because of leakage. The design forces are calculated as follows:

$$F_d = \frac{F_{\max}}{\varepsilon} \qquad \textbf{(3-54)}$$

$$F_{d\_top} = 575 \text{ N}$$

$$F_{d\_bottom} = 111 \text{ N}$$

The required magnetomotive force (MMF) is determined making use of (3-55) and using the maximum flux density $B_{max}$ = 0.8 T because the actuators will be made of mild steel.

$$NI = \frac{2.B_{\max}.g_0}{\mu_0} \qquad \textbf{(3-55)}$$
$$= 637 \text{ A.turns}$$

The minimum required air gap area for the two actuators is now determined by making use of (3-56)

$$A_{g\_\min} = \frac{F_{design} \cdot g_0^{\,2}}{\mu_0 \cdot (NI)^2} \qquad \textbf{(3-56)}$$
$$A_{g\_\min\_top} = 282.4 \times 10^{-6} \text{ m}^2$$
$$A_{g\_\min\_bottom} = 54.49 \times 10^{-6} \text{ m}^2$$

With the minimum required air gap area ($A_g$) known as well as the outside diameter of the actuator ($D_4$), the coil outside diameter can now be determined by using (3-57).

$$D_3 = \sqrt{D_4^{\,2} - \left(\frac{4.A_g}{\pi}\right)} \qquad \textbf{(3-57)}$$
$$D_{3\_top} = 77.72 \times 10^{-3} \text{ m}$$
$$D_{3\_bottom} = 79.57 \times 10^{-3} \text{ m}$$

It can however be seen that the thicknesses of the outer toroids of the two actuators are small, for the top actuator, the outside toroids thickness is 1.14 mm and the inside toroids thickness is 0.217 mm. These toroid thicknesses are not viable from a manufacturing point of view. It will also make the mounting of the coil into the actuator difficult. With these considerations in mind, the thickness of the outside toroid of the top actuator is chosen to be 4 mm and the outside toroid of the bottom actuator is chosen to be 3 mm. The outside diameter of the coils of the two actuators is then taken to be $D_{3\_top}$ = 72 x $10^{-3}$ m and $D_{3\_bottom}$ = 74 x $10^{-3}$ m.

The area of the two air gaps of the two actuators are determined once again using (3-58) in order to compare them with the minimum required air gap areas determined in (3-56).

$$A_g = \pi \cdot \left(\frac{D_4^{\,2} - D_3^{\,2}}{4}\right) \qquad \textbf{(3-58)}$$
$$A_{g\_top} = 955 \times 10^{-6} \text{ m}^2$$
$$A_{g\_bottom} = 726 \times 10^{-6} \text{ m}^2$$

From (3-58) it can be seen that the air gap areas are bigger than the minimum required air gap areas determined in (3-56). Next the coil inside diameters can be determined making use of the

outside toroids air gap areas which is determined in (3-58) and the inside diameters ($D_1$) of the magnetic thrust bearing's specification:

$$D_2 = \sqrt{\left(\frac{4.A_g}{\pi}\right) + D_1^2} \tag{3-59}$$

$$D_{2\_top} = 56.8 \times 10^{-6} \text{ m}$$

$$D_{2\_bottom} = 42.3 \times 10^{-6} \text{ m}$$

### 3.3.4 Coil geometry

With both the current density and the maximum current known, the wire area can be calculated:

$$A_{wire} = \frac{I_{\max}}{J_{CU}} \tag{3-60}$$

$$= 1.667 \times 10^{-6} \text{ m}^2$$

The wire diameter can be determined next by substituting (3-60) in (3-61):

$$D_{wire} = \sqrt{\frac{4.A_{wire}}{\pi}} \tag{3-61}$$

$$= 1.457 \times 10^{-3} \text{ m}$$

Having determined the required ampere-turns in (3-55), the number of turns can be determined using (3-62):

$$N = \frac{NI}{I_{\max}} \tag{3-62}$$

$$N_{\_top} = 138 \text{ turns}$$

$$N_{\_bottom} = 70 \text{ turns}$$

The bias current of the top actuator can now be determined. The top actuator has to support the weight of the rotor, thus the bias current has to adequate to support the weight of the rotor as well as 25 % of the dynamic force of 100 N as discussed in section 3.3.2. The bias current is determined as follows:

$$I_{bias\_top} = \sqrt{\frac{\left(\left(F_{rotor\_weight} + \frac{F_{dynamic}}{4}\right).4.{g_0}^2\right)}{\left(\varepsilon.\mu_0.{N_{top}}^2.A_{g\_top}\right)}} \tag{3-63}$$

$$I_{bias\_top} = 3.16 \text{ A}$$

Next, the peak current in the top actuator is calculated at the nominal operating air gap with maximum dynamic force using (3-64):

$$I_{peak\_top} = \sqrt{\frac{\left(\left(F_{rotor\_weight} + F_{dynamic}\right).4.g_0^{\,2}\right)}{\left(\varepsilon.\mu_0.N_{top}^{\,2}.A_{g\_top}\right)}} \qquad \textbf{(3-64)}$$

$$I_{peak\_top} = 3.693 \text{ A}$$

The control current can be determined next using (3-65):

$$I_{control\_top} = I_{peak\_top} - I_{bias\_top} \qquad \textbf{(3-65)}$$

$$I_{control\_top} = 0.532 \text{ A}$$

With the control- and bias currents known the rms current can be determined:

$$I_{rms\_top} = \sqrt{I_{bias\_top}^{\,2} + \left(\frac{I_{control\_top}}{\sqrt{2}}\right)^2} \qquad \textbf{(3-66)}$$

$$I_{rms\_top} = 3.118 \text{ A}$$

The bias current of the bottom actuator can now be determined. The bottom actuator is biased at 25 % of the dynamic force of 100 N as discussed in section 3.3.2. Since force (*F*) is proportional to the square of the current (*I*), the bias current is usually chosen to be half of the maximum current. The bias current is determined as follows:

$$I_{bias\_bottom} = \sqrt{\frac{\left(\frac{F_{dynamic}}{4}.4.g_0^{\,2}\right)}{\left(\varepsilon.\mu_0.N_{bottom}^{\,2}.A_{g\_bottom}\right)}} \qquad \textbf{(3-67)}$$

$$I_{bias\_bottom} = 2.498 \text{ A}$$

Next, the peak current in the bottom actuator is calculated at the nominal operating air gap with maximum dynamic force using (3-68):

$$I_{peak\_bottom} = \sqrt{\frac{\left(F_{dynamic}.4.g_0^{\,2}\right)}{\left(\varepsilon.\mu_0.N_{bottom}^{\,2}.A_{g\_bottom}\right)}} \qquad \textbf{(3-68)}$$

$$I_{peak\_bottom} = 4.987 \text{ A}$$

The control current can be determined next using (3-69):

$$I_{control\_bottom} = I_{peak\_bottom} - I_{bias\_bottom} \qquad \textbf{(3-69)}$$

$$I_{control\_bottom} = 2.498 \text{ A}$$

With the control- and bias currents known the rms current can be determined:

$$I_{rms\_top} = \sqrt{I_{bias\_top}{}^2 + \left(\frac{I_{control\_top}}{\sqrt{2}}\right)^2} \qquad \textbf{(3-70)}$$

$$I_{rms\_top} = 3.045 \text{ A}$$

The flux densities are determined next by making use of the adjusted air gap areas determined in (3-58). Firstly the flux densities are determined at the bias currents of each of the actuators by using (3-71).

$$B_{bias} = \frac{\mu_0 \cdot N \cdot I_{bias}}{2 \cdot g_0} \qquad \textbf{(3-71)}$$

$$B_{bias\_top} = 0.541 \text{ T}$$

$$B_{bias\_bottom} = 0.22 \text{ T}$$

Having determined the bias flux densities, the flux densities at the maximum current is determined by making use of (3-72).

$$B_{\max} = \frac{\mu_0 \cdot N \cdot I_{\max}}{2 \cdot g_0} \qquad \textbf{(3-72)}$$

$$B_{\max\_top} = 0.87 \text{ T}$$

$$B_{\max\_bottom} = 0.44 \text{ T}$$

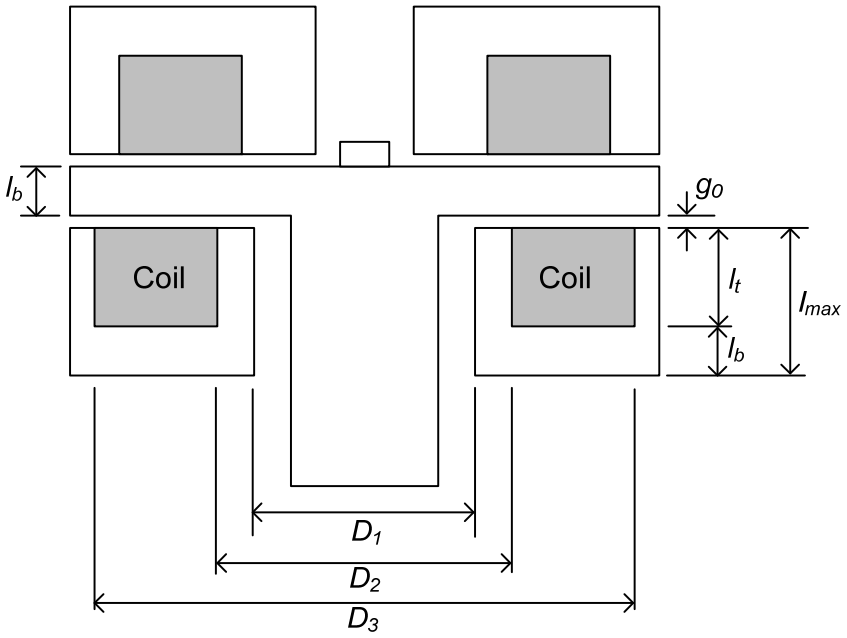


**Figure 3-21: Coil window areas of axial AMBs**

Figure 3-21 shows the coil window areas of the two actuators. The required coil areas can be determined using the number of turns ($N$) and the rms ($I_{rms}$) current:

$$A_{coil} = \frac{N.I_{rms}}{J_{CU}.F_{CU}} \quad \textbf{(3-73)}$$

$$A_{coil\_top} = 292.8 \times 10^{-6} \text{ m}^2$$

$$A_{coil\_bottom} = 142.5 \times 10^{-6} \text{ m}^2$$

Having determined the required coil area the coil height can be determined using (3-74):

$$l_t = \frac{A_{coil}}{\left(\frac{D_3 - D_2}{2}\right)} \quad \textbf{(3-74)}$$

$$l_{t\_top} = 19.7 \times 10^{-3} \text{ m}$$

$$l_{t\_bottom} = 16.6 \times 10^{-3} \text{ m}$$

The next step is to determine the thrust runner's minimum axial length:

$$l_b = \frac{D_2 - D_1}{2} \quad \textbf{(3-75)}$$

$$l_{b\_top} = 9.2 \times 10^{-3} \text{ m}$$

$$l_{b\_bottom} = 4.4 \times 10^{-3} \text{ m}$$

The total axial length of the actuator can now be determined:

$$l_{\max} = l_t + l_b \quad \textbf{(3-76)}$$

$$l_{\max\_top} = 28.9 \times 10^{-3} \text{ m}$$

$$l_{\max\_bottom} = 21 \times 10^{-3} \text{ m}$$

### *3.3.5 Magnetic circuit reluctances*

The reluctance of the entire magnetic circuit has to be determined in order to determine the magnetic flux in the circuit. Firstly the reluctance of each air gap is determined:

$$\Re_{g0} = \frac{g_0}{\mu_0.A_g} \quad \textbf{(3-77)}$$

$$\Re_{g0\_top} = 416.6 \times 10^3 \ \frac{\text{A.turns}}{\text{Wb}}$$

$$\Re_{g0\_bottom} = 548.3 \times 10^3 \ \frac{\text{A.turns}}{\text{Wb}}$$

The total length of the iron path is determined next using (3-78):

$$l_{fe} = \left(2.l_{\max}\right) + \left(D_1 - D_4\right) \quad \textbf{(3-78)}$$
$$l_{fe\_top} = 113.8 \times 10^3 \text{ m}$$
$$l_{fe\_bottom} = 74 \times 10^3 \text{ m}$$

The reluctance of the iron path is determined next by making use of the length of the iron path ($l_{fe}$) as determined in (3-78):

$$\Re_{fe} = \frac{l_{fe}}{\mu_0.\mu_R.A_g} \quad \textbf{(3-79)}$$
$$\Re_{fe\_top} = 27.1 \times 10^3 \ \frac{\text{A.turns}}{\text{Wb}}$$
$$\Re_{fe\_bottom} = 23.18 \times 10^3 \ \frac{\text{A.turns}}{\text{Wb}}$$

The total reluctance of the thrust bearing can now be determined by using the reluctances of the air gaps as determined in (3-77) and the reluctance of the iron path as determined in (3-79):

$$\Re_{total} = 2.\Re_{g0} + \Re_{fe} \quad \textbf{(3-80)}$$
$$\Re_{total\_top} = 860.3 \times 10^3 \ \frac{\text{A.turns}}{\text{Wb}}$$
$$\Re_{total\_bottom} = 1.12 \times 10^6 \ \frac{\text{A.turns}}{\text{Wb}}$$

Now the length of air ($l_{g0}$) magnetically equivalent to the total length of the iron path is determined:

$$l_{g0} = \frac{l_{fe}}{\mu_R} \quad \textbf{(3-81)}$$
$$\mathrm{l}_{g0\_top} = 32.52 \times 10^{-6} \text{ m}$$
$$\mathrm{l}_{g0\_bottom} = 21.14 \times 10^{-6} \text{ m}$$

Using the magnetically equivalent length of air the effective air gap ($g_{0\_effective}$) is determined:

$$g_{0\_effective} = 2.g_0 + l_{g0} \quad \textbf{(3-82)}$$
$$g_{0\_effective\_top} = 1.033 \times 10^{-3} \text{ m}$$
$$g_{0\_effective\_bottom} = 1.021 \times 10^{-3} \text{ m}$$

Finally the magnetic flux ($\Phi$) in the circuit is determined by making use of the effective air gap:

$$\phi_{circuit} = \frac{A_g \cdot N \cdot I_{\max} \cdot \mu_0}{g_{0\_effective}} \quad \textbf{(3-83)}$$
$$\phi_{circuit\_top} = 802 \times 10^{-6} \text{ Wb}$$
$$\phi_{circuit\_bottom} = 312.6 \times 10^{-6} \text{ Wb}$$

### 3.3.6 Coil resistance and inductance

The next step in the design process is to determine the coil resistance and coil inductance. By making use of the magnetic flux ($\Phi_{circuit}$) in the circuit the coil inductance is determined:

$$L_{coil} = \frac{N.\phi_{circuit}}{I_{max}} \quad \textbf{(3-84)}$$

$$L_{coil\_top} = 22.1\times10^{-3}\ \text{H}$$

$$L_{coil\_bottom} = 4.4\times10^{-3}\ \text{H}$$

The average coil diameters are determined next in order to approximate the coil wire length:

$$D_{coil\_avg} = \frac{D_2 + D_3}{2} \quad \textbf{(3-85)}$$

$$D_{coil\_avg\_top} = 57.2\times10^{-3}\ \text{m}$$

$$D_{coil\_avg\_bottom} = 65.4\times10^{-3}\ \text{m}$$

An estimated length for the coil wire is determined using the average diameter of the coil:

$$l_{wire} = \pi.D_{coil\_avg}.N \quad \textbf{(3-86)}$$

$$l_{wire\_top} = 24.784\ \text{m}$$

$$l_{wire\_bottom} = 14.384\ \text{m}$$

With an estimation of the length of wire of the coil, the resistance of the coil can be determined using the resistivity of copper ($\rho_c$):

$$R_{coil} = \frac{\rho_c.l_{wire}}{A_{wire}} \quad \textbf{(3-87)}$$

$$R_{coil\_top} = 284.3\times10^{-3}\ \Omega$$

$$R_{coil\_bottom} = 165\times10^{-3}\ \Omega$$

### 3.3.7 Power amplifier specification

The next step is to determine the specifications of the power amplifier that will be used. The maximum force slew rate is given by:

$$\frac{dF}{dt} = 2.\pi.F_{dynamic}.\frac{\omega}{60} \quad \textbf{(3-88)}$$

$$= 314.2\times10^{3}\ \frac{\text{N}}{\text{s}}$$

The power amplifier's maximum VA rating is given by:

$$VA_{max} = \frac{dF}{dt}.g_0 \quad \textbf{(3-89)}$$

$$= 157.1\ \text{VA}$$

The voltage rating of the amplifier is given by:

$$V_{\max} = \frac{VA_{\max}}{I_{\max}} = 31.42 \text{ V} \quad \textbf{(3-90)}$$

### 3.3.8 Axial AMB stiffness and damping

The rotor-dynamic analysis yields the following required equivalent stiffness ($k_{eq}$) and damping ($b_{eq}$) which will be used to design the PD-controller:

$$k_{eq} = 1000000 \ \frac{\text{N}}{\text{m}} \quad \textbf{(3-91)}$$

$$b_{eq} = 5000 \ \frac{\text{N.s}}{\text{m}} \quad \textbf{(3-92)}$$

The current gain $k_i$ for the magnetic thrust bearing is determined using (3-93):

$$k_i = \frac{\varepsilon.\mu_0.i_{bias}.N^2.A_g}{2.g_0^{\,2}} \quad \textbf{(3-93)}$$

$$k_{i\_top} = 130$$

$$k_{i\_bottom} = 20$$

and the position stiffness $k_s$ for the magnetic thrust bearing is determined using (3-94)

$$k_s = \frac{-\varepsilon.\mu_0.i_{bias}^{\,2}.N^2.A_g}{2.g_0^{\,3}} \quad \textbf{(3-94)}$$

$$k_{s\_top} = -822 \times 10^3$$

$$k_{s\_bottom} = -100 \times 10^3$$

The next step in the design process is the implementation of the combined thrust bearing in a simulation to verify the operation of the AMB.

### 3.3.9 MATLAB® simulations

As discussed in section 2.3, an accurate model of the AMB system is necessary in order to accurately model the behaviour of the magnetic bearing. Figure 3-22 shows the non-linear model which was used to simulate the axial AMB. The axial AMB will be implemented by using a single PD-controller.

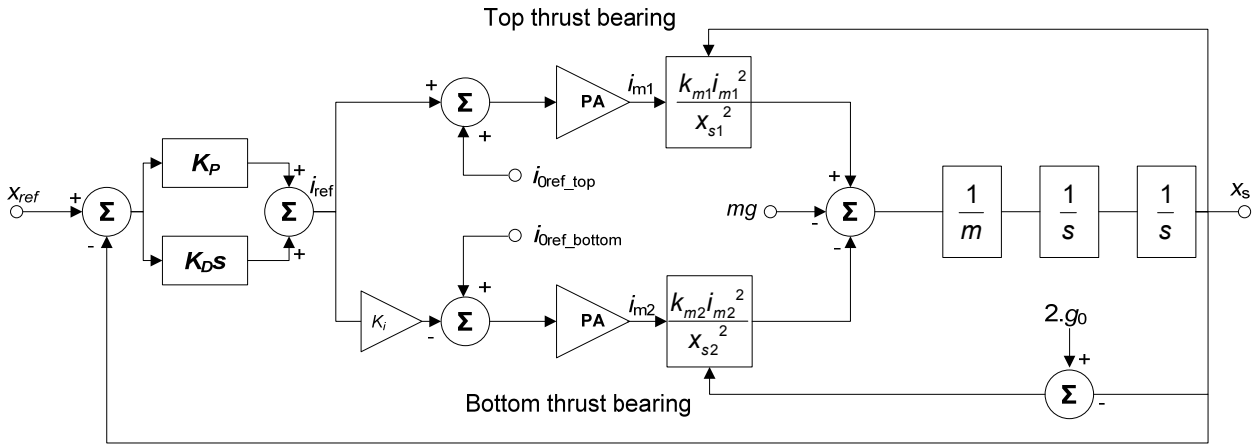


**Figure 3-22: Non-linear model of the axial AMB**

The main differences between the model of the radial AMB and the axial AMB are the fact that the axial AMB has two different bias currents for each of the two magnetic thrust bearing actuators. The model also has a current gain $K_i$ to compensate for the smaller bottom actuator.

In the case of an asymmetric configuration (as discussed in section 2.3.7) like the one that is used in the Fly-UPS system, $K_p$ is determined by using (3-95).and the differential constant $K_D$ is determined by using (3-96). It was also decided to implement the PD-controller using the proportional- and differential constants of the top actuator. Thus when determining the proportional constant $K_p$ and the differential constant $K_D$ of the PD controller, the current gain of the top actuator is used.

$$K_P = \frac{k_{eq} + \left(k_{s\_top} + k_{s\_bottom}\right)}{2 \cdot k_{i\_top}} \qquad \textbf{(3-95)}$$

$$= 7038$$

$$K_D = \frac{b_{eq}}{2 \cdot K_i} \qquad \textbf{(3-96)}$$

$$= 19.3$$

In order to compensate for the bottom actuator, a current gain $K_i$ was implemented as can be seen in Figure 3-22 which is determined by (3-97) where $k_{i\_top}$ is the current gain of the top actuator and $k_{i\_bottom}$ is the current gain of the bottom actuator.

$$K_i = \frac{k_{i\_top}}{k_{i\_bottom}} \qquad \textbf{(3-97)}$$

The model also makes use of two bias currents ($I_{0ref\_top}$) and ($I_{0ref\_bottom}$) which is an output of the design process of each of the two actuators. As discussed earlier, the top actuator will have a greater bias current than the bottom actuator due to the fact that the top actuator has to cope with

the weight of the rotor as well as a dynamic force of 100 N whereas the bottom actuator only has to cope with the 100 N dynamic load capacity.

The PD-controller which was implemented to control the axial AMB was designed using proportional constant $K_p$ = 7405 and differential constant $K_d$ = 19.5. The current gain as can be seen in Figure 3-22 which was implemented on the bottom actuator was determined to be $K_i$ = 6.3967.

The analytical bearing stiffness and damping are now verified using the simulation. From the rotor dynamic analysis, and equivalent stiffness $k_{eq}$ = 1 x $10^6$ N/m was used as well as an equivalent damping $b_{eq}$ = 5 x $10^3$ N.s/m. Firstly a 10 µm step response was introduced on the bottom AMB at 0.25 s as shown in Figure 3-23.

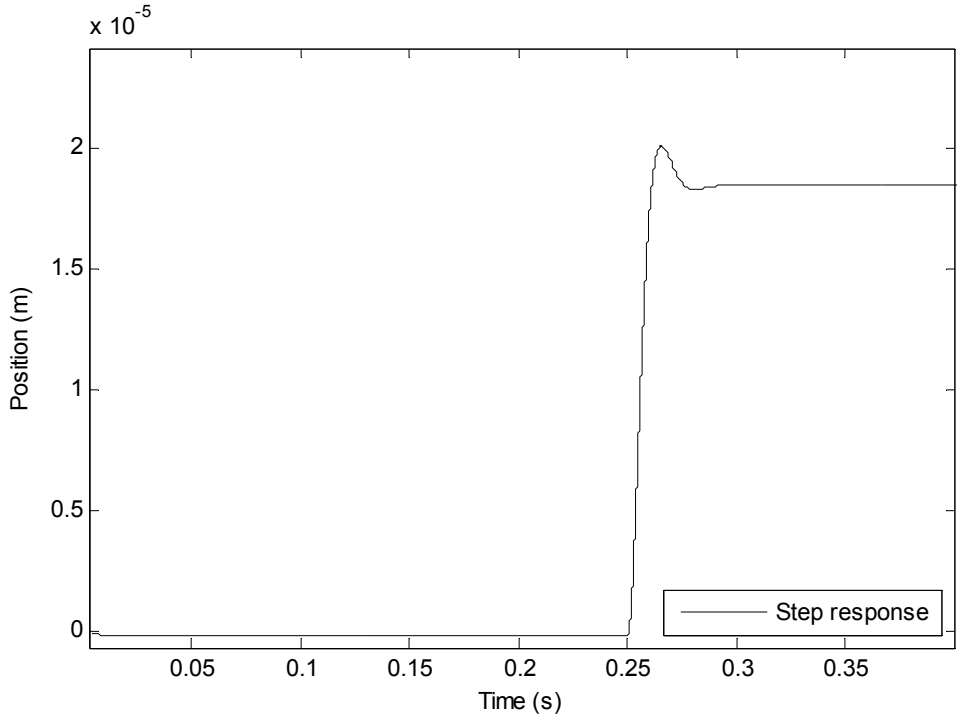


**Figure 3-23: Step response of 10 µm on axial AMB**

From Figure 3-23 the percentage overshoot (*P.O.*) is determined using (3-98)

$$P.O. = \frac{20.1\times10^{-6} - 18.47\times10^{-6}}{18.47\times10^{-6}} \times 100\ \% = 8.82\% \quad \textbf{(3-98)}$$

and settling time ($T_s$) (to within 2 % of the final value) is determined as 0.0232 s. This system can be seen as a second-order system close to its working point. It is for this reason that a step response can be used to obtain the equivalent stiffness and damping value of the system. The equivalent bearing stiffness and damping are now obtained using the process outlined in section 3.2.6. The system damping ratio is obtained using (3-99)

$$P.O. = 100e^{\frac{-\pi\zeta}{\sqrt{1-\zeta^2}}} \quad \textbf{(3-99)}$$

$$\therefore\ \zeta = 0.6126$$

The natural frequency of the system is now determined using (3-100)

$$\omega_n = \frac{4}{T_s\zeta} = 281.4 \text{ rad/s} \quad \textbf{(3-100)}$$

The equivalent stiffness for the system is now obtained using (3-101)

$$k_{eq} = \omega_n{}^2 m \quad \textbf{(3-101)}$$

$$= 1.257 \times 10^6 \text{ N/m}$$

The system's equivalent damping value is determined using (3-102)

$$b_{eq} = \zeta\left(2\sqrt{k_{eq} \cdot m}\right) \quad \textbf{(3-102)}$$

$$= 6.344 \times 10^3 \text{ N.s/m}$$

In order to verify the simulation model with the physical model a series of step responses are performed. The step size is enlarged to ensure that the nonlinear nature of the system can be compared to that of the simulation model.

Figure 3-24 shows a step response of 50 µm introduced to the AMB at 0.25 s. The system shows little overshoot and yields the following parameters: P.O. = 4.52 %, $\zeta$ = 0.7019, $T_s$ = 0.0233 s, $k_{eq}$ = 1.09x10$^6$ N/m and $b_{eq}$ = 6.3 x10$^3$ N.s/m. These parameters correlate closely to the predicted stiffness and damping parameters.

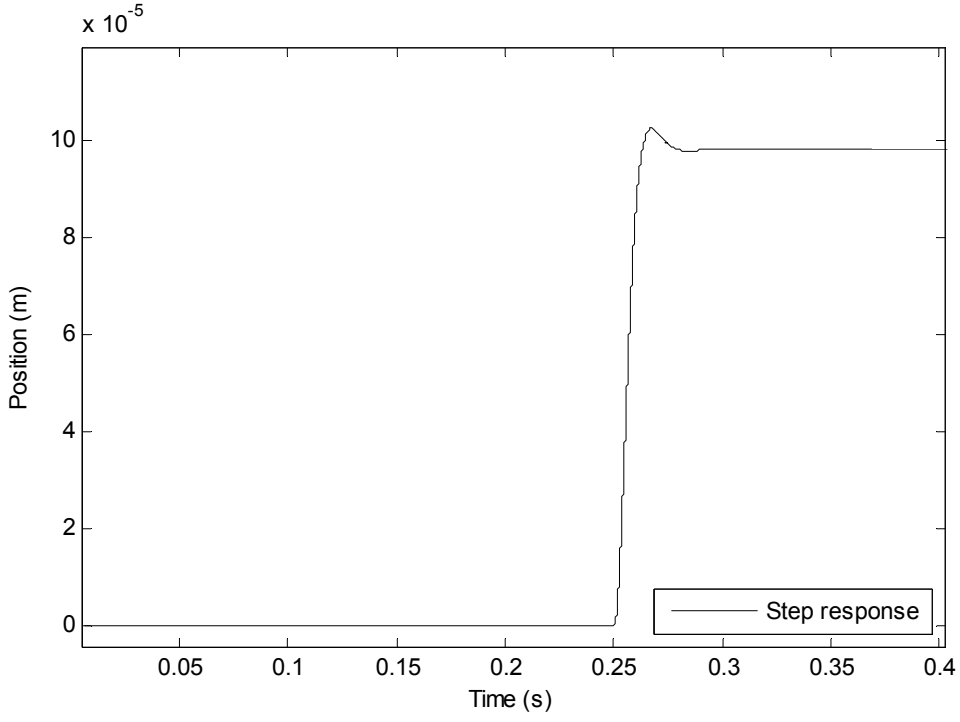


**Figure 3-24: Step response of 50 µm on the axial AMB**

### 3.3.10 FEMM analysis

The final stage of the verification process was to do a Finite Element Method (FEM) analysis of the magnetic bearing design. The FEM analysis was also done using the FEMM software package which was mentioned earlier.

The axial AMB stator and rotor were constructed within the FEMM program and all the materials including the mild steel, coils and the air gap were defined. Firstly, the analysis was done on the top actuator at the bias current of 3.118 A. Figure 3-25 shows the flux density within the stator of the AMB at bias current.

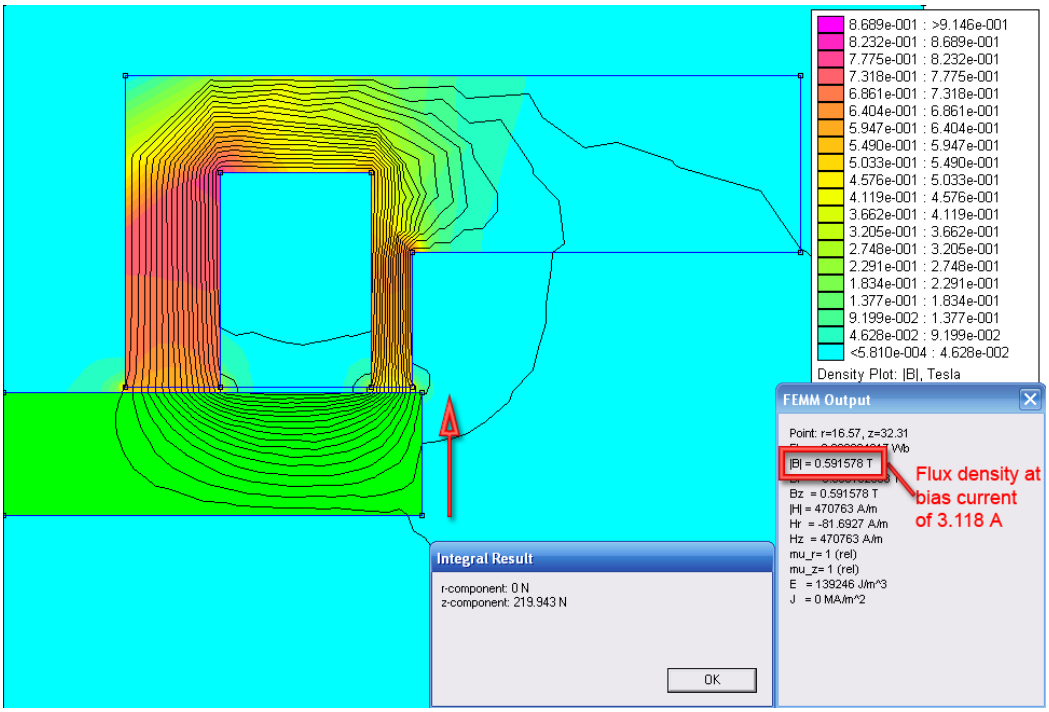


**Figure 3-25: FEM analysis of top actuator at bias current**

From Figure 3-25 it can be seen that the flux density in the air gap is 0.59 T which correlates closely to the predicted flux density of 0.541 T at the bias current of 3.118 A. It can also be seen that the actuator exerts a force of 219 N on the thrust disc (indicated by the red arrow) which correlates with the predicted force of 222 N.

Next the FEM analysis was done on the top actuator at maximum current of 5 A. Figure 3-26 shows the flux density in the air gap of the top actuator at a maximum current of 5 A. The simulated flux density is 0.91 T which is close to the predicted flux density of 0.87 T. It can also be seen that the actuator exerts a force of 522 N on the thrust disc which correlates closely with the predicted force of 514 N.

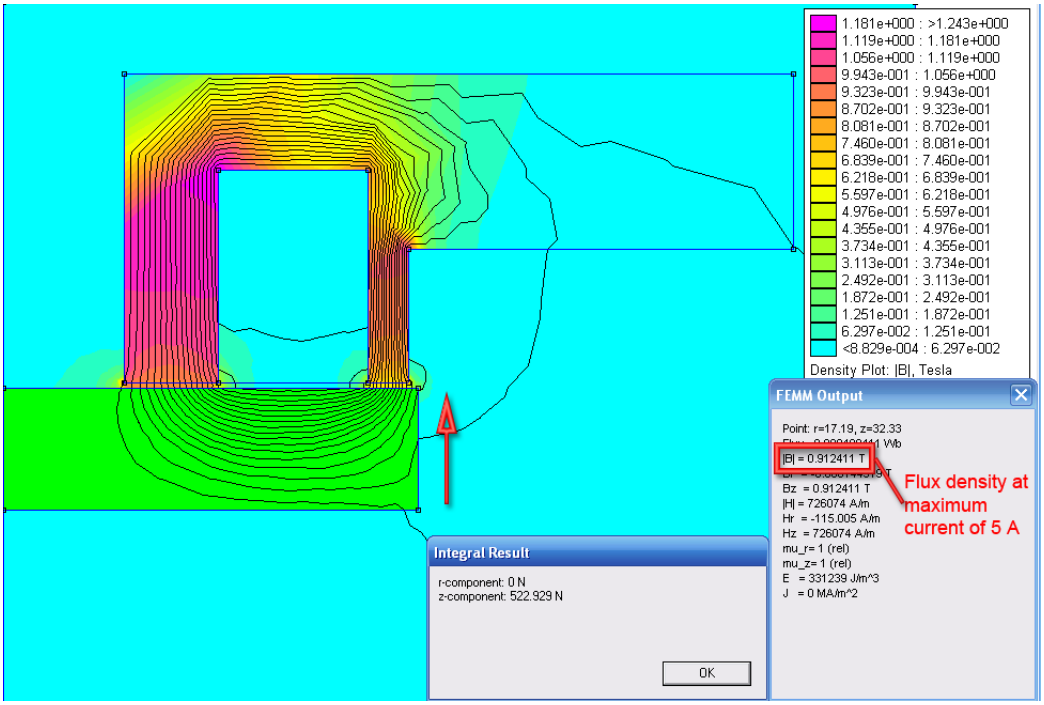


**Figure 3-26: FEM analysis of top actuator at maximum current**

The next step was to simulate the bottom actuator. The bottom actuator and rotor was constructed in the FEMM software package and all the materials were defined. Firstly the actuator was simulated at bias current of 2.49 A. Figure 3-27 shows the flux density of 0.21 T in the air gap of the bottom actuator at bias current. This correlates closely to the predicted flux density of 0.22 T.

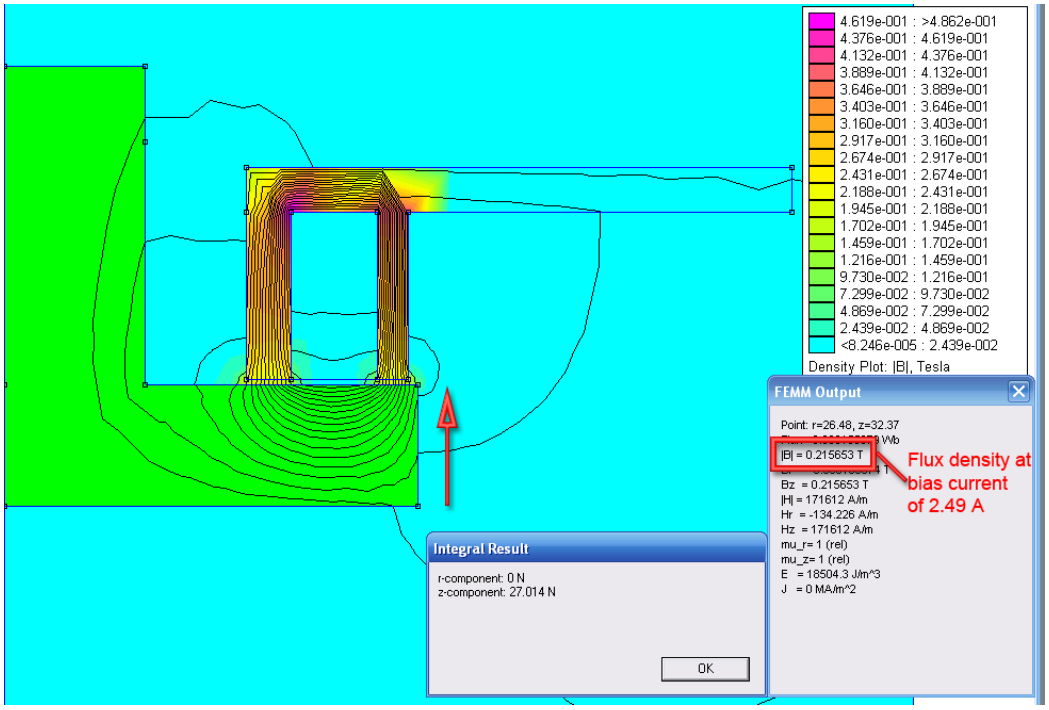


**Figure 3-27: Flux density of bottom actuator at bias current**

It can also be seen that the actuator exerts a force of 27 N on the thrust disc. This is also close to the predicted force of 25 N that the actuator will exert on the thrust disc.

Finally the bottom actuator was simulated at maximum current of 5 A. The simulated flux density within the air gap of the actuator was 0.44 T and the predicted force that the actuator will exert on the thrust disc is 100 N.

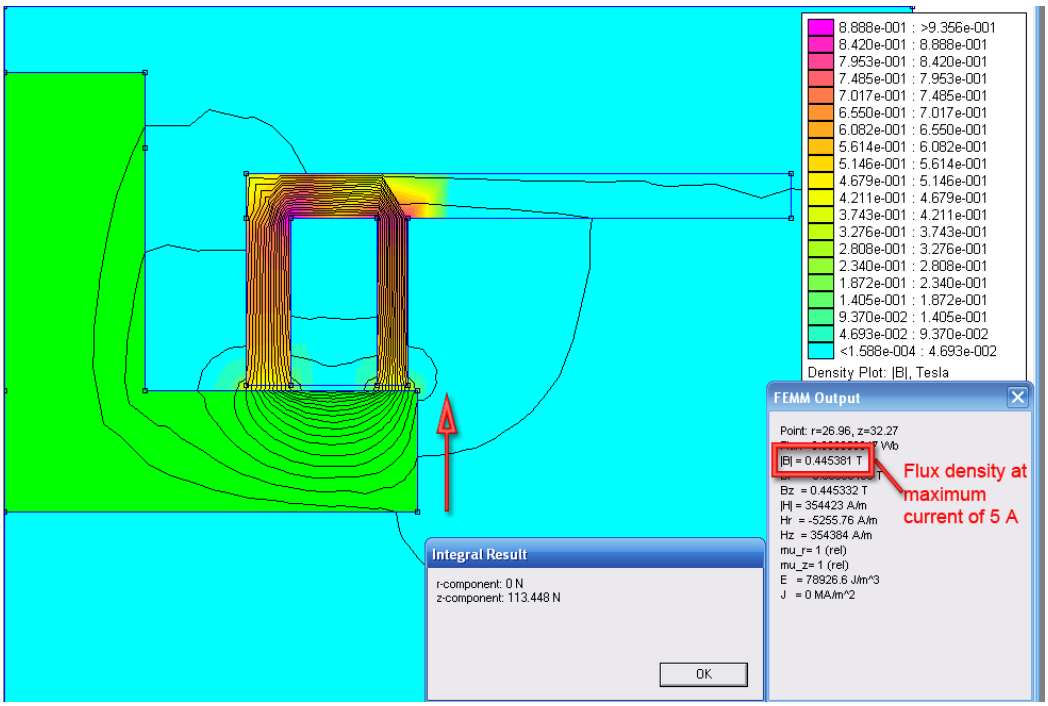


**Figure 3-28: Flux density of bottom actuator at maximum current**

The flux density in Figure 3-28 is 0.445 T and the force the actuator exerts on the thrust disc is 113 N. The actual force is slightly higher that the predicted force because of overcompensation for leakage and fringing effect. The results of the FEM analysis however correlate closely to the design results, and it was decided that the radial AMBs can be implemented.

### *3.3.11 Axial AMB implementation*

After the designs of the axial AMBs have been completed, and the designs were verified by means of a step response analysis, and a FEM analysis it was decided to implement the AMBs. SolidWorks machine drawings were done in order to manufacture the two stators of the axial AMB. Detailed machine drawings and SolidWorks® assemblies can be on the data CD in Appendix D. The two axial AMB stators were made of mild steel. The coils were wound using 1.3 mm P.I. Grade II copper wire with a temperature rating of 180 °C. The top actuator has 138 turns and the bottom actuator has 70 turn. After the two coils were wound on a jig, they were inserted into the two stators. The stator/coil assembly was then dipped in a viscous resin which can withstand high temperatures. The resin was then baked bonding the coils to the stators. After the baking process, the stators were machined to their final size and they were mounted in the modular vacuum enclosure [16] The power lead of the actuators were connected to the Conax® vacuum feedthroughs and a RTD was inserted in the top actuators coil and connected to its own feedthrough.

Figure 3-29(a) shows the completed bottom axial actuator with the actuator mounted in the modular vacuum enclosure and connected to the power feedthrough. Figure 3-29(b) shows the top axial actuator mounted in the modular vacuum enclosure and also connected to its power feedthroughs as well as the RTD's feedthrough.

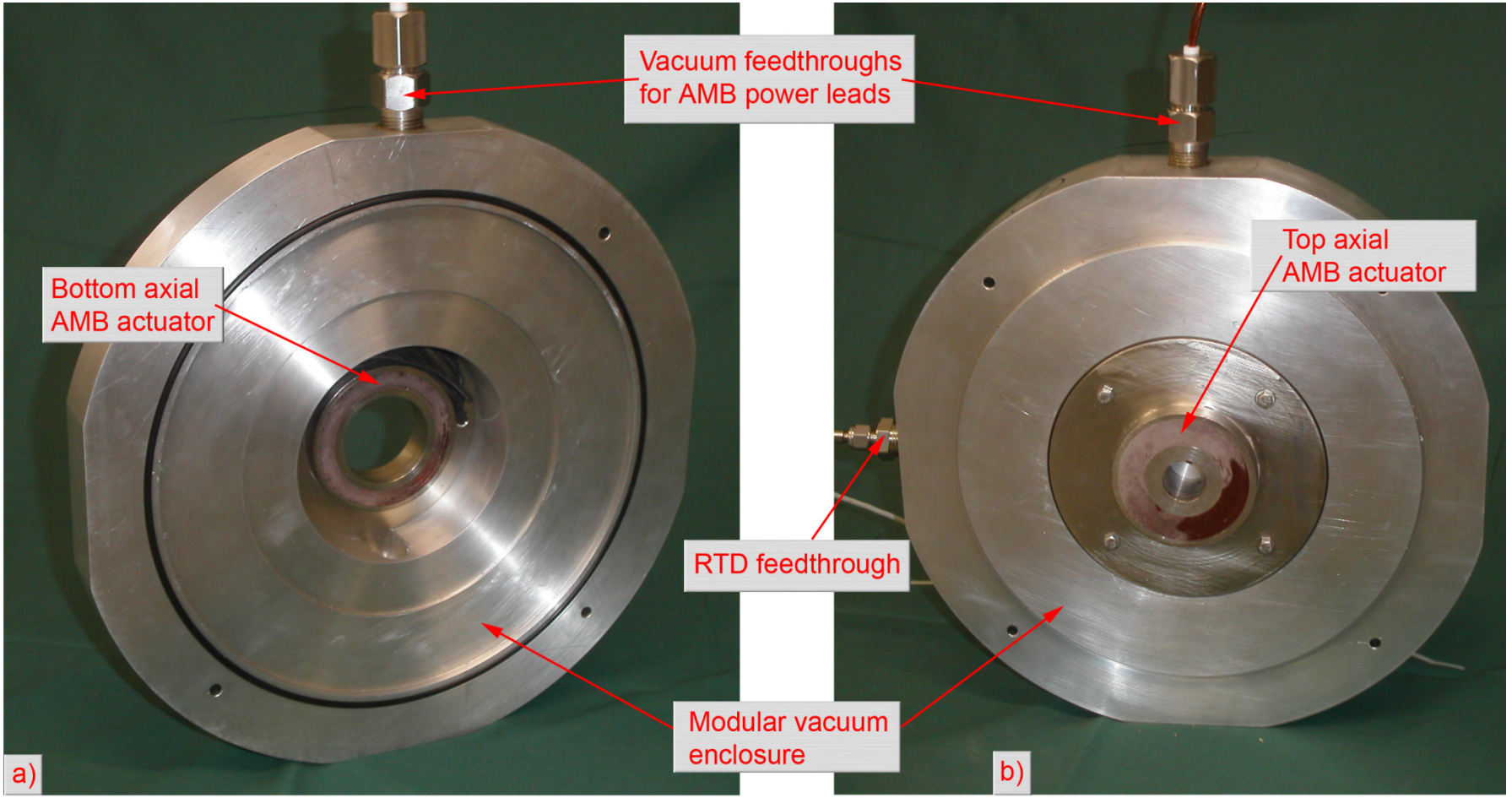


**Figure 3-29: a) Bottom axial AMB actuator assembly b) Top axial AMB actuator assembly**

Chapter 3 discussed the design process involved in developing the radial active magnetic bearings as well as the axial active magnetic bearing for the Fly-UPS system. It also showed the various simulations which were done in order to ensure that the AMBs will perform as expected. A detailed electrical system design is discussed in chapter 4.

# 4
# Chapter
# Electrical system design

*Chapter 4 contains a detailed electrical system design. First the design process that was followed is explained. This is followed by a detailed sub-system specification that highlights the aspects of the various sub-systems that should be considered in the design process. This is followed by a detailed sub-system design. Finally the implementation of the various sub-systems into the electrical enclosure is discussed.*

## 4.1 Design process

One of the main aims of the project is to develop the flywheel system to an industrial standard in order to compare the developed magnetic bearings to commercially available magnetic bearings [18]. The Fly-UPS system (as discussed in section 2.1) comprises AMBs, a rotor/flywheel, a vacuum enclosure, a PMSM as well as an electrical control enclosure. Figure 4-1 illustrates the process that was followed in order to design the electrical control enclosure of the Fly-UPS system.

Firstly, the Type-A specifications were drawn up. This document lists the scope of the project and the requirements of the system, including the system definition as well as the system characteristics. The document also lists the proposed uses of the system and the budget.

After the Type-A specification is drawn up, the system is broken down into its various sub-systems each of which is assigned to the designated engineers. These sub-systems include:

- Flywheel/Rotor
- Flywheel vacuum enclosure;
- Permanent Magnet Synchronous Machine (PMSM);
- Active Magnetic Bearings (AMBs);
- Electrical control enclosure.

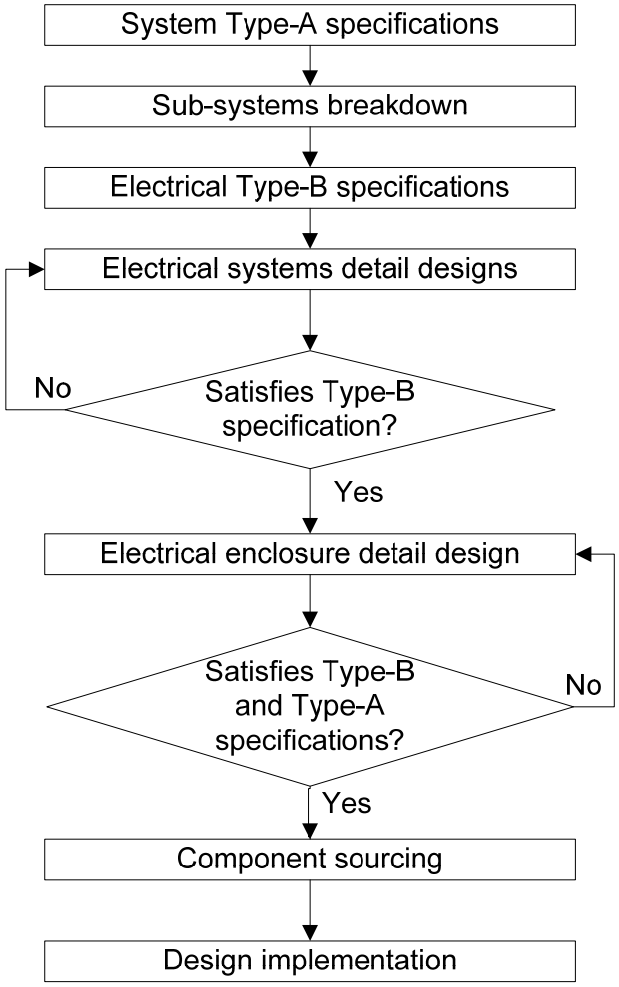


**Figure 4-1: System design process**

Type-B specifications are then drawn up for these subsystems. The Type-B specification lists the standards to which the system will be designed. It included basic diagrams of the various sub-systems, as well as the interfacing between the sub-systems and the interfacing of the Fly-UPS system to the environment. The performance characteristics of the system as a whole are listed, as well as the physical- and performance characteristics of the various sub-systems. The document also lists the materials that will be used in the construction of the system as well as the personnel requirements of the project. Safety issues regarding the system are also discussed in the Type-B specification.

When both the Type-A and the Type-B specifications are approved by the project leader, the detailed sub-system design may commence. After completion of a specific sub-system, it is measured against the Type-B specification in order to determine whether it meets the requirements. If the sub-system does not meet the requirements of the specification, the sub-system is redesigned in order to meet its requirements. The type A and –B specifications can be found in Appendix A and -B.

When all the sub-systems are designed and the specifications are met, the electrical enclosure design can start. This begins with the placement of all the various sub-systems in an industrial electrical enclosure. It also involves the interfacing between all the sub-systems, as well as the interfacing to the environment. After the enclosure design has been completed, it is measured against both the Type-A and –B specifications to determine if the specifications and requirements are met. If the specifications and requirements are not met, the enclosure design is reworked in order for it to meet the specifications and requirements. The next step is to source all the various components which will be used in the electrical control enclosure, and after this has been done, the system can be implemented.

## 4.2 Electrical system functional analysis

As mentioned above, one of the main purposes of the Fly-UPS project is to develop the system to industrial standards. This means having an industrial type electrical enclosure that houses all of the sensitive electrical components of the system. Figure 4-2 shows the functional system diagram of the electrical enclosure. The main functions of the electrical enclosure are AMB actuation, AMB control, PMSM actuation, PMSM control, over-speed protection, mechanical system interfacing and user interfacing.

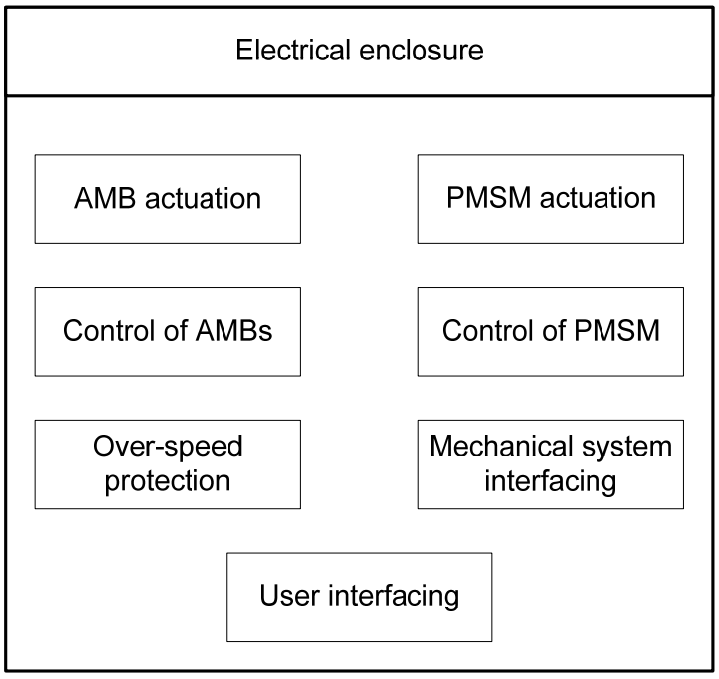


**Figure 4-2: Electrical system functional diagram**

The actuation of the AMBs involves the interfacing of the magnetic actuators with the power amplifiers that drive the AMBs. Since there are two radial AMBs and one axial AMB, ten power

amplifiers have to be employed to drive the three AMBs. The power amplifiers also need an isolated power supply to power them. The AMBs employ displacement sensors to determine the position of the rotor. There are five eddy current displacement sensors in the system; each of which has its own driver and an isolated power supply. All of these components are necessary to achieve AMB actuation and all of these components have to be housed in the electrical enclosure.

AMB control and monitoring is realised by making use of the dSPACE® controller as discussed in chapter 3. The dSPACE® controller is housed in the electrical enclosure and is interfaced with the power amplifiers and the eddy current displacement sensor drivers which are also housed in the electrical enclosure. Temperature sensing is also done on the coils of the AMBs. The drivers of the temperature sensors have to be housed in the electrical enclosure and interfaced with the dSPACE® controller.

Another function of the electrical enclosure is the actuation of the PMSM. The enclosure houses the drive of the PMSM, the LC-filter for the output of the drive as well as an isolated power supply to power the drive. As mentioned the enclosure also houses the dSPACE® controller. The motor drive is interfaced with the dSPACE® controller in order to control the drive. The dSPACE® controller is also used to sense the temperature of the winding of the PMSM as well as measuring voltages and currents in the motor leads.

The enclosure will also house the over-speed protection circuit of the system. This circuit is used to stop the machine during an emergency situation as well as when the rotational velocity of the flywheel reaches a certain threshold. The system operates independently from the dSPACE® controller and is employed to ensure safety redundancy. The over-speed circuit consists of contactors, relays and a resistor bank all of which are housed in the electrical enclosure. The resistor bank acts as a load during an emergency stop situation and dissipates the energy stored in the flywheel. The enclosure also houses the relays which are used to operate the vacuum pump and the vacuum valves on the mechanical enclosure.

The mechanical system is interfaced with the enclosure by means of cables which run from the various sub-systems in the electrical enclosure to the mechanical enclosure where the AMBs, the PMSM and the various sensors are housed. The enclosure also acts as an interface medium to the user of the Fly-UPS system since it connects the user with the system via the operator's PC. The electrical enclosure is connected to the operator's PC by a fibre-optic cable which runs to the dSPACE® controller. This allows the user to control the Fly-UPS system in real time.

# 4.3 System conceptual design

### *4.3.1 System layout*

Figure 4-3 shows the conceptual design of the electrical system of the Fly-UPS system. The mechanical enclosure houses the two radial AMBs as well as the axial AMB. Each of the AMBs has a temperature sensor (RTD) which measures the temperature within the coils of the actuators. The RTDs are connected to the interface board where the RTD drivers are situated. The RTD drivers interface with the dSPACE® controller which determines the temperature.

The mechanical enclosure houses the PMSM which also has an RTD to measure the temperature within the windings of the motor. Furthermore there is an infrared temperature sensor in the mechanical enclosure which monitors the temperature of the rotor next to the permanent magnets of the PMSM. The infra-red (IR) temperature sensor is interfaced with dSPACE® via the interface board. Since the mechanical enclosure operates at a pressure of 0.5 bar, it utilises a vacuum system consisting of a vacuum pump and vacuum valves. It also has a pressure transducer which measures the pressure inside the mechanical enclosure. The pressure transducer and the vacuum system are also interfaced to dSPACE® via the interface board.

The electrical enclosure houses the ten power amplifiers which drives the active magnetic bearings. The power amplifiers has I/O capabilities including the current reference signal, a PA status signal and a current monitor which gives a voltage signal proportional to the current flowing in the actuator leads. The power amplifiers are interfaced with the dSPACE® controller via the interface board. The dSPACE® controller generates the current reference signals of the PAs and it checks the status of the PAs. It also determines the current which flows in the actuator leads. The power amplifiers are supplied with power by an isolated power supply.

As mentioned above, the AMBs employ eddy current displacement sensors which determine the position of the rotor during operation. The eddy probes are situated within the AMBs and the probes run to the eddy probe drivers which give an output signal of 0 to 24 V. An isolated power supply delivers power to the eddy probe drivers. The voltage outputs of the eddy probe drives runs to the interface board, through a protection circuit which clamps the output voltage to 10 V. The output of the protection circuit then runs to the dSPACE® controller.

The PMSM is connected to the electrical enclosure via the over-speed protection circuit. As mentioned above the over-speed protection circuit disconnects the PMSM from the motor drive and connects it to the resistor bank in an emergency situation to stop the flywheel. The motor drive is connected to the over-speed protection circuit by the LC-filter. An isolated 230-230 V power supply powers the motor drive.

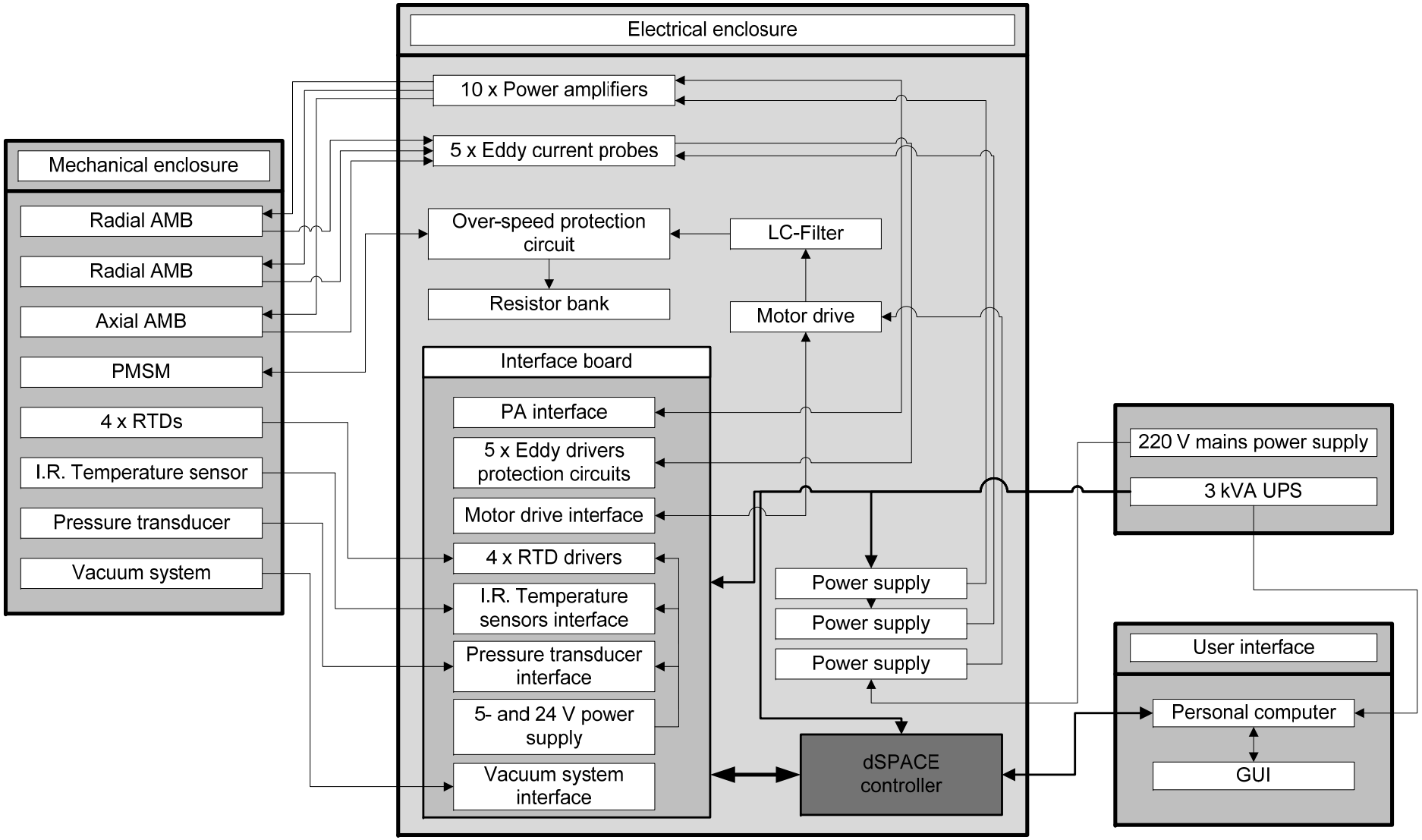


**Figure 4-3: System concept design**

The motor drive interfaces with the dSPACE® controller via the interface board. The dSPACE® controller generates PWM signals for the motor drive and measures the voltages and currents that the drive generates.

Furthermore, there is a user interface consisting of a graphical user interface which is displayed on two 22” monitors of a control PC. The GUI gives the operator full control of the Fly-UPS system. The user interface is connected to the dSPACE® controller via a bi-directional fibre-optic cable giving the user the ability to monitor and control the system in real time.

The critical systems of the Fly-UPS system is supplied by a 3 kVA Uninterruptible Power Supply (UPS) in order to ensure that the magnetic bearings system (which include the PAs, the displacements sensors, the temperature sensors, the protection circuit and the controller) does not shut down in case of a power failure and cause damage to the spinning rotor/flywheel. The motor drive is supplied by 220 V main power supply as it is not a critical system.

### *4.3.2 Design constraints*

The main design constraints regarding the electrical system include safety, operating temperature and industrial standards. Since the flywheel will rotate at 30,000 rpm and store 527 kJ of energy, safety is a big concern. The system has to have redundant safety mechanisms to stop the flywheel in case of an emergency. These safety mechanisms include an emergency stop button situated within the operators reach. An emergency stop within the GUI also has to be implemented and as mentioned above, an over-speed protection circuit has to be implemented in order to stop the flywheel when over-speed occurs.

Temperature also plays an important role in the design of the electrical enclosure. Since there are ten PAs mounted in the enclosure, a cooling mechanism has to be implemented in order to cool them to within their specified operating range. The motor drive as well as the LC filter also has to be cooled and the heat has to be extracted from the enclosure in order to keep the ambient temperature within the operating range of the dSPACE® controller.

Furthermore the presence of high switching frequencies of the PAs and the motor drive may cause noise problems within the system. In order to minimise the effects of noise, the signal cables have to be kept as short as possible and a grounding policy has to be employed.

### *4.3.3 Power distribution and grounding policy*

Special care is taken with the grounding and shielding of the various sub-systems of the electrical enclosure to ensure that the embedded noise in the system does not render the system unstable.

The chassis of the enclosure is used as an earth point in a star configuration to ensure that earth loops are not created. The shielding is also configured to ensure low noise levels. Figure 4-4 shows the power supply to the power amplifiers from the 60 V power supply. The negative output lead of the power supply is grounded to ensure a 0 to 60 V output in reference to the chassis. The signal cable is shielded on the interface board which is connected to chassis.

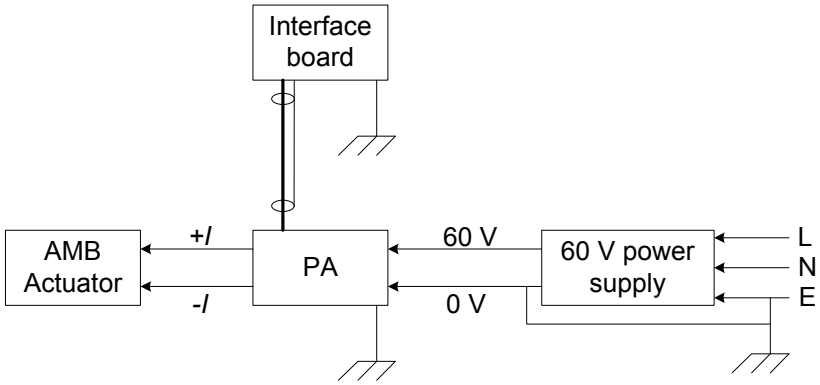


**Figure 4-4: Power amplifier power and grounding diagram**

Figure 4-5 shows the grounding of the eddy probe signal cable to the interface board which is grounded to chassis. The ± 24V power supply is supplied with 220 V and the +24 V output lead is grounded to chassis in order to ensure a 0 to -24 V supply to the eddy probe drivers.

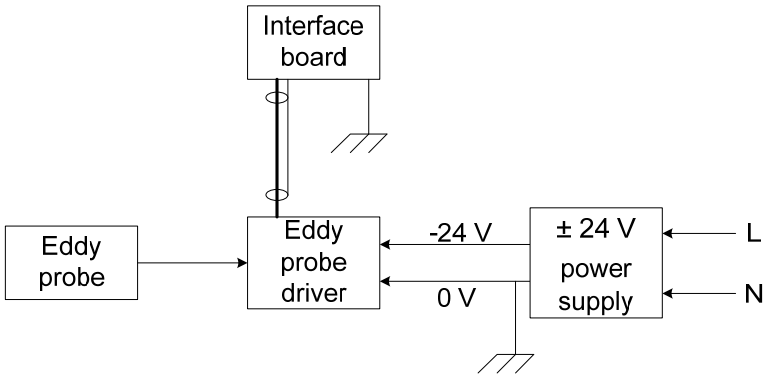


**Figure 4-5: Eddy probe driver power and grounding diagram**

The motor drive power supply is shown in Figure 4-6. A 230-230 V transformer is supplied with 220 V which is rectified. The negative lead of the rectified voltage is connected to chassis in order to ensure a 310 V output in reference to the chassis. The shields of the signal cables of the motor drive are connected to the motor drive which is grounded to chassis.

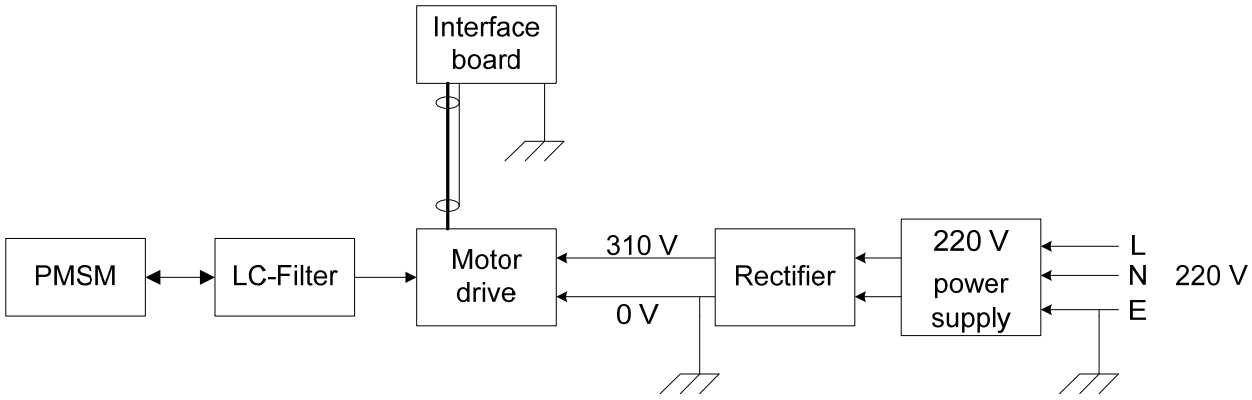


**Figure 4-6: Motor drive power and grounding diagram**

Figure 4-7 shows the rectified and regulated 5 V power supply of the RTD driver. The negative lead of the rectifier is connected to the chassis to ensure an output of 0 to 24 V in reference to chassis. The regulator supplies 5 V to the RTD driver. The shield of the RTD signal cable is grounded on the interface board.

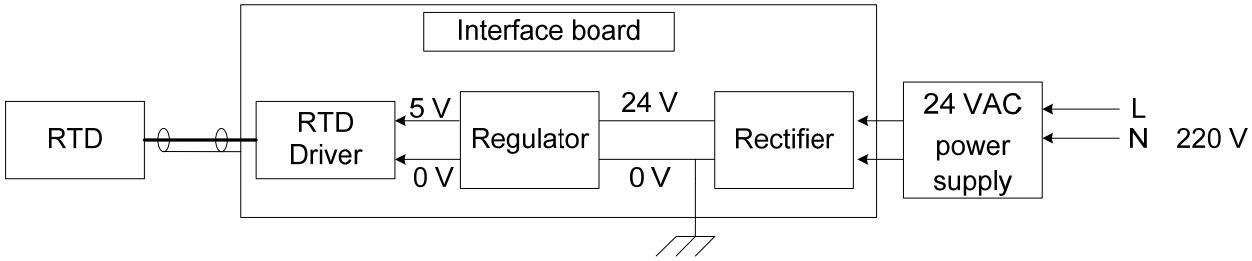


**Figure 4-7: RTDs power and grounding diagram**

The vacuum system power supply is shown in Figure 4-8. The relays which drive the vacuum pump and the vacuum valves are supplied with 24 VAC. The relays switch the vacuum pump and valves which operate on 220 V.

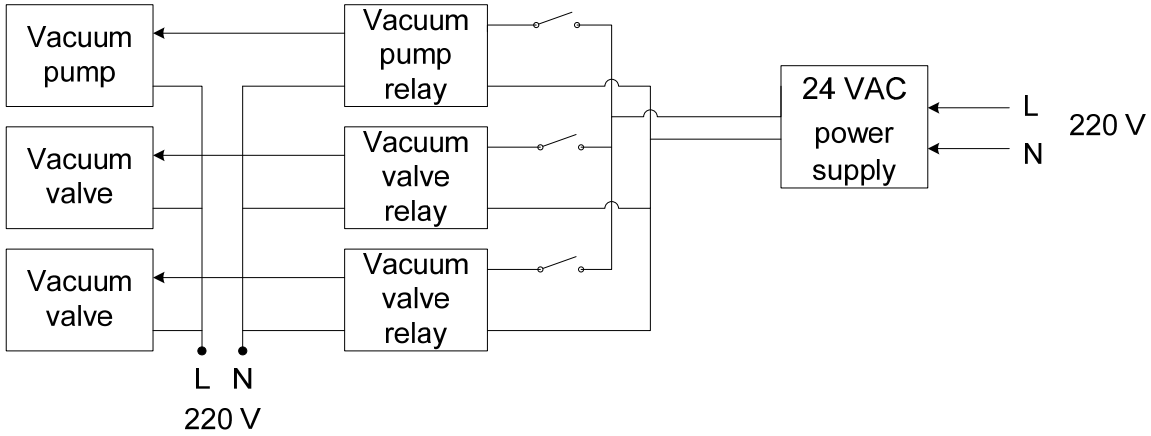


**Figure 4-8: Vacuum system power diagram**

Figure 4-9 shows the connection of the interface board to the dSPACE® controller. The controller is grounded to chassis and the signal cables which run from the dSPACE® controller to the interface board and is shielded on the interface board.

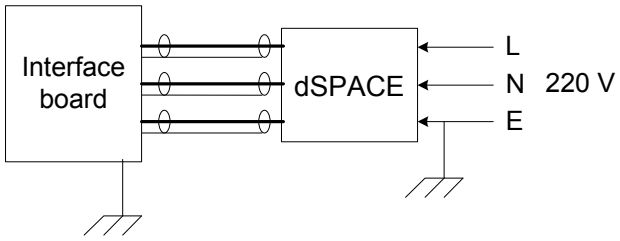


**Figure 4-9: dSPACE® power and grounding diagram**

### *4.3.4 I/O requirements*

**Table 4-1: I/O requirements of the electrical system**

| Sub-system | Purpose | I/O requirement |
|---|---|---|
| | | |
| Power amplifiers (x 10) | Current reference signal | D/A (x 10)<br>DS2103 board |
| | PA status | Digital I/O (x 10)<br>DS4002 board |
| | Current monitor | A/D (x 10), DS2003 board |
| | | |
| Eddy current sensors (x 5) | Position voltage signal | A/D (x 5), differential<br>DS2004 board |
| | | |
| RTDs (x 4) | Temperature voltage signal | A/D (x 4) , DS2003 board |
| | | |
| I.R temperature sensor | Temperature voltage signal | A/D, DS2003 board |
| | | |
| Pressure transducer | Pressure voltage signal | A/D, DS2003 board |
| | | |
| Emergency stop relay | Switching TTL relay | Digital I/O, DS4002 board |
| | | |
| Vacuum pump relay | Switching TTL relay | Digital I/O, DS4002 board |
| | | |
| Vacuum valve (N/O) relay | Switching TTL relay | Digital I/O, DS4002 board |
| | | |
| PMSM Drive | PWM signal generation | Digital PWM, 3-phase |

| | | |
|---|---|---|
| | | DS5105 board |
| | Current sensing | A/D (x 3), DS2003 board |
| | Voltage sensing | A/D (x 3), DS2003 board |
| | Pickup coils (x 3) | Digital I/O (x 3), DS4002 board |

Table 4-1 displays the I/O requirements of the various sub-systems. The specific sub-system and the purpose of the I/O are listed as well as the corresponding dSPACE® board which is used to realise the I/O requirements. A detailed discussion on sub-system interfacing to the dSPACE® controller follows in section 4.7.

## 4.4 Power amplifiers

### *4.4.1 Amplifier specification*

As discussed in section 2.5, the magnetic bearing needs power amplifiers (PAs) to power the magnetic actuators. A typical eight-pole radial magnetic bearing needs four PAs; two power amplifiers per axis. The specification of the required PAs is an output of the magnetic bearing detail design process which is discussed in chapter 3.

**Table 4-2: Power amplifier requirements**

| **Magnetic bearing power amplifier requirements** | |
|---|---|
| Maximum required current: | $I_{max}$ = 5A |
| Maximum required voltage: | $V_{max}$ = 52V |
| Power amplifier bandwidth: | $f_{bw}$ = 2.5 kHz |
| Analog input range: | ± 10V |

Table 4-2 shows the specifications to which the power amplifiers have to conform. The maximum voltage the power amplifier will be supplied with is 52 V in order to achieve the design force slew rate. The power amplifier also has to have a bandwidth of at least 2.5 kHz which is five times higher than the systems maximum rotational frequency of 500 Hz. The PA also has to have an analog input range of ± 10 V. This is the output voltage range of the Digital-to-Analog (D/A) converter of the dSPACE® controller.

Making use of the specifications listed in Table 4-2, the power amplifiers were sourced. It was decided to make use of Advanced Motion Controls® model 12A8 servo amplifiers. These amplifiers are bi-state, PWM switching amplifiers and they conform to the design requirements of the magnetic bearings.

**Table 4-3: AMC's model 12A8 servo amplifier specifications**

| **Power stage specification** | **12A8** |
|---|---|
| DC supply voltage | 20 – 80 V |
| Peak current (2 sec, internally limited) | ± 12 A |
| Maximum continuous current (adjustable) | ± 6 A |
| Switching frequency | 36 kHz |
| Case temperature range | 0 – 65°C |
| Power dissipation at continuous current | 24 W |
| Over-voltage shutdown (self reset) | 86 V |
| Bandwidth | 2.5 kHz |
| Differential analog input | ± 15 V |

Table 4-3 shows the specifications of the sourced power amplifiers. The PA has a supply voltage range of 20 – 80 VDC which satisfies the supply voltage requirement of 52 V. It has a maximum continuous current rating of ± 6 A, which satisfies the supply current requirement of 5 A. The differential analog input is ± 15 V and the bandwidth of the PA is 2.5 kHz. The power dissipated at a continuous current rating of 6 A is 24 W.

A dedicated power supply for the power amplifiers also had to be sourced. The choice of power supply was made by using (4-3) to determine the power requirements of the PAs. Firstly the number of PAs in the system, $n$, was multiplied by the power dissipation at continuous current rating, $P_{amp}$ using (4-1).

$$P_{diss\_amp\_total} = \left(n \times P_{amp}\right) \quad \textbf{(4-1)}$$

This yielded a total power dissipation of 240 W within the PAs, when all ten power amplifiers are continuously supplying 6 A. Next the power dissipated within the magnetic actuators was determined using (4-2).

$$P_{coil} = n \times \left(I^2 R_{coil}\right) \quad \textbf{(4-2)}$$

The number of PAs in the system, $n$, was multiplied by the power dissipation within the coils using the maximum current $I$ of 5 A within the coils and the resistance of the coils $R_{coil}$ of 0.304 Ω per coil as determined in chapter 3. This yielded a total power dissipation of 76 W within all ten coils at the maximum current of 5 A. The total power requirement for all ten of the PAs is given by (4-3) which came to 316 W.

$$P_{total} = \left(P_{diss\_amp\_total} + P_{coil}\right) \quad \textbf{(4-3)}$$

The Advanced Motion Controls® model PS16H60-L unregulated power supply was chosen. This power supply is supplied with 220 VAC and is capable of supplying the power amplifiers with

60 VDC and delivering 800 W of power. Figure 4-10(a) and (b) shows the sourced 12A8 servo amplifier and the sourced PS16H60-L power supply respectively.

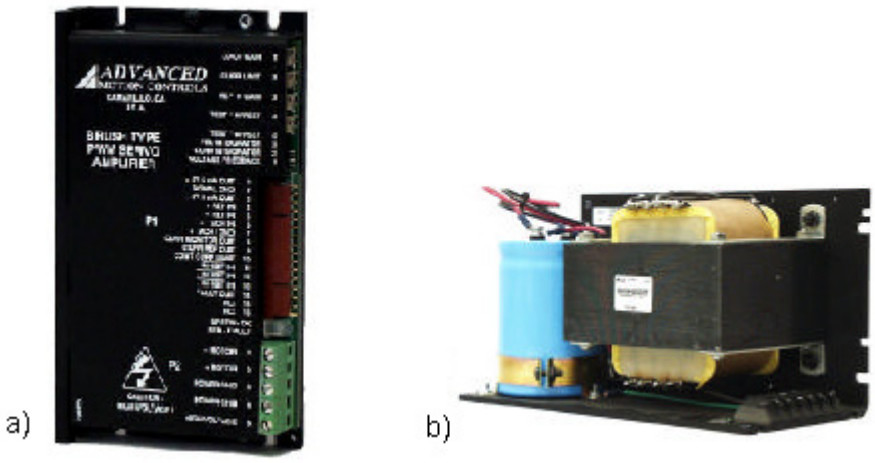


**Figure 4-10: The AMC servo amplifier (a) and the power supply (b)**

The servo amplifier has an array of input and output pins. The input pins that were used include the voltage supply connector, the differential voltage input pins (which is the analog reference signal), and the continuous current limit pin (which can be used to reduce the maximum continuous current). The output pins that were used include the power output connector to the actuator, the current monitor pin (which is an analog output that gives a signal proportional to the actual current within the output power leads) and the fault pin (which indicates the status of the PA).

### *4.4.2 Thermal design*

It was decided to mount all ten power amplifiers on one large heat sink in order to simplify the mounting of the PAs inside the electrical control enclosure. In order to mount the PAs on one heat sink, a thermal analysis had to be done to determine the temperature at which the PAs will operate. It was also necessary to do the thermal analysis in order to determine if forced air cooling would be needed. Figure 4-11 shows the thermal circuit of the power amplifier and the heat sink.

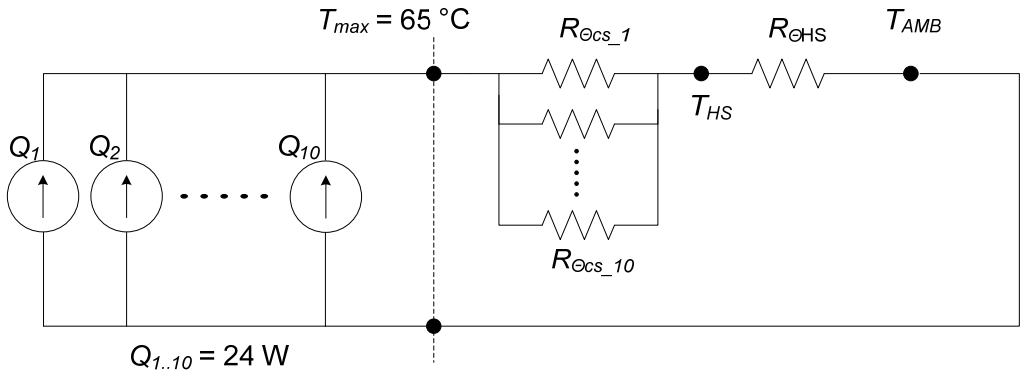


**Figure 4-11: Thermal network of power amplifier assembly**

The ambient temperature of the electrical control enclosure ($T_{AMB}$) was taken to be 30 °C. The maximum case temperature ($T_{max}$) at which the power amplifiers can operate (before the protection circuits are triggered) is taken to be 65°C. The power dissipated at maximum continuous current was taken to be $Q$ = 24 W in each PA. The power amplifiers are mounted directly on the heat sink without being electrically-isolated or making use of thermal interface pads. The case to sink thermal impedance of the power amplifiers is determined to be 0.11 °C-in$^2$/W by making use of the area of the PA case and the thermal resistance of 0.5 °C/W for direct contact between aluminium surfaces. The case to sink thermal resistance of the power amplifier's case is determined from (4-4) where $A_{PA}$ is the area of the case of the power amplifier.

$$R_{\Theta_{CS}} = \frac{0.11}{A_{PA}} \quad \textbf{(4-4)}$$
$$= \frac{0.11}{0.99 \times 5.09} \text{ °C/W}$$
$$= 21.83 \times 10^{-3} \text{ °C/W}$$

The specified power dissipation of the power amplifier is 24 W at maximum continuous current of 6 A. The AMB design process yielded an RMS current of 2.93 A which is the continuous current the PAs will deliver to the magnetic actuators. Since power ($P$) is directly proportional to current ($I$), it can be deduced that the continuous power dissipation at 2.93 A will be 14.06 W.

The maximum allowable heat sink temperature is obtained using the power dissipation and thermal resistances in (4-5).

$$T_{HS} = T_{MAX} - \left(n \cdot Q \cdot R_{\Theta_{CS}}\right) \quad \textbf{(4-5)}$$
$$= 65 - \left(10 \cdot 14.06 \times 21.83 \times 10^{-3}\right) \text{ °C}$$
$$= 61.93 \text{ °C}$$

This implies that the heat sink temperature must stay below 61.93 °C while the power amplifier is operated under normal biasing conditions. The maximum thermal resistance of the heat sink is then obtained using (4-6).

$$R_{\Theta_{HS}} = \frac{T_{HS} - T_{AMB}}{10 \cdot Q} \quad \textbf{(4-6)}$$
$$= 0.227 \text{ °C/W}$$

The geometry of the heat sink plays an important role in the sourcing of an appropriate heat sink. The necessary dimensions of the heat sink for all ten power amplifiers is 150 mm wide, 40 mm high and 450 mm long and has a thermal resistance of 0.57 °C/W. Figure 4-12 shows the PA and aluminium heat sink assembly.

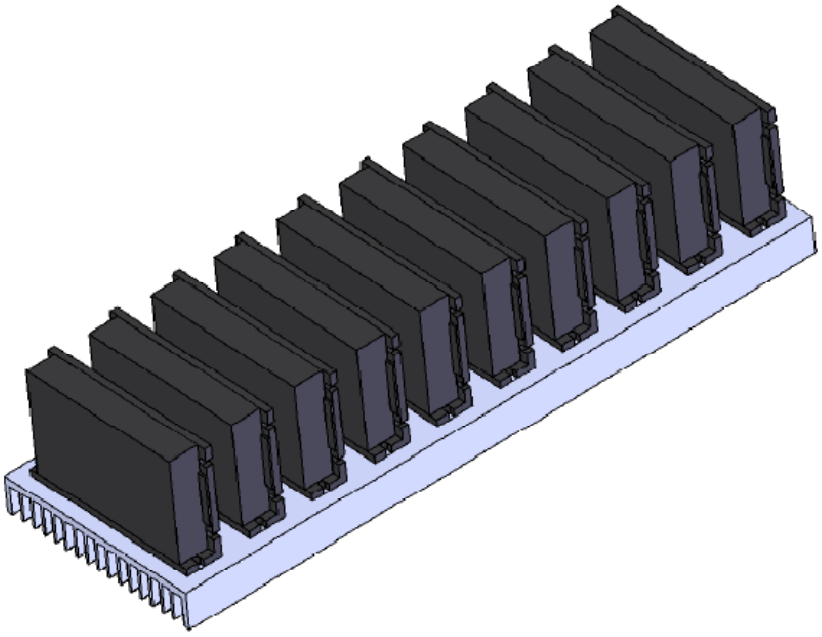

**Figure 4-12: Power amplifiers on heat sink assembly**

Since various experiments and tests will be done on the AMBs and the bias and maximum currents may be increased, an AC fan was also incorporated in the power amplifier assembly which will reduce the thermal resistance of the heat sink to well below 0.227 °C/W.

## 4.5 Sensors

### *4.5.1 Eddy-current displacement sensors*

Eddy current sensors were chosen to monitor rotor displacement due to their immunity to the high frequency noise generated by the power amplifiers. The eddy current sensor that was sourced is the SKF CMSS65/CMSS665 series 5 mm Eddy probe system.

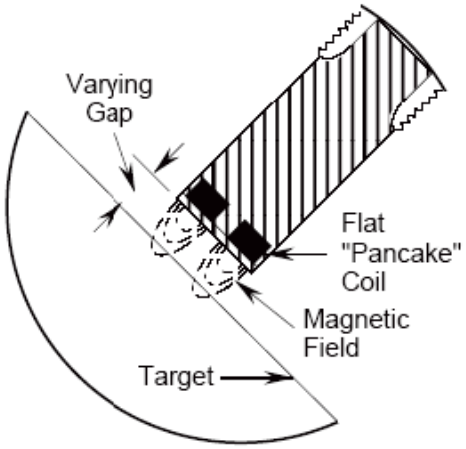


**Figure 4-13: Eddy probe tip**

As discussed in section 2.4.1, the encapsulated coil in the probe tip, radiates a high frequency magnetic field into the measured target material. The magnetic field is generated by the Eddy probe driver. As a conductive surface approaches the probe tip, eddy currents are induced which weakens the induced magnetic field. The driver produces a dc voltage representing the field strength which decreases as a conductive surface approaches the probe tip.

The driver linearises and normalises the output to a sensitivity of 7.87 mV/µm throughout its working range. The eddy probe has a useable range of up to 2 mm and a dynamic range of dc to 10 kHz (-3dB). The bandwidth of 10 kHz is more than adequate since the maximum rotational frequency of the flywheel will only be 500 Hz. The eddy probe driver requires a 15 mA, -24 V power supply unit which was also sourced from SKF. Figure 4-14a shows a picture of the eddy probe driver whereas Figure 4-14b shows the -24 V power supply.

Since the flywheel will be suspended in 5 axes, 5 eddy probe systems were sourced. There is an eddy probe situated on the x-axis as well as on the y-axis of each of the two radial AMBs to monitor the movement of the rotor in the radial position as well as an eddy probe situated on the axial AMB to monitor the movement of the rotor in the z-axis.

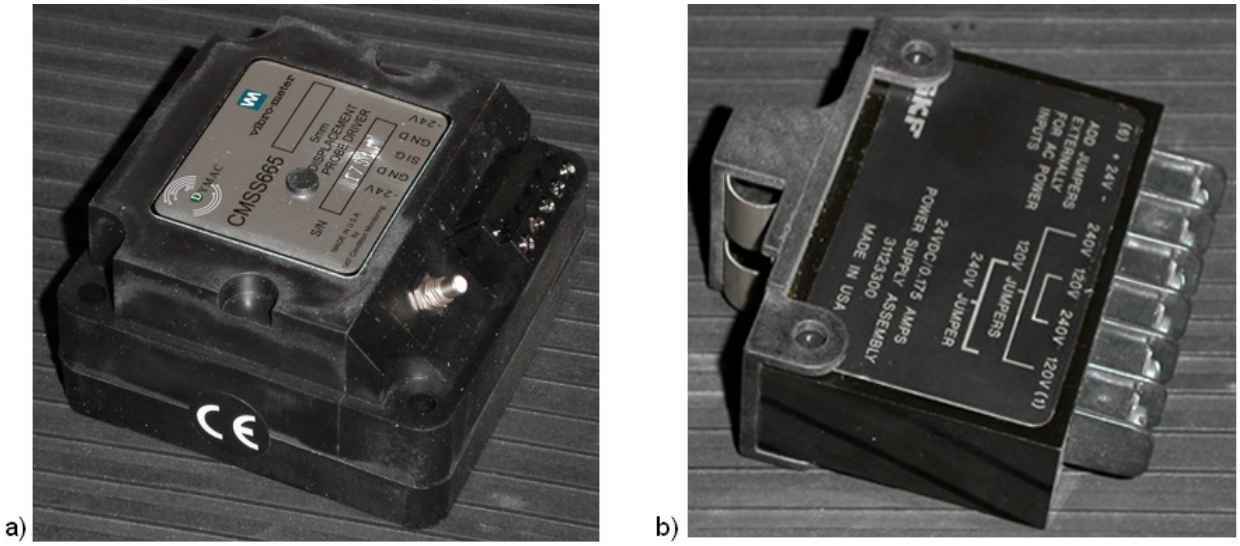


**Figure 4-14: Eddy probe driver (a) and power supply (b)**

The output of the driver varies between 0 and – 24 V while the DS2004 high-speed A/D board can only accept ± 10 V analog signals. The DS2004 board however has overvoltage protection of ±50 V. A protection circuit was added in order to clamp the eddy probe driver's output signal to between 0 and – 10V.

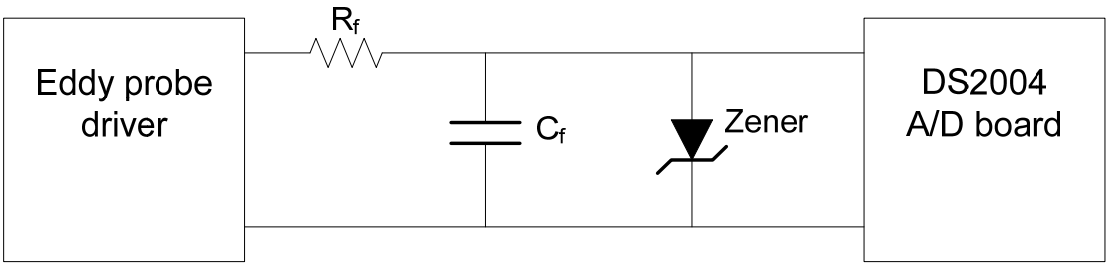


**Figure 4-15: Sensor over voltage protection circuit**

A zener diode was used in order to clamp the input voltage to the DS2004 high-speed A/D board. An 11 V zener diode was chosen so that the voltage output will be linear across the whole 0 to -10 V range. The minimum value of $R_f$ was obtained using (4-7)

$$R_f = \frac{V_{\max} - V_{\text{zener}}}{I_{\max}} \quad \textbf{(4-7)}$$
$$= \frac{24 - 11}{8 \times 10^{-3}} \ \Omega$$
$$= 1.6 \text{ k}\Omega$$

To recover all the components of the signal, a sampling rate greater than- or equal to twice the highest frequency component has to be employed. The sampling frequency ($f_S$) of the dSPACE® controller is chosen to be 10 kHz as discussed in section 5.2.1. By choosing the cut-off frequency of the anti-aliasing filter as 5 kHz (which is equal to the Nyquist frequency $f_N$), aliasing is greatly reduced. $R_f$ is chosen to be 3.3 kΩ resistor. The value of the filter capacitor ($C_f$) is then obtained using (4-8) using a cut-off frequency of 5 kHz.

$$C_f = \frac{1}{2\pi R_f f} \quad \textbf{(4-8)}$$
$$= \frac{1}{2 \times \pi \times 3.3 \times 10^{-3} \times 5000} \text{ F}$$
$$= 9.6 \text{ nF}$$

A 10 nF ceramic capacitor was implemented giving the circuit a cut-off frequency of 4.82 kHz.

### *4.5.2 Resistive temperature detector (RTD) sensors*

Resistance temperature detectors or RTDs as they are known are used to measure temperature. RTDs are very similar in appearance to thermocouples but they function completely different. Thermocouples produce a very small voltage when heated. An RTD does not produce any voltage and therefore relies on an instrument for power. RTDs are electrical resistors that change resistance as temperature changes. With all common types of RTDs, the resistance increases as the temperature increases. This is referred to as a *positive temperature coefficient* [19].

RTDs are manufactured using several different materials as the sensing element. The most common by far is the Platinum RTD. Platinum is used for several reasons including its high temperature rating, its stability and repeatability. Figure 4-16 shows a functional diagram of the RTD and its interfacing to the dSPACE® system. To utilise an RTD, a small current is passed through the element and then the voltage across it is measured. As the resistance of the element changes, due to temperature changes, the measured voltage changes. The measured voltage is usually small because the current which passes through the element may not exceed 2 mA. If the current in the element exceeds 2 mA self heating may occur which influences the temperature reading. The measured voltage serves as a reference voltage for an operational amplifier which linearises and amplifies the signal [20]. The linearised signal then serves as an input to the A/D of the dSPACE® controller. The dSPACE® controller translates the input voltage to a temperature measurement.

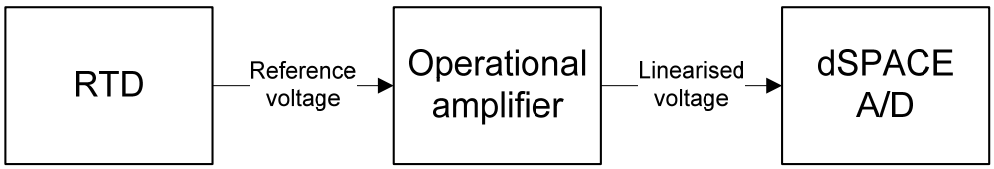


**Figure 4-16: RTD functional diagram**

The first step in designing the operational amplifier circuit is to characterise the reference voltage that the RTD will deliver at certain temperatures. The RTDs that have been sourced are platinum RTDs and from the manufacturers datasheet these RTDs have a resistance of 100 Ω at 0 °C and are nearly linear up to 168 Ω where the temperature reading will be 180 °C. Figure 4-17 shows a common voltage divider used to generate a reference voltage according to the resistive change in the RTD.

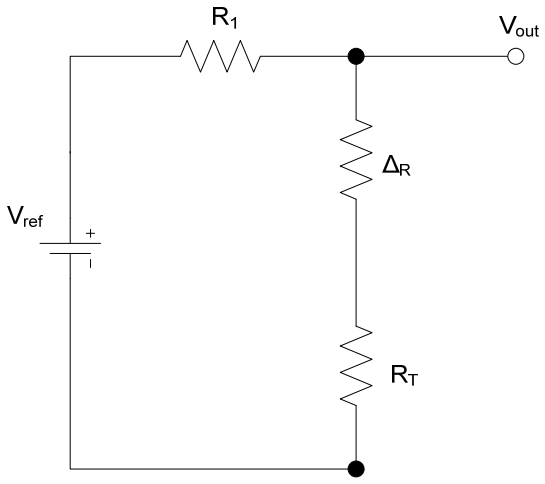


**Figure 4-17: Voltage divider circuit for RTD**

If $R_1$ is comparable in value with $R_T$, the circuit has very low sensitivity because the circuit must measure a small change in resistance in the presence of a large resistance. When the bias resistor,

$R_1$, is selected as a large value, $V_{ref}$ and $R_1$ act as a current source. Making use of (4-9) the reference voltage is characterised. Since the op-amp will operate on 5 V, the reference voltage ($V_{ref}$) is chosen to be 5 V. As mentioned above, the current in the RTD may not exceed 2 mA. $R_1$ is chosen accordingly to be 2.5 kΩ. It is known that $R_T$ = 100 Ω at 0 °C and $\Delta_R$ = 68 Ω at 180 °C.

$$V_{out} = \frac{V_{ref}}{R_1}\left(\Delta R + R_T\right) = \frac{5}{2500}\left(\Delta R + 100\right) \text{ V} \quad \textbf{(4-9)}$$

This yields a voltage range of 0.2 < $V_{out}$ < 0.36 which in turn is then used to design the operational amplifier. The TLV2461 operational amplifier was identified because of its ability to accept input voltages of 0.2 to 0.4 V as well as its ability to deliver output voltages of 0 to 5 V.

**Table 4-4: Op-Amp data points**

| **Input voltage** | **Output voltage** | |
|---|---|---|
| $V_{in1}$ = 0.2 V | $V_{out1}$ = 0 V | 1st pair of data points |
| $V_{in2}$ = 0.34 V | $V_{out2}$ = 5 V | 2nd pair of data points |

Table 4-4 shows the data points to be used in the design of the operational amplifiers. The equation of an operational amplifier is similar to the equation of a straight line given by (4-10)

$$V_{out} = mV_{in} + b \quad \textbf{(4-10)}$$

where the gradient of the straight line ($m$) is given by (4-11):

$$m = \frac{V_{out1} - V_{out2}}{V_{in1} - V_{in2}} \quad \textbf{(4-11)}$$

and intercept of the straight line ($b$) is given by (4-12):

$$b = V_{out} - mV_{in} \quad \textbf{(4-12)}$$

Substituting the data points listed in Table 4-4 into (4-11) and (4-12), equation (4-10) becomes:

$$V_{out} = 35.7 \cdot V_{in} - 7.15 \quad \textbf{(4-13)}$$

The equations for the analog amplifier are given by (4-14), (4-15) and (4-16):

$$V_{out} = V_{in} \times \left(1 + \frac{R_f}{R_G + R_1 \,||\, R_2}\right) + \left(\frac{-V_{ref} \times R_2 \times R_f}{R_G \times \left(R_1 + R_2\right) + R_1 \times R_2}\right) \quad \textbf{(4-14)}$$

$$m = 1 + \frac{R_f}{R_G + R_1 \,||\, R_2} \quad \textbf{(4-15)}$$

$$b = \frac{-V_{ref} \times R_2 \times R_f}{R_G \times (R_1 + R_2) + R_1 \times R_2} \quad \textbf{(4-16)}$$

Solving (4-15) and (4-16) yields the following resistor values for the amplifier circuit: $R_f$ = 2 MΩ, $R_g$ = 75 kΩ, $R_1$ = 75 kΩ and $R_2$ = 3 kΩ.

Since the operational amplifier will be in the presence of the motor drive and the power amplifiers (which have high switching frequencies) and the reference voltage from the RTD is comparably small, RC-filters are implemented on the reference voltage signal and the output signal of the operational amplifier. The cut-off frequency is chosen to be 1 Hz and the resistor value is chosen to be 100 kΩ. From (4-17) the capacitor value is determined to be 1.5 µF.

$$f_c = \frac{1}{2 \cdot \pi \cdot R \cdot C} \quad \textbf{(4-17)}$$

The circuit diagram of the analog amplifier is shown in Figure 4-18.

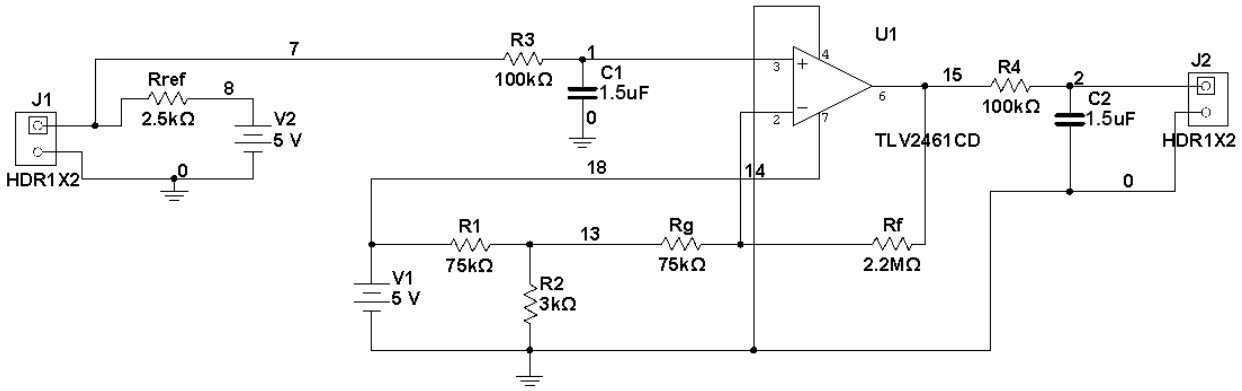


**Figure 4-18: Circuit diagram of the RTD analog amplifier**

The RTD will be connected to the analog amplifier at connector J1 as can be seen in Figure 4-18 and will be connected to the DS2003 multiplexed A/D board of the dSPACE® controller at connector J2 and will give a 0 V output for a temperature measurement of 0 °C and will react linearly through the range up to a 5 V output for a temperature measurement of 180 °C.

### *4.5.3 Pressure transducer*

Due to the fact that the mechanical rotor/flywheel enclosure will be operated at 0.5 bar vacuum [16], there had to be a means of measuring the pressure inside the pressure vessel. It was decided to make use of an electrical pressure transducer. The GEMS® model 2200 pressure transducer was sourced because of its ability to measure absolute pressure. It has a measuring range of 0 – 1 bar and has an output voltage range of 0 – 10 V which is linearly proportional to the pressure inside the measured vessel. It also has an operating temperature range of -40 °C to 125 °C.

Since the output of the pressure transducer is 0 – 10 V, no additional circuitry was needed to interface the sensor to the dSPACE® controller. The sensor however has to be supplied with 24 VDC from the interface board.

### *4.5.4 Infra-red sensor*

It was decided to measure the temperature of the rotor as close as possible to the magnets of the PMSM, so that the machine can be operated safely. If the temperature of the rotor becomes too high, the adhesive that bonds the magnets to the rotor may lose strength, and the magnets can dislodge from the rotor causing a catastrophic failure of the Fly-UPS machine.

Due to the limited space within the mechanical enclosure, it was decided to source an infra-red temperature sensor which can be mounted at a distance from the rotor. The Convir® model EL101A non-contact temperature sensor was sourced. This sensor has a field-of-view of 10:1 and has a temperature measuring range of 0 °C to 250 °C. The sensor also has an output of 4 – 20 mA which is linear to the temperature range.
Since the dSPACE® controller can only accept voltage inputs, a sense resistor had to be implemented on the interface board. The sense resistor was chosen to be 500 Ω which gives the sensor an output of 2 to 10 V. The sensor also has to be supplied with 24 VDC from the interface board.

## 4.6 Over speed protection circuit

A major safety issue in the Fly-UPS system is the speed at which the rotor/flywheel rotates. From rotor dynamic analysis the maximum speed at which the rotor can safely operate is 30,000 rpm. When this operating speed is exceeded there is a risk of catastrophic failure of the rotor/flywheel. From the speed control of the PMSM, the rotational speed of the rotor/flywheel can be determined by means of the pickup coils inside the windings op the PMSM. This information is also used to implement speed control of the PMSM. A system had to be implemented which can monitor the rotational speed of the rotor/flywheel independently from the PMSM drive in order to ensure redundancy and thus making the system more safe.

The decision was made to implement a separate speed sensor which senses the speed on the rim of the flywheel. When the threshold of 30,000 rpm is reached, the PMSM drive has to be disconnected from the PMSM and the flywheel has to be stopped as soon as possible. This means connecting the PMSM directly to a load in order to dissipate the 527 kJ of energy stored in the flywheel as soon as possible. It was decided to implement a resistor bank that would act as a load and which would be able to dissipate the 527 kJ of energy.

The system also had to be able to be stopped from an emergency stop button located next to the operator of the Fly-UPS system. When the emergency stop button is pressed, the PMSM drive has to be disconnected from the PMSM, the PMSM has to be switched to the resistor bank and the 527 kJ of energy has to be dissipated through the resistor bank.

The operator of the system also has to be able to stop the Fly-UPS system from within the dSPACE® graphical user interface (GUI). There has to be a button in the GUI which will function in the same way as the emergency stop button, stopping the flywheel as soon as possible.

Firstly a contactor was implemented which disconnects the PMSM drive from the PMSM when the power supply circuit to the contactor was broken as shown in Figure 4-19.

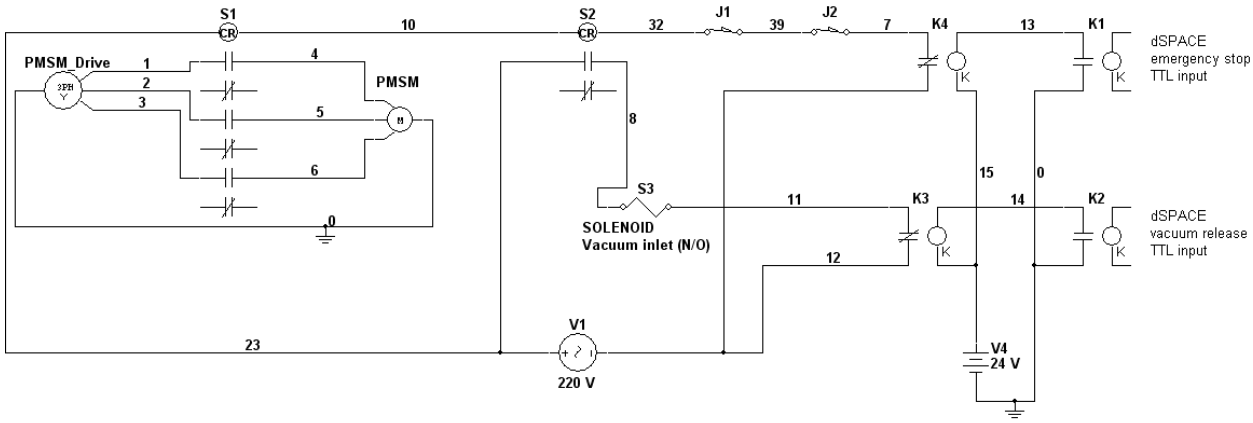


**Figure 4-19: PMSM decoupling circuit**

When the emergency stop (J1) is pressed, the circuit opens and the PMSM is disconnected from the PMSM drive via the contactor (S1). When the speed sensor measures the speed to be above the threshold of 30,000 rpm, the relay within the speed sensor (J2) opens and the PMSM is disconnected from the PMSM drive.

The dSPACE® emergency stop was implemented using a TTL relay, triggered from the DS4002 I/O board of the dSPACE® controller with a 5 V signal. When the emergency stop is pressed from within the dSPACE® GUI, the 5 V TTL relay (K1) switches on, which switches the 24 V relay (K4) which in turn opens the circuit and disconnects the PMSM from the PMSM drive.

Since the mechanical system is operated at 0.5 bar vacuum, there also had to be functionality for the vacuum valves as well as the vacuum pump. Figure 4-20 shows the vacuum system of the Fly-UPS system.

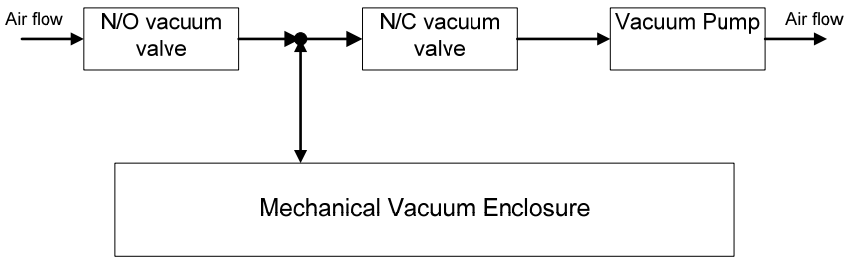


**Figure 4-20: Fly-UPS vacuum system**

When any of the above mentioned emergency stops occur, the vacuum has to be released in order to assist in the stopping of the flywheel. This was accomplished by inserting a 220 V relay (S2). When the circuit is broken by any of the emergency stop conditions, the relay opens and the vacuum valve (S3) returns to its normally open state, releasing the vacuum. The vacuum valve can also be operated from the dSPACE® GUI using a TTL relay (K2) which in turn switches a 24 V relay (K3) to control the valve.

The next step was to implement the resistor bank and its connection to the PMSM. The resistor bank's purpose is to act as a load and thus dissipate the 527 kJ of energy stored in the flywheel while rotating at 30,000 rpm, bringing the flywheel to a standstill. The design of the resistor bank does not form part of this study and was done by Dr. S.R. Holm which also designed the PMSM.

The resistor bank is connected to the PMSM when an emergency stop occurs or when over-speed is reached. The resistor bank is made up of 4 resistor stages as shown in Figure 4-21 which are switched in parallel in four stages. Each of the switches $S_1..S_4$ represent a contactor which switches in the stages of the resistor bank.

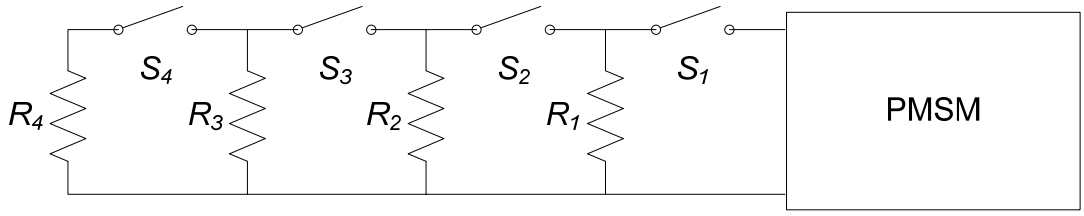


**Figure 4-21: PMSM resistor bank**

Figure 4-22 shows the emergency stop sequence. When an emergency stop occurs, the drive and the PMSM are disconnected, the first stage of the resistor bank is switched in and the first variable timer is started. From the design of the resistor bank the resistance of the first stage is determined to be 3.3 Ω and a maximum current of 28.12 A will flow in the resistors. After the timer has run out, the second stage of the resistor bank is switched in parallel and the second variable timer is started. The resistance of the second stage is 27 Ω and the maximum current that will flow in the resistors is 3.14 A. After the second variable timer has run out, the third stage is switched in parallel and the third

variable timer is started. The resistance of the third stage is 22.5 Ω and the maximum current that will flow in the resistors is 3.3 A. After the third timer has run out, the fourth and final stage of the resistor bank is switched in parallel. The resistance of the fourth stage is 18.1 Ω and a maximum of 3.61 A will flow in the resistors. This sequence will bring the rotational speed of the PMSM down from 30,000 rpm to 15,000 rpm which is a relatively safe operating speed.

The sequence above is implemented by making use of 3-phase contactors and variable pneumatic timers which are fitted on top of the contactors and can be set between 1- to 30 sec.

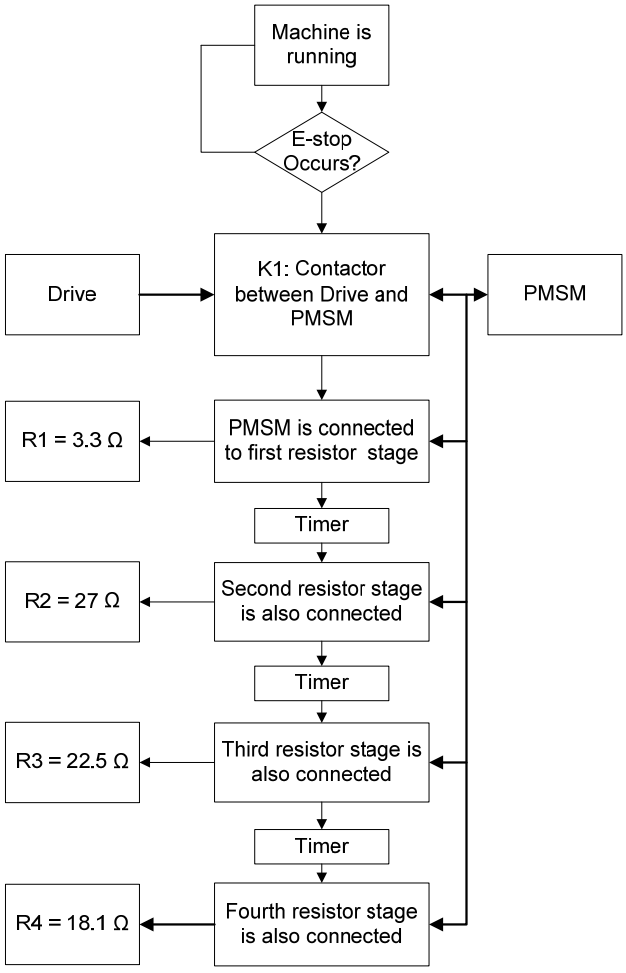


**Figure 4-22: Resistor bank switching sequence**

Figure 4-23 shows the circuit which was implemented. The contactor used to disconnect the drive from the PMSM (S1) is a normally open (N/O), 400 V, 32 A 3-phase contactor. This contactor was chosen because the maximum current that will flow between the drive and the PMSM will be 25 A, so this contactor is more than adequate. The contactor used to switch in the first resistor bank (S2) was chosen to be a normally closed (N/C), 400 V, 32 A 3-phase contactor. This contactor was chosen because the current that will flow in the first stage of the resistor bank is 28.2 A. The next three contactors (S3, S4 and S5) were chosen to be normally open (N/O), 300 V, 9 A 3-phase contactors, because the maximum current that will flow in the second to fourth stages will only be 3.61 A.

The relays (K4, K5 and K6) that were chosen are 11 pin, 24 VAC change-over (C/O) relays capable of driving the vacuum valves as well as the vacuum pump. These relays were chosen because of their low coil excitation voltage which had to be low in order to switch these 24 VAC relays with smaller TTL reed relays directly from dSPACE®. The reed relays can switch voltages of up to 170 V.

This gives the functionality of being able to fully control the vacuum valves as well as the vacuum pump from within the ControlDesk® GUI. The complete over-speed protection circuit can be found on the data CD in Appendix D.

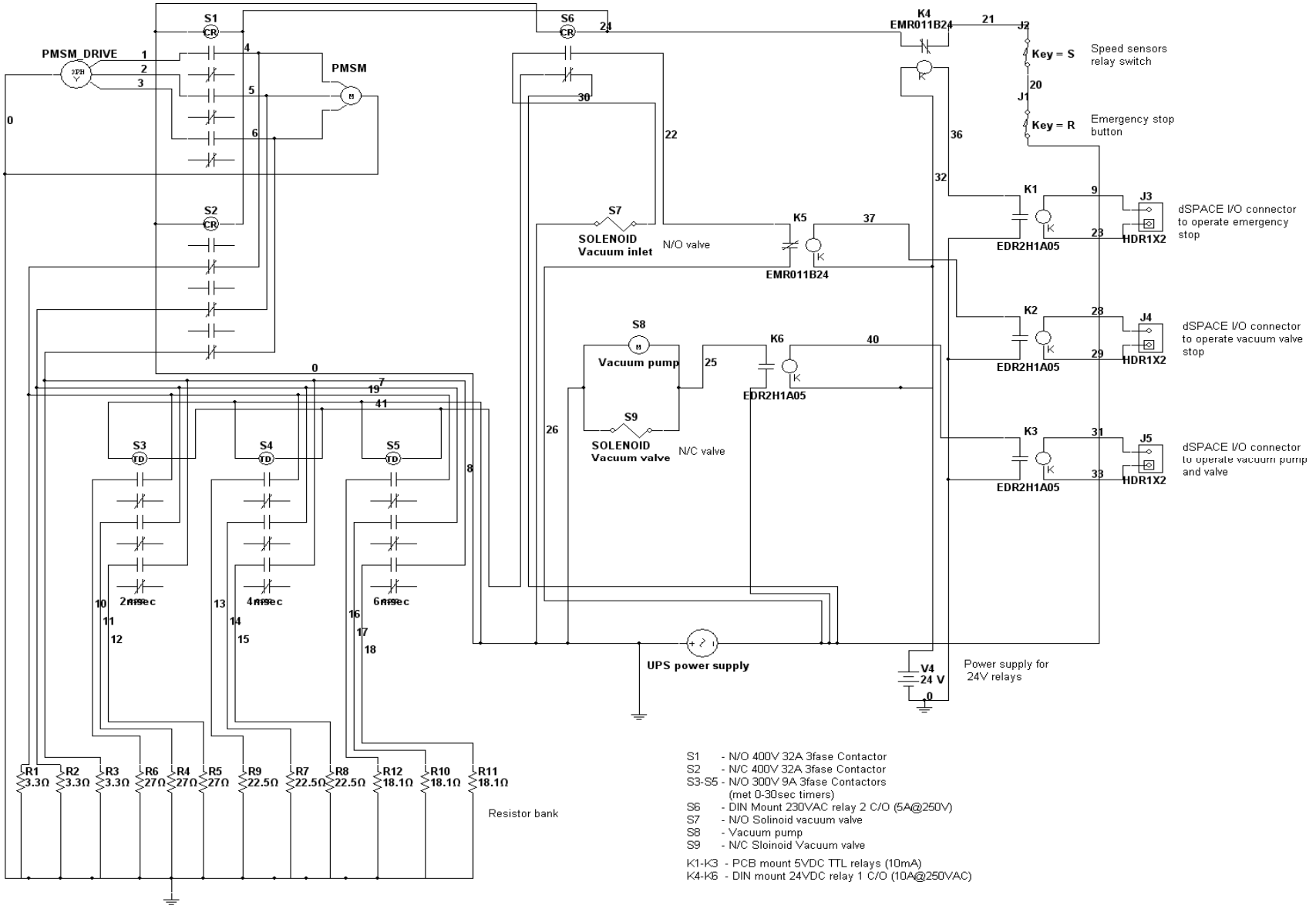


**Figure 4-23: Complete over-speed protection circuit**

## 4.7 Interface board

The purpose of the interface board is to interface all of the various components of the electrical system to the dSPACE® controller. As discussed in previous sections, the electrical system comprises the following components:

- Power amplifiers
- Eddy-current displacement probes
- Resistive temperature detectors (RTDs)
- Pressure transducer
- Infra-red temperature sensor
- Over-speed protection circuit
- Vacuum valves and vacuum pump
- PMSM drive

Figure 4-24 shows a functional block diagram of the interface board and all of the various components it interfaces with the dSPACE® controller.

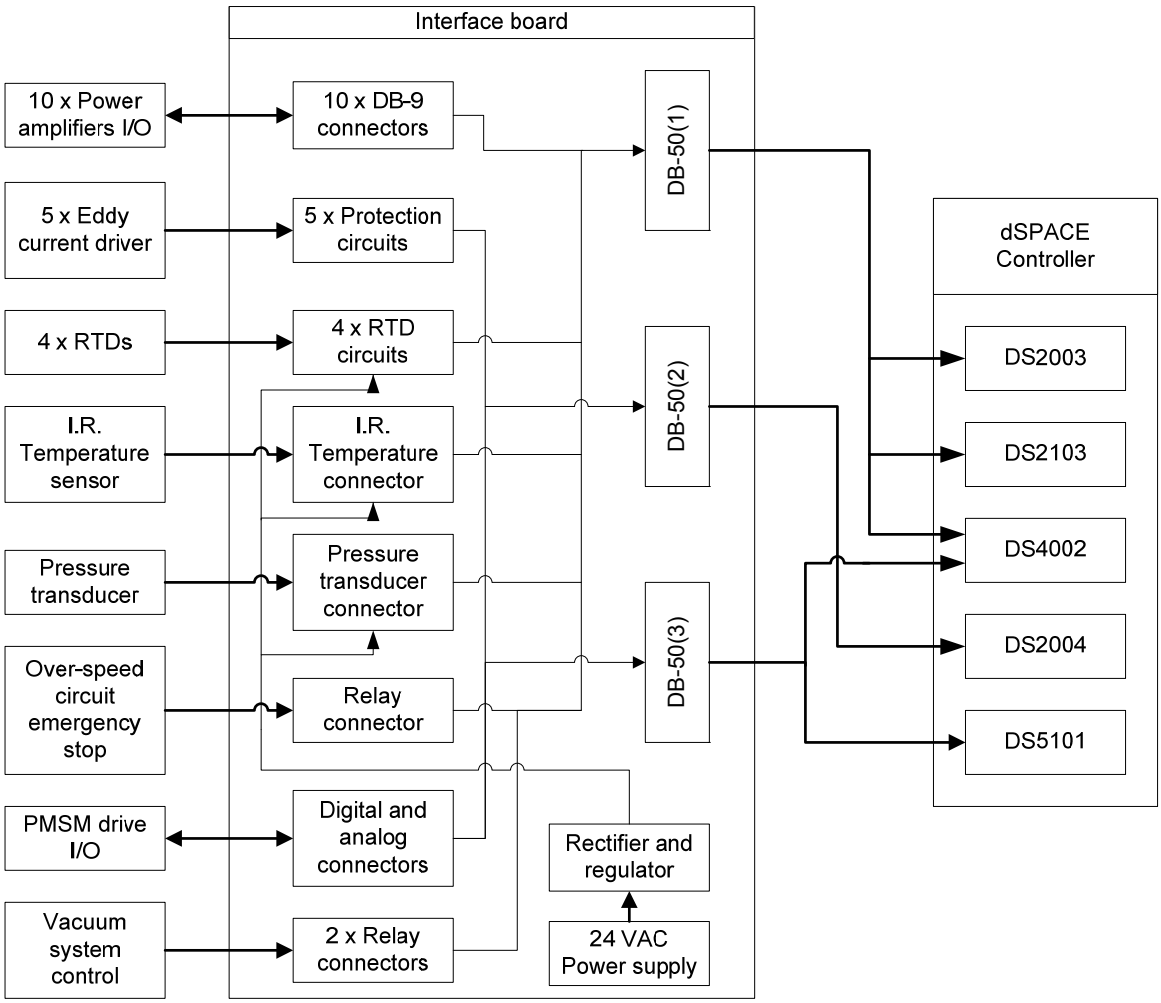


**Figure 4-24: Interface board block diagram**

All of the above mentioned systems have to be interfaced to the dSPACE® system. Three DB-50 plugs connect the interface board with the various dSPACE® boards. DB-50-(1) is the power amplifier plug which runs to the DS2003, DS2103 and DS4002 boards, DB-50-(2) is the analog plug which runs to the DS2004 board and DB-50-(3) is the digital plug which runs to the DS5101 and DS4002 boards.

### *4.7.1 Power amplifiers*

The power amplifiers, which supplies current to the magnetic actuators of the magnetic bearings have several I/O channels which run to the dSPACE® controller.

**Table 4-5: Power amplifier connection to dSPACE®**

| PA Connector Pin | Name | Description | To dSPACE board |
|---|---|---|---|
| 2 | Signal ground | | DS2103 D/A board |
| 4 | +Ref input | Differential analog signal input; ±10 V | DS2103 D/A board |
| 5 | -Ref input | | DS2103 D/A board |
| 8 | Current monitor | Signal is proportional to the current in the power leads. Scaling of 0.5 V/A. | DS2003 A/D board |
| 14 | Fault output | TTL compatible output. It becomes high during output short-circuit, over-voltage and over-heating. | DS4002 I/O board |

Table 4-5 lists the connection from the power amplifiers to the dSPACE® controller. Pin 2 on the power amplifiers' connector, is the signal ground, which is at the same level as the dSPACE® controllers' ground. Pins 4 and 5 are the differential analog input of the power amplifier and have a range of ± 10 V. These two pins run to the DS2103 D/A board which will control the amount of current delivered by the power amplifier.

Pin 8 on the power amplifiers connector is the current monitor pin. This pin, together with the signal ground (Pin 2) generates an analog signal which is proportional to the actual current running in the output power leads of the power amplifier. The signal is scaled to 0.5 V/A and is fed into the DS2003 A/D board. Pin 14 is a status output of the power amplifier. If there is any faults within the amplifier, including short-circuit, overvoltage and overheating, the pin will generate a voltage output of 5V. This output is fed into the DS4002 I/O board.

The interface board has ten DB-9 plugs to which the power amplifiers connect. The various signals are routed to the DB-50-(1) plug on the interface board from where cables run to the dSPACE® boards.

### 4.7.2 Eddy-current displacement probes

The eddy –current probes operate on -24 V which is supplied by an isolated power supply housed inside the electrical enclosure. The output signal of the eddy-probe driver is 0 to -24 V which is fed through the protection circuit discussed in section 4.5.1. The protection circuit clamps the -24 V signal to -10 V in order for the DS2004 high-speed A/D board to be able to measure the signal. The DS2004 only has a measuring range of ± 10 V. There are five of these protection circuits implemented on the interface board, one for each of the eddy current sensors. The output of the eddy probe driver plugs directly into the interface board and the output signals are routed to the DB-50-(2) plug on the interface board from where cables run to the dSPACE® boards.

### 4.7.3 Resistive temperature detectors (RTDs)

As discussed in section 4.5.2, the RTDs need an analog amplifier circuit in order for them to generate an output voltage signal at a certain temperature. The analog amplifier however needs its own 5 VDC power supply to power the operational amplifiers as well as to establish a voltage drop across the RTDs. The isolated 24 VAC power supply discussed in section 4.6 which powers the 24 V relays, also powers the RTD analog circuits. The 24 VAC runs to the interface board where it is rectified and regulated to give a 5 V output to the RTDs analog amplifiers.

There are 4 RTDs in the system, one RTD on each of the two radial AMBs, one RTD on the axial AMB and one RTD on the PMSM winding. Thus, four analog amplifier circuits were implemented on the interface board. The RTDs plug directly into the interface board and the outputs of the analog amplifiers are routed to the DB-50-(1) plug on the interface board which in turn run to the DS2003 multiplexed A/D board.

### 4.7.4 Pressure transducer

The pressure transducer discussed in section 4.5.3 reads the pressure inside the mechanical enclosure and relates this pressure to a voltage. The pressure transducer however needs a power supply of 20 – 35 V. The pressure transducer is also powered by the isolated 24 VAC power supply. As mentioned above the 24 VAC power supply runs to the interface board and is rectified. The pressure transducer plugs into the interface board and is supplied with the 24 V which runs from the isolated 24 VAC power supply and is rectified on the interface board. The pressure transducer output signal is routed to the DB-50-(1) connector. The output signal of the pressure transducer is read by the DS2003 multiplexed A/D board.

### 4.7.5 Infra-red temperature sensor

As discussed in section 4.5.4, the infra-red temperature sensor measures the temperature on the rotor close to the PMSM's magnets. The infra-red sensor also needs a 24 V power supply and get its power from the rectified 24 VAC power supply mentioned above.

The infra-red temperature sensor also plugs directly into the interface board where it is supplied with power and the output signal is routed to the DB-50-(1) plug. The output of the infra-red sensor is read by the DS2003 multiplexed A/D board.

### 4.7.6 Over-speed protection circuit

The over-speed protection is only interfaced to the dSPACE® controller by the three TTL reed relays discussed in section 4.6. Reed relay number one is used as an emergency stop of the Fly-UPS system. Reed relay number two is used to control the normally open vacuum valve on the mechanical enclosure, and reed relay number three is used to control the normally closed vacuum valve together with the vacuum pump.

These relays are implemented on the interface board. The coils of the relays are routed to the DB-50-(3) plug from where a cable runs to the DS4002 I/O board. The 24 V relays in the over-speed protection circuit plugs into the contacts of the relays on the interface board. The interface to the reed relays is illustrated in Figure 4-23.

### 4.7.7 Interface board implementation

The interface board's circuit diagram was drawn up integrating the above mentioned sub-systems into one PCB. A detailed circuit diagram can be on the data CD in Appendix D. Figure 4-25 shows the completed circuit board. The circuit board connects the power amplifiers, the eddy current probes, the four RTDs, the infra-red temperature sensor, the pressure transducer, the over-speed protection circuit and the motor drive to the dSPACE® controller via the three DB-50 connectors on the board. The board is also supplied with 24 VAC as shown, to power the RTD analog amplifiers, the pressure transducer and the infra-red temperature sensor.

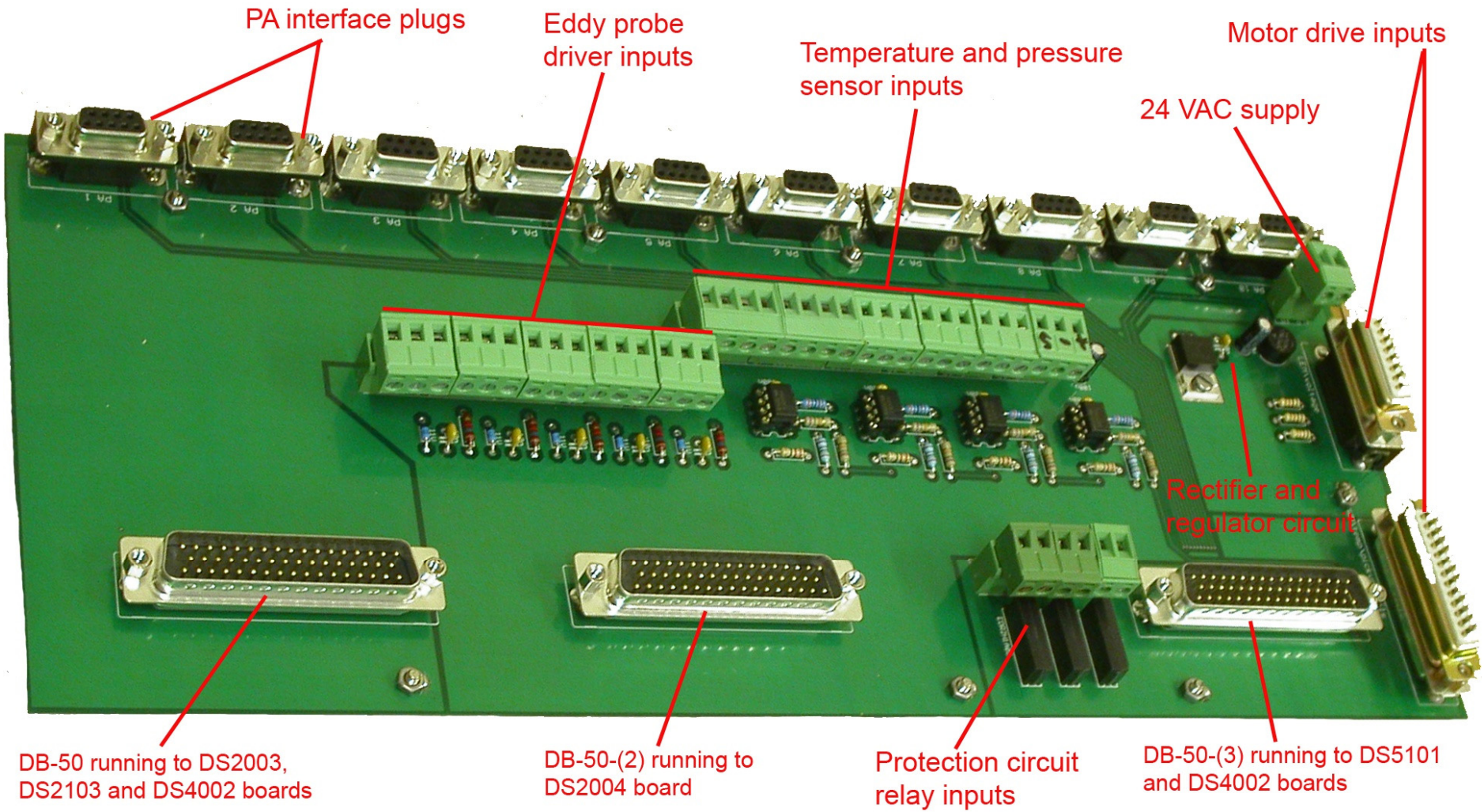


**Figure 4-25: Interface board**

## 4.8 Electrical enclosure implementation

Finally the electrical enclosure design was done. All of the electrical systems discussed in sections 4.4 to 4.7 were incorporated into one electrical enclosure. The dimensions of the enclosure were determined by the actual size of the various components. The depth of the enclosure was mainly determined by the dSPACE® controller. The height and width of the enclosure were determined by the dimensions of the resistor bank, the over-speed circuit assembly, the drive and the power amplifier assembly. After all the dimensions of the separate systems were considered and a preliminary layout of the enclosure was done the dimensions on the electrical enclosure was determined and a 1000 x 800 x 400 mm IP55 electrical enclosure was sourced.

### *4.8.1 Power amplifier assembly*

As discussed in section 4.4, all ten of the power amplifiers were mounted on one heat sink with dimension 450 x 150 x 40 mm. The power amplifier assembly was mounted as close as possible to the interface board and the dSPACE® controller. This was done to cut back on noise caused by the high switching frequencies of the power amplifiers (36 kHz) and the high voltage and high switching frequency of the motor drive (50 kHz). Figure 4-26 shows the PA assembly as well as the power supply of the power amplifiers.

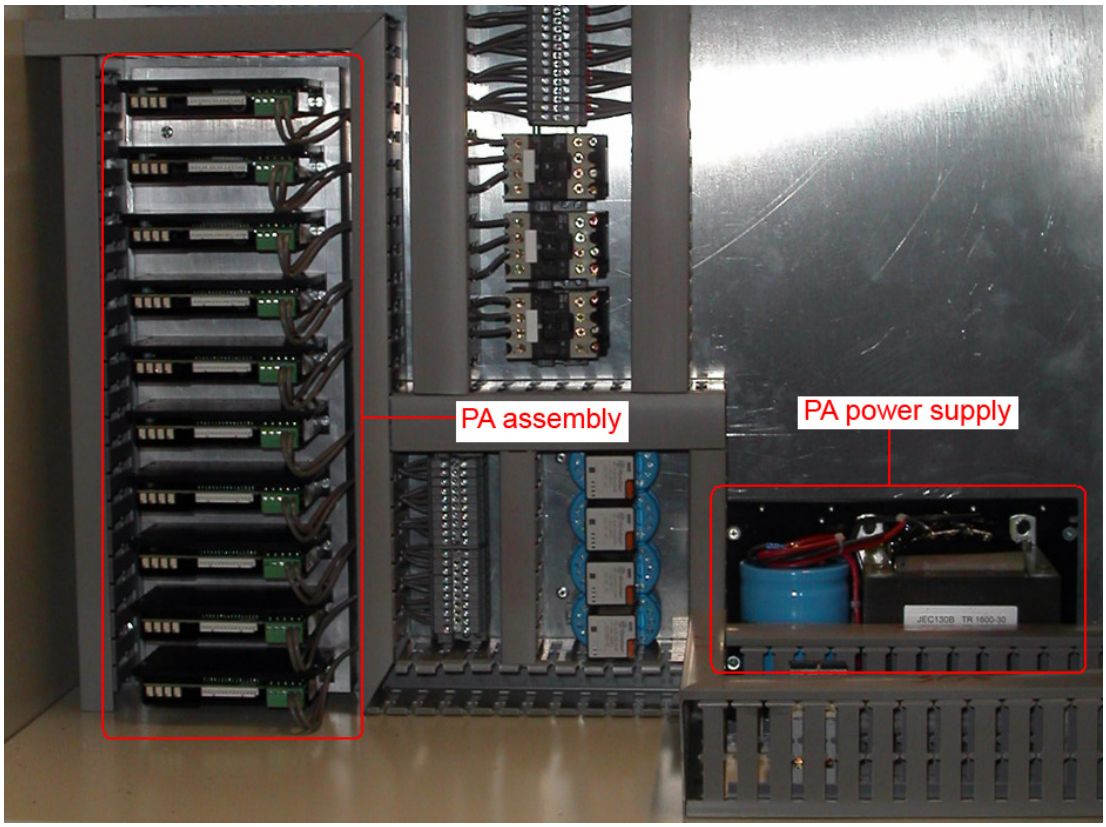


**Figure 4-26: Power amplifier assembly**

The power amplifiers also had to be cooled in order to keep the heat sink cool. This was done by cutting two holes in the electrical enclosure directly beneath the power amplifiers' heat sink. One hole was cut at the bottom part of the heat sink and one hole was cut at the top part of the heat sink assembly. An AC fan was mounted at the back of the enclosure on the bottom hole which blows air into the fins of the heat sink while the upper hole acts as a vent, allowing the hot air to pass through to the outside of the enclosure.

The power supply shown in Figure 4-26 is connected to the main 220 V power terminal, and the negative side of the rectified 60 VDC output is grounded to the chassis. The terminal block situated to the right bottom of the PA assembly is the connection between the power amplifiers and the power supply. 2.5 $mm^2$ panel wire was used to connect the power supply to the terminal block as well as connecting the PAs to the terminal block. The cable which was chosen to run from the power amplifiers to the AMBs is 1.5 $mm^2$, shielded twisted pair instrument cable. The shielding of the instrument cable is connected to the heat sink assembly. The signal cable which runs from the power amplifiers to the interface board is 6-core, 0.5 $mm^2$ shielded cable and is connected to the interface board via a DB-9 connecter. The shielding of the signal cable is connected to the ground plane of the interface board.

### *4.8.2 Eddy probe drivers*

The eddy probe system that was sourced from SKF has DIN rail mountable drivers as well as a DIN rail mountable power supply. The eddy probe drivers had to be mounted as close as possible to the interface board and the dSPACE® controller in order to cut back on the noise caused by the high switching frequency on the power amplifiers and the motor drive. A metal shielding plate was also constructed and installed in the enclosure to act as a shield between the high voltage components and the low voltage, sensitive equipment in the enclosure.

Figure 4-27 shows the eddy drivers mounted on the G-type DIN rail mounted in the lower left side of the enclosure as well as the power supply of the eddy probe drivers mounted on a separate G-type DIN rail. Figure 4-27 also shows the metal shielding plate that was mounted horizontally in the electrical enclosure. The flex glands in the side of the enclosure can also be seen. These glands are where the eddy probe' cables runs through the enclosure from the outside to the inside of the enclosure where they are connected to the eddy drivers.

The eddy drivers' power supply can also be seen together with its terminal block which connects the eddy drivers to the power supply. The power supply is supplied with 220 VAC from the main power terminal and the +24 V output of the power supply was grounded to the chassis in order for it to supply the drivers with 0 to -24 V.

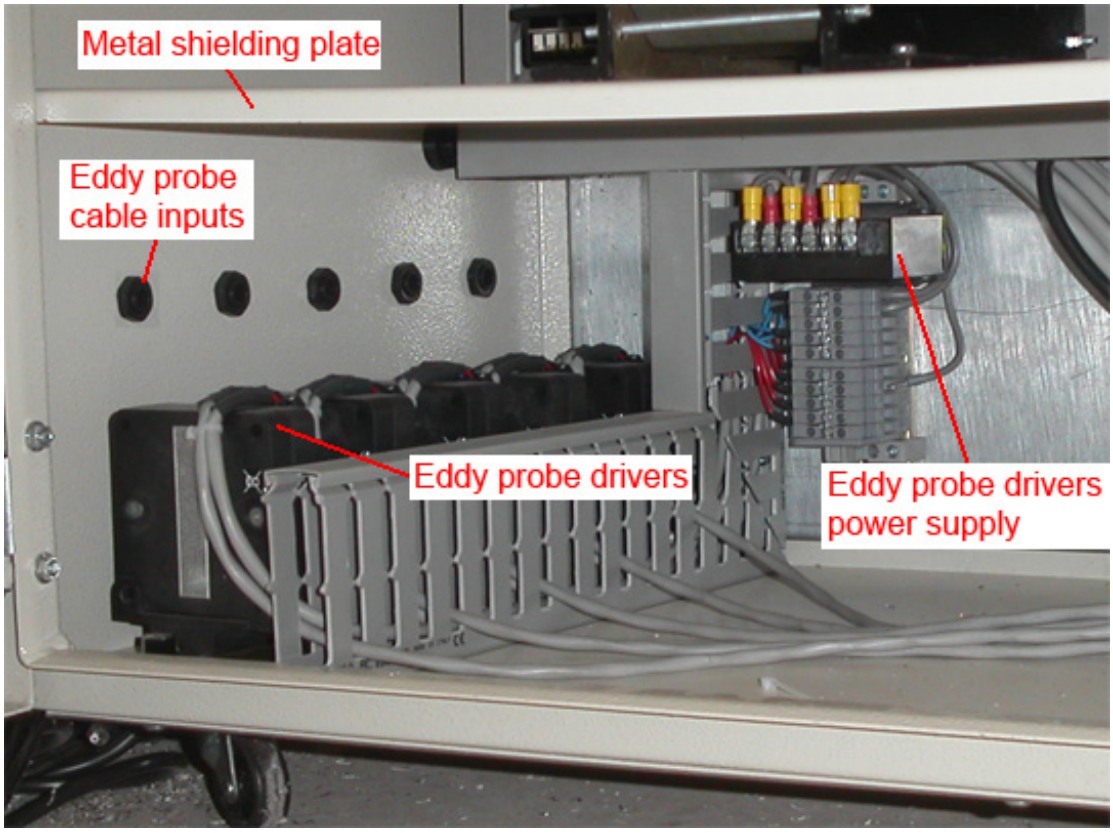


**Figure 4-27: Eddy probe drivers assembly**

The signal cables used to connect the eddy drivers to the interface board is 2-core, 0.5 $mm^2$ shielded cable and is connected to the interface board via a plug-in terminal. The shielding of the signal cable is grounded on the interface board's ground plane (which is connected to the chassis).

### *4.8.3 Over-speed protection circuit*

All of the components that were sourced for the over-speed protection circuit are T-type DIN rail mountable. All five contactors as well as the necessary terminals were mounted on one DIN rail as can be seen in Figure 4-28. The protection circuit was mounted in the top part of the electrical enclosure close to the motor drive to ensure that the PMSM's high voltage supply cable is kept as short as possible inside the enclosure. The top contactor connects the motor drive to the PMSM. The top terminal block connects the PMSM to the second contactor which is connected to the first stage of the resistor bank. The second terminal block is used to connect

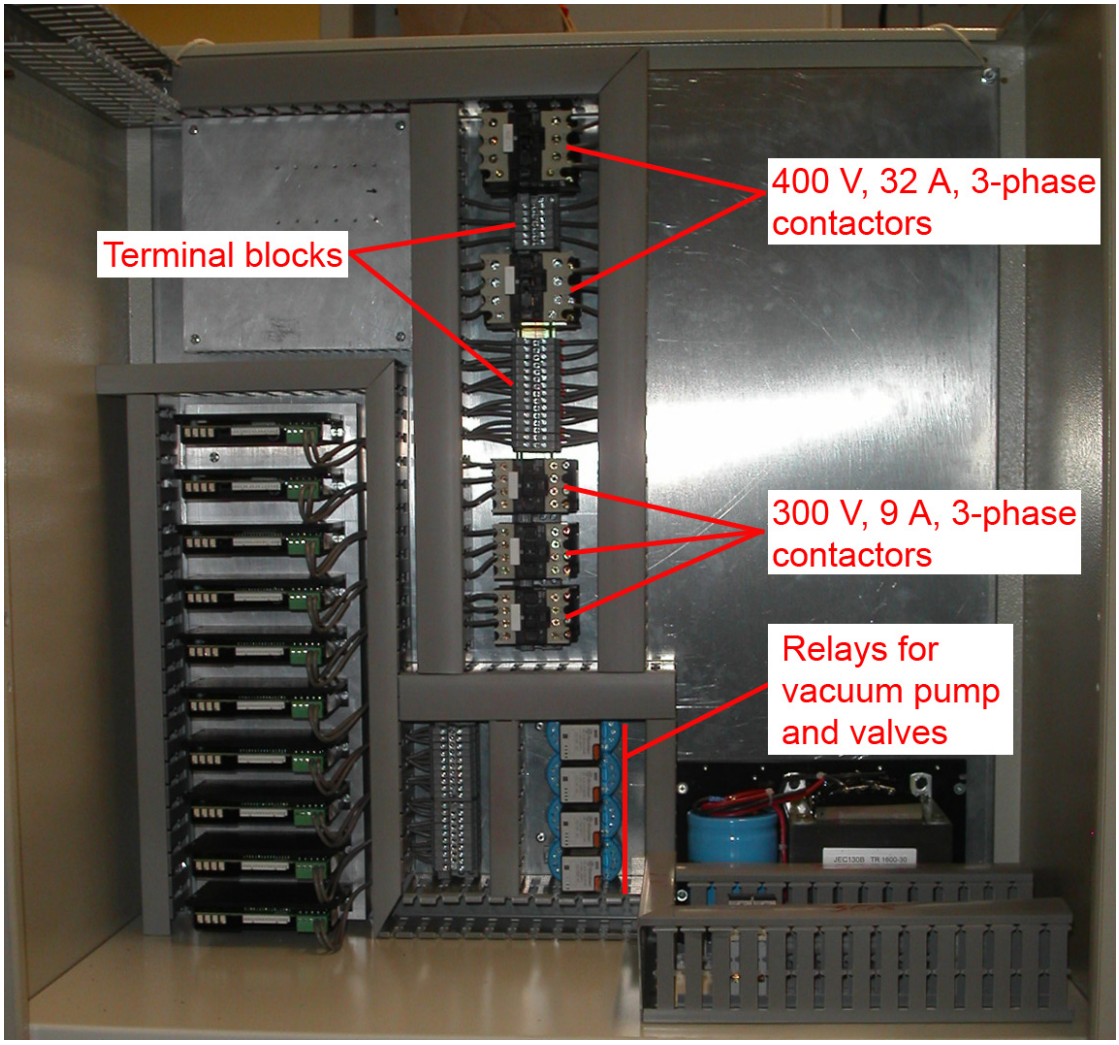


**Figure 4-28: Over-speed protection assembly**

all of the remaining three contactors in parallel to the first stage of the resistor bank. The last three contactors are connected to the resistor bank's 2nd, 3rd and 4th stage respectively.

The relays are also mounted on a T-type DIN rail and is supplied with 24 VAC from the isolated power supply mounted on the main power terminal. Each of the contactors is supplied with 220 VAC, as discussed in section 4.6, from the main power terminal. All the connections between the contactors, relays, terminals, resistor bank stages and power supplies were made using 2.5 $mm^2$ panel wire which is capable of handling 25 A of current. The connecting wires as well as the PMSM supply cable were routed inside the grey trunking in order to give a professional look to the enclosure.

### *4.8.4 Resistor bank*

The resistor bank was implemented by designing a metal enclosure to house the 12 resistors which make up the resistor bank. Each of the resistors was mounted inside the metal enclosure using a

bracket to space the resistors evenly in layers on top of each other. The resistors were wired taking special care not to let the panel wire touch the resistors. When 527 kJ of energy is dissipated inside the resistor bank, the heat may cause the isolation of the panel wire to melt when the wire touches the resistors. Figure 4-29 shows the inside of the resistor bank where it is mounted next to the over-speed protection circuit and connected to the various contactors.


**Figure 4-29: Resistor bank assembly**

The resistor bank also had to be cooled, so a hole was cut in the bottom part of the metal resistor bank enclosure and at the back of the electrical enclosure. Two vents were also cut in the top of the resistor bank's enclosure. An AC fan was mounted at the back of the electrical enclosure forcing air into the resistor bank and blowing the warm air out the top of the resistor bank through the two vents.

### 4.8.5 PMSM drive

The motor drive also had to be installed in the electrical enclosure. The PCB of the motor drive was mounted on a 200 x 200 x 40 mm finned aluminium heat sink. Since the drive assembly also needed a fan to cool its heat sink, a hole was cut in the electrical enclosure directly beneath the mounted motor drive. An AC fan was installed which blows air into the fins of the motor drives heat sink and forces the warm air out the top of the enclosure.

An LC-filter was installed between the drive and the PMSM in order to reduce the voltage ripple on the output of the drive. A metal enclosure was designed to house the LC-filter with its own dedicated AC fan to cool the filter. Figure 4-30 shows the motor drive mounted in the top left corner of the electrical enclosure as well as the LC-filter mounted next to the motor drive.

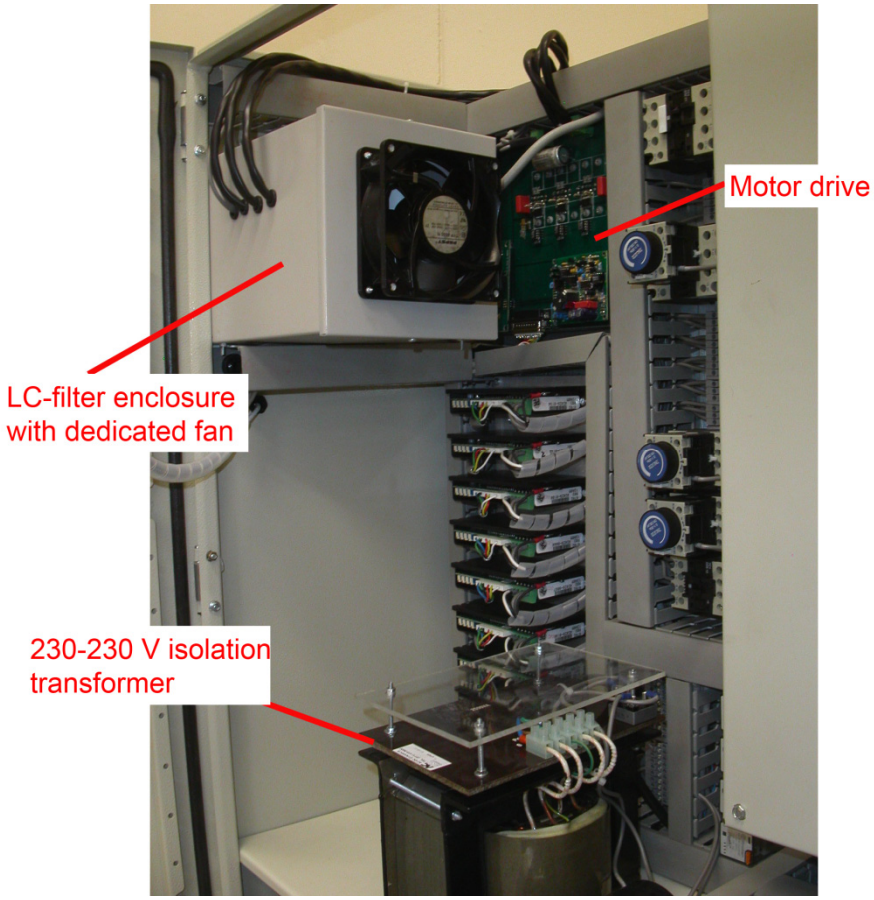


**Figure 4-30: PMSM drive assembly**

The motor drive also needed a 230-230 V isolation transformer to power the 2 kW PMSM. A 2.5 kVA, 230 -230 V transformer was sourced and installed in the electrical enclosure. The transformer is supplied with 220 VAC from the main power terminal. The output of the transformer was rectified and a 4700 µF capacitor was installed to reduce the voltage ripple of the 310 VDC output to the motor drive.

The motor drive has to be connected to the dSPACE® controller since the motor speed control is implemented on the dSPACE® system. The dSPACE® controller supplies the motor drive with PWM signals and measures the various voltages and currents within the motor drive. The motor drive is connected to the interface board via two 25 core, 0.5 $mm^2$ shielded cables and the shielding of the cables is grounded to the interface board's ground plane. The drive is connected to the isolated power supply by 2.5 $mm^2$ panel wire, and the drive is connected to the PMSM by an 8 core, 3 $mm^2$ shielded cable to shield the components from the high switching frequencies of the drive.

### *4.8.6 Speed sensor*

The external speed sensor, which forms part of the over-speed protection circuit, is mounted in the door of the electrical enclosure as shown in Figure 4-31.

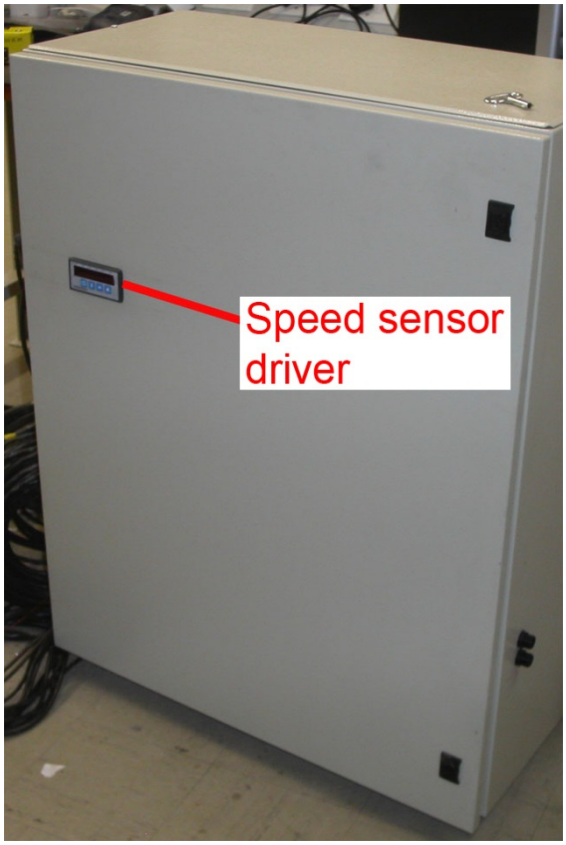


**Figure 4-31: Speed sensor installation**

The speed sensor is supplied with 220 VAC from the main power terminal using 2.5 $mm^2$ panel wire. The relay of the speed sensor, which switches when a predetermined threshold is reached, is connected to the over-speed protection circuit as discussed in section 4.6. The speed sensor's probe runs from the mechanical enclosure, through a flex-gland in the side of the enclosure into the speed sensor driver.

### 4.8.7 dSPACE® controller and interface board

The dSPACE® controller is mounted in the lower right-hand side of the enclosure and the interface board is mounted next to the dSPACE® controller in order to keep the signal cables as short as possible. The dSPACE® controller is supplied by 220 VAC from the main terminal block by a 3-core, 1 $mm^2$ power cable. The interface board is connected to the various dSPACE® boards via three DB-50 connectors on the interface board as discussed in section 4.7. Figure 4-32 shows the dSPACE® controller connected to the interface board as well as all the external devices connected to the interface board including the power amplifiers, eddy probe drivers, RTDs, pressure transducer, IR temperature sensor, vacuum system and the motor drive.

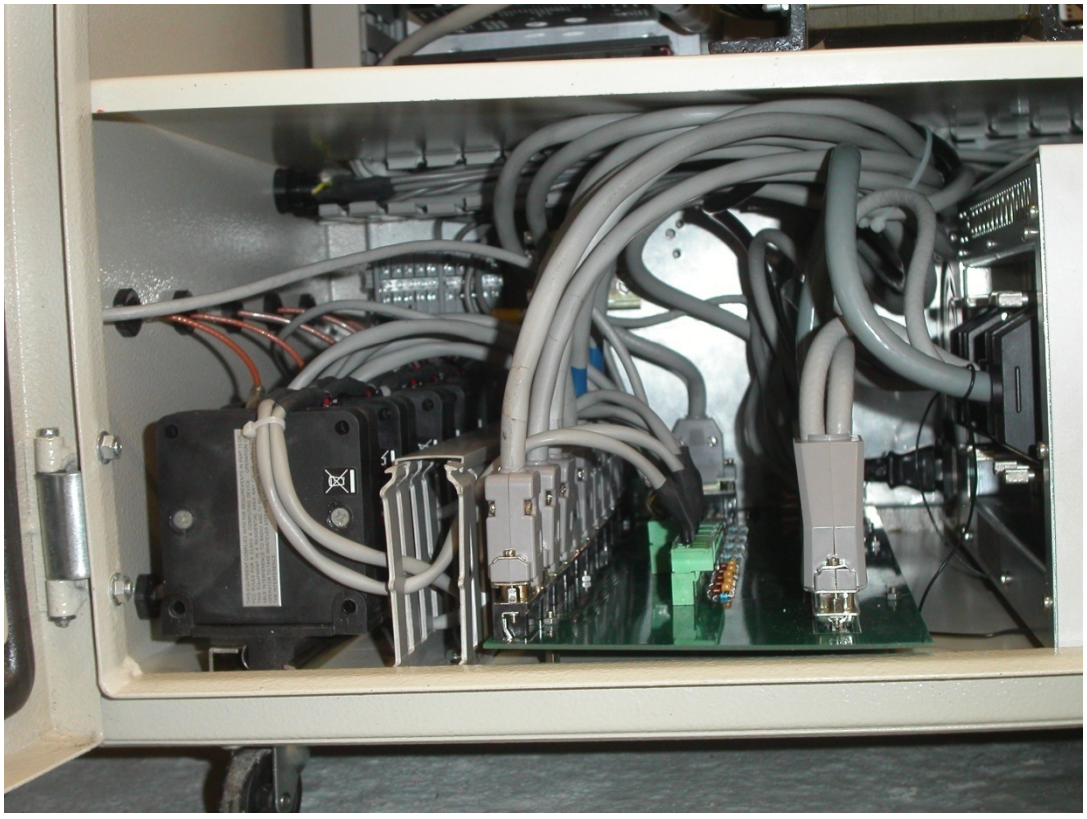

**Figure 4-32: dSPACE® connected to the interface board**

### 4.8.8 Main power terminal

The main power terminal is where the main supply of the system is situated. The main power terminal is divided into two sections: the one section is power from 220 V mains supply and the second section is powered from a 220 V, 3 kVA UPS. The reason why one section of the system runs from a UPS is a safety reason. In case of a power failure, the controller, the eddy current displacement sensors and the power amplifiers will shut down and the rotor/flywheel will fall onto its backup bearings which may cause serious damage to the rotor/flywheel. The over-speed protection

circuit is also supplied from the UPS to ensure that the rotor/flywheel can safely be stopped. The second section of the main power terminal which is supplied by 220 V mains power is the motor drive. The motor drive is not a critical system in terms of system safety. In case of a power failure the motor drive will merely stop supplying the PMSM with power and the rotor/flywheel will start to spin down. Figure 4-33 shows the main power terminal indicating the 24 VAC power supply and the two sections of the power supply system.

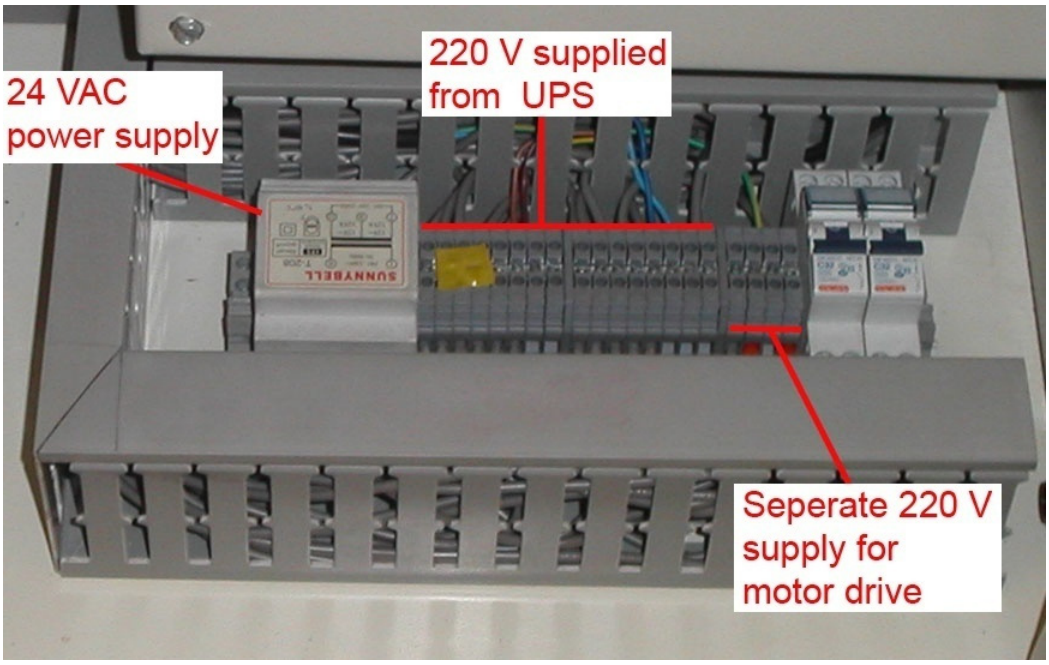


**Figure 4-33: Main power terminal**

### *4.8.9 Final electrical control enclosure*

All of the above mentioned sub-systems is incorporated into the 1000 x 800 x 400 mm electrical enclosure and is shown in Figure 4-34. The motor drive can be seen mounted behind the LC-filter as well as the power supply for the drive. The protection circuit is mounted in the middle of the enclosure next to the resistor bank. The speed sensor is mounted in the door of the enclosure. The PA assembly and its power supply can be seen mounted next to the main power terminal. In the bottom section of the enclosure the eddy drivers and the interface board can be seen as well as the dSPACE® controller.

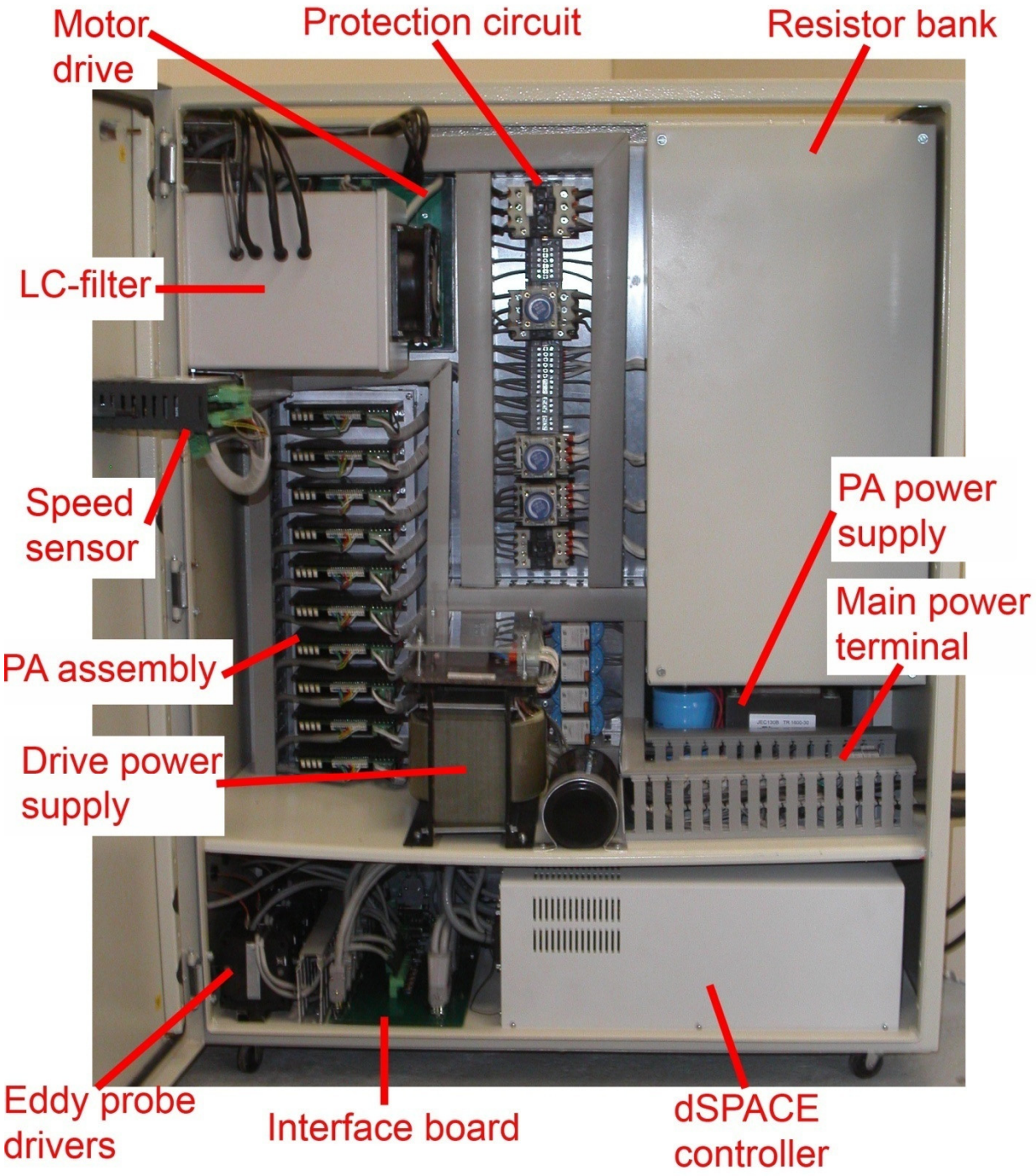


**Figure 4-34: Final electrical control enclosure**

Chapter 4 discussed the design process involved in developing an electrical control enclosure for a fully suspended AMB system. Detailed sub-system designs are also included. The implementation of the various sub-systems and the installation of these sub-systems into the electrical control enclosure are discussed. The detailed controller model design as well as the Graphical User Interface (GUI) of the Fly-UPS system is discussed in chapter 5.

# 5
# Chapter

# Graphical User Interface (GUI)

*Chapter 5 contains a detailed description of the* Simulink® *model of the controller of the Fly-UPS system as well as the layout of the Graphical User Interface (GUI) which was implemented in order to control the Fly-UPS system.*

## 5.1 Introduction

As discussed in chapter 2 a digital controller is used for the Fly-UPS system. The controller consists of a dedicated processor board, a high-speed A/D converter board, a multiplexed A/D converter board, a digital waveform board, two digital I/O boards and two D/A converter boards.

A simple PD-controller is used to control the rotor/flywheel in its reference position since current controlled power amplifiers are used. The controller is simplified more due to the fact that the magnetic circuit does not make use of flux splitting as discussed in section 3.2.1. This implies that the x- and y-axis of the rotor/flywheel can be controlled independently in each radial AMB. The axial AMB is also controlled independently. The control parameters obtained from the MATLAB® simulation model in chapter 3 are implemented in a Simulink® model of the system.

Figure 5-1 shows the functions of the GUI. The GUI will enable the operator of the system to:

- Control the AMBs. The proportional-, differential- and integral gains as well as the bias current levels of the AMBs will be adjustable in real-time.
- Monitor the Fly-UPS system:
    - The temperatures of the three AMBs' coils will be displayed within the GUI as well as the temperature of the PMSM windings.
    - The temperature of the rotor/flywheel will be displayed along with the rotational speed of the rotor/flywheel.
    - The pressure inside the mechanical enclosure will also be displayed.
- Control the vacuum system. The vacuum valves as well as the vacuum pump will be controllable from within the GUI.

- Control and monitor the PMSM drive. The GUI will allow the operator to adjust the rotational speed of the rotor/flywheel and will display the current- and voltage levels of the PMSM drive.
- Stop the rotor/flywheel. An emergency stop function in the GUI will enable the operator to stop the rotor/flywheel in case of an emergency.

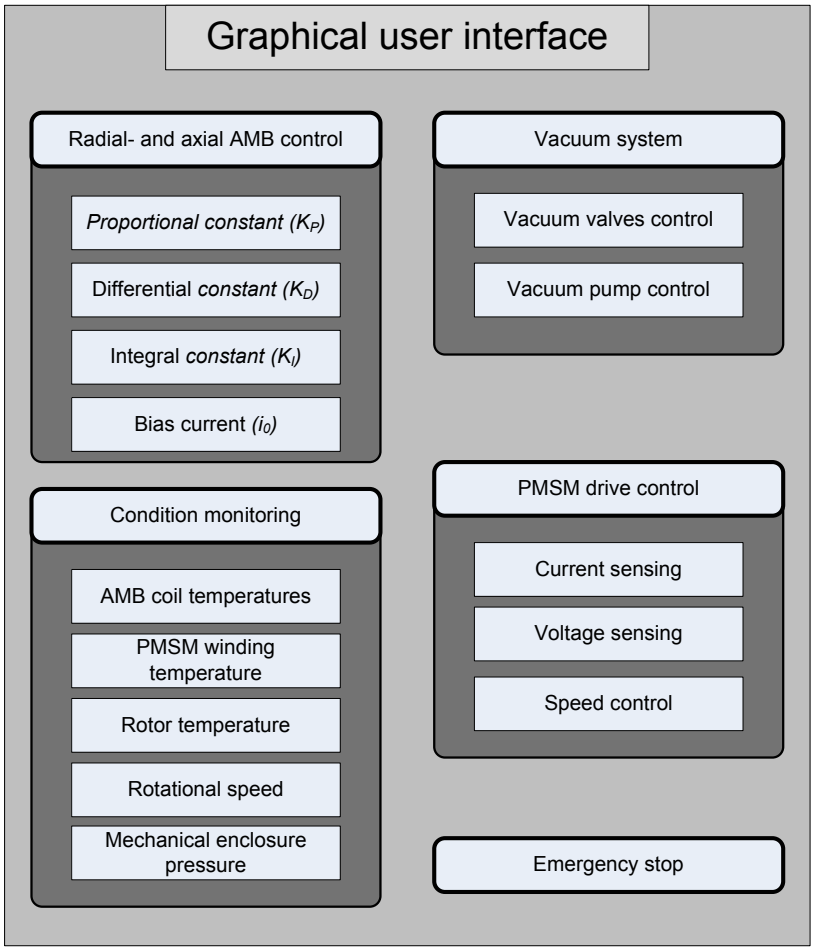


**Figure 5-1: GUI functions**

## 5.2 Simulink® model

### *5.2.1 Radial AMBs*

Since the x- and y-axis of each radial magnetic bearing is controlled separately, a single PD-controller is implemented on each axis of each of the two radial AMBs. From the vertical orientation of the rotor/flywheel it is assumed that the control of all four axes of the radial AMBs is identical. Figure 5-2 shows the Simulink® model of the control for a single axis of the lower radial AMB. An eddy probe measures the displacement of the rotor which produces and analog voltage signal. This signal is converted into a 16-bit digital value by the analog-to-digital (ADC) shown in the

left side of Figure 5-2. The DS2004 high-speed ADC board converts a voltage of 10 V to a digital floating point value representing 1.

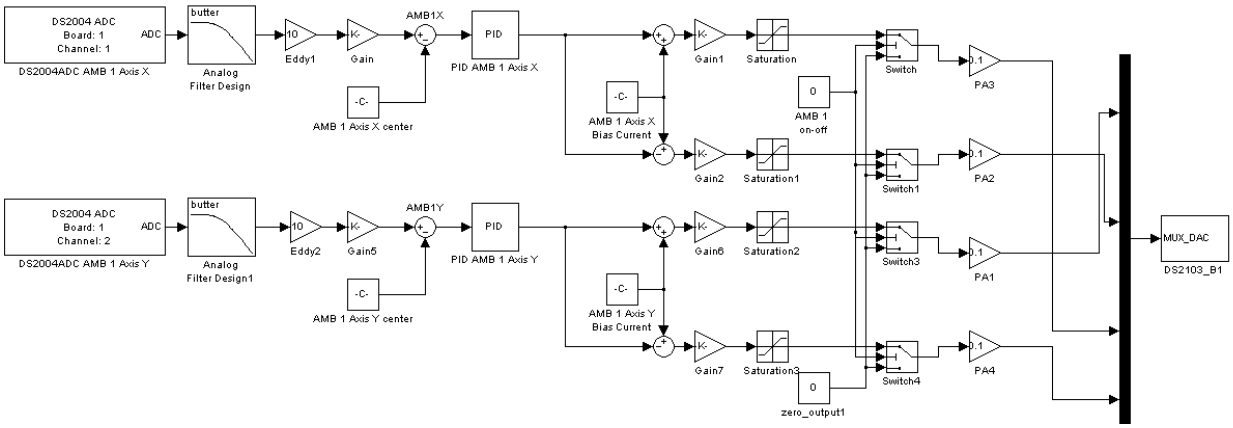


**Figure 5-2: Simulink® model of the controller of one radial AMB**

The ADCs of the active magnetic bearings (which process the position signal of the eddy probes) operate at a sampling rate of 10 kHz and an anti-aliasing filter is employed as discussed in section 4.5.1. As mentioned in chapter 4, the eddy probe drivers operate in a noisy environment, close to the switching power amplifiers and the motor drive. The output signal of the ADC runs into a digital 2.5 kHz low pass filter in order to filter out the high frequency components of the position signal. The sensor's sensitivity of 7.87 mV/µm is attenuated by a factor 10 due to the ADC's conversion of a 10 V signal to a digital floating point value representing 1. To correct this conversion a scaling factor of 10 (Eddy1 and Eddy2 in Figure 5-2) is applied to the position signal to give a proportional voltage output to the displacement of the rotor/flywheel. A further scaling factor (Gain and Gain5 in Figure 5-2) which converts the input to meters is obtained using (5-1).

$$Sensitivity = \frac{7.87\times10^{-3}}{1\times10^{-6}} \ \text{V}/\text{m} \qquad \textbf{(5-1)}$$

$$\Delta x = \frac{1\times10^{-6}}{7.87\times10^{-3}}\Delta v \ \text{[m]}$$

$$= 127.1\times10^{-6}\cdot\Delta v \ \text{[m]}$$

The centre position reference is subtracted from the position signal in order to obtain the error signal which is sent to the digital PD-controller. The PD-controller generates a control current reference signal which is added to the bias current signal of the one power amplifier and is subtracted from the bias current signal of the other power amplifier. This then generates the current reference signal for each PA. The current reference signal is then scaled to match the sensitivity of the power amplifiers of 0.7143 V/A (Gain1, Gain2, Gain6 and Gain7 in Figure 5-2). A saturation element is also inserted in order to ensure that the output current reference does not exceed the maximum design current of 5 A as determined in section 3.2.

A switch is implemented in order to force the power amplifier reference current to zero which disables it. The output of the switch is connected to a gain element of 0.1 (PA1, PA2, PA3 and PA4 in Figure 5-2) which decreases the current reference signal by a factor of 10 since the DAC only accepts signals ranging from -1 to 1 which represents a voltage output of -10 V to 10 V. The output of the gain element is connected to the DAC which produces an analog output for each PA. The program cycle time is determined by the complexity of the model and is obtained experimentally. For this specific application a cycle time of 100 µs which relates to a sampling frequency of 10 kHz is implemented.

### *5.2.2 Axial AMB*

Similar to the axes of the radial AMBs, the axial AMB is controlled by one PD-controller. Figure 5-3 shows the Simulink® model of the controller of the axial AMB. The difference between the radial AMB controller and the axial AMB controller is the current gain (Gain 3 in Figure 5-3) which is the current gain due to the asymmetric design of the axial AMB as discussed in section 3.3. The value of this gain is determined as being 6.484 by making use of (3-97). The other difference is the two bias levels of the two actuators. The PD-controller generates a control current reference signal which is added to the bias current signal of the one power amplifier. The current reference signal multiplied by the current gain and is then subtracted from the bias current signal of the other power amplifier. This then generates the current reference signal for each PA.

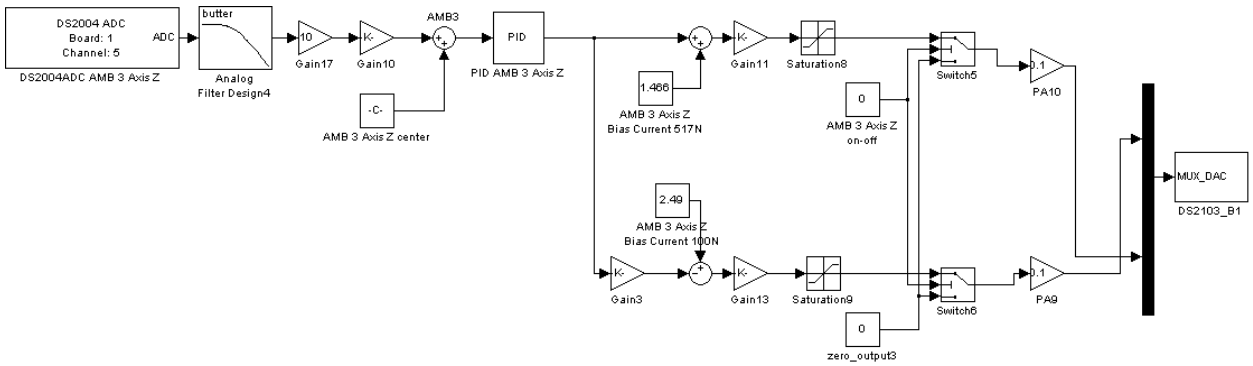


**Figure 5-3: Simulink® model of the controller of the axial AMB**

The current reference signals also run through switches which are used to disable the power amplifiers, thus disabling the AMB.

### *5.2.3 Sensors*

As discussed in chapter 4, the output signals of the various temperature sensing devices are fed into the DS2003 multiplexed ADC. The output signals of the four RTDs, the infra-red temperature sensor and the pressure transducer are filtered by 1 Hz digital low pass filters since the time constant for the

change in pressure and temperature is fairly low. Figure 5-4 shows the sensor adjustment which is done on each of the sensors to calibrate them.

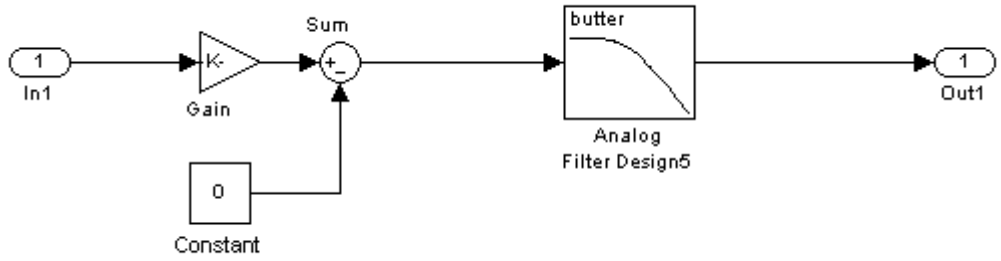


**Figure 5-4: Simulink® model for sensor adjustment and filtering**

Since the output of the sensors is linear, the output of the various sensors can be related to a straight line. The Gain in Figure 5-4 can be related to the gradient of the straight line whereas the constant represents the intersection point of the straight line.

On the left side of Figure 5-5 the calibration blocks of each of the sensors can be seen as well as their connection to the DS2003 ADC board. On the right side of Figure 5-5 the vacuum release switch can be seen, as well as the control for the operation of the vacuum pump. The output of the pressure transducer is also connected to the vacuum pump. This is done to automatically switch on the vacuum pump when the pressure rises to above 0.5 bar. The vacuum pump can also be manually controlled.

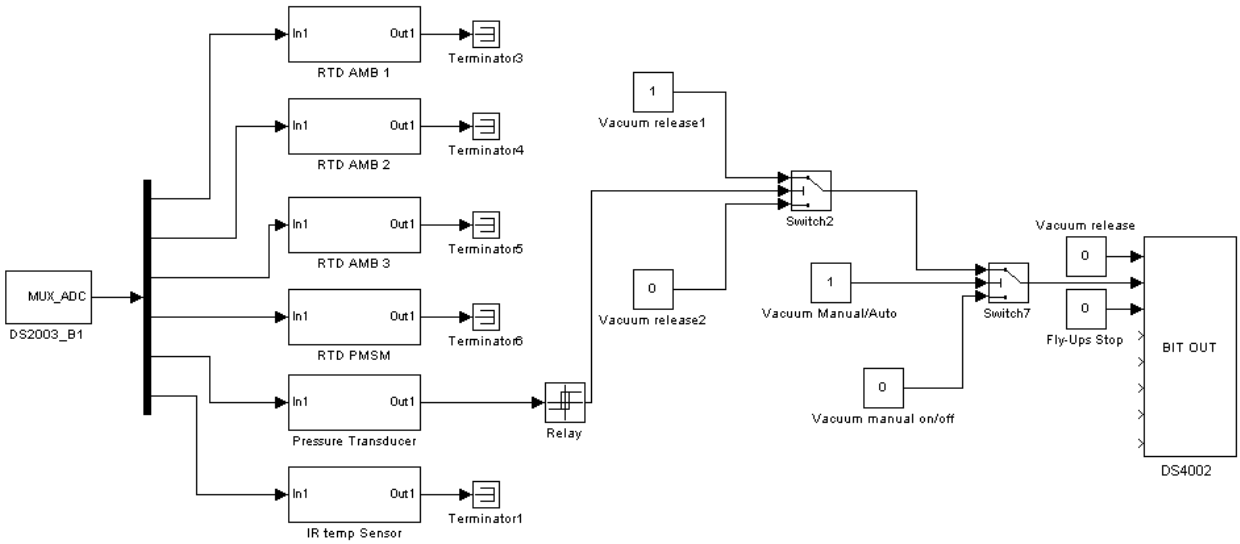


**Figure 5-5: Simulink® model of sensor and vacuum control**

The emergency stop switch for the Fly-UPS system (Fly-Ups stop in Figure 5-5) can also be seen. When the stop is triggered from the GUI, the over-speed protection circuit is activated as discussed in section 4.6.

Figure 5-6 shows the connection of the fault status pins of the power amplifiers to the DS4002 I/O board. This allows the operator of the Fly-UPS to see the status of each of the power amplifiers in the GUI.

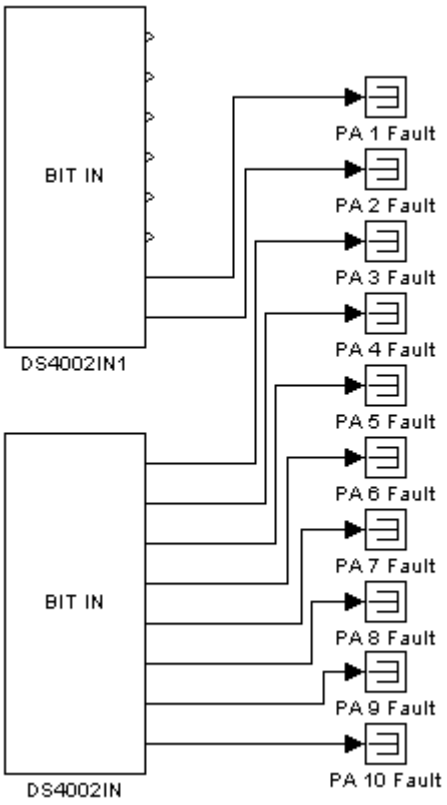


**Figure 5-6: Simulink® model of the PA fault status**

A complete Simulink® model which incorporates all the various functionalities of the system can be found on the data CD in Appendix D.

## 5.3 ControlDesk® GUI

ControlDesk® is the dSPACE® software which provides the user with the ability to control real-world systems via a Graphical User Interface (GUI). It enables the user to monitor and control systems in real-time. ControlDesk® interfaces with Simulink® and enables the user to manipulate variables contained in Simulink® models and to conduct experiments and capture data from the system it controls.

Figure 5-7 shows the GUI which controls the radial AMBs. The lower radial AMBs' control is displayed on the left side. It can be seen that the rotor's position is displayed on an X-Y plot window. The PD-controllers constants can also be seen and can be manipulated in real-time as well as the bias current for each of the axis of the radial AMBs. Each of the AMBs has an on/off switch as well as status displays for each of the power amplifiers.

There is also a temperature display which indicates the temperature of the coils of the AMBs, the temperature of the PMSM windings as well as the temperature of the rotor/flywheel closest to the PMSM. This information is used to safely operate the Fly-UPS system. There is also a large display which indicates the reference rotational speed of the rotor/flywheel.

Figure 5-8 shows the GUI which controls the axial AMB. The PD-controller constants and bias currents are also displayed and can be manipulated in real-time. The rotor/flywheel position in the vertical z-axis is also displayed in the plot window. The temperature of the top axial actuator is also displayed.

On the right side of Figure 5-8 the vacuum controls can be seen. From this area the vacuum valves and the vacuum pump can be operated. There is also a display which shows the pressure inside the mechanical vacuum enclosure. The pump can be set to work automatically, switching on when the pressure inside the mechanical vacuum enclosure rises above a certain threshold or it can be operated manually. One of the emergency stops of the Fly-UPS system can also be seen on the right side of Figure 5-8. When this emergency stop is triggered the system enables the over-speed protection circuit as discussed in section 4.6.

Every aspect of the Fly-UPS system can be controlled from these GUIs. Each of the GUIs is displayed on a separate screen of the control PC making monitoring and control of the Fly-UPS system that much easier and fool proof.

Figure 5-9 shows the control computer running the Simulink GUI. The GUI is displayed on two LCD screens and is controlled via a mouse and keyboard. The red emergency stop button can also be seen next to the control computer within reach of the operator.

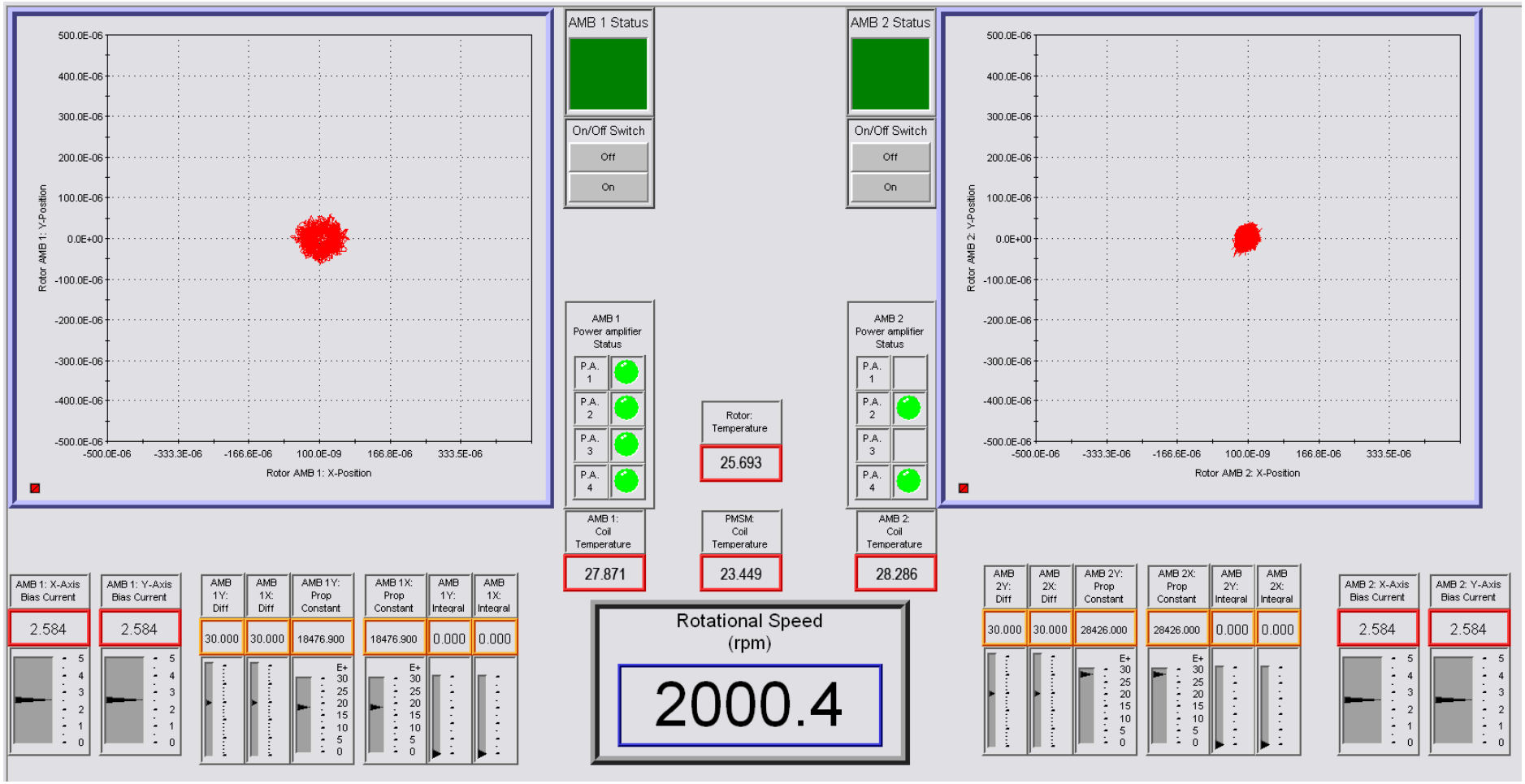


**Figure 5-7: ControlDesk GUI for radial AMBs**

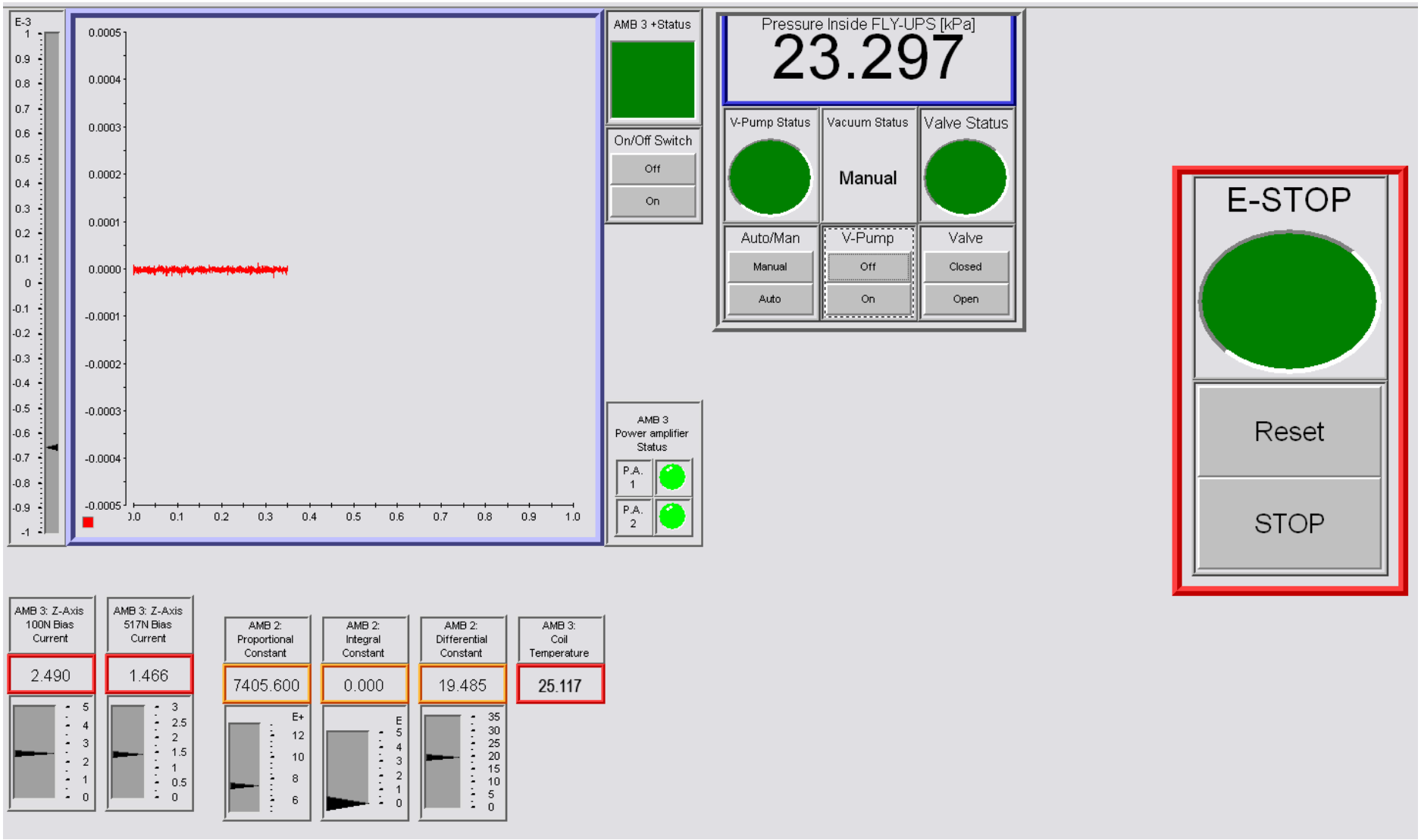


**Figure 5-8: ControlDesk GUI for axial AMB, vacuum system and emergency stop**


**Figure 5-9: Control PC running the Simulink® GUI**

*Chapter 5 discusses the Simulink® model of the controller of the Fly-UPS system. The layout of the Graphical User Interface (GUI) which is used to control the various sub-systems of the Fly-UPS system is also discussed. The system will now be characterised in Chapter 6.*

# 6
# Chapter
# System characterisation

*Chapter 6 starts off with a verification of the system's stiffness and damping characteristics by making use of a step response on each of the AMBs. This is followed by a verification of the sensitivity of the three magnetic bearings in accordance to the ISO CD 14839-3 standard on stability margins of AMBs.*

## 6.1 Introduction

After the implementation of the system as discussed in chapters 3, 4 and 5 the rotor/flywheel is successfully suspended in 5-axes of freedom. A noise problem has however become apparent due to the high switching frequencies of the power amplifiers and the motor drive. The noise problem has influenced the maximum attainable value of the derivative constant ($K_D$) of each of the PD-controllers of the axes of the AMB system. The derivative constant had to be decreased from its determined value of 50 to a mere 30. When the derivative constant is increased beyond 30, the system becomes unstable due to the amplification of the noise within the system. This influences the maximum attainable damping of the AMB system.

## 6.2 Step response verification

By injecting a reference disturbance ($x_{dist}$) into the control loop as shown in Figure 6-1 and measuring the rotor deflection ($x_{ref}$), the equivalent stiffness and damping of the magnetic bearings can be obtained. A 10 µm step disturbance is introduced and the rotor deflection is measured and logged with the dSPACE controller.

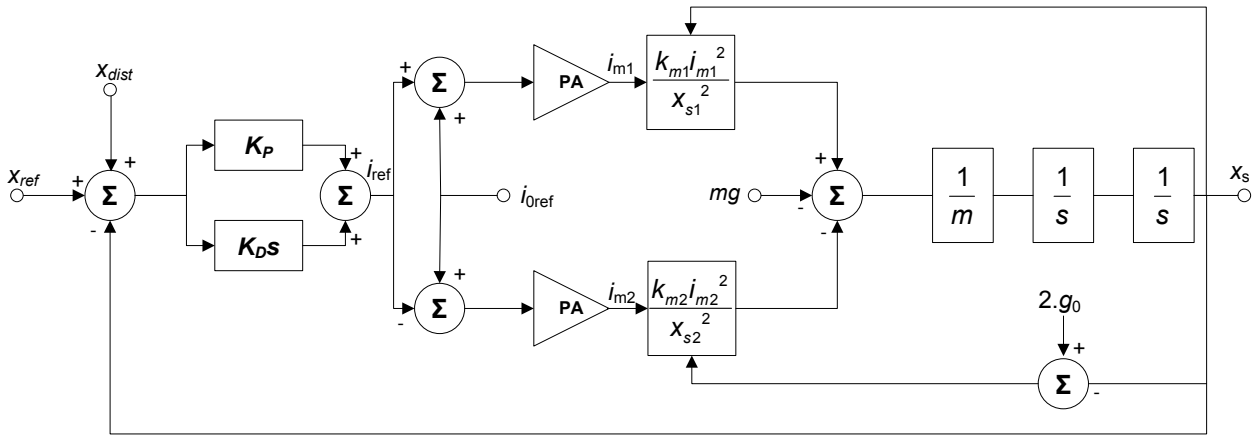


**Figure 6-1: Non-linear AMB model for step response measurement**

Figure 6-2 shows the response of the bottom radial AMBs' x-axis. A 10 µm step reference disturbance is applied to the rotor and the rotor deflection is measured. When the bottom radial AMB was disturbed the rotor/flywheel was pulled against the top AMB backup bearing. This ensures that the rotor/flywheel does not rotate about its centre of mass. From Figure 6-2 the simulated AMB response and the actual AMB response is shown to correlate closely. The actual equivalent stiffness is determined graphically to be $k_{eq}$ = 1.365 x $10^6$ N/m and the equivalent damping is determined to be $b_{eq}$ = 2.073 x $10^3$ N·s/m by making use of the percentage overshoot (P.O.), the damping ratio and the natural frequency as discussed in section 3.2.7. However with the presence of switching noise in the system, the equivalent stiffness and damping cannot be accurately determined.

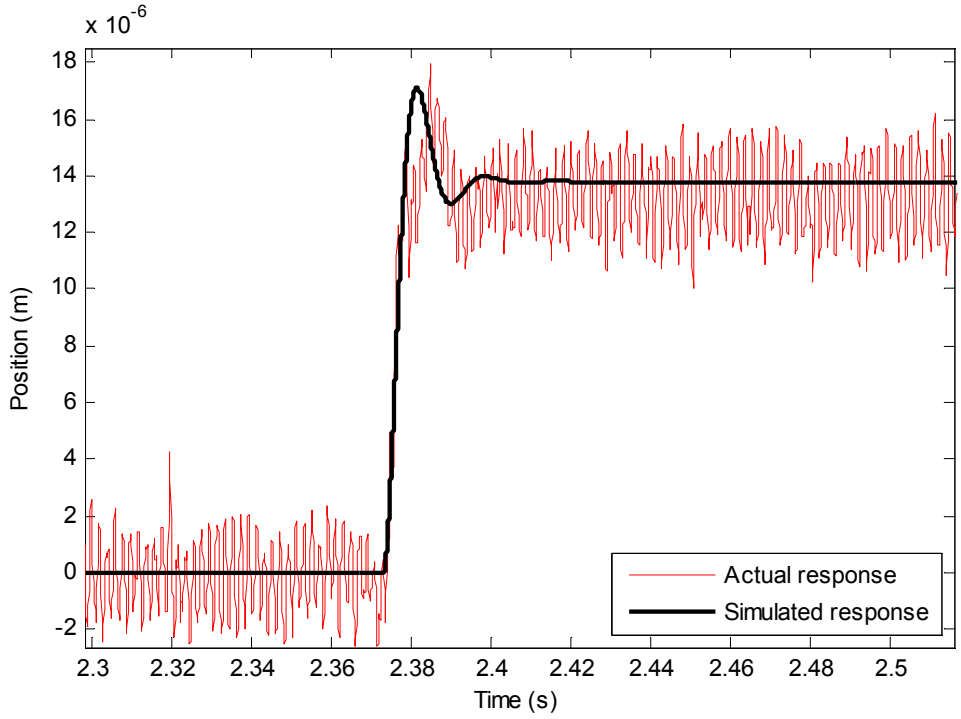


**Figure 6-2: Bottom radial AMB x-axis step response (10 µm disturbance)**

The actual stiffness and damping values correlate closely to the simulated equivalent stiffness $k_{eq\_simulated}$ = 1.18 x $10^6$ N/m and damping $b_{eq\_simulated}$ = 2.085 x $10^3$ N·s/m.

Figure 6-3 shows the step response of the bottom radial AMBs' y-axis. Here too a 10 µm step reference disturbance is applied. A slight deviation from the simulated results can be seen. This could be due to a gain discrepancy within the power amplifiers of the y-axis of the bottom AMB since the gains in the control loop are all identical. Further adjustment to the gains of the y-axis power amplifiers is needed. The actual equivalent stiffness ($k_{eq}$) is determined to be 1.285 x $10^6$ N/m and the actual equivalent damping ($b_{eq}$) is determined to be 1.952 x $10^3$ N·s/m. This also correlates closely to the simulated stiffness $k_{eq\_simulated}$ and equivalent damping $b_{eq\_simulated}$ as determined above.

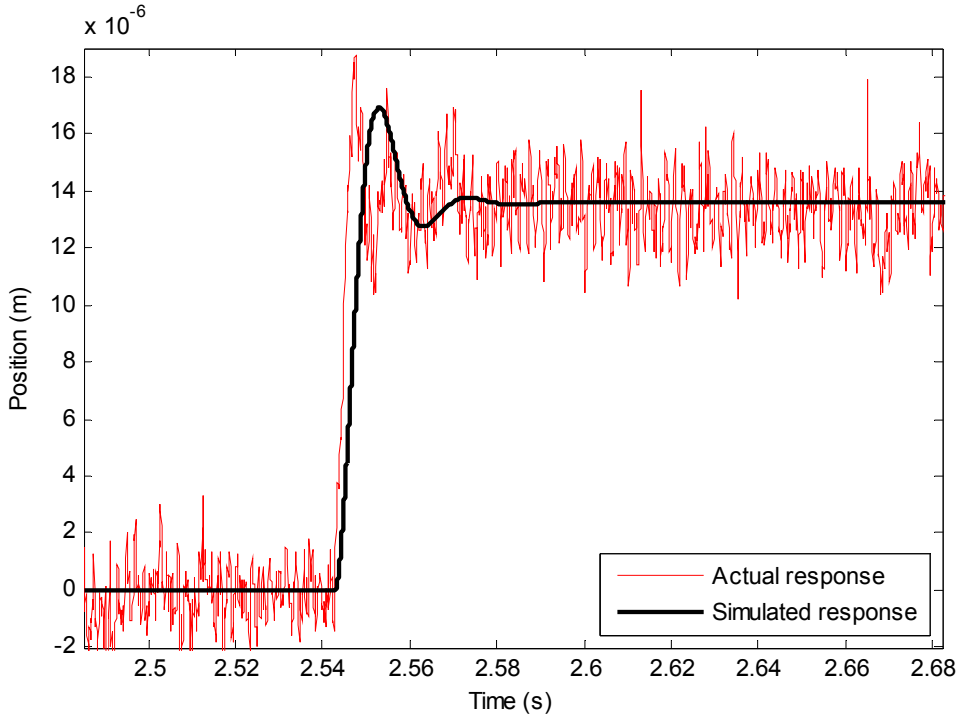


**Figure 6-3: Bottom radial AMB y-axis step response (10 µm disturbance)**

A 10 µm step reference disturbance is applied to the top radial AMBs' x-axis and the step response is shown in Figure 6-4. It can be seen that the overshoot of the actual step response is slightly higher than the simulated step response. This is due to the inertia of the rotor/flywheel at the top radial AMB since the equivalent mass of the rotor at the top AMB is 13.22 kg in comparison to the equivalent mass of the rotor at the bottom AMB which is 5.38 kg. The equivalent stiffness ($k_{eq}$) is graphically determined to be 6.381 x $10^5$ N/m and the equivalent damping ($b_{eq}$) is determined to be 1.437 x $10^3$ N·s/m. These values correlate closely to the simulated stiffness $k_{eq\_simulated}$ = 6.235 x $10^5$ N/m and the simulated damping $b_{eq\_simulated}$ = 1.625 x $10^3$ N·s/m. The values of the equivalent bearing stiffness and damping deviate from the design stiffness of 500 x $10^3$ N/m and the design damping of 2.5 x $10^3$ N·s/m and the deviations are discussed in chapter 7.

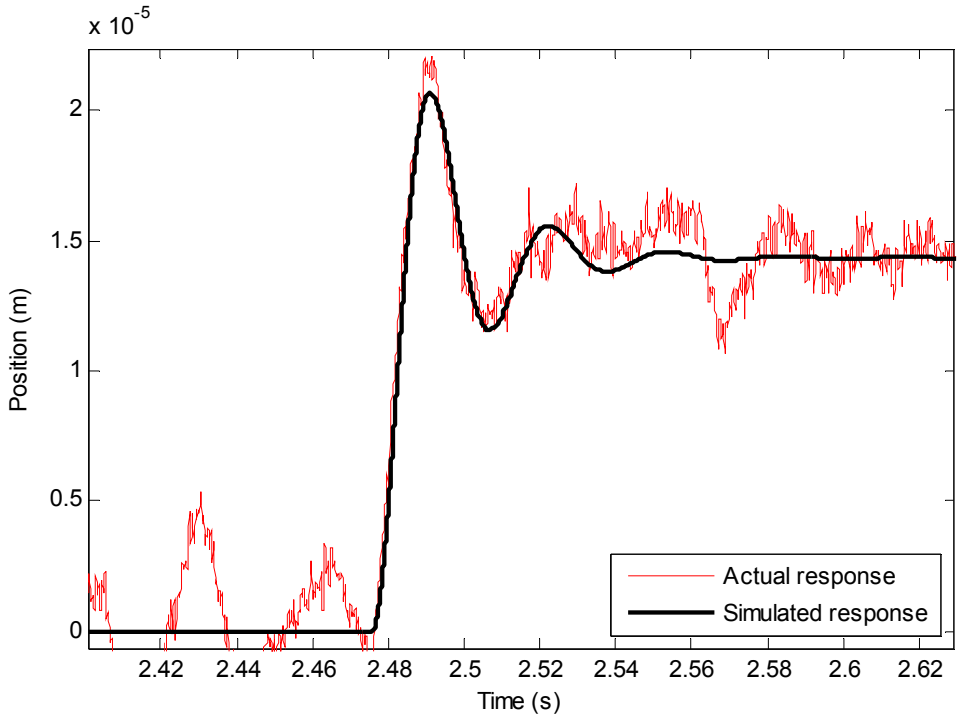


**Figure 6-4: Top radial AMB x-axis step response (10 µm disturbance)**

The step response of the top radial AMBs' y-axis is shown in Figure 6-5. It can also be seen that the overshoot due to the inertia of the rotor/flywheel is slightly above the simulated step response. The equivalent stiffness ($k_{eq}$) is graphically determined to be 7.156 x $10^5$ N/m and the equivalent damping ($b_{eq}$) is determined to be 1.478 x $10^3$ N·s/m.

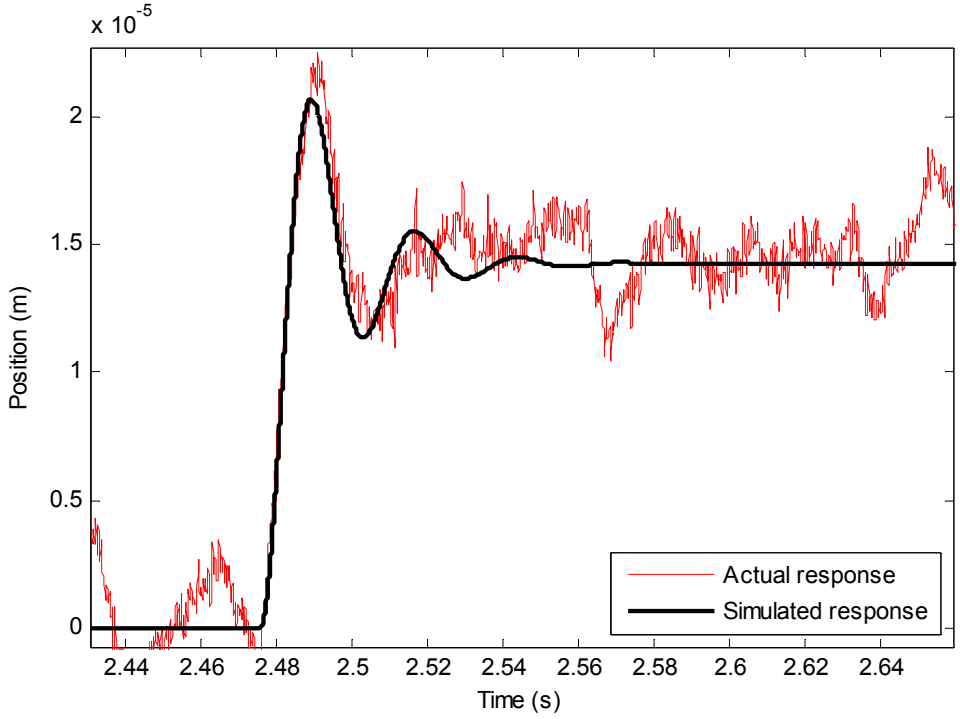


**Figure 6-5: Top radial AMB y-axis step response (10 µm disturbance)**

Finally the step response of the axial AMB is determined also by applying a 10 µm step reference disturbance to the rotor in the axial direction. Figure 6-6 shows the actual response as well as the simulated response of the axial AMB. It can be seen that the settling time of the actual system is lower than the simulated settling time. This may be because of a discrepancy in the weight of the rotor. The actual stiffness ($k_{eq}$) of the axial AMB is determined to be 8.442 x $10^5$ N/m and the actual damping ($b_{eq}$) is determined to be 2.374 x $10^3$ N·s/m. These values correlate closely to the simulated stiffness $k_{eq\_simulated}$ = 8.294 x $10^5$ N/m and damping $b_{eq\_simulated}$ = 2.251 x $10^3$ N·s/m.

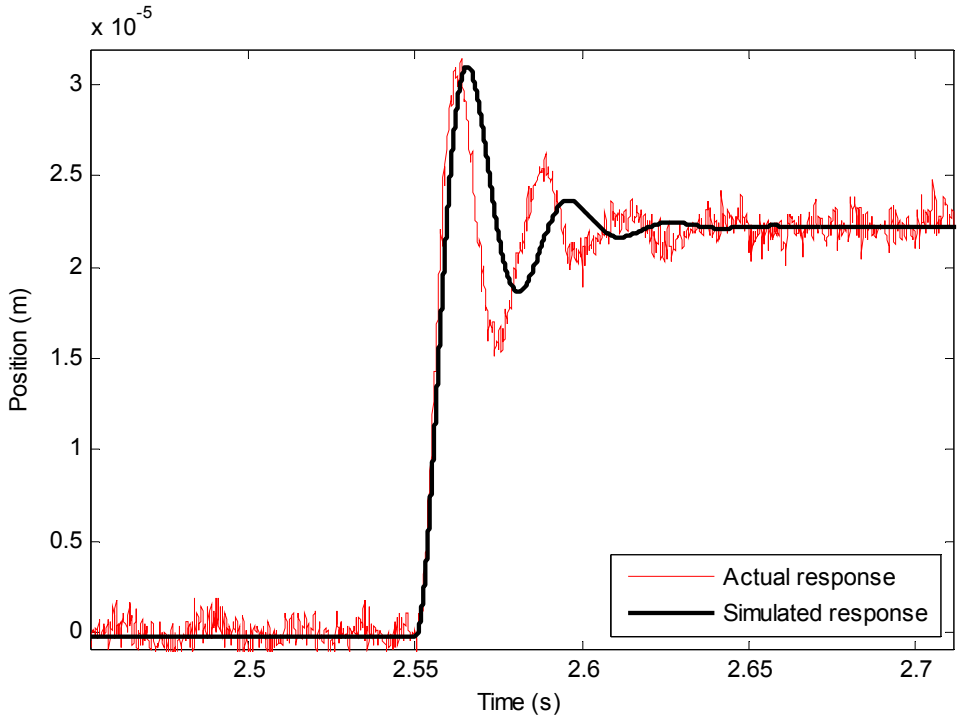


**Figure 6-6: Axial AMB step response (10 µm disturbance)**

## 6.3 System sensitivity verification

While passive bearings are almost stable systems, magnetic bearings are inherently unstable due to the negative stiffness resulting from static magnetic forces. The ISO CD 14839-3 standard is used to provide an evaluation method for the stability margin of AMBs as well as serve as a guideline to provide information on the stability margins of AMBs. Although the Nyquist plot can be used to determine marginal stability, the method proposed by ISO CD 14839-3 is the sensitivity function [18].

The sensitivity function is defined as the ratio of $v_R$ over $v_D$ where $v_D$ is a sinusoidal disturbance of which the frequency is varied. The system sensitivity (in dB) is obtained using (6-1).

$$G_s(s) = 20 \cdot \log\left(\frac{v_R(s)}{v_D(s)}\right) \qquad \textbf{(6-1)}$$

The non-linear AMB model shown in Figure 6-7 indicates where the disturbance signal ($v_D$) is injected into the control loop as well as the measured error signal ($v_R$).

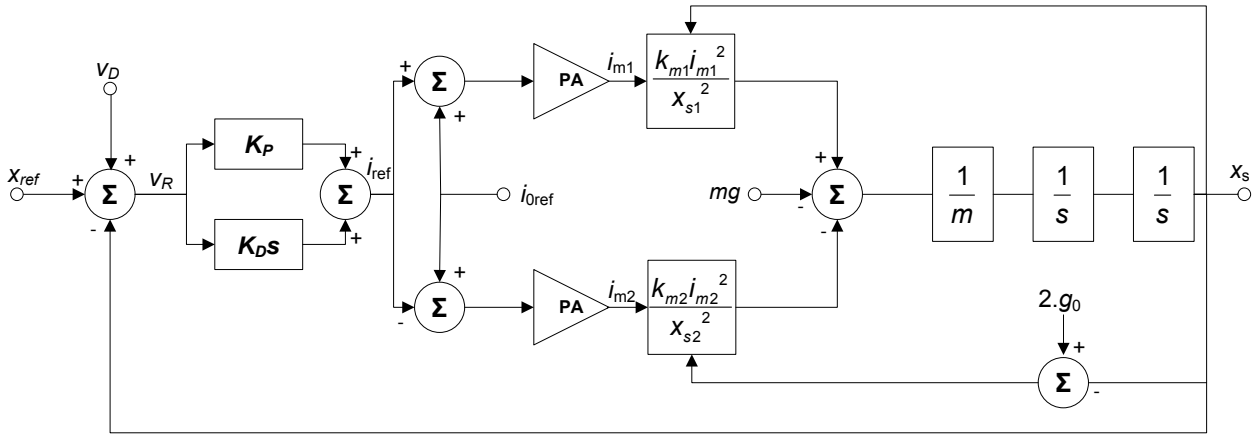


**Figure 6-7: Non-linear AMB model for sensitivity measurement**

The ISO CD 14839-3 standard specifies that the sensitivity has to be characterised up to a frequency ($f_{max}$) of the larger of three times the rated speed or a maximum frequency of 2 kHz. It also states that the stability margin of each axis of the AMB system have to be determined. The system's overall rating is determined by the worst rating of any of the measured axes.

The rotor system is required to behave stably for normal excitations and expected changes of the operating conditions. Therefore the measurement is taken at rotor standstill as well as at maximum continuous rated speed [18].

Figure 6-8 shows the sensitivity of the bottom radial AMB as a function of frequency. Since three times the rated speed translates to 1.5 kHz, the sensitivity analysis has to be done for a frequency range of 0 – 2 kHz. From Figure 6-8 the critical frequencies of the rotor can be seen, the first critical frequency situated at 48 Hz (2,880 rpm), the second critical frequency situated at 174 Hz (10,440 rpm) and the third critical frequency situated at 732 Hz (43,920 rpm). The sensitivity at the first critical frequency is -13.8 dB, the sensitivity at the second critical frequency is 7.37 dB and the sensitivity at the third critical frequency is 8.21 dB.

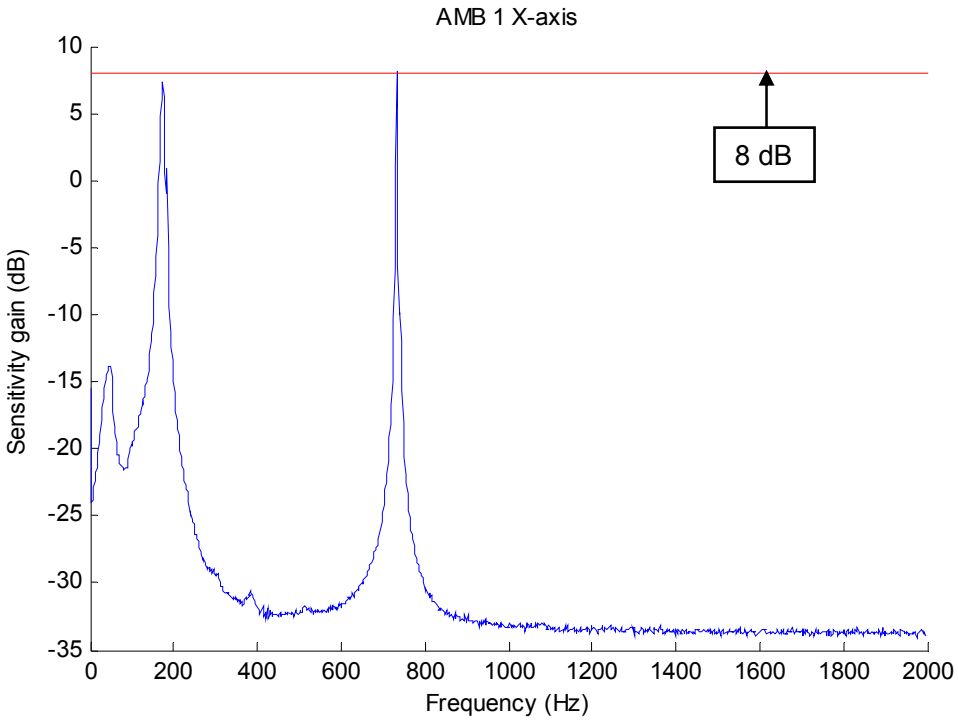


**Figure 6-8: Bottom radial AMB's sensitivity**

The sensitivity of the top radial AMB is shown in Figure 6-9. The sensitivity at the first critical frequency is -12.57 dB, the sensitivity at the second critical frequency is 1.09 dB and the sensitivity at the third critical frequency is -7.05 dB.

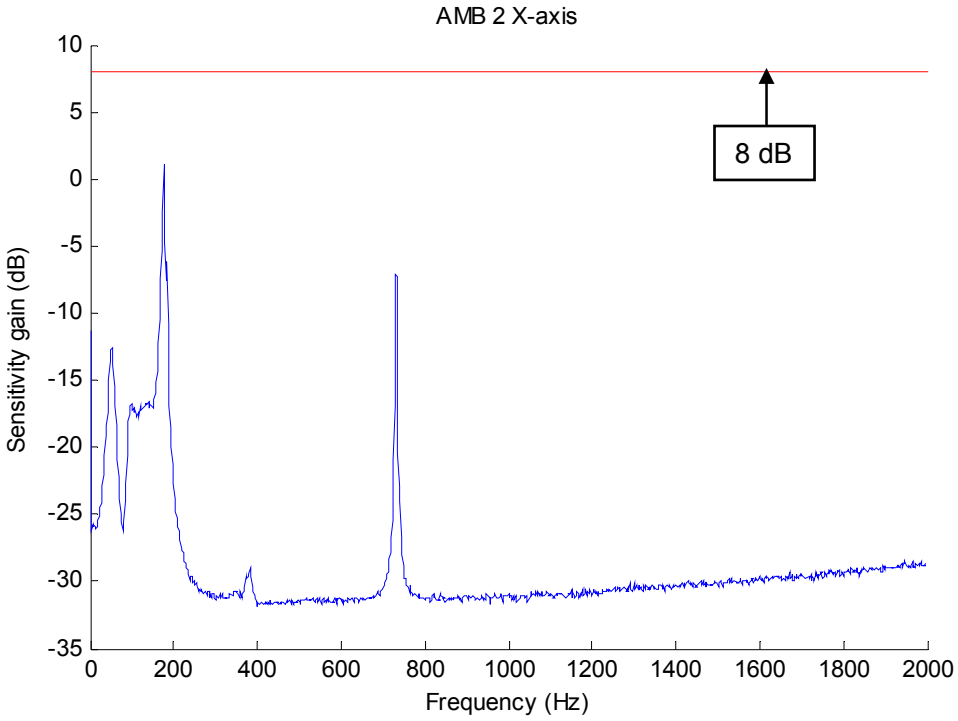


**Figure 6-9: Top radial AMB's sensitivity**

From Figure 6-8 and Figure 6-9 it can be seen that the sensitivity of the bottom radial AMB is much higher than the top radial AMB. As discussed in section 3.2.7 the equivalent mass of the rotor at the top radial AMB translates to 13.22 kg and the equivalent mass of the rotor at the bottom radial AMB translates to 5.38 kg. The difference in sensitivity of the top- and bottom radial AMBs is due to the difference in inertia of the rotor at the top- and bottom radial AMB.

Figure 6-10 shows the sensitivity of the axial AMB. The rotor has an axial critical frequency at 42 Hz at which the sensitivity of the axial AMB is -11.7 dB.

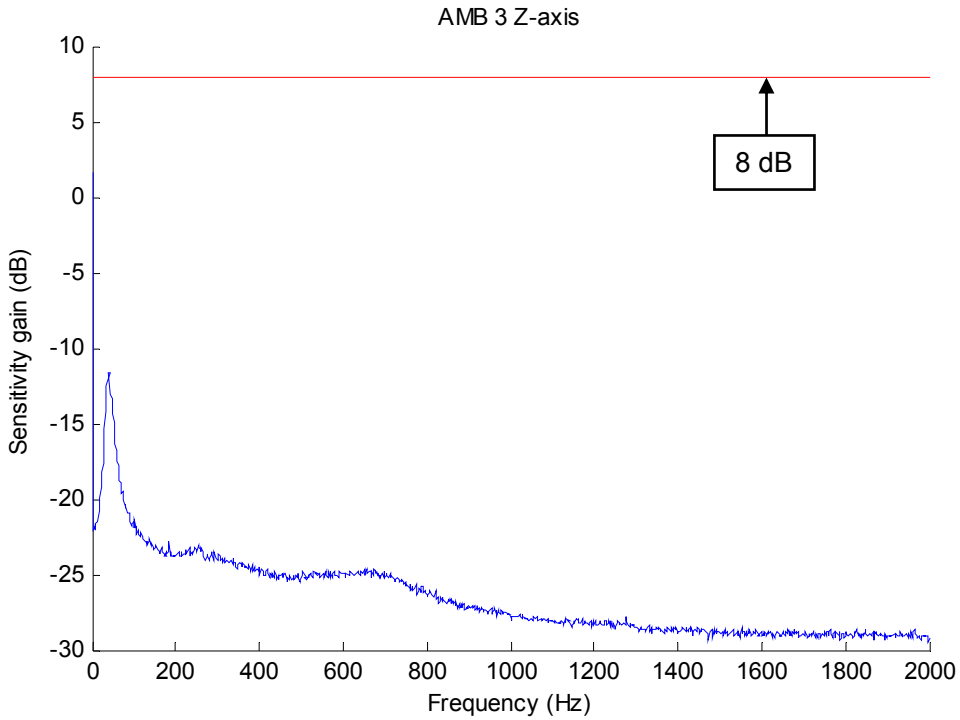


**Figure 6-10: Axial AMB's sensitivity**

In accordance to ISO CD 14839-3 the sensitivity function for newly commissioned AMB systems should fall within zone A. This implies that the sensitivity of the AMBs should fall below 8 dB. This international standard implies to industrial machines operating at nominal power greater than 15 kW and is not limited by size or operational speed [18].

**Table 6-1: Peak sensitivity at zone limits [18]**

| Zone | Peak sensitivity |
|---|---|
| A/B | 8 dB |
| B/C | 12 dB |
| C/D | 14 dB |

**Zone A**: The sensitivity functions of newly commissioned machines would normally fall within this zone.
**Zone B**: Machines with the sensitivity functions within this zone are normally considered acceptable for unrestricted long-term operation.
**Zone C**: Machines with the sensitivity functions within this zone are normally considered unsatisfactory for long-term continuous operation. Generally, the machine may be operated for a limited period in this condition until a suitable opportunity arises for remedial action.
**Zone D**: The sensitivity functions within this zone are normally considered to be sufficiently severs to cause damage to the machine.

From the sensitivity analysis shown in Figure 6-8, Figure 6-9 and Figure 6-10 it is established that the overall AMB system sensitivity falls within zone A since the maximum operating speed of the machine is 30,000 rpm (500 Hz). All three AMBs' sensitivity margins fall below 8 dB up to 732 Hz (43,920 rpm) where the bottom radial AMBs' sensitivity margin rises to 8.21 dB. The sensitivity of the bottom radial AMB may be improved by controller optimisation as well as bias current adjustment which will result in a sensitivity margin below 8 dB throughout the entire 0 – 2 kHz range.

*Chapter 6 discusses the three magnetic bearings' responses to a step reference disturbance as well as the sensitivity of the three AMBs in accordance to the ISO CD 14839-3 standard. Conclusions and recommendations will be made in Chapter 7.*

# 7
# Chapter
# Conclusions and recommendations

*Chapter 7 starts off with a discussion on the stiffness and damping discrepancies encountered after experimental characterisation. This is followed by conclusions drawn with regards to the active magnetic bearings as well as the electrical enclosure. Finally future work on the system is discussed followed by a closure statement.*

## 7.1 Stiffness and damping discrepancies

As mentioned in chapter 6, the equivalent stiffness of the radial AMBs is significantly higher than the design stiffness of 500 x $10^3$ N/m. This is due to an adjustment made on the bias levels of the radial AMBs in an attempt to ensure more stable operation since there is an unbalance on the rotor/flywheel. The bias current ($I_0$) levels were adjusted from 2.06 A to 2.54 A. This increased the current gain ($k_i$) from 24.8 to 30.48. It also decreased the position stiffness ($k_s$) from -1.025 x $10^5$ N/m to -1.548 x $10^5$ N/m. The PD-controllers' proportional constant ($K_P$) is however kept at its original value of 14213. From (7-1) it can be seen that the increase in $k_i$ and $k_s$ results in an increased equivalent stiffness.

$$k_{eq} = 2 \cdot K_p \cdot k_i + 2 \cdot k_s \qquad \textbf{(7-1)}$$

The deviation in equivalent stiffness of the radial AMBs can however be rectified by determining the proportional constants of the PD-controllers in accordance to the adjusted current gain and position stiffness. A proportional constant ($K_P$) value of 13,280 will result in the design equivalent stiffness of 500 x $10^3$ N/m.

Another cause of the deviation in bearing stiffness may be the actual air gaps of the radial AMBs. Since the radial AMB stators were vacuum impregnated with resin, the actual air gaps may have been decreased due to resin build-up on the pole faces. The air gaps influence the position stiffness ($k_s$) and the current gain ($k_i$) of the AMB as can be seen in (3-33) and (3-34). This in turn influences the equivalent stiffness of the AMBs.

The deviations in the damping of the radial AMBs as mentioned in chapter 6 are due to the fact that the differential constant ($K_D$) of the PD-controllers had to be lowered from 50 to 30. This is due to the

high switching noise within the electrical enclosure caused by the power amplifiers and the motor drive. By experimentation the maximum attainable value of the differential constant is determined to be 30. When the differential constant is increased above 30 the radial AMBs become unstable due to the amplification of the noise within the system. From (7-2) the maximum attainable equivalent damping ($b_{eq}$) is determined to be 1.828 x $10^3$ N·s/m with $K_D$ = 30 and $k_i$ = 30.48.

$$b_{eq} = 2 \cdot K_D \cdot k_i \tag{7-2}$$

In order for the radial AMBs to achieve the design stiffness of 500 x $10^3$ N/m and damping of 2.5 x $10^3$ N·s/m the bias current levels can be increased.

**Table 7-1: Proposed controller adjustments**

| Parameter | Current value | Adjusted value |
|---|---|---|
| Bias current | $I_0$ = 2.54 A | $I_0$ = 3.45 A |
| Current gain | $k_i$ = 30.48 | $k_i$ = 41.4 |
| Position stiffness | $k_s$ = -1.548 x $10^5$ | $k_s$ = -2.857 x $10^5$ |
| Proportional constant | $K_P$ = 14,213 | $K_P$ = 12,939 |
| Differential constant | $K_D$ = 30 | $K_D$ = 30.2 |

Table 7-1 shows the proposed PD-controller adjustments which can be made in order for the radial AMBs to achieve the design stiffness and damping specification. A drawback however of adjusting the bias current level to 3.45 A is that the control current is then limited to a mere 1.55 A.

The deviations in stiffness and damping of the axial AMB as mentioned in chapter 6 are due to the difference in air gaps due to the modular designs of the Fly-UPS mechanical enclosure [16]. Since the mechanical enclosure is made up of 7 modules the build-up in tolerances influences the air gaps of the axial AMB. The bias current levels of the axial AMB had to be adjusted in order to achieve stable suspension of the rotor/flywheel in the axial direction. As mentioned above the adjustment of the bias current levels influences the current gain and positions stiffness which in turn influences the equivalent stiffness and damping of the magnetic bearing. An accurate measurement has to be done to determine the actual air gaps of the axial AMB which will then be used to determine the optimal proportional- and derivative constants for the PD-controller of the axial AMB.

Since the simulated and the actual results correlate so closely, the simulation can be used to investigate the deviations of the actual results. Simulation parameters such as the air gap and the bias current can be manipulated in order to determine the cause of the discrepancy of the bearing stiffness.

## 7.2 Conclusion

### *7.2.1 Active magnetic bearings*

The two radial- and one axial AMBs were designed by making use of the design procedures outlined in chapter 3. The output parameters of the AMB designs were implemented in a MATLAB® model in order to simulate the response of the AMBs. The radial- and axial AMBs' responses to a step reference disturbance were verified as well as the response to a sinusoidal disturbance force. The simulation also verified the dynamic stiffness of the radial AMBs to be above the necessary stiffness throughout the operating range. After the simulation of the AMBs had been completed and satisfactory results were obtained, the AMBs were implemented.

The implemented AMBs' performance was verified to ensure that the performance requirements were met. The stiffness and damping were verified through input response. From the experimental results, the performance of the AMBs was determined to be in accordance to the specification set by the rotor-dynamic analysis of the rotor/flywheel. The sensitivity of the AMBs was also determined in accordance to the ISO CD 14839-3 standard. From the experimental results it is concluded that the magnetic bearing system falls within zone A which is the ISO standard for newly commissioned magnetic bearings. The design process was also verified since the simulated and the actual results correlate so closely.

### *7.2.2 Electrical enclosure*

The design procedure outlined in chapter 4 was used to implement the electrical system and produced outstanding results. All of the electrical sub-systems were integrated into one industrial electrical enclosure. The various sub-systems were interfaced with the dSPACE® controller which controls the entire Fly-UPS system via a GUI on a stand-alone personal computer. The functionality of each of the electrical sub-systems was verified to ensure that the type-B specification of the electrical system was met and to ensure safe operation of the Fly-UPS system.

The emergency stop functionality of the electrical system was also verified to ensure that the energy stored in the rotor/flywheel can safely be dissipated in the resistor bank in order to bring the rotor/flywheel to a stop in an emergency situation.

## 7.3 Future work

### *7.3.1 Full-speed testing*

Full speed testing cannot yet be performed on the Fly-UPS system due to safety concerns. Since the rotor/flywheel operates at 30,000 rpm and stores 527 kJ of energy, safety is an issue to be addressed. Sandbags have to be stacked around the mechanical enclosure in order to dissipate the energy of the rotor/flywheel since the aluminium mechanical enclosure is not able to contain the rotor/flywheel in the case of a critical failure. The area in which the Fly-UPS is operated has to be inspected and a safety assessment has to be done in order to ensure the safety of personnel.

### *7.3.2 PMSM drive*

The PMSM drive is also developed within the McTronX research group as part of a Masters study. The reliability of the drive is however still in question since it is a first generation prototype. Further development is needed to produce a second generation drive which is more reliable and has lower losses. A digital PMSM drive is also an option which may be investigated since the reference inputs of digital drives is not as susceptible to high switching noise as analog drives. Lower noise within the system will improve the performance of the AMBs of the Fly-UPS system.

### *7.3.3 Speed sensor*

As mentioned in chapter 4 the electrical system makes use of a dedicated speed sensor which senses the rotational speed of the rotor/flywheel. The speed sensor has not yet been interfaced with the dSPACE® controller to log the actual speed of the rotor/flywheel. The speed sensor is equipped with an RS-485 communications bus, but the dSPACE® system does not yet feature RS-485 communications functionality. A separate communications board will have to be acquired and installed in the dSPACE® system to interface the speed sensor with the dSPACE® controller and give extra functionality to the dSPACE® controller for further development of the Fly-UPS system.

### *7.3.4 Power amplifiers*

A major issue within the electrical system is switching noise. One of the greatest sources of noise within the electrical system is the power amplifiers switching at 36 kHz. The noise problem can be greatly reduced if the PWM generation of the power amplifiers can be synchronised with the control cycle and specifically the A/D sampling rate of 10 kHz of the position signals. The AMC® power amplifiers do not have PWM synchronisation functionality. Further investigation needs to be done in order to devise a synchronisation circuit that will be able to synchronise the PWM generation of all ten power amplifiers within the system.

Another area that needs to be investigated is the use of digital power amplifiers operating on a bus architecture. This will greatly reduce the noise problems within the electrical system and will also improve the reliability of the Fly-UPS system.

### *7.3.5 Single board computer*

In order to deliver a fully industrial standard Fly-UPS system, the size of the electrical control system needs to be reduced and the reliability of the system has to be ensured. Since dSPACE® is a development tool, a dedicated controller has to be implemented. A way of ensuring a more compact, more reliable and industrial standard electrical system is to make use of an industrial single-board computer to control the FLY-UPS system. The controller needs to be connected to the PAs and the sensors via a bus architecture ensuring full industrial compliance and a reduced size of the control unit.

## 7.4 Closure

The aim of the project was to develop a fully suspended active magnetic bearing system for a high-speed flywheel application. The system had to magnetically suspend a rotor/flywheel in five axes of freedom at an operating speed of 30,000 rpm. An industrial electrical control enclosure also had to be devised in order to house the electrical control system for the FLY-UPS system. From the results it can be seen that the main goals of the project have been reached. The system is fully functional and is delivered to and industrial standard. The rotor/flywheel however displayed an unbalance which made it impossible to rotate the rotor/flywheel at its rated speed of 30,000 rpm. The project serves as a baseline for further research on AMBs and high-speed flywheels. The developed AMB system is the first fully suspended AMB system within the McTronX research group.

# *APPENDIX*

## *Appendix A: Type-A specification*

**TITLE:** SYSTEM SPECIFICATION FOR THE HIGH SPEED AMB FLYWHEEL ENERGY STORAGE SYSTEM (FLY-UPS)

**DOCUMENT NUMBER:** TYPE-A

**VERSION:** A

**APPROVAL:**

| **NWU PUKKE** | |
|---|---|
| Signature: | Signature: |
| Name: JJ Janse van Rensburg | Name: Eugen Ranft |

# Table of Contents

**Page**

# SYSTEM SPECIFICATIONS FOR THE HIGH-SPEED ACTIVE MAGNETIC BEARING (AMB) FLYWHEEL ENERGY STORAGE SYSTEM

## SCOPE

This document defines the system requirements for the high speed AMB flywheel energy storage system (FLY-UPS).

## IDENTIFICATION

HSAFESS01, high speed AMB flywheel energy storage system, FLY-UPS

## DESCRIPTION OF TYPE OF SYSTEM

The FLY-UPS is a vertical flywheel system and consists of:

- 1 Mounting
- 1 Flywheel
- 2 Radial AMBs
- 1 Axial AMB
- 1 Motor
- Electrical control enclosure

## REQUIREMENTS

## SYSTEM DEFINITION

### *General description*

The FLY-UPS supplies uninterrupted power to a load of at least 300 W for at least 15 minutes. The system uses a magnetically suspended flywheel to store energy gained from a high-speed motor/generator, the energy gained from the motor is then used to power a load of 300 W for 15 minutes or more.

### *Operational requirements*

#### *Need*

The need for such an energy storage system has become apparent in the use of emergency backup power systems. The backup generators needs time to start up, this system will be the “in-between” system for equipment that is sensitive to such power outages or dips in mains power.

***Mission***
The mission of this first phase development is to be able to study the uses of flywheel energy storage thus enabling the production of larger scale flywheel systems, in areas such as renewable energy

***Use profile***
The usage of such a system is of such a nature that it will always be running in the a mode of energy input, but energy will only be extracted from the system during a power dip or a power failure.

***Distribution***
The FLY-UPS will be installed in the AMB laboratory of the North-West University.

***Life cycle***
The system will be designed for a life cycle of 8 years.

## *Maintenance concept*

A modular approach to maintenance will be used where the system will be divided into smaller system which can be replaced if failure occurs. Thus a Corrective Maintenance policy will be used in this system with the possibility of investigating preventative maintenance on later systems.

## *Functional analysis and system definition*

The functions of the system are:

- To enable further research into Flywheels and AMBs as well as to enhance the collaboration between the mechanical and electrical departments on the North-West University.
- To enhance the knowledge on systems engineering in the electrical engineering department.
- To establish a knowledge base in the field of mechatronics within the faculty.

## *Allocation of Requirements*

FLY-UPS:

Time power level can be maintained

| | |
|---|---|
| 300 W (NET) mode: | 15 minutes |
| 1100 W (NET) mode | 5 minutes |

| | | |
|---|---|---|
| A_o= | 0.9835 | (Operational availability) |
| A_i= | 0.9997 | (inherent availability) |
| MTBM= | 10 000 hr | (Mean Time Between Maintenance) |
| MTBF= | 20 000 hr | (Mean Time Between Failure) |
| MDT= | 168 hr (1week) | (Maintenance downtime) |
| Mct= | 6hr | (Mean corrective maintenance time) |

| | | |
|---|---|---|
| MLH/OH= | 0.0006 | (Maintenance labour hours per operating hour) |
| Cost | R300 000 | |
| Skill level needed: | High (For Maintenance) - Low (for Operation) | |

# SYSTEM CHARACTERISTICS

## *Performance Characteristics*

The FLY-UPS's rotational speed needs to be at least 28 000 RPM.

The FLY-UPS has to be able to supply 300W of uninterrupted power after mains power is shut off.

## *Physical Characteristics*

The FLY-UPS should not exceed 1.2m X 1.2m X 1.5m (L X B X H)

Should not weigh more than 200 kg

## *Effectiveness Requirements*

The FLY-UPS needs to be at least 85% efficient when operating in a near vacuum

## *Reliability*

The FLY-UPS should be able to run continuously for 10 000 hours with at least 25 full-rundown cycles.

## *Maintainability*

The FLY-UPS will use a modular maintenance policy. The different components should be able to be replaced by another module within 3 hours

## *Usability (human factors)*

The FLY-UPS has to be able to be used by unschooled labour, but the maintenance requires schooled labour. Modular replacement of components should be able to be done by unschooled labour.

# NOTES

## PROPOSED USES OF FLY-UPS

The use of the FLY-UPS will primarily be for researching and developing other Flywheel and AMB systems. The FLY-UPS may also be used for testing advanced control algorithms. The FLY-UPS is one of the first steps for developing a flywheel based renewable energy system.

# *Appendix B: Type-B specification*

**TITLE:** SUB-SYSTEM SPECIFICATION FOR THE HIGH SPEED AMB FLYWHEEL ENERGY STORAGE SYSTEM (FLY-UPS)

**DOCUMENT NO:** TYPE B

**VERSION:** D

**APPROVAL:**

| **NWU PUKKE** | |
|---|---|
| Signature: | Signature: |
| Name: S. Myburgh | Name: Eugen Ranft |

# TABLE OF CONTENTS

Page

# TYPE B SPECIFICATION OF THE FLY-UPS SYSTEM

## SCOPE

This document specifies the requirements on the sub-systems of the FLY-UPS system.

## APPROPRIATE DOCUMENTS

### STANDARDS

| | |
|---|---|
| API 612 | Petroleum, petrochemical and natural gas industries - -steam turbines – special-purpose applications |
| ISO/CD 14839-3 | mechanical vibration – vibration of rotating machinery equipped with active magnetic bearings – Part 3: Evaluation of stability margin |
| ISO/FDIS 14839-2 | mechanical vibration – vibration of rotating machinery equipped with active magnetic bearings – Part 2: Evaluation of vibration |
| ISO 1940/1 | Balance quality Requirements of rigid rotors |

MIL-STD-1472 Department of defence design criteria – Human engineering

## REQUIREMENTS

### ITEM DEFINITION

The FLY-UPS system's main purpose is to serve an uninterrupted power supply system. Secondly the system will be used for future research in self-sensing and motor drive development.

## *ITEM DIAGRAM*

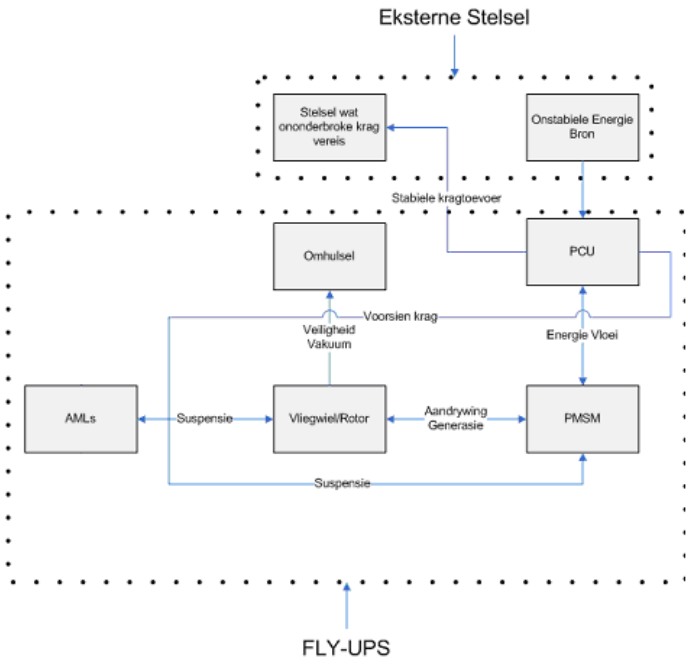


Note: AMB active magnetic bearing

PCU power conversion unit

The FLU-UPS consists of 5 basic components namely:

- PCU
- Enclosure
- PMSM
- Rotor
- AMBs

## *INTERFACE DEFINITION*

The system interfaces with the following conditions:

The air pressure of the surroundings: 1 atm.

The physical surroundings the FLY-UPS should fit through a standard door (780 x 2100mm).

## *MAIN COMPONENT LIST*

***Radial AMBs (x2)***
***Axial AMB (x1)***
***Permanent magnet machine (x1)***
***Flywheel/rotor assembly (x1)***
***Flywheel/rotor enclosure (x1)***

# CHARACTERISTICS

## *PERFORMANCE*

| | | | |
|---|---|---|---|
| 3.2.1.1 | Minimum gross power: | 2000 | W |
| 3.2.1.2 | Minimum net power: | 1300 | W |
| 3.2.1.3 | Unbalance | ISO G6.3 | ISO1940/ 1 |
| 3.2.1.4 | Minimum time of power output | 3 | Min |
| 3.2.1.5 | Life cycle: | 10 | year |
| 3.2.1.6 | Maximum rotational speed for trip | 30000 | RPM |

## *PHYSICAL CHARACTERISTICS*

| | | | |
|---|---|---|---|
| 3.2.2.1 | Maximum mass of each module | 25.4 | kg |
| 3.2.2.2 | Maximum sizes: | | |
| | Flywheel diameter | 300 | mm |
| 3.2.2.2.1 | FLY-UPS diameter | 500 | mm |
| | Rotor-length | 500 | mm |
| 3.2.2.2.2 | FLY-UPS height | 700 | mm |

## *SERVICEABILITY*

| | | | |
|---|---|---|---|
| 3.2.4.1 | Mean time to repair (MTTR): | 1,0 | h |
| 3.2.4.2 | Skill level of maintenance personnel: | high | |

### *ENVIRONMENTAL FACTORS*

| | | | |
|---|---|---|---|
| 3.2.5.1 | Maximum temperature: | 30,0 | °C |
| 3.2.5.2 | Minimum temperature: | 0 | °C |
| 3.2.5.3 | Maximum relative humidity: | 80,0 | % |
| 3.2.5.4 | Minimum relative humidity: | 5,0 | % |

# DEVELOPMENT

### *COMPONENTS*

Standard items will be used as much as possible.

### *ELECTROMAGNETIC RADIATION*

(To be determined at a later stage).

### *SAFETY*

A minimum factor of safety of 1.5 (based on the von Misses stress) will be used throughout the design phase.

### *ERGONOMIC FACTORS*

***The noise that the FLY-UPS produces should be less than 80dB.***
***For the handling of modules the standard MIL-STD-1472 is applicable.***

# DOCUMENTATION

The minimum required documentation is a design report.

# LOGISTICS

### *MAINTENANCE*

The maintenance philosophy is a modular replacement of failed or near failed components.

### *FACILITIES AND EQUIPMENT*

A safety room will be built for the testing purposes of the FLY-UPS system

# PERSONNEL AND TRAINING

### *PERSONNEL*

Item design personnel

| Item | No. of personnel | Training level | |
|---|---|---|---|
| **FLY-UPS** | 6 | High | |

Operational personnel: 1

Service personnel: 1

### *TRAINING*

Training takes place at North-West University within the McTronX research group.

# MAIN COMPONENT CHARACTERISTICS

## *Radial AMB*

#### *PERFORMANCE*

| | | | |
|---|---|---|---|
| 3.7.1.1.1 | Maximum power used per radial AMB: | 100 | W |
| 3.7.1.1.2 | Minimum force applied to rotor by AMB | 150 | N |
| 3.7.1.1.3 | Maximum allowable displacement of rotor | 0.35 | mm |

## *Axial AMB*

#### *PERFORMANCE*

| | | | |
|---|---|---|---|
| 3.7.2.1.1 | Minimum force applied to the rotor by the upper axial AMB unit | 517 | N |
| 3.7.2.1.2 | Minimum force applied to the rotor by the | 100 | N |

| | | | |
|---|---|---|---|
| | lower axial AMB unit | | |
| 3.7.2.1.3 | Maximum allowable displacement of rotor | 0.35 | mm |
| 3.7.2.1.4 | Maximum power usage | 40 | W |

## *PERMANENT MAGNET SYNCHRONOUS MACHINE*

### *PERFORMANCE*

| | | | |
|---|---|---|---|
| 3.7.3.1.1 | Minimum power output at 15000 rpm: | 2000 | W |
| 3.7.3.1.2 | Trip speed | 33,000 | rpm |
| 3.7.3.1.3 | Operating speed | 30,000 | rpm |

## *FLYWHEEL/ROTOR*

### *PERFORMANCE*

| | | | |
|---|---|---|---|
| 3.7.4.1.1 | Minimum energy storage potential | 550 | kJ |
| 3.7.4.1.2 | Maximum losses | 100 | W |
| 3.7.4.1.3 | Maximum unbalance | ISO 6.3G | ISO 1940/1 |
| 3.7.4.1.4 | Design rotational speed | 30,000 | rpm |

### *FLYWHEEL/ROTOR ENCLOSURE*

#### *PERFORMANCE*

| | | | |
|---|---|---|---|
| 3.7.5.1.1 | Maximum absolute pressure inside enclosure | 50 | kPa |

#### *PHYSICAL CHARACTERISTICS*

| | | | |
|---|---|---|---|
| 3.7.5.2.1 | Maximum sizes: | | |
| | Enclosure diameter | 500 | mm |
| | Enclosure height | 700 | mm |

## IMPORTANCE

The relative importance of the characteristics of the FLY-UPS is shown in table 3.8.1, a scale of 1 (min) to 9 (max) is used to define the relative importance.

**TABLE 3.8.1: IMPORTANCE TABLE**

| No | Ref. No. | PARAMETER | IMPORTANCE |
|---|---|---|---|
| 3.8.1 | 3.1 & 3.7.4.1.1 | Energy storing capabilities | 9 |
| 3.8.2 | 3.2.1.5 | Life-cycle | 5 |
| 3.8.3 | 3.2.3 | Reliability | 7 |
| 3.8.4 | | Cost | 2 |
| 3.8.5 | 3.2.2.1 | Mass | 4 |
| 3.8.6 | 3.3.4 | Human factors | 4 |
| 3.8.8 | 3.2.4<br>3.5.1 | Serviceability | 5 |
| 3.8.9 | 3.2.5 | Operational environment conditions | 8 |

# *Appendix C: Photos of completed system*


**Figure C - 1: Control computer an GUI interface**

**Figure C - 2: Final hardware installation**

# *Appendix D: Data CD*

## *D.1: MATLAB® code*

## *D.2: Simulink® models*

## *D.3: MathCAD® designs*

## *D.4: Electronic system designs*

## *D.5: SolidWorks® drawings*

## *D.6: Photos*

# *REFERENCES*


[1] Bolund, B., Bernhoff, H., Leijon, M., 2005. Flywheel energy and power storage systems, Renewable and Sustainable Energy Reviews, xx 1-25

[2] Alternative Energy Storage Methods. [Online]. Available: www.mpoweruk.com, [Date of access: April 2006].

[3] Chris Ellis, “Flywheel Power to Increase Hybrid Efficiency”. [Online]. Available: www.hybridcars.com/technology.html, [Date of access: January 2006].

[4] O.J. Fiske, M.R. Ricci, “Third Generation Flywheels For High Power Electricity Storage”, *LaunchPoint Technologies, Inc., Goleta, California, USA*

[5] Active Power, Cleansource Flywheel Technology. [Online]. Available: http://www.activepower.com/index.asp?pg=technology_typical _application, [Date of access February 2006].

[6] Flywheels and energy Storage. [Online]. Available: http://zebu.uoregon.edu/ 1996/ph162/10a.html. [Date of access: March 2006].

[7] G. Schweitzer, H. Bleuler, A. Traxler, “Active Magnetic Bearings: Basics, Properties and Applications of Active Magnetic Bearings”, Authors Reprint, Zürich, 2003.

[8] Revolve Magnetic Bearings Inc. Magnetic bearings. [Online]. Available: http://www.revolve.com/Technology/magbearings.html, [Date of access: February 2003].

[9] dSPACE Solutions for Control. [Online] available http://www.dspace.de/ww/en/pub/home.htm [Date of access: March. 2004].

[10] M.E.F. Kasarda, “An Overview of Active Magnetic Bearing Technology and Applications,” The Shock and Vibration Digest, vol. 32, No. 2, pp. 91-99, March 2000.

[11] P.Allaire, C.R. Knospe, *et al*, “Short course on magnetic bearings”, Alexandria Virginia United Stetes of America: University of Virginia 1997.

[12] T.E. Seiphethlo, “Power electronic activation for active magnetic bearings,” Dissertation M.Eng North-West University, Potchefstroom Campus, 2006

[13] E.O. Ranft, “The development of a flexible rotor active magnetic bearing system,” Dissertation M.Eng North-West University, Potchefstroom Campus, 2005

[14] Magnetic Bearings. [Online]. Available: http://www.calnetix.com/howbearingswork.cfm, [Date of access: March 2006].

[15] F. Worlitz, H. Stegemann, T. Rottenbach, A. Dörrer, R. Hampel, “Simulation-based design method of active magnetic bearings according to the criterion of dynamic stiffness (DDS)”, Institute of Process Technique, Automation and Measurement Technique, University of Applied Science Zittau/Görlitz

[16] J.J. Janse van Rensburg, " Development of a flywheel energy storage system – uninterruptable power supply (FLY-UPS)", Dissertation M.Eng North-West Iniversity, Potchefstroom Campus, 2007

[17] B. B. Banerjee and L. E. Barrett. (June, 1988). Analysis and design of magnetic thrust bearings. ROMAC Report NO. 277.

[18] ISO TC108/SC2/WG7, "Active magnetic bearing – Evaluation of stability margin," ISO CD148393-3, Oct. 7, 2003

[19] Ron Mancini, "Op amp's for everyone," Newnes, 2003, pp. 174-191.

[20] Stuart Ball, "Analog interfacing to embedded microprocessors: Real world designs," Newnes , 2001, pp.47–58.